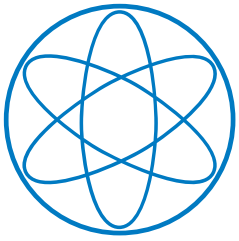

Fakultät für Physik

Fundamental physics with neutrons

Creation of ultra-low remanent fields and homogeneous NMR fields for precision experiments

Stefan A. Stuiber

Vollständiger Abdruck der von der Fakultät für Physik der Technischen Universität München zur Erlangung des akademischen Grades eines

Doktors der Naturwissenschaften (Dr. rer. nat.)

genehmigten Dissertation.

Vorsitzender:	Prof. Dr. Alejandro Ibarra
Prüfer der Dissertation:	
1.	Prof. Dr. Peter Fierlinger
2.	Prof. Dr. Lothar Oberauer

Die Dissertation wurde am 30.04.2018 bei der Technischen Universität München eingereicht und durch die Fakultät für Physik am 25.05.2018 angenommen.

Abstract

A non–zero electric dipole moment (EDM) of a fundamental quantum system is a manifestation of a process violating charge (C) and parity (P) symmetry. The neutron is a prominent example of such a system due to its comparably easy to understand structure. To explain the dominance of matter over anti-matter in the universe, new sources of CP violation are necessary, as the ones from the Standard Model (SM) are not sufficient. Since CP violation from the SM causes only very small EDMs, searches for EDMs turn out to be an important probe for physics beyond the Standard Model (BSM).

The next generation of nEDM experiments aims to improve the current limit of $d_n = 3 \times 10^{-26}$ ecm by two orders of magnitude. Consequently, unprecedented control over systematic effects is required. One main class of systematics is comprised of many effects related to magnetic fields. In order to reach the projected sensitivity of 10^{-28} ecm, the spatial distribution of the magnetic fields has to be controlled on the level of 100 pT. For the temporal stability of the corresponding gradients, control on the level of few $10\,\mathrm{fT\,m^{-1}\,s^{-1}}$ is needed.

Control over the magnetic fields is achieved by providing a non-magnetic environment and shielding the experiment from external magnetic disturbances. Spatial gradients in the magnetic field cause geometric phases, which are the dominating systematic effect for particles precessing in non–homogeneous fields. Contamination of the spatial homogeneity can come from every part of the experiment that has a magnetization. Very careful screening of all parts in close vicinity to the experiment is necessary. Imperfections in the field creation also cause spatial gradients. Another important contribution comes from the wall material of the shielded rooms.

The creation of ultra-low residual fields comprises one part of the work in this thesis: residual fields inside magnetically shielded rooms (MSRs) are influenced by a variety of factors, like the geometry and construction of the room, the shielding material, all kinds of imperfections and even temperature. For reliable low fields inside MSRs, they are regularly degaussed, or magnetically equilibrated. Degaussing is a process to remove the magnetization of a ferromagnetic material, by cycling the magnetization through shrinking hysteresis loops. A setup to equilibrate the TUM MSRs has been built and automated in order to integrate it in the nEDM experimental control system.

To be able to understand this equilibration process better, it would be very useful if it could be simulated in advance, before actually building the MSR, so that the design of the room could be optimized for this purpose. Time–independent simulations are used to investigate and improve field distributions inside the material and make predictions about the residual field from them. This has also been applied to shielding enclosures for other experiments. For the nEDM measurement, this resulted in a new configuration for the equilibration coils, which allows faster equilibration. This directly improves the statistical sensitivity of the nEDM measurement, which is especially important since increasing the neutron density for higher statistics is difficult to achieve.

Time–dependent simulations of the equilibration process were implemented to inves-

tigate the influence of equilibration parameters on the residual field. Starting from the Jiles–Atherton model for ferromagnetic hysteresis, the magnetization of the material is calculated for an applied external field, considering the previous magnetization state of the material. These simulations yielded results in good qualitative agreement with measured field distributions for simple test geometries.

Using the quality of the residual fields, it is feasible to create homogeneous magnetic fields suitable for an nEDM experiment, which is the second focus of this work. A coil system, which couples non-linearly to the shield, is simulated and developed to produce the homogeneous magnetic fields. After the construction and set up of this coil system, a way to characterize the field with the required accuracy over the experimental volume was developed. All spatial components of the magnetic field are needed and have to be resolved. The angular arrangement of the sensors for the spatial components is a big issue for the characterization of homogeneous fields. Due to the construction of these sensors, the specified angular accuracy is up to a factor of 100 worse than required and has to be determined and corrected. A calibration setup has been built and a calibration procedure developed. With the calibrated sensors, maps of the created magnetic field have been measured. It was found that the field from the built coil system deviated from the calculated one, and therefore further corrections have been implemented to reach a field homogeneity that is suitable to the first stage of the nEDM experiment.

Homogeneous magnetic fields have been developed, implemented and characterized. The results enable next–generation nEDM measurement to improve of the current limit of the nEDM by an order of magnitude. Tools employed for this development have also been applied in a broader context for applications in other experiments.

Contents

Acronyms

Notation	Description
EDM	electric dipole moment
FEM	finite element method
JA model	Jiles-Atherton model
MSR	magnetically shielded room
nEDM	neutron electric dipole moment
SF	shielding factor
UCN	ultra-cold neutrons

1. Introduction

1.1 Motivation

Ultra low magnetic fields are a highly relevant prerequisite for precision experiments at low energies. Prominent examples are searches for electric dipole moments (EDMs), which are also the primary motivation for this work [1]. However, searches for new physics at extreme scales, like tests of the CPT theorem[1] and Lorentz invariance violation or ultra light dark matter experiments also rely on techniques to achieve ultra-low magnetic fields.

EDMs are particularly interesting, because an EDM in a fundamental system will violate T and CP symmetry [2] (if CPT is conserved) and therefore they are directly related to a fundamental question that is still unresolved [3]: why is there more matter than antimatter in the universe. Precise measurements of the cosmic microwave background (CMB) yield a ratio of the difference of baryon and antibaryon number densities $n_B = n_b - n_{\bar{b}}$ to the photon number density n_γ of [4]

$$\eta = \frac{n_B}{n_\gamma} = 6 \times 10^{-10}. \tag{1.1}$$

This ratio is eight orders of magnitude bigger than what is expected from the Standard Model (SM). Several models are able to generate baryons in the early universe. For all of them the so–called Sakharov conditions [5] have to be fulfilled to allow baryogenesis. They are

- A baryon number violating process must exist
  Baryon number has to be violated if baryons are to be created.
- Additional sources of C and CP violation must be present
  C violation is required because otherwise there will an anti-baryon creating process for every baryon creating one.
  CP has to be violated because otherwise the rate of baryon production and anti-baryon production will also be equal.
- Departure from thermal equilibrium in the early universe
  In thermal equilibrium the production process and the inverse process will have the same rate.

All of these conditions can be accommodated within the SM. Processes to generate a net baryon number in the universe can be motivated without requiring new physics models, also interactions outside of thermal equilibrium are provided through the evolution of the early universe.

P and C are conserved in strong and electromagnetic interactions. In the weak interaction however, P violation was observed in the experiment by Wu [6]. For nuclear

1 where C,P and T stand for charge conjugation, parity transformation and time reversal

spin polarized ^{60}Co, the direction of the electron emitted in a weak decay was measured. They were always observed in the direction opposite to the nuclear spin orientation. This implies that parity is violated and maximally broken in the weak interaction. The fact that only left-handed neutrinos and right-handed anti-neutrinos are observed means that C is also strongly violated in the weak interaction.

CP violation is also present in the SM, from at least three different sources. In the weak sector, CP violation was observed in the weak decay of neutral kaons [7], and later also in $B^0 - \overline{B}^0$ systems [8]. The CKM matrix describing the mixing of the three quark generations contains the observed CP violation as a complex phase δ in addition to the three real Cabibbo angles θ_{12},θ_{23} and θ_{13}. The CP violation from the CKM matrix is measured very accurately [9].

In the strong interaction Langragian, CP violation occurs naturally in the θ-term. But the experimental limit on the neutron electric dipole moment (nEDM) already strongly constraints CP violation from the θ-term to be extremely small. The nEDM calculated from θ [10] is

$$d_n \approx 10^{-16}\theta \text{ ecm}. \tag{1.2}$$

The current limit from [11] of $d_n < 3 \times 10^{-26}$ requires $\theta < 10^{-10}$. This is the so-called strong CP problem, which could be resolved by axions [12, 13].

The third source of CP violation lies in the PMNS matrix for the lepton sector. A complex phase here would allow baryogenesis through leptogenesis [14], but for now it is unclear whether the amount is sufficient to explain the observed baryon asymmetry.

Before the Higgs boson, the elektroweak phase transition would have allowed to create the observed baryon asymmetry. But for this, the Higgs mass had to be constrained to $m_H < 90$ GeV. With the measured value of $m_H \approx 125$ GeV [15, 16], the SM cannot account for the whole baryogenesis through the electroweak phase transition.

The largest contributions in the SM to the nEDM come from higher order loops, generated by so–called penguin diagrams, which are enhanced by a pion loop, as shown in figure 1.1[17]. The corresponding predictions for EDMs are given in table 1.1. All of them are several orders of magnitude smaller than the current experimental limits and out of reach for current and next generation experiments. However, several frameworks for BSM physics lead to higher values for EDMs and predict values that are in range of next generation experiments. Instead of probing BSM at very high energies which require more powerful accelerators, BSM can also be investigated in high precision

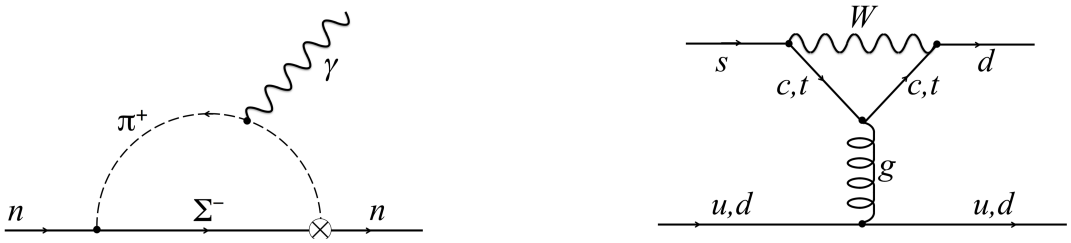

(a) SM contribution to the nEDM. The ⊗ indicates a CP-violating $\Delta S = 1$ vertex.

(b) Penguin diagram that gives the CP-violating interaction in the SM.

Figure 1.1: Higher order loop contribution to the nEDM within the SM.

experiments on ordinary matter. EDM experiments have a reach comparable to or even surpassing the ones of accelerators, while being on a much smaller scale. For example electron EDM measurements probe supersymmetric particles on energy scales of up to 100 TeV[18].

In high precision experiments, the underlying physics is accessible via a set of low energy parameters. These parameters, like the nEDM d_n, describe the interaction strengths in an effective quantum field theory. In different systems, different linear combinations of these parameters are experimentally accessible. This allows to use combinations of experiments to constrain the parameters further than would be possible with single source analysis [23].

The Schiff theorem states that non-relativistic electrons surrounding a point-like nucleus rearrange themselves in such a way that they develop an dipole moment that is exactly opposite to that of the nucleus, resulting in a vanishing net EDM for an atom [24]. Therefore, the Schiff moment has to be considered carefully, when analyzing EDM measurements. While it is not directly a problem for the neutron EDM measurement, the Schiff screening is still relevant here if, for example, a Hg comagnetometer is used. The Schiff screening suppresses the influence of the applied electric field on the precession frequency of the Hg atoms.

Experiments searching for an nEDM are based on the fact that it couples to an electric field and the corresponding shift in energy can be detected. A particle with a net angular momentum $\boldsymbol{F}$, having a magnetic moment μ and an EDM d placed in a magnetic field $\boldsymbol{B}$ and an electric field $\boldsymbol{E}$ can be described by the non-relativistic Hamiltonian[25]

$$H = -(\mu \boldsymbol{B} + d\boldsymbol{E})\frac{\boldsymbol{F}}{|F|}. \tag{1.3}$$

The energy shift due to an EDM can be detected by measuring the shift in Larmor precession frequency for the two cases that $\boldsymbol{B}$ and $\boldsymbol{E}$ are parallel ($\omega_{\uparrow\uparrow}$) and anti-parallel ($\omega_{\uparrow\downarrow}$). For the current limit of

$$d_n = 3.0 \times 10^{-26}\, e\text{cm (90\% CL)} \tag{1.4}$$

for the nEDM from [11], the level splitting is on the order of 10^{-22} eV, resulting in a frequency shift of $\Delta\nu = 1 \times 10^{-7}$ Hz for an electric field of $E = 20\,\text{kV/cm}$. The precession frequency due to the magnetic field is 29 Hz in a field of 1 µT. This makes the need for controlled and very precisely monitored magnetic field conditions obvious. More details on direct and indirect influences on the precession frequencies will be given later.

Table 1.1: Current experimental limits of EDMs for the neutron, electron and two diamagnetic atoms and the corresponding goals for next-generation experiments, with their predicted values from the Standard Model.

	Experimental limit/ecm	Goal/ecm	SM prediction/ecm
n	3×10^{-26} (90% CL) [11]	$\sim 10^{-28}$	$\sim 10^{-31} - 10^{-32}$
e	9.4×10^{-29} (90% CL) [19, 20]	$\sim 10^{-32}$	$\sim 10^{-38}$
^{199}Hg	7.4×10^{-30} (95% CL) [21]	$\sim 10^{-29}$	$\sim 10^{-34} - 10^{-35}$
^{129}Xe	$0.7 \pm 3.3 \times 10^{-27}$ [22]	$\sim 10^{-29}$	$\sim 10^{-33} - 10^{-34}$

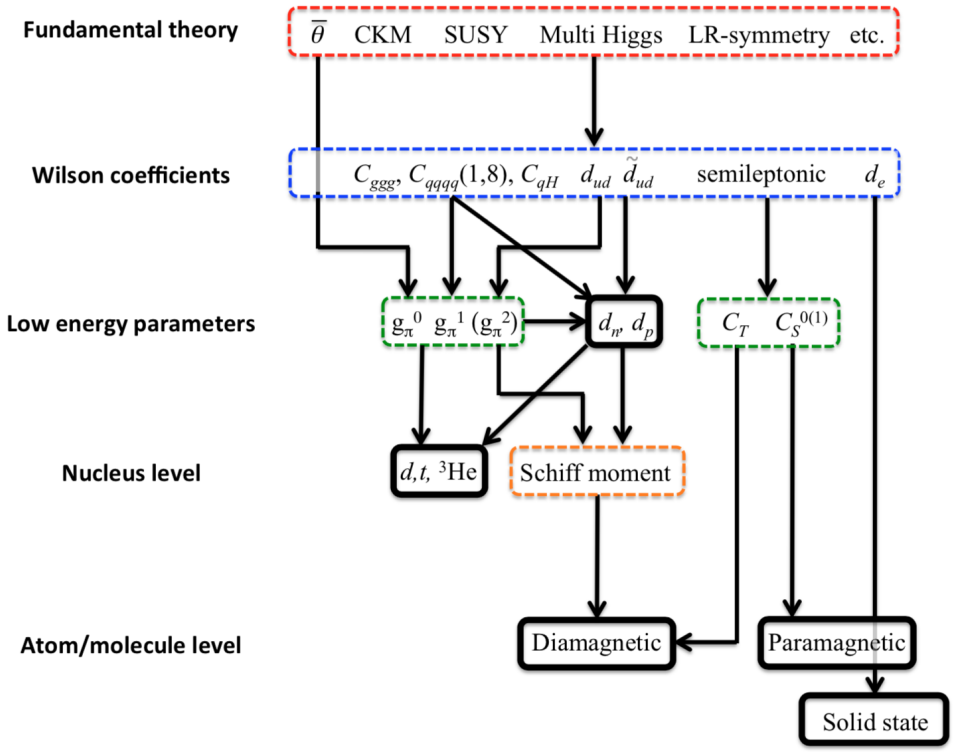

Figure 1.2: Illustration of the connections from fundamental theory to experimentally accessible parameters. The SM and BSM physics models are reduced to Wilson coefficients. These in turn are connected to electron and nuclei via low energy parameters. From [2]

Another example of fundamental experiments that rely on stable magnetic field conditions are searches for Lorentz invariance violating effects [26]. Lorentz invariance is one of the fundamental symmetries in modern physics. Nevertheless, there is interest in testing its validity, because a violation of CPT would immediately lead to Lorentz invariance [27]. The mass scales for these test are beyond the reach of current colliders. But small effects of Lorentz invariance violation can be visible in high precision experiments. For example, clock comparison experiments can search for sidereal modulation of the precession frequency when Earth moves through a relic background field [28]. These extremely precise measurement also rely on very small and stable magnetic field conditions and need the same experimental techniques as nEDM experiments. Further applications of magnetic field technology are for example in atomic fountains[29], medical imaging[30] or in semiconductor processing.

For the measurement of exotic spin-dependent interactions, the question has to be asked, whether the magnetic shielding used to provide the stable conditions in which the experiments take place, have an influence on the signal detected by the spin systems or not. In [31] it is stated that there is only one case in which the shielding material has an influence, that is, when the exotic field couples to electron spins and the shield is made from soft ferromagnetic material. Then the exotic field will produce an induced magnetic field inside the shield. The sensitivity of an experiment to purely nuclear spin-dependent interactions is essentially unaffected by the presence of magnetic shields.

1.2 Measurements in small magnetic fields

The experimental technique to determine frequencies with high accuracy is Ramsey's method of separated oscillatory fields [32]. An ensemble of spins is polarized along the Z axis in a magnetic field B_0, creating a macroscopic polarization $P_z = P_0$. A radio-frequency (RF) field with an amplitude B_1 is applied perpendicular to the Z axis for a time τ such that $\gamma B_1 \tau/2 = \pi/2$ is fulfilled. Then, the polarization precesses around this field and rotates into the X-Y plane. Here, the spins precess freely for a storage time T. Afterwards, a second $\pi/2$ pulse, phase-coherent to the first, is applied. In the case $\omega_1 = \omega_L$ this pulse rotates the polarization into -Z direction. In the off-resonant case a relative phase $\phi = \Delta\omega T$ between ω_1 and ω_L was acquired during the free pecession time, making the flip less efficient and the resulting polarization is $P_z = -P_0 \cos\phi$. For the nEDM, the polarization is measured by counting the neutrons in the up $N_\uparrow$ and down state $N_\downarrow$:

$$P_z = \frac{N_\uparrow - N_\downarrow}{N_\downarrow + N_\downarrow}, \tag{1.5}$$

and the precession frequency can be determined.

The Ramsey method prepares a superposition state, lets it evolve over time and then interrogates the state of the system to determine the acquired phase difference to an external clock during the evolution time. This corresponds to an interferometer in the time domain, with an resulting interference pattern similar to an double-slit experiment. Due to the high sensitivity, a lot of effort has to be paid to understand

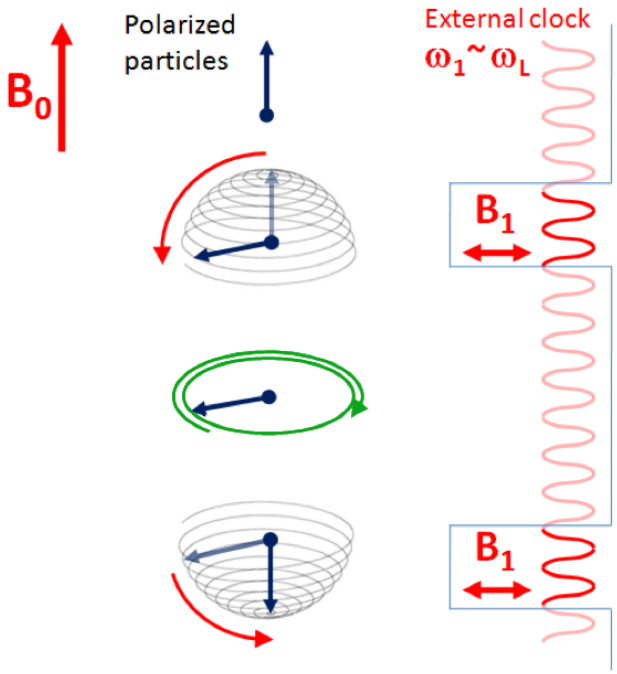

Figure 1.3: Scheme of a Ramsey cycle. The external clock is running with a frequency ω_1 close to the Larmor frequency of the particles in the field B_0. Two pulses are applied, flipping the polarization from +Z to -Z direction. The sequence is described in the text.

and control any influences on the signal.

The way the measurements of the precession frequency are actually performed is, by choosing working points slightly off resonance and fitting the measured data to the function for the central fringes of the Ramsey pattern (see eg. [33]).

From equation 1.3 follows

$$d_n = \frac{\hbar \Delta\omega}{4E}, \tag{1.6}$$

for $\Delta\omega = \omega_{\uparrow\uparrow} - \omega_{\uparrow\downarrow}$ the frequency difference between two measurements with E and B parallel and anti-parallel. The statistical sensitivity of the frequency measurement for the Ramsey technique is

$$\sigma_\omega = \frac{\sigma_{P_z}}{T} \tag{1.7}$$

resulting in the statistical nEDM sensitivity of

$$\sigma_d = \frac{\hbar}{2\alpha E T \sqrt{N}\sqrt{M}}, \tag{1.8}$$

where N is the total number of neutrons, α a visibility parameter and with an additional factor $1/\sqrt{M}$ for an number of M repeated measurements. These equations are only true if B is constant during the measurement of the frequencies $\omega_{\uparrow\uparrow}$ and $\omega_{\uparrow\downarrow}$. A magnetic field change of ΔB between the two measurements contributes

$$\sigma_d(B) = \frac{\mu \Delta B}{2E} \tag{1.9}$$

to the nEDM value. With the neutron magnetic moment of $\mu = 60\,\mathrm{neV/T}$ and an electric field of 20 kV, an ΔB of 1 fT results in a false nEDM value of $d_n = 1.5 \times 10^{-27}$ecm. From this it is again obvious that the magnetic environment has to be controlled and monitored very accurately.

Possible causes for a field change ΔB can be a temporal drift of the magnetic field in case $\omega_{\uparrow\uparrow}$ and $\omega_{\uparrow\downarrow}$ are measured consecutively. This effect can be addressed by using a comagnetometer where a different species of spins occupies the same volume to measure the magnetic field. For the nEDM experiment, Hg atoms are filled into the same precession chamber as the neutrons. The Hg atoms are polarized by optically pumping the Zeeman-split hyperfine levels. After flipping the magnetization, the transmission of a weaker laser beam through the atomic vapor is modulated with the Larmor precession frequency of the magnetization in the magnetic field. The Hg atoms sample the entire storage chamber and therefore give an volume-averaged magnetic field. Since their mean velocity is much higher than the one for ultra-cold neutrons (UCN) ($v_{Hg} \approx 200$ m/s and $v_n \approx 8$ m/s), the center of gravity for the two species is slightly different $\Delta h \approx 2.8$mm [34]. When the measured frequency ratio for neutrons and Hg differs from the expected value according to the gyromagnetic ratios, a volume-averaged estimate of the vertical magnetic field gradient over the storage chamber can be obtained from this. More details on Hg magnetometry in the nEDM experiment can be found in [35].

Comagnetometers are also more widely used in spin clock experiments. Two species occupy the same volume, based on the fact that one of them is sensitive to an interaction while the other one is not, they can be used for example for axion-like particle and

dark matter searches [36].

Another approach to the problem of temporal magnetic field stability is to perform the two frequency measurements at the same time. In a double chamber experiment, one chamber is exposed to the E and B fields parallel and the other chamber anti-parallel (cf. figure 1.4). Then, any spatially homogeneous field drift affects both chambers in the same way and cancels in the frequency difference. Field gradient drifts become the leading systematic effect. If the gradients are stable enough, it is in principle possible to omit the comagnetometers, as they also present several disadvantages when used in an nEDM experiment. As a gas in the high voltage chamber, Hg limits the breakdown voltage to approximately 200 kV. A special wall coating of the neutron chambers [37], to prevent spin depolarization for the Hg atoms, reduces the neutron storage times by a factor of two. Furthermore, also systematic effects for next-generation experiments are dominated by Hg comagnetometer (see below). If the comagnetometer is omitted, additional magnetometry has to be employed to obtain the required field information. One possible concept is a 4π magnetometer discussed in [38]. The experimental volume is surrounded by sensitive magnetic field sensors [39] that monitor the magnetic flux on ideally the whole 4π solid angle. Then the flux distribution inside this volume is also known, except for localized sources within the volume. These localized sources can for example be leakage currents that would have to be monitored with additional high-bandwidth magnetometers, like SQUIDs or all optical Cs magnetometers [40, 41, 42].

Small gradients in the magnetic fields over the volume of the precession chamber are important for the spins to maintain polarization. In [43] the effect of field gradients on the spin relaxation times of particles in cells are described. The transverse relaxation time T_2 for the polarized UCNs should exceed the measurement time for a Ramsey cycle. For UCN the low pressure regime defined by

$$\frac{\omega_0 R^2}{D} = \frac{p}{p*} = \frac{\tau_d}{\tau_l} \ll 1 \tag{1.10}$$

is valid and the T_2 relaxation rate is given

$$\frac{1}{T_2} \approx \frac{4R^4\gamma^2}{175D}\left(\left|\frac{\partial B_x}{\partial x}\right|^2 + \left|\frac{\partial B_y}{\partial y}\right|^2 + \left|\frac{\partial B_z}{\partial z}\right|^2\right). \tag{1.11}$$

Estimating the diffusion constant D for ballistic motion of the neutrons from their velocity and the characteristic cell dimension, gradients of better than 10 nT/m are necessary to achieve T_2 times of 250 s.

A major source of systematic errors are Ramsey-Bloch-Siegert shifts, found by Ramsey [44] when he generalized the results of Bloch and Siegert [45]. Spins precess in a constant magnetic field B_z with a frequency $\omega_L = \omega_0 = -\gamma B_z$. When an additional magnetic field B_{xy} exists in the X-Y plane, rotating with a frequency ω_r, the Larmor precession frequency is shifted away from ω_0 by an amount $\Delta\omega$; this shift is called Ramsey-Bloch-Siegert shift:

$$\Delta\omega = \sqrt{(\omega_0 - \omega_r)^2 + \omega_{xy}^2} - (\omega_0 - \omega_r), \tag{1.12}$$

where $\omega_{xy} = -\gamma B_{xy}$. To first order, the shift, for $\omega_{xy} >> (\omega_0 - \omega_r)$, is

$$\Delta\omega = \frac{\omega_{xy}^2}{2(\omega_0 - \omega_r)}. \tag{1.13}$$

Field sources creating the B_{xy} contribution can be of various types. For example, a particle with a velocity $\boldsymbol{v}$ in a trap that is subject to an electric field $\boldsymbol{E}$ experiences a motional magnetic field (eg. [46])

$$\boldsymbol{B}_v = \frac{\boldsymbol{v} \times \boldsymbol{E}}{c^2}, \tag{1.14}$$

which is linear in $\boldsymbol{E}$ and can therefore mimic an EDM signal. However, if $\boldsymbol{E}$ and $\boldsymbol{B}$ are parallel, only a net rotation of the UCN and the motion of the center of mass of the UCN can produce a false signal due to a first-order $\boldsymbol{v} \times \boldsymbol{E}$ effect. For symmetric motion in the trap, it averages to zero.

A vertical gradient of the magnetic holding field $\partial B_z/\partial z$ also produces transverse components. For a cylindrical symmetry, the corresponding field in the X-Y plane is

$$\boldsymbol{B}_{0xy} = \boldsymbol{B}_r = -\left(\frac{\partial B_z}{\partial z}\right)\frac{\boldsymbol{r}}{2}. \tag{1.15}$$

Together, these fields produce

$$\boldsymbol{B}_{xy} = -\left(\frac{\partial B_z}{\partial z}\right)\frac{\boldsymbol{r}}{2} + \frac{\boldsymbol{v} \times \boldsymbol{E}}{c^2}. \tag{1.16}$$

which results in a frequency shift of

$$\Delta\omega_{xy}^2 = \gamma^2\left(\left(\frac{\partial B_z}{\partial z}\alpha\right)^2 + \left(\frac{\boldsymbol{v} \times \boldsymbol{E}}{c^2}\right)^2 + 2\left(\frac{\partial B_z}{\partial z}\alpha \cdot \frac{\boldsymbol{v} \times \boldsymbol{E}}{c^2}\right)\right). \tag{1.17}$$

In the presence of a magnetic field gradient, the precession frequency is shifted proportional to the electric field, resulting in a false EDM signal. In [2] the false nEDM due to these so called geometric phase effects [47] is given for a cylindrical volume

$$d_{false}^{GP} = \frac{\hbar\gamma^2 \frac{\partial B_z}{\partial z} v_\phi^2 R^2/c^2}{4(v_L^2 - v_\phi^2)}, \tag{1.18}$$

with the velocity $v_L = R\gamma B_z$, R is the size of the cell and v_ϕ the effective azimuthal velocity.

1.3 PanEDM: statistical reach and systematic effects

In figure 1.4 the nEDM setup for the PanEDM experiment is shown. Four cylindrical cells are stacked vertically inside a vacuum chamber. The inner two chambers are UCN storage chambers, separated by a high voltage electrode. Hg may be added as a comagnetometer to these two cells. The outer two chambers only contain Hg and are used to measure magnetic field gradients. Ground electrodes are located between the UCN and the Hg cells. With the two UCN chambers, both frequencies $\omega_{\uparrow\uparrow}$ and $\omega_{\uparrow\downarrow}$

can be measured at the same time, because the magnetic field is in the same direction for both cells, whereas the electric fields have the opposite direction. For additional monitoring of magnetic fields, access tubes to the vacuum vessel are available. They are vented and allow SQUIDs or optical magnetometers to be inserted and to be moved close to the cell stack.

The PanEDM experiment was moved from the FRMII to ILL, in order to use the available UCN source SuperSUN[48, 49, 50], which can deliver a density of approximately 7 UCN/cm^3 to the cells at the experiment [51]. With this, the statistical sensitivity according to equation 1.8 can be estimated. A precession time of $T = 250\,\mathrm{s}$ is possible with the soft UCN spectrum produced by the source with energies $< 74\,\mathrm{neV}$ [52]. A value of $\alpha = 0.85$ has also been demonstrated in [52]. The applied electric field is 20 kV/cm. In total, the statistical sensitivity of for one measurement with two cells is $\sigma_{d_n} = 2.7 \times 10^{-25}\,\mathrm{ecm}$. Estimating a preparation time of 150 s for each measurement, for filling and counting of neutrons, as well as equilibration of the shield, 216 measurements per day can be performed. After 100 days of measurements, the goal for the first stage of

$$d_n = 3.0 \times 10^{-27}\,\mathrm{ecm}\ (90\%\ \mathrm{CL}) \tag{1.19}$$

can be reached. For the second stage, the UCN source will be upgraded to provide a 20 times higher UCN density for the goal of $d_n = 7.0 \times 10^{-28}\,\mathrm{ecm}$.

As previously discussed, geometric phases are a main source of systematic effects. Their contribution to an nEDM measurement can be estimated as follows. For UCNs

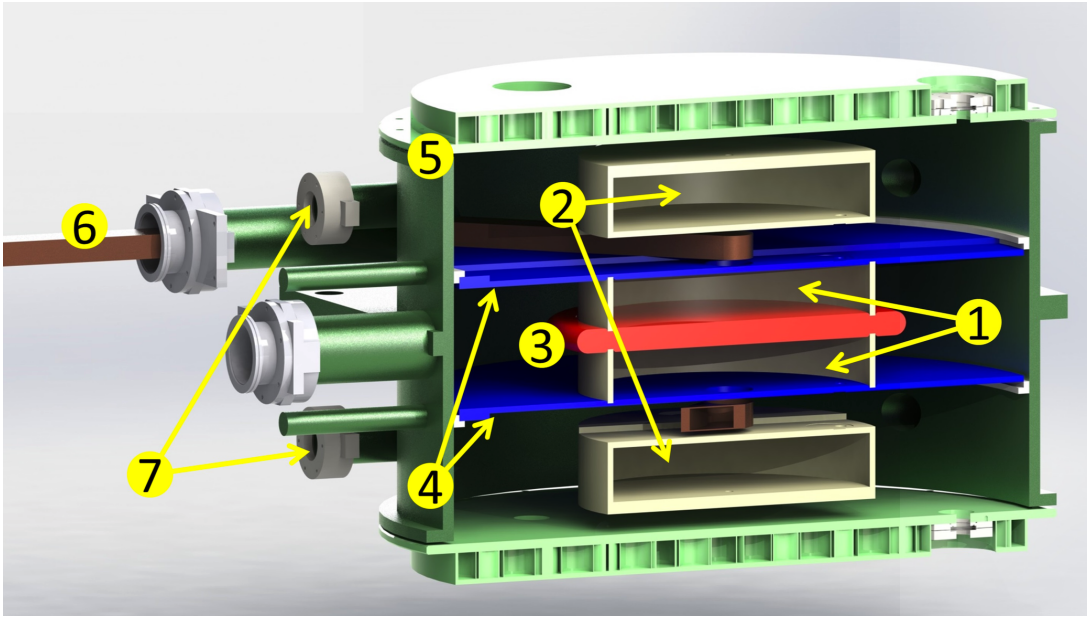

Figure 1.4: Sketch of the TUM nEDM apparatus: Two UCN chambers (1) with 48 cm diameter and 10 cm height have a high voltage electrode (3) in between them. Additional Hg chambers (2) are used for optical magnetometry. Through UCN guides (6) the chambers (1) are filled with UCNs. A voltage of 200 kV can be applied between the high voltage electrode and the ground electrodes (4). The vacuum chamber (5) has further access channels for additional magnetometry.

Table 1.2: Table from [11] giving a summary of systematic error and their uncertainties, in units of 10^{-26} ecm for the previous nEDM result.

Effect	Shift	σ
ν_{Hg} light shift (included in d_x)	(0.35)	0.08
χ^2_ν =1.2 adjustment	0	0.68
Quadrupol field and Earth rotation	0.33	0.14
Dipole field	-0.71	0.07
Hg Door PMD	0.00	0.60
$\boldsymbol{v} \times \boldsymbol{E}$ translational	0.000	0.001
$\boldsymbol{v} \times \boldsymbol{E}$ rotational	0.00	0.05
Second order $\boldsymbol{v} \times \boldsymbol{E}$	0.000	0.000
Uncompensated $\boldsymbol{B}$ drift	0.00	0.34
Hg atom EDM	-0.002	0.006
Electric forces	0.00	0.04
Leakage currents	0.00	0.01
AC fields	0.000	0.001
Nonuniform Hg depolarization	0.000	0.001
Total shift of d_x	-0.38	0.99

with velocity $v_\phi \approx 8\,\mathrm{m/s}$ in a cell with radius $R = 0.23\,\mathrm{m}$ and height $h = 0.12\,\mathrm{m}$ the Larmor velocity $v_L = R\gamma B_z$ is $\approx 200\,\mathrm{m/s}$. Assuming a gradient of 0.3 nT/m, the geometric false effect amounts to $d^{GP}_{false} \approx 1 \times 10^{-28}$ ecm. For room-temperature Hg, with velocities $v_\phi \approx 200\,\mathrm{m/s}$ and $v_L \approx 50\,\mathrm{m/s}$, the false effect is $d^{GP}_{false} \approx 1 \times 10^{-26}$ ecm. This geometric phase effect is much more relevant for the Hg comagnetometer (cf. also [53]). This is one reason why it would be advantageous to omit the comagnetometers.

Further systematic errors from the previous nEDM result are listed in table 1.2. Many of these are related to magnetic fields. Without the Hg comagnetometer, all effects relating to Hg do not need to be considered. Uncompensated B drift is handled by the double chamber approach. Dipole contaminations can be reduced by careful magnetic screening of all parts inside the neutron chamber. Nevertheless, they play an important role as a source of geometric phase effects, if they are located for example on the electrode surfaces.

Additional false effects are related to a motional magnetic field $B_m = \frac{\boldsymbol{v}\times\boldsymbol{E}}{c^2}$, that particles experience due to moving in an electric field. These effects make it necessary that $\boldsymbol{E}$ and $\boldsymbol{B}$ are aligned closely and that the volume average of the velocity $\boldsymbol{v}$ is ideally zero. A source of translational movement of the UCN can be inelastic collisions of the UCN with the walls of the storage chambers, increasing the UCN energy and shifting the center of mass upwards, or the movement of the UCN center of mass after filling them off-center into the trap. The second motion should already be averaged out by the wall bounces before the RF pulse is applied. Rotational $\boldsymbol{v} \times \boldsymbol{E}$ are suppressed in the same manner.

A new class of systematic effects has been found recently in [54] whose influence on next generation measurements is not yet clear. Under conditions that are fulfilled for the UCN in the nEDM experiment, non-equilibrium spin transport in non-dissipative systems, the spin phase distribution as a function of time can deviate from a Gaussian.

This can modify already known systematic effects in a nonlinear and time– dependent manner, and will have to be studied very carefully for next- generation experiments.

1.4 Overview of the setup for PanEDM

The nEDM experiment at TUM was located in the Neutron Guide Hall East at the Forschungs-Neutronenquelle Heinz-Maier-Leibnitz (FRM II). The situation there is illustrated in figure 1.5.

The floor was replaced by a new construction due to strongly magnetic steel reinforcements in the concrete. A hole was built from nonmagnetic and non-magnetizable materials, that is also electrically and vibrationally decoupled from the rest of the building. Inside the hole active compensation system (ACS) was set up.

The ACS is a $9\,\mathrm{m} \times 6\,\mathrm{m} \times 6\,\mathrm{m}$ aluminum construction with 24 coils and 60 three-axis fluxgate sensors. The fluxgates record the magnetic field at their positions and an algorithm calculates currents that are fed to the coils to compensate for external magnetic field disturbances and keep the magnetic field inside a volume of interest as homogeneous as possible. Targeted is a field of approximately $4\,\mu\mathrm{T}$. The aluminum structure is equipped with walls made from transparent and non-transparent PVC panels. They provide a closed shell around the experiment and protect the mumetal from direct sunlight to prevent strong temperature gradients in the material, which would induce stray magnetic fields due to thermal currents and vary the magnetic permeability μ. Furthermore, the ACS provides a closed-off environment, in which the experiment is protected from dust and can be temperature controlled with filtered air from an air conditioning unit.

Two passive magnetically shielded rooms (MSRs) shield the nEDM experiment from external magnetic disturbances. With a combined reduction of external field by over factor 10^6 at 1 mHz they represent the strongest large-scale magnetic shield in the world. A major part of the work on this thesis is concerned with these two shields and they will be discussed in more details in the following chapters. The outer one is a room (referred to as MSR from now on) that can easily be accessed by people setting up the experiment. The inner passive shield (referred to as insert) adds more shielding and also houses the coil system to create the homogeneous magnetic fields B_0 and B_1 for the Ramsey experiment. The B_0 and B_1 coils are mounted in the same glass-fiber reinforced plastics (GFRP) structure as the innermost shielding layer.

The vacuum chamber houses the actual nEDM experiment. It is situated inside the shielded rooms, and accessible when the insert is removed from the MSR. The vacuum chamber is made from GFRP, which had to be manufactured without any magnetic contaminations.

Recently, the experiment has been moved to the Institute Laue Langevin (ILL) in Grenoble, France in order to measure the nEDM at the already available UCN source SUN. The two passive MSRs were transported, there is not enough space for the ACS. The setup at the ILL position is shown in figure 1.6.

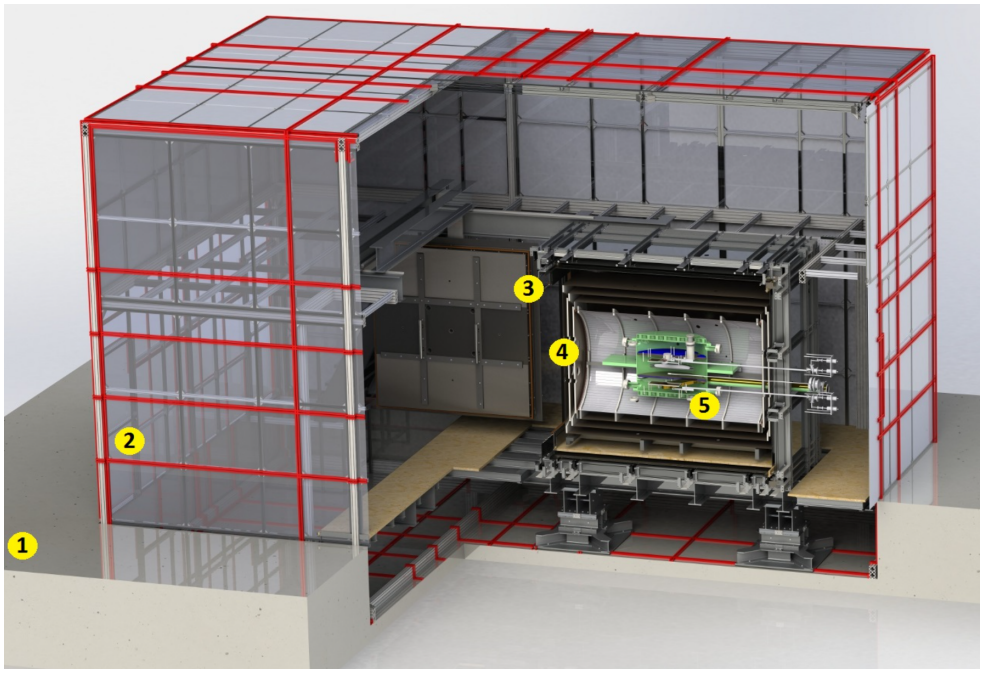

Figure 1.5: Image of the whole setup providing a magnetically shielded environment for the nEDM experiment at TUM. A hole of nonmagnetic concrete (1) houses the ACS system with its aluminum structure (2). Inside it, the outer (3) and inner (4) magnetically shielded rooms enclose the vacuum chamber (5) with the nEDM setup. The B_0 coil system is part of the inner MSR. Picture from [38].

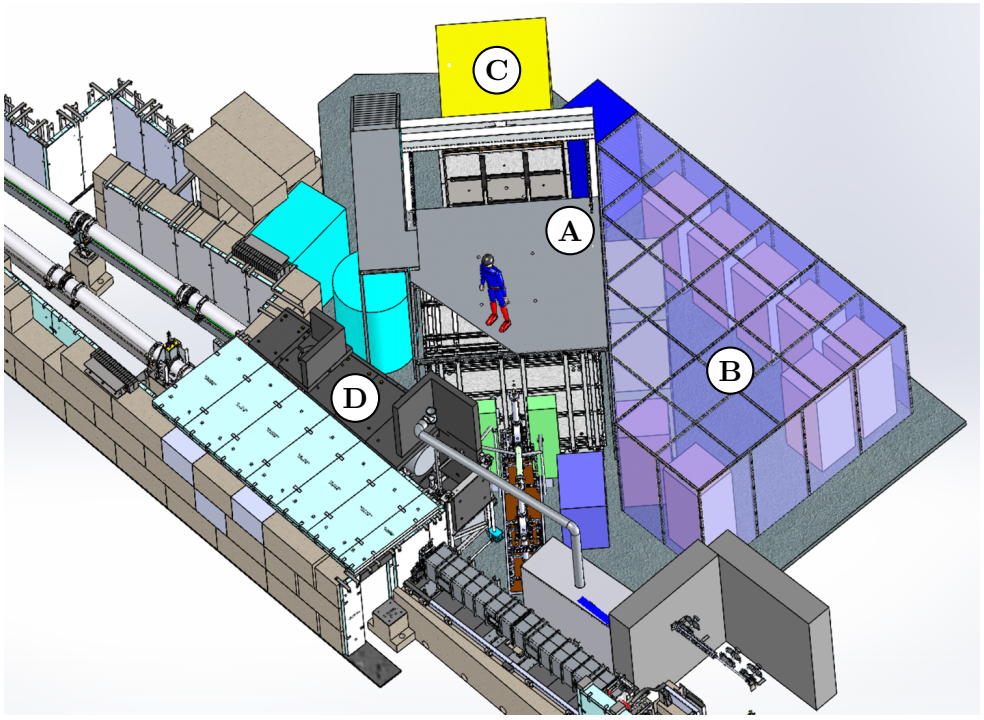

Figure 1.6: Sketch of the PanEDM setup at ILL. The MSR (1) stays in position close to the UCN source (B), the insert (C) can be placed in front of the MSR for magnetic field test. A clean room environment (D) is setup next to the MSR to house equipment.

2. Magnetic shielding

2.1 Principles of magnetic shielding

There are several ways to prevent a magnetic field from entering a volume where an experiment will take place, based on different physical mechanisms. Each has its own advantages and disadvantages, which have to be considered when designing a magnetic shield for an experiment. These mechanisms, illustrated in figure 2.1, are b) repulsion, c) counteracting, or d) diverting of magnetic fields. In the following sections the different shielding mechanisms will be discussed in more detail.

To quantify the effectiveness of a magnetic shield, the so-called shielding factor (SF) is used. Several definitions of SFs can be found in the literature. In this thesis, the following one will be used, where the SF is the ratio between the field measured at a position without the shield present B_0 and the field measured at the same position with the shield present B_i:

$$SF(\omega) = \frac{B_0}{B_i}(\omega). \tag{2.1}$$

In general, this SF depends on a multitude of factors: it can be complex for alternating fields, it can depend on the frequency and on the magnitude of the excitation or on the position where the field is measured.

2.1.1 Quasi–static ferromagnetic shielding

One option to shield a volume from magnetic fields is to enclose it in a material with high permeability μ, thereby guiding the magnetic field in the material around the volume to be shielded. This is also called flux-shunting and a direct consequence of Maxwell's equations as can be understood from the following. Ampere's and Gauss' Law require that the tangential component of the H field and the normal component of the magnetic flux density B are continuous at the interface between two materials.

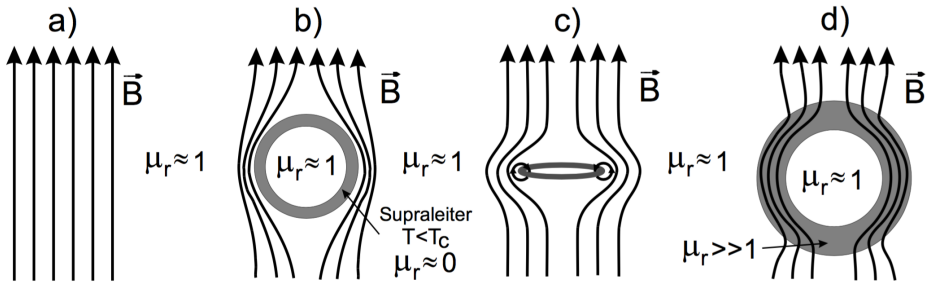

Figure 2.1: Illustration of shielding mechanisms. a) unhindered flux density, b) shielded by repulsion from superconductor, c) counteracting field produced by coil, d) flux-shunting through high μ material. Picture from [55]

This leads to a law of refraction for magnetic field lines:

$$\frac{\tan \alpha_1}{\tan \alpha_2} = \frac{\mu_1}{\mu_2}. \tag{2.2}$$

In air, the magnetic flux density is $B = \mu_0 H$ with $\mu_1 = 1$ while inside the material, it is $B = \mu_0 \mu_2 H$. This means the field lines must abruptly change direction when entering the material, and that they are attracted to the material with high μ. So they hit the surface more or less perpendicular and are then bent inside the material to go on almost parallel to the surface. The field lines continue within the material and circumvent the shielded volume. Flux-shunting occurs for both DC and AC external fields. The SF for this type of shielding can be calculated analytically for simple geometries. A spherical shield with diameter D and wall thickness Δ has a SF_{sp} of [56]

$$SF_{sp} = \frac{2}{3}\frac{\mu_r \Delta}{D} + 1 \tag{2.3}$$

when $D >> \Delta$ and $\mu >> 1$. For cylindrical shields, shielding factors are given by [57]

$$S_{cyl,t} = \frac{\mu_r \Delta}{D} \qquad \text{transverse} \tag{2.4}$$

$$S_{cyl,t} = 1 + \frac{N}{\pi} S_{cyl,t} \qquad \text{longitudinal} \tag{2.5}$$

again when $D >> \Delta$ and $\mu >> 1$. Longitudinal corresponds to the axial direction of the cylinder and transverse means in radial direction. N is the demagnetizing factor (for an ellipsoid in this case) that is only dependent on the geometry of the problem. The demagnetizing factor expresses how much a magnetic field inside the material H_{in} is smaller than the magnetic field outside the material H_{out}. When a material is magnetized, magnetic poles form at its boundaries and these poles establish a counter-field that reduces the field inside the material. For cubic shields, only a value of

$$S_c = \frac{4}{5}\frac{\mu_r \Delta}{L} + 1 \tag{2.6}$$

is given [58], where L is the side length of the cube and Δ the wall thickness.

From these expressions an obvious way to increase the shielding is to increase the thickness of the material layer. But this comes with practical disadvantages as material costs also increase. A more effective way is using more layers of material with gaps of air in between.

The SF of an n-layer system can be calculated with recursive relations that take into

account the interaction of a layer with its neighbors [59]

$$\begin{aligned} S^T = 1 &+ \sum_{i=0}^{n} S_i^T + \sum_{i=1}^{n-1}\sum_{j>i}^{n} S_i^T S_j^T \left[1 - \left(\frac{R_i}{R_j}\right)^2\right] \\ &+ \sum_{i=1}^{n-2}\sum_{j>i}^{n-1}\sum_{k>j}^{n} S_i^T S_j^T S_k^T \left[1 - \left(\frac{R_j}{R_k}\right)^2\right]\left[1 - \left(\frac{R_i}{R_j}\right)^2\right] \\ &+ \cdots \\ &+ S_1^T S_2^T \ldots S_n^T \left[1 - \left(\frac{R_1}{R_2}\right)^2\right] \ldots \left[1 - \left(\frac{R_{n-1}}{R_n}\right)^2\right]. \end{aligned} \tag{2.7}$$

$S_i^T = \frac{\mu_r \Delta}{D}$ are the individual layer SFs, and R_i the radii of the layers. This expression reduces to the sum of the individual SF when the width of the air gaps (or the distance between the layers $R_j - R_i$) goes to zero, as it would for a layer with the combined thickness. On the other hand, when the layers are very far apart the last term is dominant and the SF approaches the value

$$S^T = \prod_{i=1}^{n-1} S_n^T S_i^T \left[1 - \left(\frac{R_i}{R_{i+1}}\right)^2\right], \tag{2.8}$$

the layers are numbered from the inside to the outside. By forming the derivative of this equation an optimal layer distance can be calculated. 90% of the maximum SF is already reached with smaller gaps, meaning that with a significantly cheaper and lighter shield almost the same performance can be achieved [60]. The optimal distance can only be calculated analytically only for the simplest cases, but can be estimated by empirical formula provided in [60]. In figure 2.2, the dependence of the shielding performance on the air gap between the layers is shown. Equal-mass shields, where the layers have the same mass and therefore a reduced thickness as they grow larger, are compared to the more practical case of equal-thickness shields. For cylindrical equal-thickness shields, for example, the air gap can be reduced von 70% to 40% to still reach 90% of the shielding performance.

The given formula for the SFs assume a known μ that is constant for the entire shield. But the value of μ can change within the shell due to mechanical stress, welds or temperature dependence. For example, in a nickel iron alloy with a 80% - 15% composition, μ changes by approximately 1%/°C in a 10° range around room temperature [62].

Further, the value of μ that is effective for a current shielding situation depends on the magnitude of the excitation according to the $B(H)$ hysteresis curve of the material used. For ferromagnetic shielding materials, μ can vary over a wide range. To calculate SFs for a given situation, an effective μ value has to be used taking into account all of these effects.

The dependence of the SF on μ is used in the shaking technique to increase SFs for specific situations. The (outermost) shield is magnetized by an alternating current to a point on the hysteresis curve where the permeability is high. Small low frequency disturbances are then shielded with this incremental permeability value. Of course

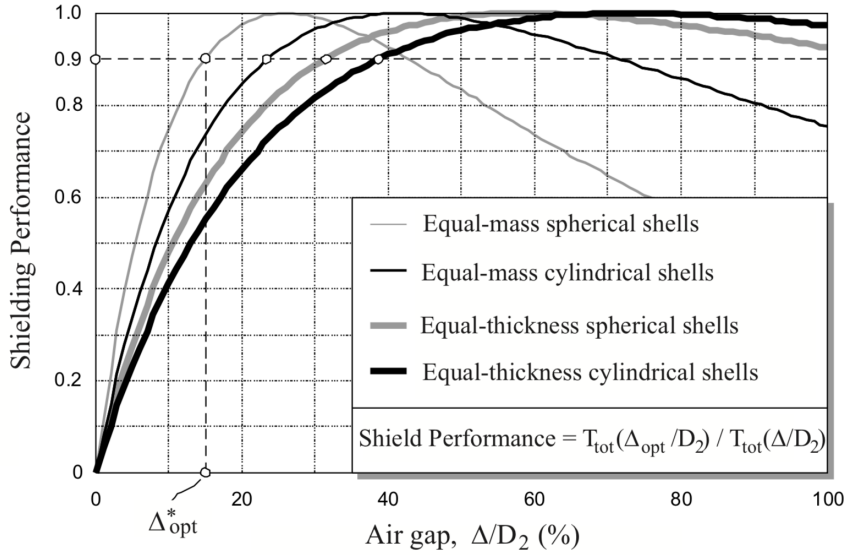

Figure 2.2: The plot shows the effect of the relative air gap Δ/D_2 on the shielding performance of double-shell spherical and cylindrical shields. Equal-mass shields reach 90% of the optimal performance at smaller separations than equal-thickness shields. But equal-thickness shields are much more practical due to constant material thickness. Picture from [61]

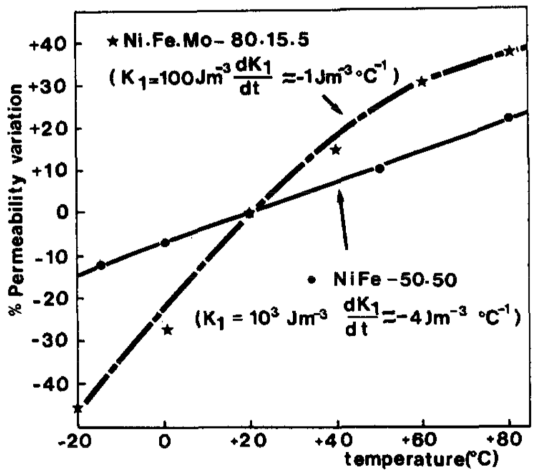

Figure 2.3: Temperature dependence of two different Ni-Fe permalloys in a low field. Picture from [62]

this techniques causes other problems due to an increased noise inside the shielded environment.

For alternating external magnetic fields additional shielding occurs due to eddy-current cancellation. The magnetic fields induce an electric field inside the material, and when the material is conductive, eddy currents arise. These currents cancel out the incident magnetic fields and prevent them from entering the shielded volume. The induced current and the total flux density decay exponentially with distance to the material surface. The skin depth

$$\delta = \sqrt{\frac{2}{\omega\mu\ \sigma}} \tag{2.9}$$

is the characteristic length scale of the exponential decay for a field with frequency ω. For this process, the SF is a complex quantity, where the phase describes the phase difference between the field inside and outside the shield. For example for a spherical shield[63]

$$S = 1 + i\omega\frac{\tau}{3} \text{ with } \tau = \mu_0\sigma a\Delta. \tag{2.10}$$

Even when $\delta \gg \Delta$, and induced currents flow uniformly over the shield thickness, a shielding effect occurs for material where the conductivity is high enough. When currents can flow over the dimensions of the whole shield and the induced flux density is comparable to the imposed flux density the field is significantly reduced inside. For $\delta \ll \Delta$ shielding occurs because the field cannot penetrate the shielding material. This effect can yield very high SFs.

Taking into account both shielding effects, flux-shunting and eddy-current cancelation, the SF for a sphere has been given by equation (9) in [63]. The formula will not be quoted here, instead the results shown in figure 2.4 will be discussed briefly. For small conductivities no eddy-current shielding takes place and the curves approach the SF values given by equation 2.3, i.e. the DC values. For higher conductivities, but still $\delta \ll \Delta$, uniform induced currents improve shielding in comparison to the DC range, as given by equation 2.10. When the conductivity and the permeability reach values so that $\delta \gg \Delta$ the SF increases rapidly. In this regime the analysis is more difficult because the resulting SFs depend on the current distribution within the material. This covers some aspects of ferromagnetic shielding. The application will be discussed further in the chapter about the magnetically shielded room and the creation of small residual fields.

2.1.2 Active compensation

Disturbances of magnetic fields can also be reduced by producing counter acting fields, so that the sum of the fields cancels to zero. Such counter acting fields can be produced by either permanent magnets or by current-driven coils. Coils with corresponding current supplies have the advantage that they can be adjusted to changing external conditions and also that alternating fields can be compensated up to a certain frequency. A disadvantage of the active compensation is that the coil geometry has to match the field distribution of the disturbing source. The compensation of fields works perfectly for one point in space, but in order to minimize the field over an extended volume, the placement of coils and magnetometers has to be optimized. For the TUM setup this has been done with a Monte Carlo based approach. The exact procedure is described

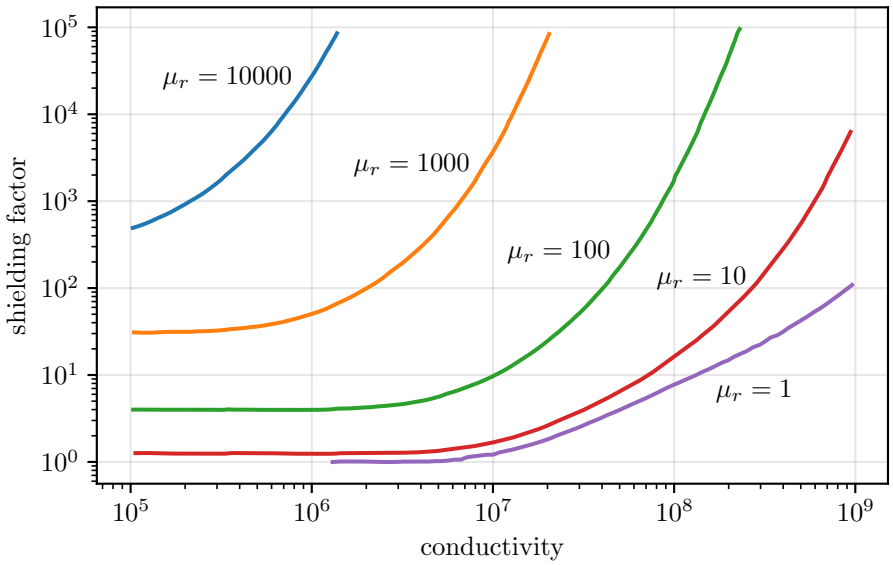

Figure 2.4: Calculated shielding factors, with both eddy-current shielding and flux-shunting considered. The SF is shown as a function of the conductivity for different values of magnetic permeability μ/μ_0. The parameters for the shield are $r = 0.1\,\mathrm{m}$, $\Delta = 5\,\mathrm{mm}$, for a frequency of 60 Hz. Data taken from figure 6 in [63].

in [38], and the resulting active compensation setup (ACS) has 24 coils as shown in figure 2.5. Three coil pairs per spatial direction produce homogeneous fields along their respective axes over the extended volume in which the MSR as well as the insert reside. Additionally, the outermost coil of each direction is split into two parts. By supplying a different current to each half a gradient field with transverse components can be produced. The magnetic field to be compensated (or to be kept constant) is measured with 60 three-axis sensors situated within the field cage and surrounding the MSR. Their placement also takes into account the distortion of the coils' fields due to the presence of the highly magnetizable material of the MSR. A feedback algorithm calculates the currents for the coils according to the real-time measurements of the field. In this active compensation mode, disturbances with a frequency of up to 3 Hz can be compensated.

For completely homogeneous fields, the field magnitude can in principal be reduced to approximately 1 µT. However, in reality the external fields are not completely homogeneous and an average field of 6 µT over the fiducial volume at the nEDM site is achieved. This corresponds to a reduction of a factor 7. Higher-order inhomogeneities in the fields due to magnetized concrete near the edge of the nEDM hole are responsible for this slightly less optimal performance.

On the other hand, absolute field strength not a big issue, because the main feature of the ACS is to compensate slow field drifts and to provide a time-stable field for the MSR. By magnetic equilibration (which will be introduced in the following chapter 3), the MSR will be brought into a time-stable equilibrium state with the surrounding fields and the fields inside the MSR will be stable. A strong change in the external fields will require further magnetic equilibration.

The performance of the ACS can be summed up with a plot of the Allan deviation

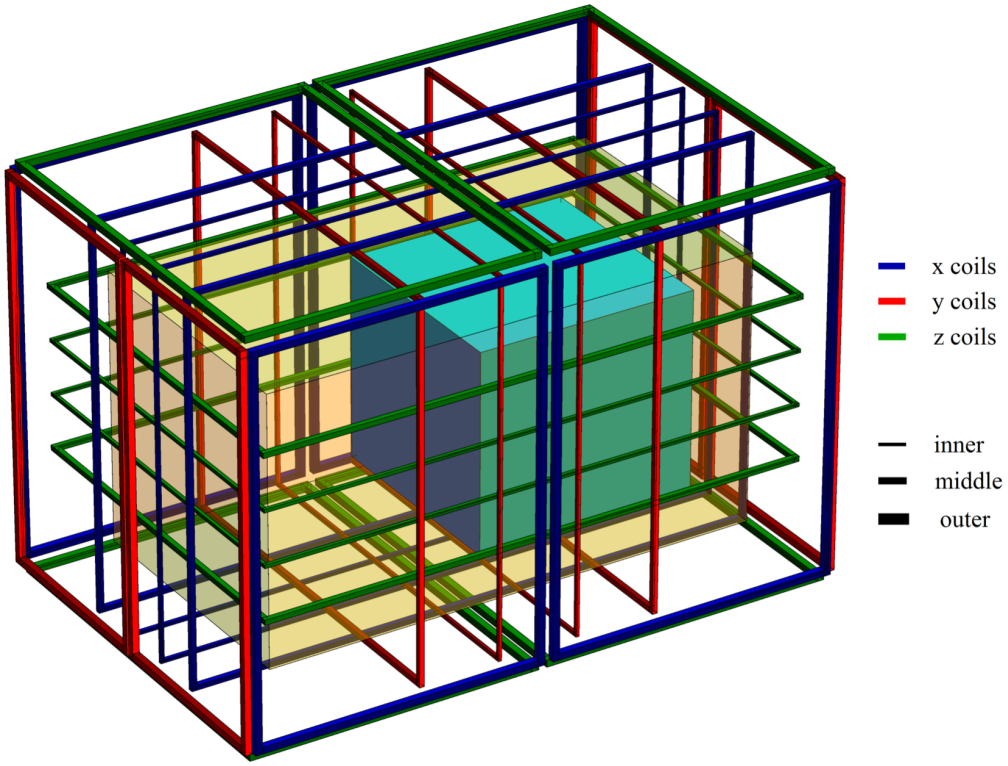

Figure 2.5: Sketch of the ACS. The six coils for each direction are shown, with the line thickness indicating pairs. The outermost coil is split into two coils to create transverse field gradients. The volume in cyan shows where the MSR is positioned and the yellow volume indicates the relevant volume in which the field is optimized by the ACS. This includes the MSR and additional space in front of the door where the inner shield is sitting, when it is removed from the MSR. Picture from [38]

for the field stability, measured at one sensor. The Allan deviation corresponds to the mean spread of two consecutive averaged bins of data points of a time series. By varying the number of data points in each bin, the noise and drift behavior of the data set can be easily visualized [64]. In the compensated case, field drifts for integration times $\tau > 1000\,\mathrm{s}$ are reduced by a factor of about 2.

Another practical use for more simple active compensation is a cylindrical shield with an open end. According to [57], the outside field leaks into the shielded volume and decays exponentially with the distance x to the open end

$$H_{in} = H_{ext}\, \mathrm{e}^{-kx/D}. \tag{2.11}$$

The factor k is given to be $k_t \approx 7.0$ and $k_l \approx 4.5$ for transverse or longitudinal fields respectively, and D is the cylinder diameter. A simple loop of wire around the circumference of the cylinder produces a field along the cylinder axis. Positioned at the end of the cylindrical shield, this field can be used to compensate an external field and strongly reduce the field inside the shielded volume. This has been demonstrated for a three meter long cylindrical shield with one open end, where the flux density

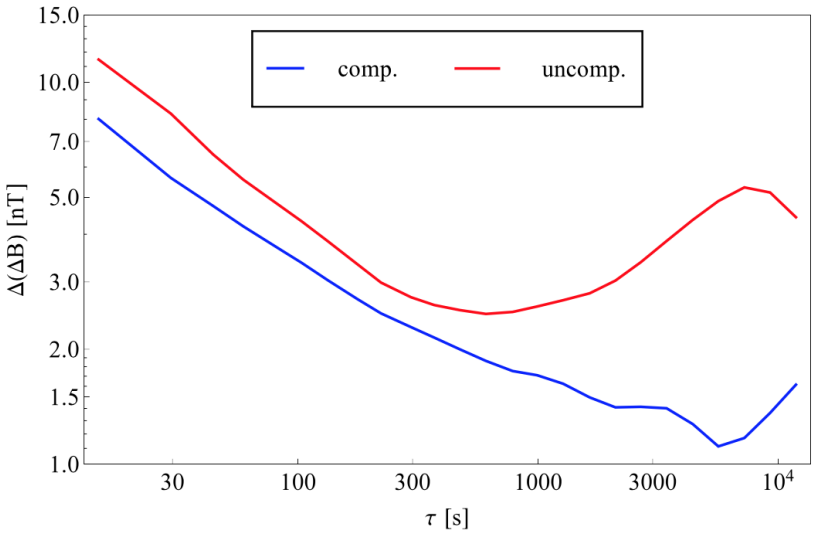

Figure 2.6: Allan deviation of the field inside the ACS. ΔB is the average field change per sensor over all 180 fluxgates. The compensated field (blue) is the measured field, the uncompensated field (red) shows the reconstructed field inside the ACS, calculated from the change in currents for the coils. The uncompensated field is dominated by drifts for $\tau > 1000\,\mathrm{s}$ with a minimum of 2.5 nT at 370 s. The compensated field is more stable and has a minimum of 1.1 nT at 5600 s. Picture from [38].

inside the shield has been reduced by a factor of ten in 90 cm distance to the open end. By applying a current through a five loop coil, the longitudinal field could be reduced from 300 nT to 30 nT. This way, the region with low residual fields could be increased significantly by about 0.5 m.

2.1.3 Superconducting shielding

Superconducting materials repel magnetic fields due to the Meissner effect. In ideal conditions all magnetic flux would be repelled by the superconducting shield. In reality, however, magnetic flux can be trapped during the cool down process due to impurities in the material. Therefore, the residual field inside the shield depends on the field in which the superconductor was cooled down; as such the cooling should take place in an already field-free region. For time-dependent magnetic fields with low frequencies ($<$ kHz) the shielding properties of the superconducting shield are comparable to conventional passive shielding, but with less material and therefore less weight necessary. On the other hand, cryogenics are needed. Since superconducting shields are not used in our shielding strategy, they only mentioned here very briefly for completeness' sake.

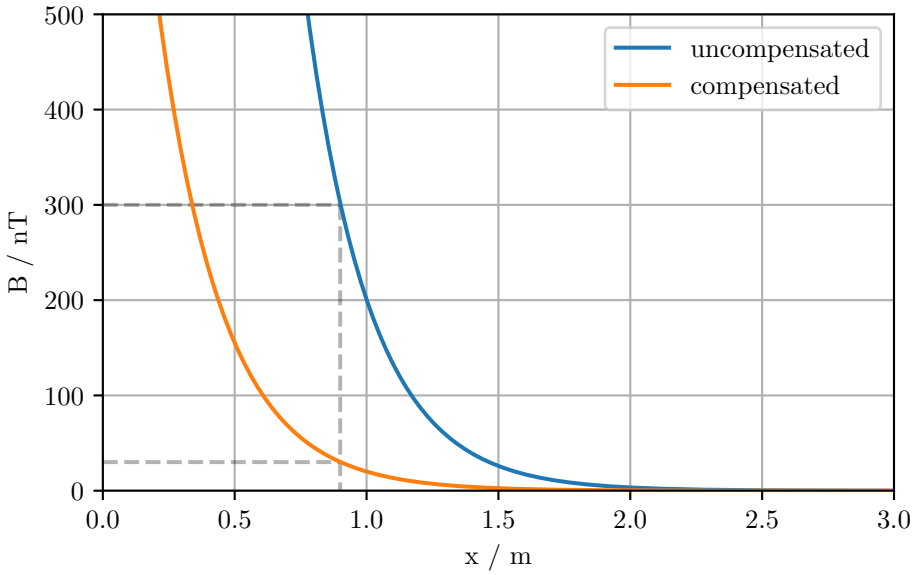

Figure 2.7: Plot of the longitudinal component of the magnetic field leaking into the open end of the cylindrical shield, according to the exponential model given in [57]. A magnitude of 12 µT, corresponding to the approximate horizontal component of the earth magnetic field is used, to give 300 nT at 0.90 m for the uncompensated case. With compensation the external field is reduced to 1.2 µT resulting in 30 nT at 0.90 m, thereby increasing the region of low field by 0.5 m.

2.2 Magnetically shielded rooms for the PanEDM

In this section, the passive shield of the TUM nEDM experiment will be described in more detail. This has been published in [65] and [66] and will be reproduced here briefly. The passive shielding consists of two separate parts, an outer shielded room, the MSR, and an inner passive shield, the insert. The nEDM setup, a vacuum chamber with the nEDM cell stack, will be mounted in the MSR, where it can be accessed and tested. A scissor lift table will sit on top of the MSR. Through the access holes in the ceiling of the MSR the lift table will be connected to either lid of the vacuum chamber to open and close it, where as the weight of the vacuum chamber will be sitting on the wooden floor on top of the MSR. This way the nEDM setup can be accessed conveniently for setup and maintenance.

The insert is placed on an a rail system in front of the MSR. Setup and testing of the magnetic field system can take place there. Then both shields can be combined for high shielding factors and to apply homogeneous fields to the nEDM setup.

2.2.1 Outer MSR

The MSR has three shielding layers, two made from high-permeability material (VDM® MAG 7904) and one highly conducting aluminum layer sitting in between. The mumetal layers are 2 mm thick and consist of 2×1 mm thick heat-treated mumetal sheets. The distance between the two layers is approximately 0.25 m. The aluminum shell is 8 mm thick. All 74 feedthroughs into the MSR are made from 0.25 m long aluminum tubes that are welded to the aluminum shell so that they are RF-tight. The mumetal layers have corresponding holes, large enough to avoid electrical contact and keep all three

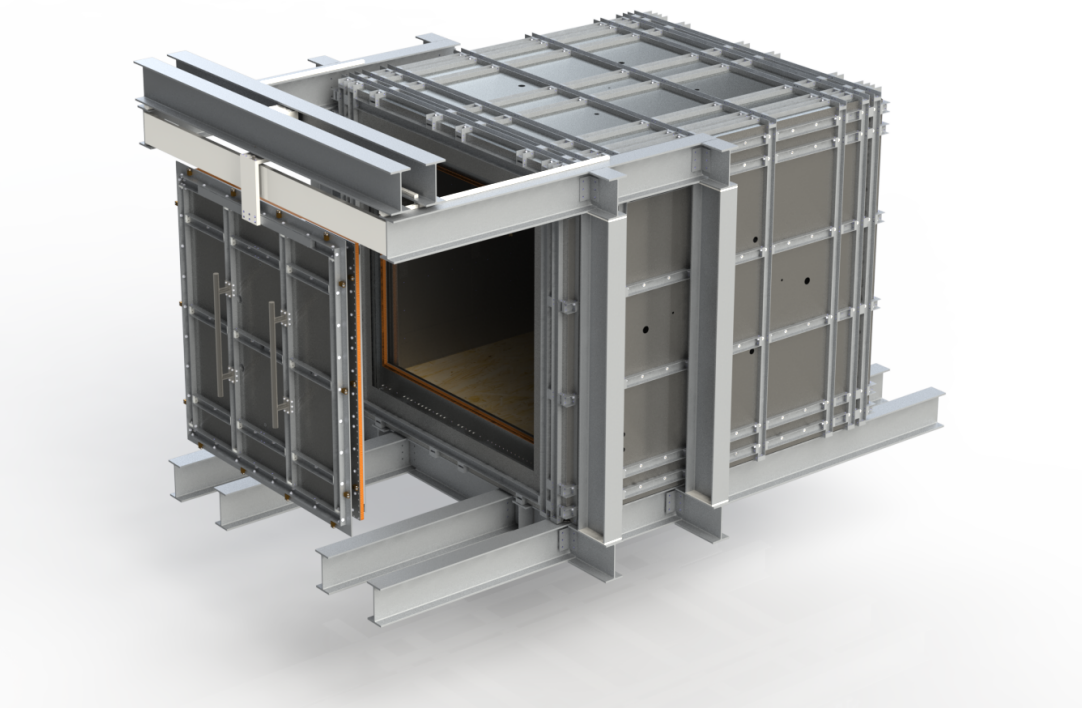

Figure 2.8: Rendered view of the MSR with the door opened.

layers electrically isolated from each other.

The inner dimensions of the room are 2.5 m(X)×2.78 m(Y)×2.35 m(Z). On the one side of the room, a 1.92 m×2 m door allows access to the inside. When closed, the door is pneumatically clamped to the MSR walls to ensure good magnetic contact between the shielding material for the 65 mm wide overlap. The door itself is mounted on a rail system and hangs from one central point to allow rotation and to be able to remove it completely from the front of the MSR.

The floor of the room is laid out with wooden panels that do not put weight on the mumetal. 28 additional load bearing points inside the MSR can carry up to 5.5 tons of weight by distributing it to the support structure of the MSR. On these points the non-magnetic rail system is mounted to move the insert into the MSR. Lighting inside the room is provided by non-magnetic LEDs.

The MSR itself rests on four feet with the option to adjust its height above the floor by putting additional spacers in the feet. The feet are foreseen to include an additional active feedback mechanism to reduce mechanical vibration. The major resonance frequencies for mechanical vibrations of the MSR are 8, 10, 16, 20, and 22.3 Hz. A surrounding balcony allows access to all exterior sides of the MSR.

2.2.2 Insert

The insert is an additional magnetic shield consisting of three layers of VDM® MAG 7904 with 1.92 m width, 1.92 m height and 2.7 m length. Via a detachable set of rails

it can be moved into the MSR by a manually operated, mechanical winch.

The mumetal layers of the insert have varying thickness, with the outer shell consisting of 2×1 mm mumetal sheets, the middle layer of 4×1 mm and the innermost shell again 2×1 mm. The middle layer is thicker for an increased shielding factor, whereas the inner layer has been kept thinner for better magnetic equilibration. The shells have a distance of only 80 mm to each other. A distance this small was against common design principles for magnetically shielded rooms at the time as it is much smaller than the optimal layer distance. Nevertheless very good shielding factors have been achieved (table 2.1 and [66]). When the insert is inside the MSR, the mumetal wall distances between the outer layer of the insert and the inner layer of the MSR are 250 mm in the X direction, 120 mm in the X direction and 220 mm in the X direction. The space in the gap between the MSR and the insert may be used to deploy sensitive electronics, for example for SQUID readout. These electronics can be operated without influencing the magnetic field inside the insert, but are still within the low-magnetic-field environment and RF shielding of the MSR.

The inner dimensions of the insert are 1.54 m width, 1.54 m height and 2.2 m length. In this space another 1.6 mm thick cylindrical shell of VDM® MAG 7904 is installed that comprises the B_0 and B_1 coil system (cf. chapter 7). In figure 2.10 the cylindrical innermost layer together with its mounting structure and the copper tubes for the coil systems are shown during the assembly procedure. For mechanical precision and to keep its shape the cylinder is mounted in a structure of GFRP. The copper tubes form the coils for the B_0 system, tubes were chosen because they have stability so they do not bend between the GFRP structure. The holes in the six GFRP rings for the copper tubes are machined with a precision of 0.1 mm.

The end cap of the insert is mounted to the back wall of the MSR opposite the door. This allows the nEDM vacuum chamber to stay inside the MSR and still be accessible. A photograph of a test assembly can be seen in figure 2.11. The insert can be closed by sixteen 2.8 m long titanium bolts that are situated between the outermost and the middle layer of the insert. Once the titanium bolts are tightened with a defined torque, the two inner shells of the insert end cap can be pneumatically pressed against the inner two shells of the insert.

In table 2.1, the measured shielding factors for the shielding system and the individual layers are presented. The extraordinary shielding performance represents an improvement of the state-of-the-art by more than an order of magnitude for the very low-frequency regime, making it the strongest damping large-scale magnetic shield.

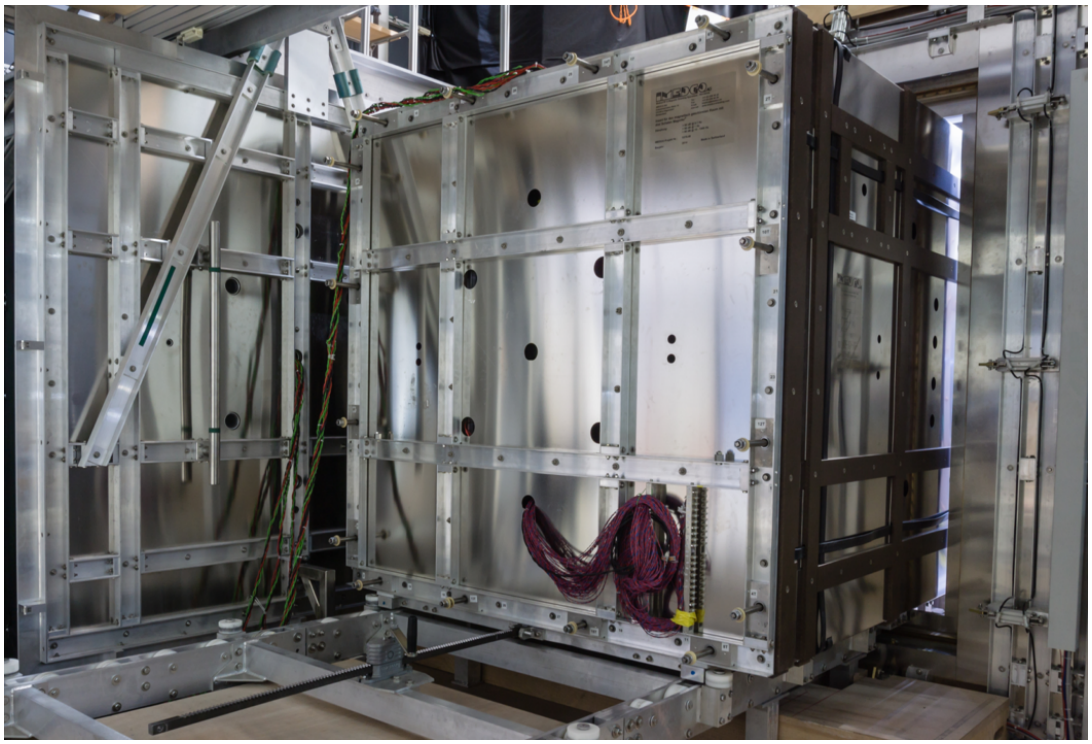

Figure 2.9: A photograph of the whole passive shielding, with the insert halfway into the MSR. The insert is moved on the rail system with plastic wheels in an aluminum frame, by manually operating a winch. The MSR door is moved completely to one side to allow access for the insert. When the insert is completely inside the MSR, a part of the rail system can be removed to allow the door to be closed. The wires connect the B0 system to the current sources.

Table 2.1: Measured shielding factors for different excitation frequencies f and peak-to-peak amplitudes B_{ext}. Different sensor types are used: fluxgates (FG), SQUIDS (SQ) and a mercury nuclear spin magnetometer (Hg). (l) and (t) indicate measurements in the longitudinal and transverse direction respectively.

Shield	f/Hz	B_{ext}/µT	Sensor	SF
MSR outside layer	0.01	2 (pp)	FG	33
MSR both layers (t)	0.01	2 (pp)	FG	279
MSR both layers (l)	0.01	2 (pp)	FG	260
MSR both layers (t)	0.01	32 (pp)	FG	400
MSR both layers (l)	0.01	32 (pp)	FG	350
Insert layer 1	0.01	2 (pp)	FG	40
Insert layer 1+2	0.01	2 (pp)	FG	600
Insert (l)	0.01	2 (pp)	FG	4700
Insert (t)	0.01	2 (pp)	FG	6500
MSR + insert (l)	0.001	16.25 (pp)	HG	971000
MSR + insert (l)	0.001	16.25 (pp)	SQ	938000
MSR + insert (t)	0.001	16.25 (pp)	HG	1231060
MSR + insert (t)	0.001	16.25 (pp)	SQ	1173300
BMSR-2[67]	0.01	1 (rms)		75000
BMSR-2	1	1 (rms)		2000000

Figure 2.10: Photograph taken during the assembly of the insert and the cylindrical shield with the B_0 coils. The printed circuit boards (PCBs) that connect the individual tubes to form single or multi-turn coils were not yet mounted for this picture.

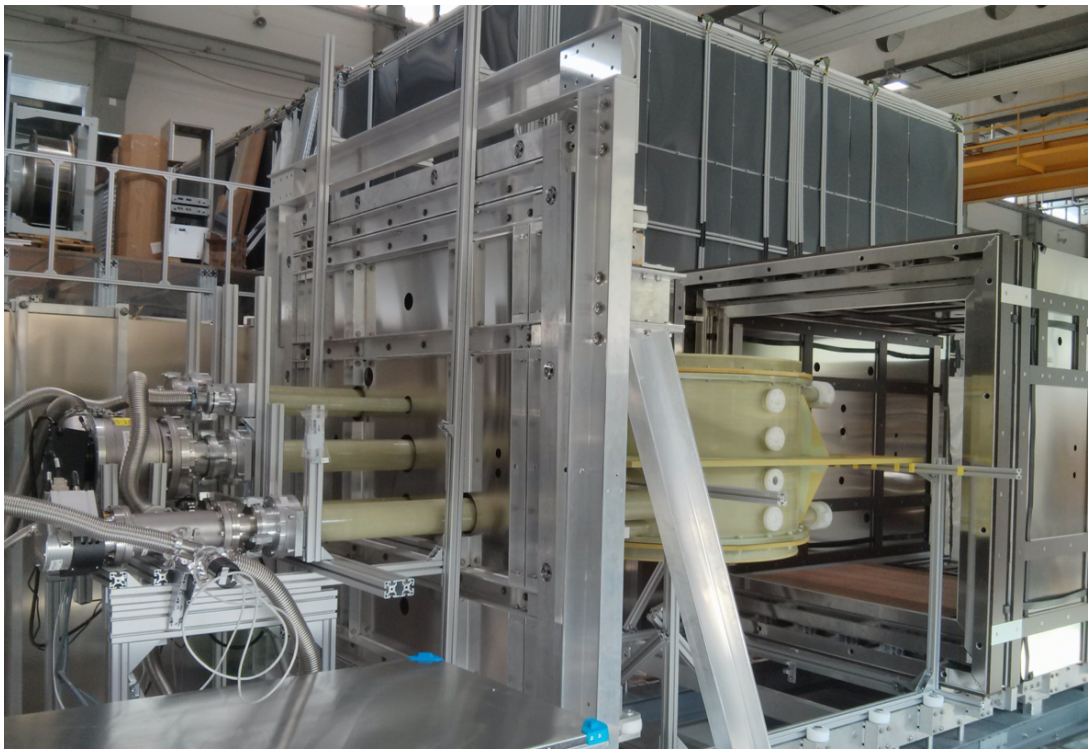

Figure 2.11: Photograph of the test assembly, where the vacuum chamber has been mounted in the back door of the insert and was evacuated.

3. Degaussing

In this chapter the concept of magnetic equilibration is introduced. The principles are explained, and the experimental setup used to equilibrate the nEDM shields is described.

Magnetically shielded rooms are, as described in the previous chapter, made from highly permeable materials that have a small, but nonetheless finite remanence: even when all field sources are removed, the material remains in a magnetized state. For a sufficient amount of shielding, in the static case ($\omega = 0$), the field within an MSR is dominated by this residual field from the shielding material and not by the effect of external fields. The process to remove this remanent magnetization and achieve very small residual fields is called degaussing or magnetic equilibration.

Typically, it is performed by applying an alternating current to coils that are wound around the shielding material. The current's amplitude is reduced to zero over a given period of time, thereby slowly cycling the magnetization of the material through shrinking hysteresis loops. At the end, one ideally ends up at B = 0. The process is illustrated in figure 3.1.

The term "degaussing" is widely used for this concept. In its strict sense, i.e. that the material ends at $B = 0$, this is only true, if the process is done in in zero magnetic field. Only then the material ends at in a "degaussed" state, because all domains will then be oriented randomly. In the presence of a magnetic field, the term magnetic equilibration is more accurate, because the material will be brought into an equilibrium state at the prevailing field. This is not a state where the magnetization is $M = 0$. Here, the cycling through hysteresis loops provides the energy for the domain walls to overcome pinning sites in the material, so that they can align with respect to the external field and arrange in a way that minimizes the magnetostatic energy; then also the residual field is smallest. The state in which the domain walls are in equilibrium

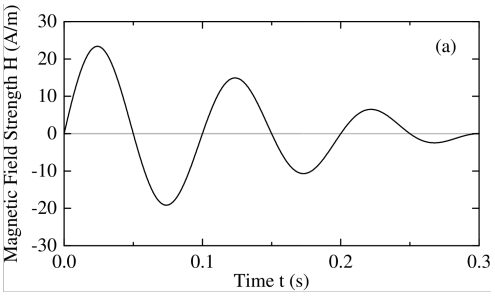

(a) Waveform of the applied current with decreasing amplitude through the equilibration coils.

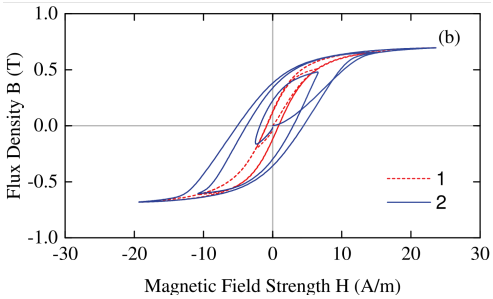

(b) The magnetization cycling through hysteresis loops as the current amplitude decreases.

Figure 3.1: Principle of magnetic equilibration. A sinusoidal current with decreasing amplitude (a) forces the magnetization of the material through hysteresis loops and the flux density ideally ends up at $B = 0$. More details can be found in chapter 6.

under the prevailing field lies on the anhysteretic magnetization curve (cf. chapter 6 and [68]). This means that equilibration in a external field returns the magnetization of the material to the anhysteretic curve. As a note, the anhysteretic curve can be measured experimentally by setting a constant external field and then superimposing a decaying sinusoidal field to that constant field [69].

Degaussing has been studied in detail [70], and residual fields inside shielded rooms achieved have already reached the level of nT (for example [65], [71]). For further improvement, the material production and manufacturing quality becomes increasingly important, since the residual field becomes limited by stray fields from imperfections of a granular nature or stress in the shielding material (c.f. [59]).

As has been mentioned, magnetic equilibration is done by applying an AC current with a decaying amplitude to coils that are wound around the shielding material. The amplitude of the current has to be large enough to saturate the magnetization (ideally) everywhere within the material. The material has to provide a closed path for the magnetic flux; otherwise saturation will not be reached, and also stray fields will create localized spots of magnetization.

Even though arguments have been made for using optimized envelope functions for the decaying amplitude [72], a simple linear decrease has worked very well for all our experiments. Still, the progression of the amplitude decrease is an important factor, especially at the very end of the equilibration process. The last half-wave determines the remaining magnetization in the material. It provides the smallest amount of energy for the domain walls to overcome pinning sites. For bigger amplitude steps more energy is deposited in the material, which in turns leaves the domain walls in states of higher energy and therefore increases the residual field. The size of this last amplitude is determined by the resolution of the digital-analog converter (DAC) device to create the waveform and the ability of the amplifier to output small currents. Therefore, a high quality amplifier with low noise and without an DC offset is necessary.

3.1 Setup

Development of an automated setup for magnetic equilibration of the nEDM experiment was part of the work for this thesis. The basic components necessary for an equilibration setup are shown in figure 3.2. A personal computer (PC) is used to control the hardware and create the waveform for the sinusoidal current with a decaying envelope function. Via a 16-bit resolution DAC [1], the waveform is output as an analog voltage signal. An optional attenuator allows to reduce the signal amplitude, in case small current amplitudes are needed and the full 10 V range of the DAC has to be used for smaller DAC resolution steps. A amplifier[2] capable of providing enough current to saturate the material converts the voltage to a current, and a transformer is used as a high-pass filter to remove a DC offset from the amplifier output. The current is distributed to the coils for the individual shielding layers via relays. All of the hardware, except the large amplifier, was built into a movable 19-inch rack, a photograph is shown in figure 3.3.

1 National Instruments NI USB-6259 BNC
2 Hero Power PA2088B custom made by Rohrer GmbH, München

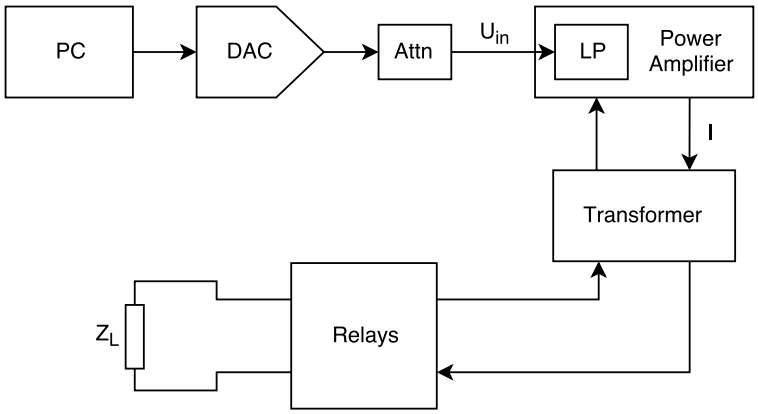

Figure 3.2: Principal components of a setup for magnetic equilibration. A more detailed description is given in the text.

Figure 3.3: Photograph of the equilibration setup. A 19-inch rack houses all of the equipment, except the amplifier. On the top a touch screen PC allows control of the process. The (closed) relay box below the PC distributes the current, after it has been filtered by 80 kg transformer on the bottom. The amplifier comes in its own movable rack.

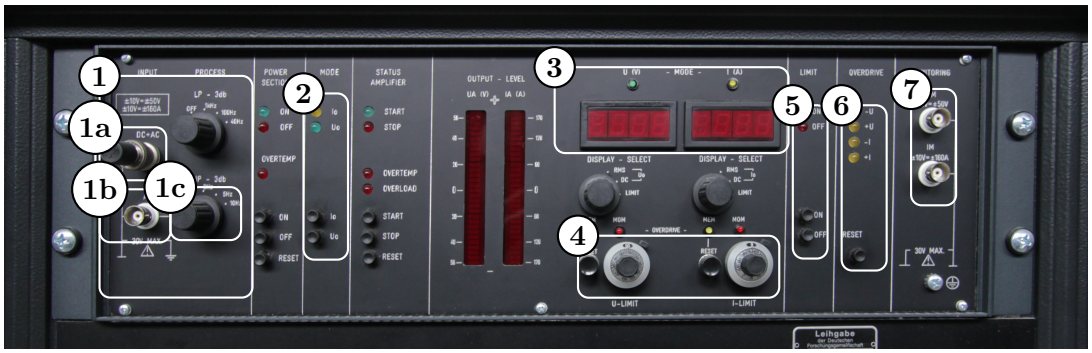

Figure 3.4: Elements of the amplifier control panel: (1) Voltage inputs with DC and AC coupling (1a) and with AC coupling only (1b) and selectors for the respective cut-off frequencies (1c), (2) selection of current or voltage mode, (3) displays to monitor voltage and current output, (4) turn-knobs to set limits for voltage and current output, (5) de-/activate limits (6) reset if limit has been reached and (7) BNC connectors for monitoring.

Amplifier

The amplifier is a high precision power amplifier that can supply up to 160 A at up to 50 V. Two operation modes are available, voltage or current output. In voltage mode, the sensitivity is 5 V/V, for the current mode the scaling is 16 A/V, meaning 1 V at the input will produce 5 V or 16 A at the output, respectively. The current mode of the amplifier was found to be more slightly noisy than the voltage mode. Therefore, in our setup the amplifier is used in voltage mode. Two inputs are available, one with a high pass filter included (labeled AC in the amplifier front panel) and one without (labeled DC + AC). Furthermore, two adjustable filters for the inputs signals can be set to cut high and low frequencies (see also figure 3.4). The amplifier is supplied by a 400V/32A mains line. The ground connection was removed from the mains line and set to a central grounding point for the experiment, giving the amplifier and the equilibration rack the same reference potential as the MSR. This way, 50 Hz noise could be reduced.

The amplifier was chosen to allow not only consecutive single layer equilibration but also equilibration of all layers at once. For this a very high current would have been necessary. It turned out that smaller currents are necessary to equilibrate the TUM MSR than was initially anticipated. To scale down to smaller currents, an analog voltage divider is available, that can be activated to reduce the voltage supplied to the amplifier. The current from the amplifier is supplied to a transformer with a winding ratio of 1:1, so that only alternating currents are supplied to the equilibration coils, since any DC component at the end of the equilibration process would magnetize the material again. The transformer can withstand 30 V and 33 A for several minutes before overheating and even higher currents for shorter periods. For monitoring, temperature sensors are included on the primary as well as on the secondary side of the transformer.

Relay box

Distribution of the current to the individual equilibration coils after the transformer is handled by a set of relays. For each coil, a two-channel latching relay rated for 230 V and 32 A can open and close the coil's connection to the transformer. Here, latching means that the relay retains its state after being activated by a current impulse. The

relays are mechanical in order to completely separate the coils from the power supply and prevent leakage of currents to the other equilibration coils. They require a voltage of 12 V to switch, this is more than the TTL signals from common digital outputs provide. Therefore, an additional stage of relays is needed. These are actuated by the TTL signals from digital outputs and then connect a 12 V power supply to the switching input of the high power relays for 0.5 s. In total, there are 14 channels available.

Two different types of high power relays are used. A readout for the state of the relays has been added. For the second type of high power relays (made by Finder) a 5 V DC signal is connected to one of the channels and then to a digital input card. This is necessary since the relays can become unreliable after some operation time. Of course this then requires two relays for each coil.

Equilibration Coils

The outer MSR was equipped with 12 equilibration coils for each of the two layers, one along each edge of the cube. The single coils along each of the edges initially consisted of three cables with 7 strands each, forming a 21 loop coil. Four of these coils were connected in series to form a closed loop of magnetic flux around one spatial direction, giving 84 windings in total.

The two layers of the MSR are equilibrated separately, first the inner layer, then the outer one, and after that the inner one again. For each layer, first the X direction is equilibrated, followed by the Z direction and then the Y direction. It was found that equilibration of one direction is not sufficient: subsequent equilibration runs in the second and third direction each improved the result. This can be easily understood: Since the coils are wound around the walls of the MSR, they have to penetrate the adjacent faces of the cube. These faces are not included in the closed loop of flux for equilibration in one direction and the magnetization is not properly removed. This will be further elaborated on in chapter 5.

A sinusoidal current with a peak amplitude of about 21×7 Ampere×turns (depending on the layer) and a frequency of 10 Hz is applied. The amplitude decreases over 2000 periods (“cycles”) to a value as close to zero as technically achievable. Equilibration therefore takes 600 s for each layer. With this procedure residual fields below 1.5 nT

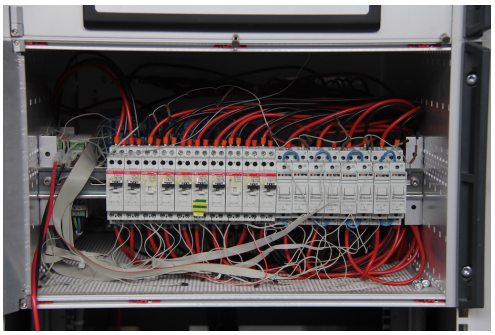

(a) View of the relays. Two different types are used.

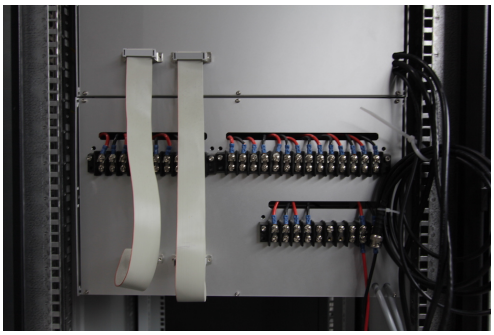

(b) View of the connection terminals where the coils have to be connected.

Figure 3.5: Set of relays connecting the transformer to up to 14 equilibration coils for the magnetically shielded rooms.

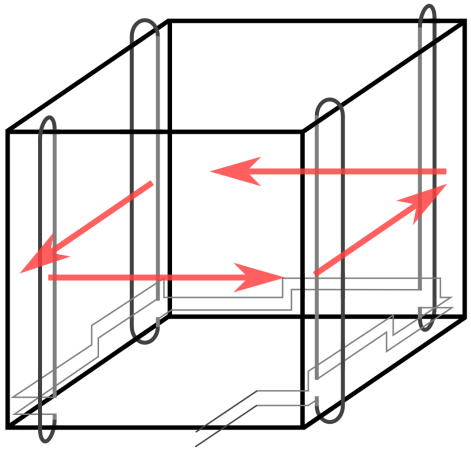

Figure 3.6: Illustration of the equilibration coils and their arrangement. Shown are the coils for the Z direction, which produce a closed loop of flux as indicated by the arrows. Also shown are the connections between the coils and the current return path, which are arranged in a such way that fields originating from connecting wires cancel each other.

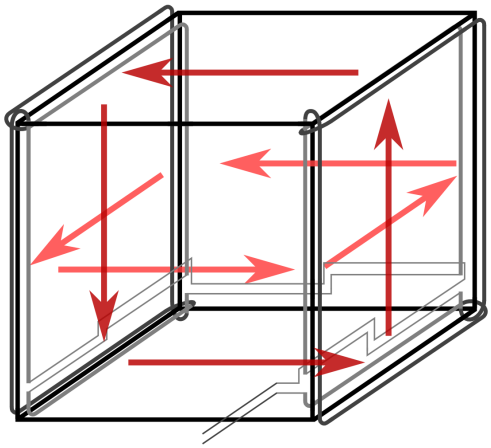

Figure 3.7: Illustration of the new equilibration coils. Shown are the L-shaped coils for combined equilibration of the Y and Z direction, producing a closed loop of flux as indicated by the arrows.

and gradients smaller than 2 nT/m have been achieved [70]. The resulting fields for the TUM MSR will be presented in chapter 4.

This arrangement of the coils has been modified [73]. First, it was found that the connecting wires from one coil to the next were forming an additional loop of current that magnetized the material. So the connections were rewired to cancel this current (also shown in figure 3.6). Second, the wiring of the coils themselves has been changed to address the problem mentioned above, the creation of magnetization in the adjacent face of the cube. Two coil sets of the previous configuration, for the Y and Z directions, were reconnected to form an "L-shaped" coil pattern along two edges of the MSR. Four of these Ls are again connected in series (see figure 3.7). In this way two

spatial direction are equilibrated at the same time. This reduces the time needed for equilibration, while keeping the residual fields on the same magnitude.

Furthermore, to reduce the resistance of the coils and to use higher currents instead of higher voltages, which is more suitable for the amplifier, the coil wires have been to changed to a parallel configuration instead of a serial connection. Instead of 84 loops with 2.5 mm^2 cross section, the coil now consists of 28 loops with 7.5 mm^2 wire cross section.

The achieved residual fields with both of these configurations will be discussed in chapter 4.

3.2 Current and parameter determination

From previously determined parameters for successful equilibration of a known MSR, suitable parameters for another MSR of similar construction can be estimated. The magnetic field produced by a given set of coils is

$$H = \frac{NI}{L}, \tag{3.1}$$

where N is the total number of turns for all coils, I the current and L corresponds to the length of the magnetic flux path. For a box-shaped MSR, L is given by the length of the walls along one spatial direction, for a cylindrical shield L is the circumference of the cylinder. The field strengths necessary to equilibrate are on the order of $H = 30\,\mathrm{A/m}$ for our MSRs with a wall thickness of 2 mm. This is much higher than mentioned in [74] where the recommendation is that the maximum field for degaussing should be five times H_c. For Krupp Magnifier, the coercivity is $H_c = 1.2\,\mathrm{A/m}$. Material overlaps and air gaps increase the magnetic resistance and create loses of flux, which in turn requires higher currents for the equilibration processes.

The experimentally determined parameters for equilibration of several MSRs are given in table 3.1. To scale a current used for one geometry to another MSR the equation

$$I_2 = \frac{N_1}{N_2}\frac{L_2}{L_1}I_1 \tag{3.2}$$

can be used. This can, of course, only provide an estimate of the required equilibration current. Other important factors like material overlaps, reduced magnetic contact (cf. chapter 5) between material sheets, holes, or the spatial arrangement of the equilibration coils are not considered here, and for MSRs with a different construction, this approach to estimate the necessary currents could also give less accurate results.

According to the equation 3.1, the thickness of the wall material does not influence

Table 3.1: Dimensions and equilibration parameters of the TUM MSRs.

MSR	L / m	W / m	H / m	T / m	Turns	I / A	H / A/m
Outer 1	3.3	3.0	2.85	0.002	84	4	26.7
Outer 2	2.8	2.5	2.35	0.002	28	12	31.7
Inner 1	2.7	1.9	1.9	0.002	28	9	27.4
Inner 2	2.45	1.75	1.75	0.004	28	18	60.0
Inner 3	2.2	1.6	1.6	0.002	28	9	33.2

the current necessary for magnetic equilibration. The flux density inside a material is independent of the material volume when it is placed inside a coils. However, in the course of equilibration experiments for this thesis it was found that for layers with thicker mumetal walls, the current had to be increased to reach low residual fields. A possible reason for this could be that the penetration depth (cf. equation 2.9) of the field into the material of approximately 0.7 mm (for VDM® MAG 7904 at 10 Hz) is already so small that material of 4 mm thickness is not saturate fully to yield good equilibration results. Therefore the current for the "Inner 2" is increased by a factor of 2, as given in table 3.1.

3.3 Control

In the following the control software is described. In order to equilibrate a MSR, the individual equilibration coils have to be activated in a defined sequence and a current waveform with correct parameters for each coil has to be output by the amplifier. In the TUM setup this sequence is controlled by a number of python scripts. Two control systems are available for equilibration: The first one is tied in with the experimental control of the nEDM experiment which is based on a central CouchDB[1] database, so that equilibration can be run as a part of the full nEDM measurement cycle. The second way of control is a standalone system that does not rely on the overall instrument control and can be operated individually. This means that the configurations are either saved as documents in the CouchDB or as simple text files on the equilibration control computer. Their content however is the same in both systems. For the CouchDB system, the interface also resides in the database and can be accessed with a web browser as part of the overall control system. For the standalone system the user interface is realized as a graphical user interface written in wxPython[2].

In the database controlled version, the touchscreen PC dedicated to the equilibration setup runs a script that connects to the *nEDM/degaussing* database, and listens to its changesfeed. The changesfeed is a feature of CouchDB, that reports whenever a change happens in a database. When a command document is posted to this database from any web browser (and by a user having the appropriate credentials), the command document is retrieved by the listener and will be checked against a dictionary whether the command given in the document is accepted by the listener. Then, the command will be passed on to a controller instance created by the listener.

The execution is handled by *controller.py* for both versions. The controller object retrieves the configuration and the settings from the database on its creation, when the listener is started (meaning, if the configuration is changed, the listener has to be restarted). Settings are then chosen depending on which equilibration scenario is to be run.

The controller object uses separate modules for controlling digital I/O ports used to switch relays, a module to create the equilibration waveform and run this waveform as an analog voltage output task on the DAC hardware. The controller further provides functions to check whether equilibration is in progress and to interrupt a running process.

1 http://couchdb.apache.org
2 https://www.wxpython.org

The sequence for the equilibration coils can be defined in a configuration file in the format of a dictionary:

```
{
  "Name": "MSR",
  "Config": "msr_config",
  "Sequence": ["L-coil", "A-X", "A-Z", "A-Y", "L-coil"]
}
```

Listing 3.1: Example of configuration file to define a equilibration sequence

In "Sequence" the order of the coils for equilibration is defined. The key "Config" specifies which configuration document/file is to be read for the parameters for each coil. This document is also a dictionary containing key value pairs as shown in the following example:

```
{
     "L-coil": {
        "Amp": 9,
        "Freq": 10,
        "Dur": 50,
        "Keep": 10,
        "RelayPort": 0,
        "VoltageDivider": 5
    },
    "Offset": 0,
    "Device": "Dev1"
}
```

Listing 3.2: Example of an entry in a configuration file to specify waveform parameters for a coil.

The values for "Amp" and "Freq" give the amplitude in V and frequency in Hz for the sinusoidal waveform. "Dur" and "Keep" specify the duration of the equilibration process and how long the maximum amplitude at the beginning of the equilibration process is kept, respectively. The number for "RelayPort" corresponds to the number of the terminal on the backside of the relay box where the corresponding coils are connected. In the setup, five different voltage dividers are available, the one to be used for a particular coil is also given in the configuration file. The last two keys allow to set a global offset for all created waveforms and specify the name under which the DAC device for the waveform output is registered in the operation system. The python scripts take the information from these files and run the equilibration process.

The waveform is created according to the parameters and put out via the National Instruments analog output channel. The digital outputs of the National Instruments device are used to activate the coils and voltage dividers. This sequence is controlled by the python script *model.py*. Here the information from the configuration files is collected and distributed to the sub scripts that handle different tasks, for example *digiport.py* to control the digital outputs.

The settings for all coils that have been used for the TUM MSRs can be found in appendix A.

Table 3.2: Voltage and current settings for equilibration of the outer MSR.

Coil	U_{rms}/V	I_{rms}/A
A-X	24.1	4.0
A-Y	23.0	3.7
A-Z	24.0	4.0
L	24.1	12
I-X	12.2	8.4

Table 3.3: Voltage and current settings for equilibration of the inner MSR.

Coil	U/V	I/A
1r X	18.5	8.5
1g Y	17.3	8.4
2r X	30.5	17.4
2s Z	32.3	17.2
2g Y	34.6	18.0
3r X	14.1	8.0
3s Z	15.4	8.1
3g Y	17.6	8.8
Cylinder	26.6	48.0

4. Residual fields in shielded rooms

MSRs do not only provide damping of external disturbances for experiments, but also set up a space of very low residual magnetic fields and low gradients. These requirements are important for a wide variety of experiments, ranging from biomagnetism like magnetocardiography (MCG) and magnetoencephalography (MCG) [75] over low and zero field NMR techniques [76] to liquid detection in security applications [77] and fundamental physics experiments, for example measurements of the equivalence principle [29] and the nEDM experiments [66, 34, 78]. For spin precession experiments the relaxation times depends on the field gradients over the sample volume.

Reaching reach ultra low residual field requires a lot of effort. The MSR itself has to be constructed carefully (i.e. placement of door, overlaps and feedthroughs), the shielding material has to be manufactured and treated with care, everything that goes inside the MSR has to be magnetically screened and tested to be not magnetizable, and the magnetic equilibration setup and procedure has to be optimized for a particular MSR.

The magnitude of the residual fields indicates how well the magnetic equilibration procedures work. If the equilibration produces a very small residual field without any applied fields, the magnetization everywhere in the material is reached by the equilibration field and optimized to the prevailing field conditions after equilibration. Localized spots of magnetization everywhere in the material can be removed and inside the shielded volume small fields and gradients are the result. When there are additional applied fields, inside the shielded room for experiments, successful equilibration brings the material into a state of minimal energy with respect to the prevailing field and therefore creates a time stable field configuration. When the shielding material is adapted to the existing field in this way, gradients in the field due to the presence of high permeable materials are reduced.

Residual magnetization spots in the walls, or other gradients in the residual field combined with unavoidable mechanical vibrations of the walls or the equipment and sensors inside the MSR with respect to the walls, can create magnetic noise in the frequency range of the mechanical vibrations up to 40 Hz. This noise might interfere with measurements, because this is the relevant frequency range for the neutron and comagnetometer precession frequencies in the nEDM experiment.

4.1 Measurements

Residual fields inside MSRs are on the order of nT and below. This proves difficult to measure absolutely, for several reasons. The sensors need to be accurate enough, and for absolute field measurements offsets have to be determined with the same accuracy. For three-axis sensors, the angular accuracy for the orthogonality of the sensors with respect to each other is not that important, since no component is expected to be significantly larger than the others.

Several types of sensors are sensitive enough to measure magnetic fields on this level. Optical magnetometers, SQUIDs or fluxgates all can have the required sensitivity.

Optically pumped magnetometers (OPMs) are based on the measurement of the Larmor precession of spin polarized atoms in a magnetic field. Atomic vapor, for example Cs or Hg, is polarized by driving transitions between Zeeman split levels of the atoms or nuclei with laser light. The polarized atoms are subject to a magnetic field around which they precess. An additional read-out laser beam is guided through the vapor and the transmission or the Faraday rotation for linearly polarized light is measured. This way the measurement of magnetic fields corresponds to a frequency measurement. The precession frequency is

$$\omega = -\gamma|B| \tag{4.1}$$

and proportional to the absolute magnetic fields, with the gyromagnetic ratio γ. Therefore these magnetometers offer a scalar field measurement, with a very high sensitivity of $10\,\mathrm{fT}/\sqrt{\mathrm{Hz}}$ [79]. For very small magnetic fields in the below-nT range, the corresponding precession frequencies are also very small, $\mathcal{O}(1\,\mathrm{Hz})$ for Cs and $\mathcal{O}(1\,\mathrm{mHz})$ range for Hg, and an accurate measurement would require long integration times. OPM can be operated to measure vectorial field information [40]. Apart from long integration times, there are other problems why they are not especially suitable for measurement of residual field maps. Placement of OPMs anywhere within a volume of approximately $1 \times 1 \times 1\mathrm{m}^3$ proves difficult due to the fact that the laser light has to be guided to the cells. For free space operation, a system of mirrors would have to be used, and for fiber-coupled systems movement of the sensors puts strain in the fibers and could cause defects. Furthermore, commercial systems of OPMs only very recently became available[1].

Super conducting quantum interference devices (SQUIDs) are currently the most sensitive magnetic flux detectors in existence, with field resolutions in the 10 aT range [80]. A SQUID consists of a loop of superconducting material interrupted by two Josephson contacts. Magnetic field measurements are based on the effect that magnetic flux changes through the loop induce a screening current inside the loop to keep the flux density constant. When a bias current is applied to the junctions, the induced current changes the voltage drop across the junctions and these voltage changes can be measured. In this way SQUIDs convert flux Φ to voltage V.

With flux-lock loop (FLL) electronics, the flux through the loop is kept constant with a feedback current through a magnetically coupled coil near the SQUID; then the voltage drop across a feedback resistor is a measure of the magnetic field. With the FLL, the SQUID can be operated at the steepest point of the V-Φ-curve, improving the sensitivity. SQUIDs are only sensitive to the projection of the magnetic flux density onto the normal vector of the loop surface. Therefore, three separate sensors are necessary for the three vector components of $\boldsymbol{B}$.

Since SQUIDs have to be superconducting they are cooled down below the critical temperature and require cryogenics. For mobile systems, which are necessary for mapping fields, a small liquid helium dewar can be used [55]. It has to be refilled at regular intervals which makes the setup more difficult to handle.

Fluxgate sensors are based on Faraday's law of induction and principally consist of

1 for example https://quspin.com

a small ferromagnetic core that has two coils wound around it [81]. The ferromagnetic core collects the flux to be measured and gates it through the coils. Through one coil an oscillating excitation current is fed that saturates the magnetic core. With the other coil, the induced voltage due to the magnetic flux is measured. In the absence of a additional external magnetic field, the core saturates the same for both half waves of the excitation current. If there is an additional external field present, for one half wave the saturation occurs earlier than for the other. This leads to a distortion in the induced voltage in the second core, which is used to measure the magnetic field [82]. For vector information about the field, three fluxgate sensors are necessary. Fluxgates are very robust and stable sensors, which have a big range of operation of typically 0.1 nT to 100 µT with sensitivities of $6\,\mathrm{pT}/\sqrt{\mathrm{Hz}}$ [1]. They only require a readout electronic and a power supply and are therefore easy to operate. With offset calibration fluxgates can measure the absolute magnetic flux density.

Offset calibration

Both types of sensors, SQUIDs and fluxgates, measure an offset O in addition to the actual magnetic flux density B:

$$M = B + O. \tag{4.2}$$

For fluxgates, the offset is influenced by several factors: these are for example supply voltage, temperature, the fluxgate excitation electronics and the ferromagnetic core itself. In SQUIDs, the offset is due to the FLL electronic operating at an unknown working point. The FLL creates a linear correspondence between the flux through the SQUID loop and the output voltage. The working point and the offset are stable in time as long as the range of the feedback loop is not exceeded. As such it can be calibrated and treated as a DC offset.

To determine an offset for any kind of sensor, two measurements have to be made, at the same point in space but with the sensor rotated by 180° around an axis perpendicular to the sensitive direction for which the field is to be measured. Then, the offset O and the magnetic field B at this point are given by:

$$O = \frac{M_1 + M_2}{2} = \frac{B + O + (-B + O)}{2} \tag{4.3}$$

and

$$B = \frac{M_1 - M_2}{2} = \frac{B + O - (-B + O)}{2} \tag{4.4}$$

respectively. This offset calibration is necessary for every individual sensor. For fluxgates, the offset is not time-stable, for example due to temperature changes, therefore the calibration has to be repeated when the offset has drifted to far for the required measurement accuracy. Typically, electronic drifts of the fluxgate sensors are on the order of $< 10\,\mathrm{pT\,min^{-1}}$.

The offset calibration determines the error of the absolute flux density measurement. With SQUIDs typically 50 pT are achieved. For fluxgates the offset accuracy is approximately 0.1 nT

1 Bartington Mag03 specifications

Fluxgate setup

The fluxgate sensors[1] operate with a supply voltage of ±12 V. In order to reduce 50 Hz noise coming from the main power line, our fluxgates are powered by two sets of 12V batteries, that are connected to provide the supply voltage as well as 0 V reference. A python script on a raspberry pi controls which set of batteries is connected to the sensor and switches to the other one after a predetermined time of operation. The set not in use will be recharged automatically by connecting the batteries to a charger. A photograph of this battery box is shown in figure 4.1. Schematic drawings of the circuits can be found in the appendix.

The fluxgate sensors are read out with a USB ADC device[2]. The analog voltages from the fluxgate electronics are sampled with a frequency of 4096 Hz for one second. The data is then averaged, and one value per second is saved. Since we are interested in small residual fields, the ADC is operated in the smallest voltage range of 625 mV, which allows the measurement of fields up to 4.3 µT. The average of the data samples is calculated in a C++ program interfacing with the hardware driver. Only the averaged values are returned to the python software handling the database interfacing. A fast readout for a sampling rate of 16 kHz is also made available in the software. For the measurement of residual fields, the requirements for the angular alignment between the fluxgate sensors are quite relaxed, less than 5° is sufficient, because all components have approximately the same magnitude.

Figure 4.2 shows the performance of the fluxgate magnetometer using an Allan deviation plot. To obtain the optimal performance, an integration time of about 100 s would be required. For shorter times, noise has an increasing effect on the signals. For

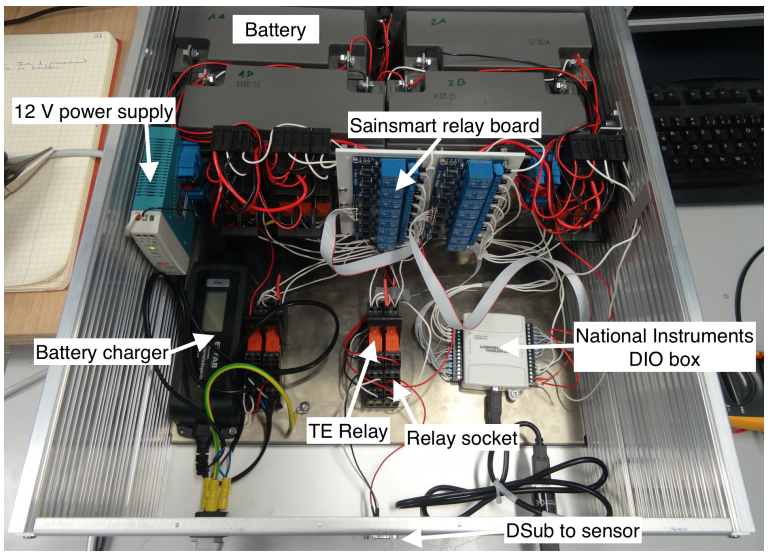

Figure 4.1: Battery box used as a power supply for the fluxgate sensors. The relays are actuated by the National Instruments device and connect the batteries to either the output or the charger. The 12 V power supply is necessary to switch the TE relays.

1 Bartington Mag03-IEHV with custom length flying leads
2 Advantech USB-4716

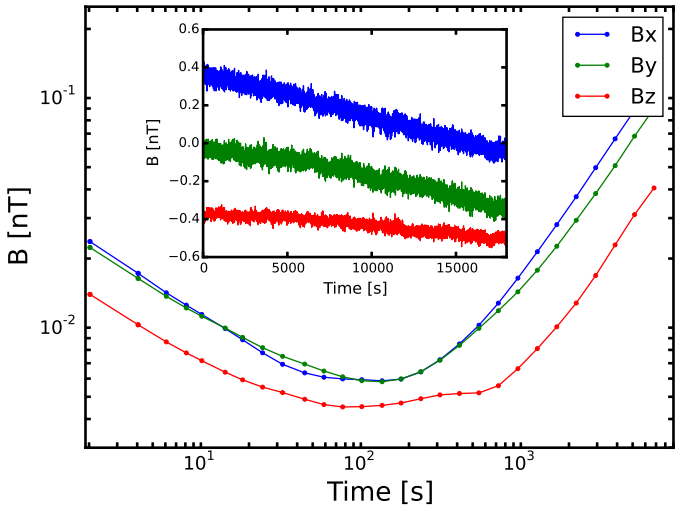

Figure 4.2: Allan deviation calculated for data recorded with the fluxgate inside the 2-layer MSR for a total measurement time of 20 000 s. The inset shows the corresponding time data, shifted to 0 at $t = 0$. Bx and Bz have been offset by 0.4 nT and -0.4 nT, respectively, for clarity. The smooth change of the magnetic field over time correlates with a smooth, monotonic drop of 0.2° in the environmental temperature inside the ACS.

longer times, the measurement is dominated by drifts, e.g. from changing offsets or drifts of the readout electronics. To keep the measurement time per point short while keeping the resolution, an integration time of 1 s was chosen. It can be seen that, here, the Allan deviation is already below 30 pT. With this and repeated offset calibration, an overall accuracy of 0.3 nT can be reached. Figure 4.2 also shows that drift processes start to influence the measurement more than the sensor noise only after more than 1000 s. Since drifts in the electronics are a possible source for this, this provides the time frame after which sensor re-calibration becomes necessary.

4.2 MSR maps

After equilibration in the earth magnetic field maps of the magnetic flux density inside the MSR were recorded for the respective configuration of the equilibration coils (c.f. section 3). Each of the maps consists of 108 points on a 6x6 grid in three different XY planes in the center of the room, 35 cm below and 35 cm above. The distance between the points along each axis is 10 cm. The sensor was moved manually which allowed a position accuracy of 0.5 cm and an angular alignment of better than a few degrees. The sensor positions within the mounting structure are 2 cm apart, so the overall position accuracy is 2 cm. The previously used configuration is shown in the first column of figure 4.3, labeled a). In columns b) and c) two maps for the new configuration are shown, measured with several days in between to show reproducibility.

The results for the previous configuration are that the residual field is on the order of 0.8 nT in the lower plane and near the door of the MSR. The duration for the equilibration procedure was approximately 100 s per layer and direction, i.e. 600 s in total. The higher values near the door are likely caused by stray fields in the last

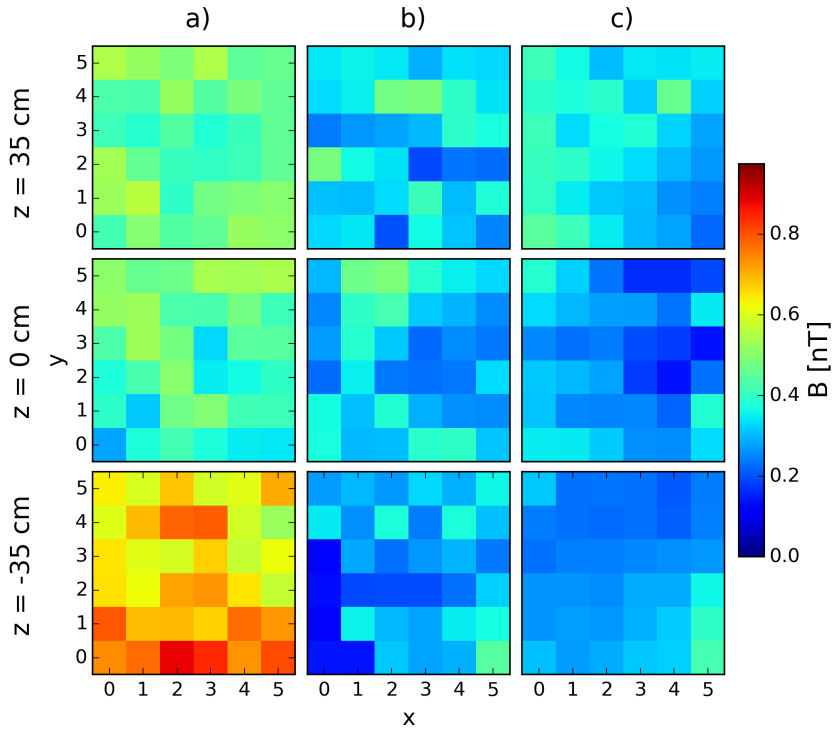

Figure 4.3: Maps of the residual magnetic flux density in the 2-layer MSR after magnetic equilibration, measured in three XY planes at different heights. The points are 10 cm apart in each direction. In column a) the previous configuration is shown, in b) and c) the L-shaped configuration. Between the measurements in b) and c) several days have passed.

equilibration step. The overlap at the door retains some magnetization. In the higher planes, the residual field is slightly smaller, with values of 0.5 nT.

For the L-shaped configuration, the resulting residual fields are slightly smaller with values of about 0.5 nT or below, but in much short time. The duration can be reduced to 50 s for the modified layer. The outer layer is not modified, but there the duration could be even further reduced since its influence on the residual field is less critical. In total the equilibration would take only 100 s (or less) for both layers, making it six times faster. This would directly improve the statistical reach of the nEDM experiment due to a higher duty cycle. Also the prominent features in the lower plane are not visible anymore. By equilibrating two direction at the same time, both a re-magnetization of adjacent walls is avoided and the disturbance at the overlap can be reduced, yielding smaller residual fields.

In [70], one of the main criteria for a reproducible procedure is the step size of the amplitude decrease. The difference in amplitude between two subsequent maxima of the sinusoidal current should be as small as possible as this delta corresponds to an error in the residual field. Therefore, it is suggested to use several thousand cycles. In our approach a much smaller number of cycles is used while still achieving the same residual field values.

4.2.1 Reach of disturbances into the shielded volume

Overlaps and holes in the wall of MSRs influence the residual field inside the shielded room, since fields from the outside can leak through holes. Overlaps of two shielding material layers are difficult to equilibrate, because the material cross section changes. When there are additional air gaps between the material layers, the quality of the equilibration will deteriorate further (cf. chapter 5). The resulting field distributions in front of an overlap has been measured in the 2-layer MSR, after magnetic equilibration. This measurement has been performed with a fluxgate, in 6 lines 6 cm apart in X direction and at points 1.5 cm apart in Y direction. Figure 4.4(a) shows the measured magnetic flux projected onto a horizontal XY plane at an overlap where the door presses against the frame. The plane lies in the vertical center of the MSR, and the coordinate (0,0) corresponds to the front, right corner of the MSR. The black arrows indicate the location of the overlap. It is clearly visible how the field penetrates into the room. This visible characteristic pattern is caused by the remaining magnetization in the overlap where the equilibration process was not able to reach saturation and therefore could not reduce the magnetization to a low value. This can be confirmed by FEM simulations, as will be shown in chapter 5.

In figure 4.4(b), the magnetic flux density is plotted along the dashed line, to show how fast it decreases with distance to the wall. After about 40 cm, the magnitude of the flux density is already below 2 nT.

In figure 4.5 the influence of holes on the magnetic flux density is illustrated. The magnitude $|B|$ is plotted along a line through the center of feedthroughs of various sizes. For feedthroughs with diameter <60 mm, the field decreases rapidly with distance and is <3 nT at a distance of 50 mm from the inner wall. As expected, the field drops more slowly for the 130 mm diameter feedthroughs. The curve shows a bump at 15 cm distance due to the presence of a fixed magnetic object nearby.

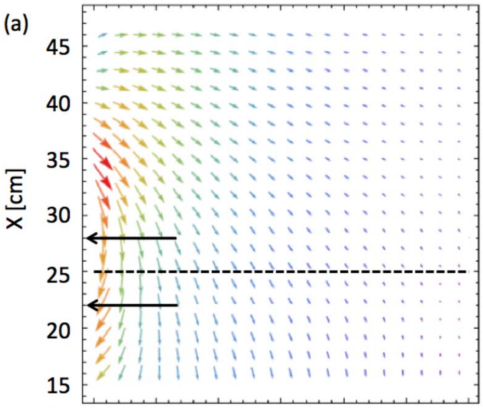

(a) Measured flux density projected into the XY plane at a door overlap in the MSR. The arrows indicate the position of the overlap and the dashed line shows the positions along which the data in (b) is plotted.

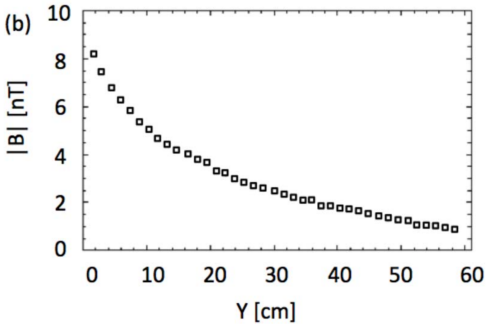

(b) The magnitude of B plotted along the dashed line.

Figure 4.4: Field at an overlap and its decrease with distance to the wall.

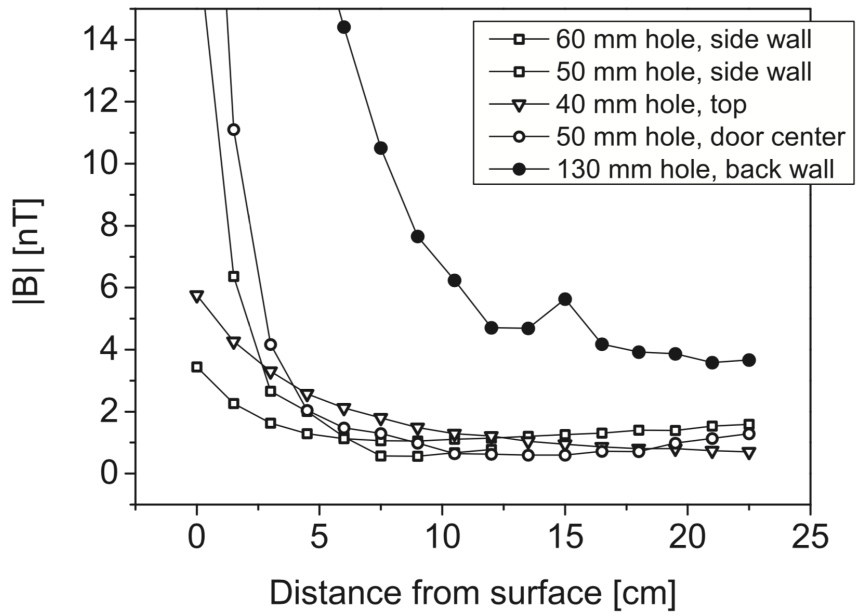

Figure 4.5: Magnitude of the magnetic flux density inside the shield as function of distance from the wall in the 2 layer room. The curves show the magnitude of the residual field measured along a line normal to the shielding material surface and centered on the corresponding feature as indicated. The values are reproducible at the level of about 1 nT after repeated equilibration over a period of several weeks. Note that distance = 0 corresponds to the fluxgate-probe placed in the center of a hole at the surface of the wall, with the actual probe placed 10 mm away inside the housing. The map is corrected for the positions of the respective probes inside the fluxgate sensor.

4.3 Maps of the insert

Residual fields have also been measured inside the full TUM shield, where the insert with its cylinder was placed inside the outer shielded room. The cylinder inside the box-shaped shield posed a new challenge to reach ultra-low residual fields due to the interaction of its layers in the equilibration process. The equilibration coils of the cylinder are in close proximity of the end caps of the box-shaped insert, and since the cylinder requires high currents for the equilibration, the walls of the box might be remagnetized when equilibrating the cylinder.

In the following, the measurement procedure for residual fields inside the the full shield is described, and the resulting fields are presented. The best configuration resulted in residual fields below 150 pT over an extended volume.

Measurement procedure

The resolution of the fluxgate sensors was not sufficient to measure the ultra-low residual fields inside the 5+1 layered shielded room, and the fields had to measured with SQUIDs, resulting in a more involved measurement procedure.

The system used (from [55]) has 16 SQUID sensors that are mounted on the faces of a cube with 5 cm side length. Figure 4.6 shows the arrangement and naming convention. SQUIDs on opposite sides of the cube measure in anti-parallel directions. By combining four sensors, a so called virtual SQUID is constructed that estimates the field in the

center of the cube

$$V_i0 = \frac{i1 + i3 - i5 - i7}{4} \tag{4.5}$$

where $i = X,Y,Z$ stands for the spatial directions and the numbers refer to the SQUID names. As a cross check, the value for VY0 can be compared with the actual Y0 sensor, sitting in the physical center of the cube. Also for the virtual sensors an offset can be determined. These three virtual sensors are used for the field maps.

The SQUIDs are kept at their working temperature inside a liquid helium dewar with a volume of 3.2 liter, which requires refilling after about 20 hours of operation. When the dewar is tilted, which becomes necessary for offset calibration and absolute field measurements, the additional boil-off reduces the operation time by approximately one hour per tilt.

After refilling the dewar with liquid helium, the system drifts on the order of 20 pT in the first three hours, the Z direction drifting the most. Reasons for these drifts are additional boil-off due to moving helium inside the dewar and temperature gradients. Afterwards, the drift is much smaller and well below 2 pT/hour. Following a tilt of the dewar, the recovery time to stable operation is much shorter. For the time it took to measure one field map (about 30 minutes) the drift is expected to be on the percent level. By measuring the same point of the map repeatedly, an estimate of the actual drift can be obtained.

The dewar with the SQUIDs is mounted in a manipulator that allows it to be moved for the offset calibration procedure. In figure 4.7, the apparatus is shown. For the SQUIDs measuring in Z direction, a 180° rotation is obviously not possible. By tilting the dewar by 45° around the X axis, and then rotating it by 180° around the Z axis, also the Z sensor offsets can be determined.

In order to measure at different positions the entire system has to be moved. For this, another structure is mounted in the insert, as shown in figure 4.8. A frame made from non-magnetic profiles rests on the rails for the vacuum chamber, where it can be moved along the Y direction. For movement in X direction also Teflon rails for low friction are mounted, and the movement is guided by pins fitting into the profile. The

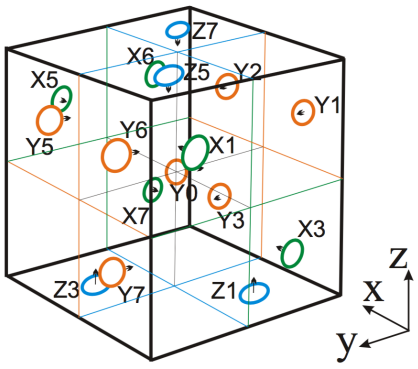

Figure 4.6: Sketch of the sensor head holding the 16 SQUID channels. The sensors are mounted on the faces of the cube and measure the fields along a spatial direction, as indicated by the arrows. Sensors on opposing faces measure in anti-parallel direction. One additional sensor called Y0 sits in the center of the cube.

maps presented here have been measured in the central XY plane at $Z = 0$ only, due to limited availability of the SQUID system.

Since persons cannot be inside the cylindrical shield during measurements, all movements have to operated from outside of the shielded rooms. The manipulator and the mounting structure (shown in figure 4.8) are equipped with a set of strings that allowed these movements from the outside. The position of the system has been determined by either moving into an known end position in X direction or by measuring the distance with a laser distance meter for the Y direction, allowing a positioning accuracy of about 1.0 mm for both directions.

Residual fields

For these experiments, the previously determined equilibration currents were used, since the values to saturate the layers have already been determined in previous experiments. The fact that the cylindrical layer and the end caps of the box are very close to each other and mutually magnetize each other during subsequent equilibration made it necessary to equilibrate both layers at the same time. As the layers require different currents, their equilibration coils could not just be connected in series. Instead, two separate power amplifiers were used. To avoid an unknown and possibly varying phase between the two equilibration currents, both amplifiers received their respective waveform from the same ADC, and to account for the different current requirements an analog voltage divider was used for one of the amplifiers. The sequence in which the layers were equilibrated was: A-X, A-Z, A-Y, L for the MSR, followed by: 1r, 1s, 1g, 2r, 2s, 2g, 3r, 3s, 3g, and cylinder alone with one amplifier. Afterwards, the cylinder

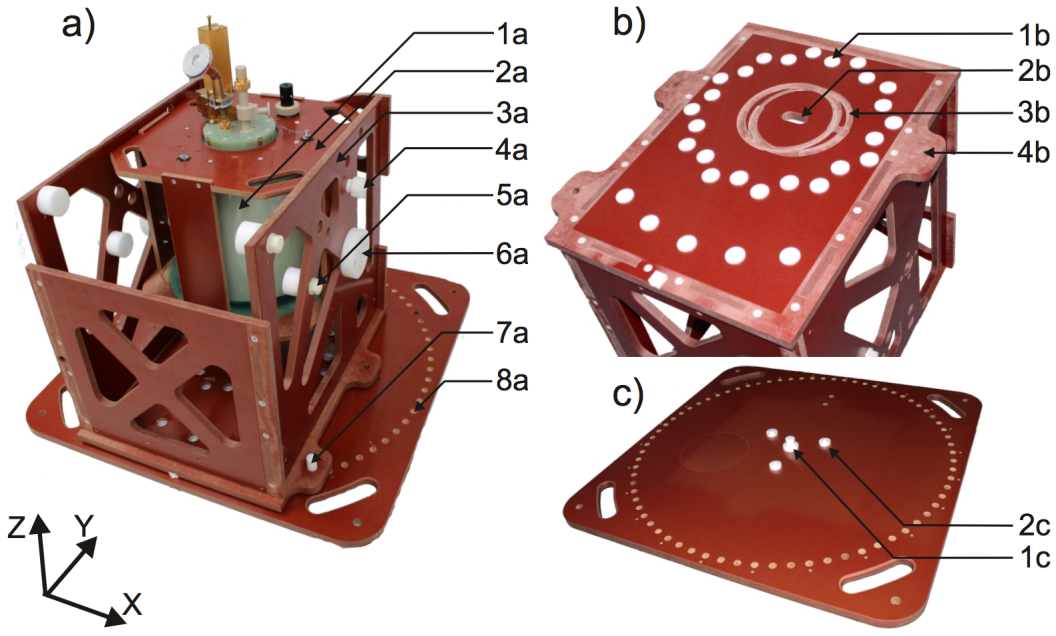

Figure 4.7: Photograph of the SQUID dewar in the manipulator for offset calibration. 1a) dewar, 1b) holding structure for the dewar, 1c) rotation frame, 4a) safety pin, 5a) 45°, 6a) rotation axis, 7a) holding pin, 8a) plate with rotation marks every 5°. Picture from [55]

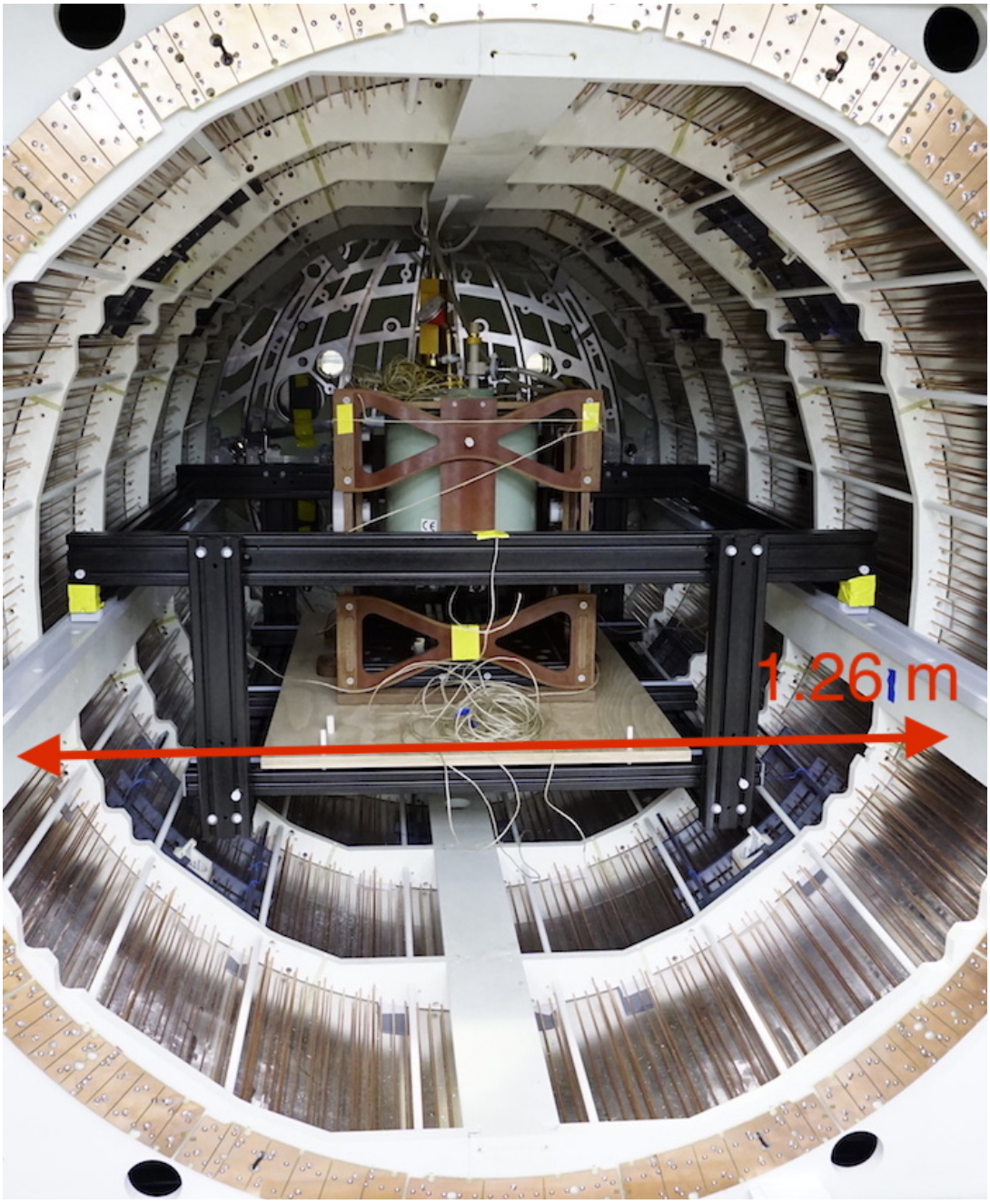

Figure 4.8: Photograph of the manipulator inside the insert, with the SQUID system to measure the residual fields. The strings used to move the dewar can be seen in front, when the insert is closed, they are guided through the holes on the side to be pulled from the outside. Photograph courtesy of J.Voigt

and the Inner-X layer of the insert (3r) were equilibrated at the same time with two amplifiers.

A comparison of the values measured at the center point before and after the map was recorded, allows to determine the drift during the measurement time. The drift was

$$\boldsymbol{B} = \begin{pmatrix} 5 \\ 10 \\ -23 \end{pmatrix} \text{ pT in 30 min,} \tag{4.6}$$

which is more than the expected 2 pT/hour for ideal conditions. But it is consistent with the fact that the sensor for the Z direction shows the largest drifts, and that the dewar has been tilted back to vertical orientation right before the first measurement point from the offset calibration, also resulting in a larger drift. This is included into the field results as an uncertainty.

The resulting residual field is shown in figure 4.9. Each component is below 120 pT. The strong feature in the central $X = 0$ line from the center to the back can be attributed to the cable connecting the FLL electronics to the data acquisition outside the shielded room [83].

If the drift given before is assumed to be linear in time, the maps can be corrected by just subtracting it. This yields the maps shown in figure 4.10. But since the validity of this assumption cannot be confirmed, neither that the drift is linear in time nor that is only due to the sensor, the uncorrected fields will be given as a result with the drift as an uncertainty. Still, it can be estimated conservatively that the absolute residual field is below 150 pT in the central plane within an area of about $120 \times 40\,\text{cm}^2$.

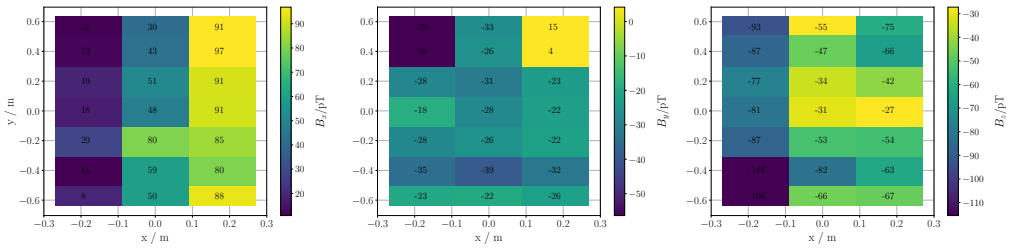

Figure 4.9: The residual field in the insert measured in the central XY plane at a height of $Z = 0$. The three plots show the B_X, B_Y and B_Z component.

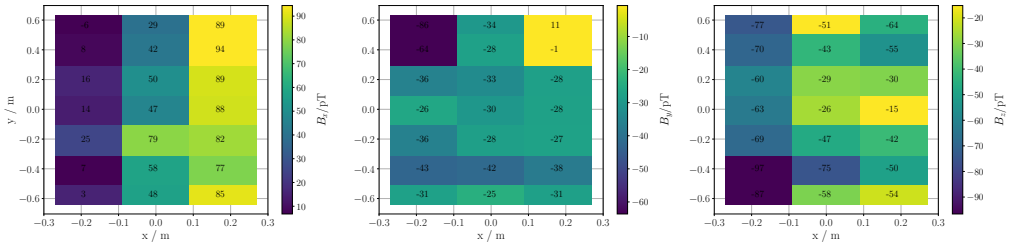

Figure 4.10: The residual field in the insert measured in the central XY plane at a height of $Z = 0$. The three plots show the B_X, B_Y and B_Z component. The data for this plot has been corrected for a linear drift of the sensor during the measurement time.

Quality of magnetic contact between layers

The door mechanism of the inner shielded room allows to apply a pressure of about 0.6 bar to a balloon which presses the VDM® MAG 7904 layers of the door and the room against each other for better magnetic contact. The manufacturer of the insert allows a maximum pressure of 0.9 bar.

To determine how the equilibration process is affected by the pressure between the layers, the field was measured with fluxgate sensors along the Y direction from the center towards the end cap, through the central hole in the shield. Equilibration was performed with and without applied pressure. With pressure, the field does not exceed 0.3 nT until the fluxgate passes the mumetal wall. With no contact pressure during equilibration, a larger residual field is observed; values of about 0.5 nT were recorded when approaching the wall. Also, in the center the field values are higher, with 0.18 nT compared to 0.12 nT in the former case. This confirms that good contact between the layers at the overlaps is important for the effectiveness of magnetic equilibration.

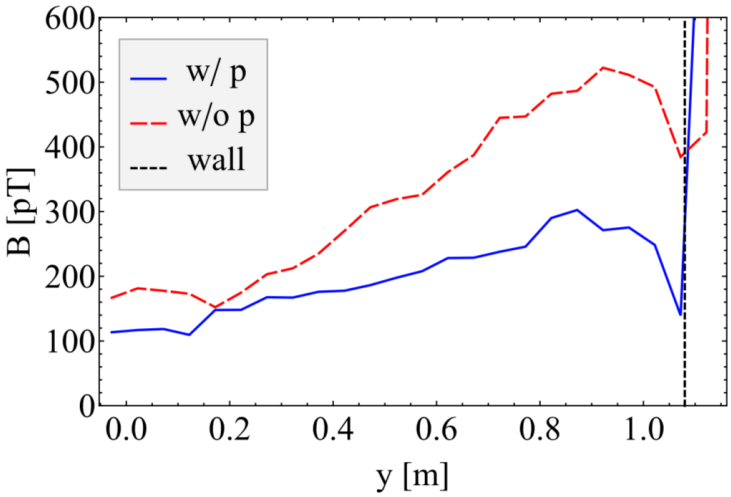

Figure 4.11: Magnitude of the magnetic flux density of the five layer shield measured with a fluxgate along the central line from the back wall of the shield. The position $Y = 0$ corresponds to the center of the shield and at $Y \approx 1.1\,\mathrm{m}$ the innermost layer is reached. The magnetic field was measured with the end cap closed with (blue) and without (red) pneumatic pressure. In both cases the shield was magnetically equilibrated.

Temporal stability of the residual field

The temporal stability of the whole nEDM shield has been measured with the SQUID system in [38]. After the first hour, the field drifts less than 5 pT in eight hours. The Allan deviation has been calculated for the time interval $2\,\mathrm{h} < t < 6\,\mathrm{h}$ of the time series in figure 4.12 to exclude the initial drift and the start of technical operations in the lab environment after $t \approx 6\,\mathrm{h}$. For an integration time of 250 s, the temporal stability is 10 fT.

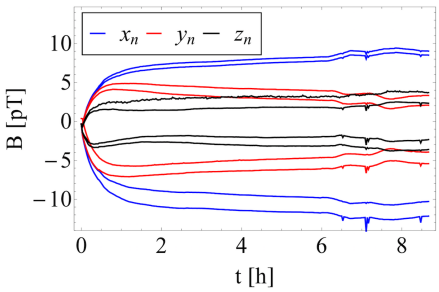

(a) Field data measured over approximately nine hours.

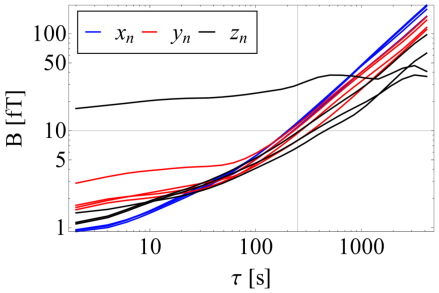

(b) Allan deviation for the interval of $2\,\mathrm{h} < t < 6\,\mathrm{h}$ data in a)

Figure 4.12: Temporal stability of the combined shield, MSR and insert, measured with the SQUID system. Pictures taken from [38]

4.4 Conclusion

In this chapter, the achieved residual fields inside the two TUM shields have been presented. Inside the MSR, the new coil configuration produces lower residual fields in shorter times than the old configuration, with fields below 0.5 nT in the central volume of $0.6 \times 0.6 \times 0.7\,\mathrm{m}^3$.

For the insert the resulting fields are even lower, which made measurements with a SQUID system necessary. Here, residual fields on the order of 150 pT in the central plane within an area of about $120 \times 40\,\mathrm{cm}^2$ have been reached.

5. Static simulations of remanent fields

In this chapter, time–independent finite element (FEM) simulations in Comsol will be introduced as a tool to study residual fields inside MSRs. Without time-dependence, the hysteretic behavior of the material is not taken into account. Nevertheless, the magnetization of the material and the resulting residual fields can be studied. According to the Jiles-Atherton model, successful magnetic equilibration returns the material to the anhysteretic magnetization curve. Employing the anhysteretic curve in simulations to describe the material in the already equilibrated state, allows to determine the field created by the flux density distribution in the material. The influence of geometric features like material overlaps and air gaps can be investigated. The advantage of time-independent simulations is that they require significantly less computing power and time. On the other hand, time-dependent simulation of real 3D MSR geometries requires dedicated, high-power computing clusters.

5.1 2D simulation of overlaps

With 2D simulations, the effect of overlaps in the path of the magnetic flux can be studied. The simulations are set up in the following way. A layer of mumetal is modeled as a box with a door on the -X side. The dimensions of the box correspond to the size of the inner mumetal layer of the TUM MSR with a length of 2.8 m and a width of 2.5 m. The width of the door is 2.13 m, and overlaps with the box for 6.5 cm on each side, making the opening 2 m wide. The mumetal thickness is increased by a factor of ten to 1 cm, reducing the number of mesh elements for the FEM to keep computation times short.

Material properties are assigned to the different geometric domains in the model. Inside and outside the box, there is air with with a permeability and a conductivity of one, whereas the box layer has the properties of a high magnetizable material assigned to it. A separate Ampere's Law node is added to calculate the magnetization of the material according to the specified $B(H)$ curve.

DC currents are supplied to a simulated coil on each corner. On the inside of the box, the current flows into the picture plane, outside of the box it goes in the opposite direction, producing a loop of flux in the clockwise direction in the material. For static simulations, only DC currents are used, since there is no time dependence.

To estimate the remaining magnetization after an equilibration process the last current step is estimated. The smallest voltage step produced by a 16-bit ADC in the full voltage range is

$$\Delta V = \frac{20\,\mathrm{V}}{2^{16}} = 0.3\,\mathrm{mV}, \tag{5.1}$$

causing an output of 1.5 mV at the amplifier. From a resistance of the equilibration coils of about 1 Ω follows a current of 1.5 mA, which creates a magnetic field of approximately $H = 4\,\mathrm{mA/m}$. The last amplitude step in an equilibration process leaves the shielding material magnetized by this magnetic field. For the simulations, a corresponding current is used to create a magnetic field of that magnitude.

5.1.1 Material properties

The results of the simulations strongly depend on the selected material properties. For the static simulation of equilibration processes, the hysteretic nature of ferromagnetic materials does not need to be considered, since the static simulation does not contain any previous history of the material. Instead, the strongly non-linear behavior of the material is of interest, for example, to find the currents necessary to reach saturation, or to investigate how the material is magnetized by very small currents due to the last steps in the equilibration process. As also described in chapter 6, magnetic equilibration brings the magnetization into a state of equilibrium at the prevalent magnetic field. This state is described by the anhysteretic magnetization curve. The Jiles-Atherton model (JA model) uses a modified Langevin function to describe the anhysteretic magnetization. Here, a term $\mu_0 H$ has been added to obtain $B(H)$:

$$B(H) = \mu_0(M + H) = B_s\left(\coth\left(\frac{H}{a}\right) - \left(\frac{a}{H}\right)\right) + \mu_0 H. \tag{5.2}$$

On the other hand, the initial magnetization curve describes the magnetization when a field is applied to the perfectly degaussed state of the material, i.e. starting from $B = 0\,\mathrm{T}$.

As a side-note, experimentally the anhysteretic curve is determined by applying a DC magnetic field and adding a sinusoidal field with decreasing amplitude. As the amplitude goes to zero, the flux density B converges to the anhysteretic value at the applied DC field.

In figure 5.1, the initial and the anhysteretic magnetization curves of a ferromagnetic steel sample are shown. The anhysteretic curve gives the state where changes of the

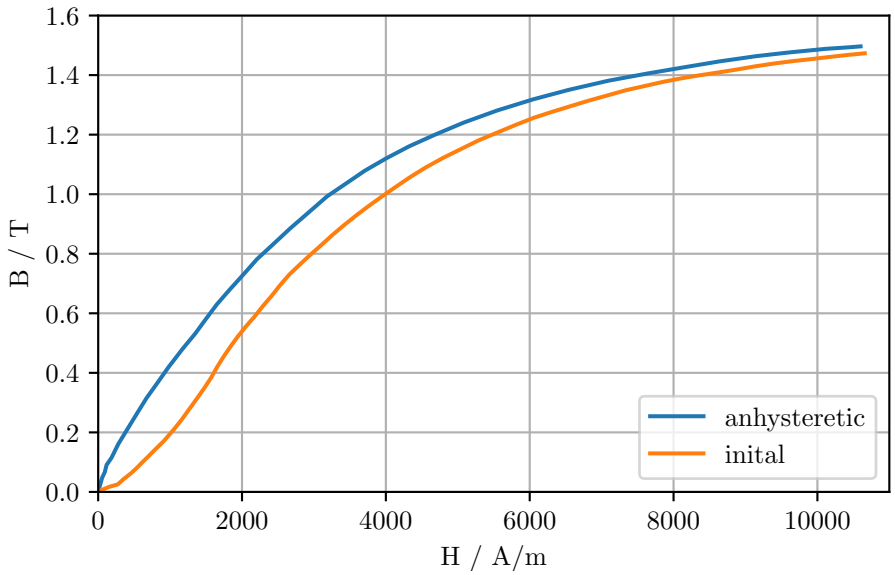

Figure 5.1: Initial and anhysteretic magnetization curves for a sample of ferromagnetic steel, the initial curve is always below the anhysteretic. Data taken from [68] figure 4 with the y axis converted to Tesla.

magnetization are not impeded by pinning of the domain walls (cf. section 6.1.1). The initial magnetization always lies below the anhysteretic curve because unlike for the anhysteretic curve domain walls cannot move freely throughout the whole $B(H)$ curve, which reduces the magnetization with respect to the anhysteretic case. For very small H values, the magnetization increases slowly because energy is needed for the domain walls to overcome pinning sites. Only once irreversible changes are introduced, the magnetization increases more strongly. This is also the reason why, starting from an equilibrated state the magnetization follows a curve similar to the initial curve; changes in the external field, at first, do not create strong a magnetization in the material, because no irreversible changes in the domain structure occur.

In figure 5.2, magnetization curves for different materials are shown. Two are measured curves for samples of commercially available nickel alloys. The blue one is the material from which the TUM MSRs are made, VDM® MAG 7904[1]. It is specifically designed to have a high saturation induction of $M_S \approx 0.8\,\mathrm{T}$ and a very low coercivity of $H_c \leq 1\,\mathrm{A/m}$, resulting in a very narrow and steep hysteresis loop. The green curve is MuMETAL®[2], a similar nickel molybdenum alloy. The data has been taken from the respective data sheet by the manufacturers ([84] and [85]).

These curves are initial magnetization curves as can be seen by the change in curvature for small H values in the inset. Modified Langevin functions (according to equation 6.4) have been fitted to approximate their shape. The parameters have been chosen so that the measured initial curves always lie below the Langevin functions. MuMETAL® has a steeper curve than VDM® MAG 7904 and therefore the slope parameter a for the corresponding Langevin function is smaller.

In the Comsol material library, properties for two types of nickel steel mumetal are included, with nickel contents of 77% and 80%. Even though VDM® MAG 7904 also contains 80% of nickel, it exhibits quite different magnetic properties. Furthermore, a $B(H)$ curve is shown that has been measured for Krupp Magnifier 7904[3] by the authors of [86]. This curve also displays a different behavior than given by the material data sheet.

For the simulations described in the following, three material curves have been used. For high currents, the initial curve approaches the anhysteretic curve, therefore for investigations of the saturation behavior both curves yield the same results. For low currents the anhysteretic curve is used since we are interested in the material state after an equilibration process, which brings the magnetization of the material exactly to this curve. The Langevin approximations of the VDM® MAG 7904 and MuMETAL® data are therefore used for the simulations as well as the predefined material from the Comsol library for comparison.

5.1.2 Flux density saturation

With these simulations, the magnetization of the material and the flux density distribution can be investigated. For the equilibration process it is important to reach saturation of the magnetization everywhere in the material in order to have the previous

1 VDM® MAG 7904 is a trademark by VDM Metals GmbH, Plettenberger Straße 2, 58791 Werdohl, Germany

2 MuMETAL, is a registered trademark of Magnetic Shield Corporation, U.S.A.

3 An alternative name for VDM® MAG 7904.

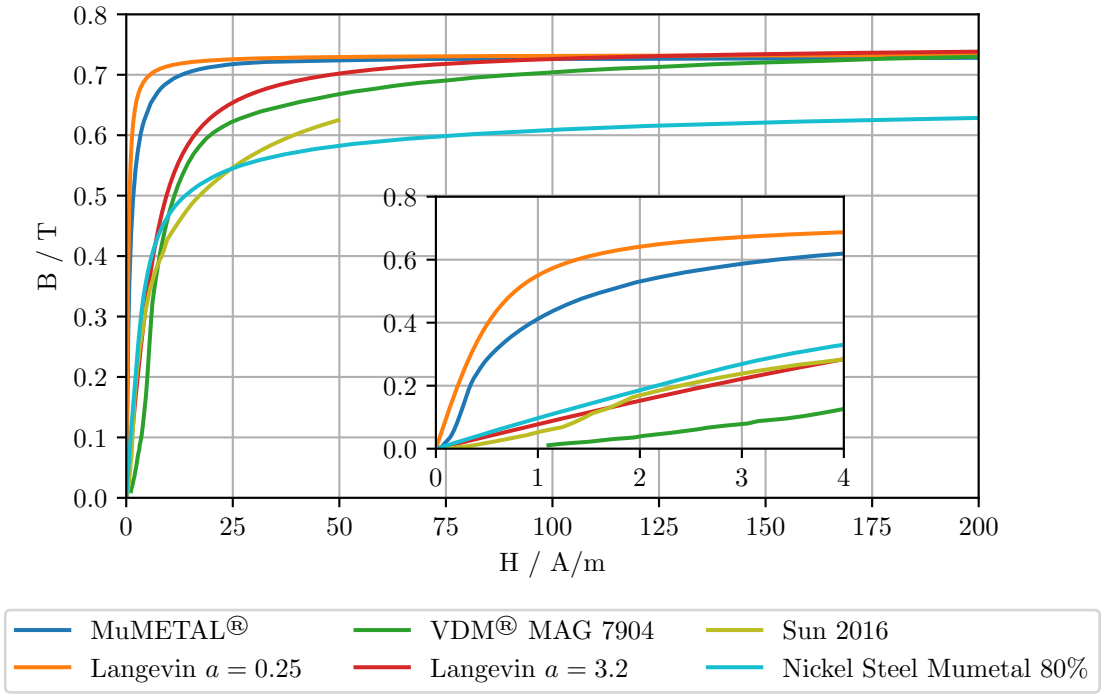

Figure 5.2: Several measured $B(H)$ curves for different materials and modeled curves to describe their behavior in simulations. The MuMETAL® and VDM® MAG 7904 curves are taken from their respective data sheets, Sun 2016 is measured by the authors of [86]. The two curves labeled "Langevin" are graphs of by equation 5.2 with $a = 0.25$, $B_S = 0.73\,\mathrm{T}$ and $a = 3.2$, $B_S = 0.75\,\mathrm{T}$. Nickel Steel Mumetal 80% data is exported from Comsol.

magnetization history completely removed (i.e. [70]). The domain walls need to be mobilized and enough energy has to be provided to overcome all pinning sites.

Figure 5.4 shows the magnetization inside the material along the black line in figure 5.3, starting from the top. The simulations started with a current of 84 A supplied to a single loop coil. This corresponds to the real situation of the TUM MSR, where a current of 12 A flows in a 7 turn coil on each edge. With a length of the magnetic path of 10.6 m, this produces a magnetic field of $H = 32\,\mathrm{A/m}$.

Before the overlap, the MuMETAL is saturated, already at 84 A. The VDM® MAG 7904 is not saturated at this current and even with a current four times higher the saturation flux density of 0.75 T is not reached. At the overlap the cross section of the material doubles and the flux density correspondingly drops to half the previous value, more or less independent of the applied current. This has consequences for the equilibration processes. Changes in cross section of the material in the path of the magnetic flux prevent the material from being saturated. Even with very high currents saturation cannot be achieved, because the material next to the overlap is already saturated and cannot transport more flux to the overlap region. The feature observable at approximately $s = 0.5\,\mathrm{m}$ is caused by the edge of the box, where the flux density is not constant over the cross section, but decreases towards the outer edge (cf. figure 5.3).

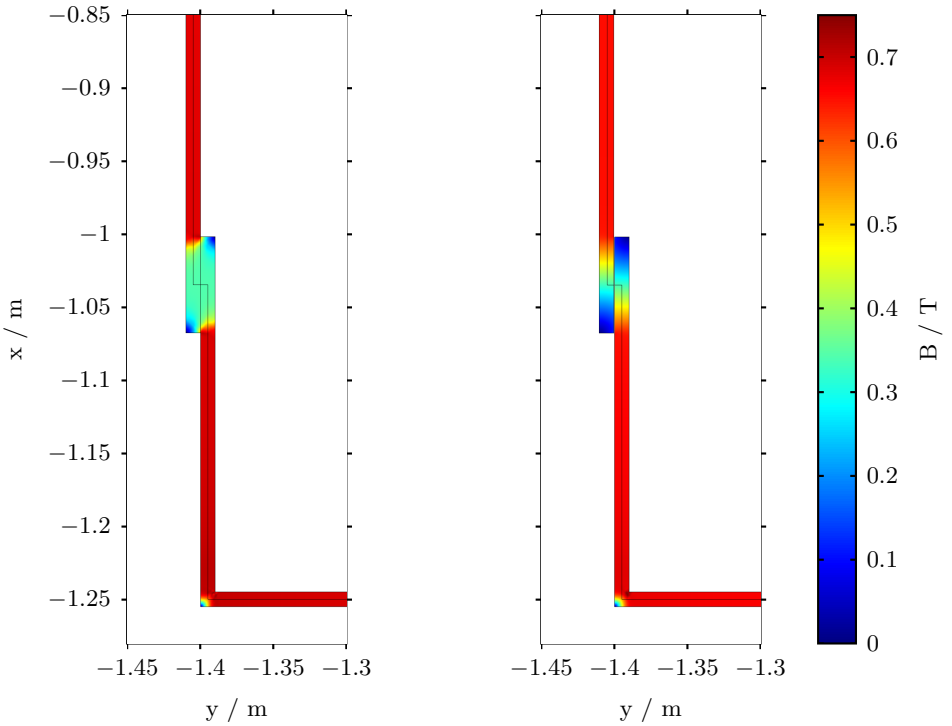

Figure 5.3: Comparison of the magnetic flux density inside the material (VDM® MAG 7904) at the overlap without an air gap (left) and with an air gap (right). A current of 84 A was simulated in 4 coils in the corners. The air gap reduces the flux density in the overlap, as well as far away from the overlap. The data in figures 5.4 and 5.5 the flux density is plotted along the black line in the middle of the material in these graphs.

Air gaps in the overlap

If there is an additional air gap between the mumetal layers in the overlap, the flux density in the material decreases further. In the example shown in figure 5.5, the width of the air gap is 0.5 mm. The magnetic contact between the layers is reduced and the flux distribution in the overlap changes. The flux density in the door is consequently also reduced. The air gap also reduces the flux density in the material far away from the overlap itself, as can be seen by the shift of the curves in figure 5.5. To compensate for this much higher currents are needed. Every air gap in the MSR walls reduces the flux density throughout the material.

At air gaps, the permeability of the flux path is strongly reduced, causing the flux to leak into the shielded volume and change the field distribution in the MSR. Figure 5.6 shows the calculated flux density caused by the air gap for this geometry. The material magnetization is induced by a current through the equilibration coils in the four corners of the room. To remove the effect of the coils, the plot shows the difference of the magnetic field for two simulations, one with an air gap and the other one without the air gap. The simulation result matches the measured field in figure 4.4(a) quite well, even though the agreement is not perfect.

According to the results described in the previous sections in this chapter, overlaps, or any other places where the material cross section increases, prove difficult to equilibrate properly. At this places it is not possible to reach saturation of the magnetization

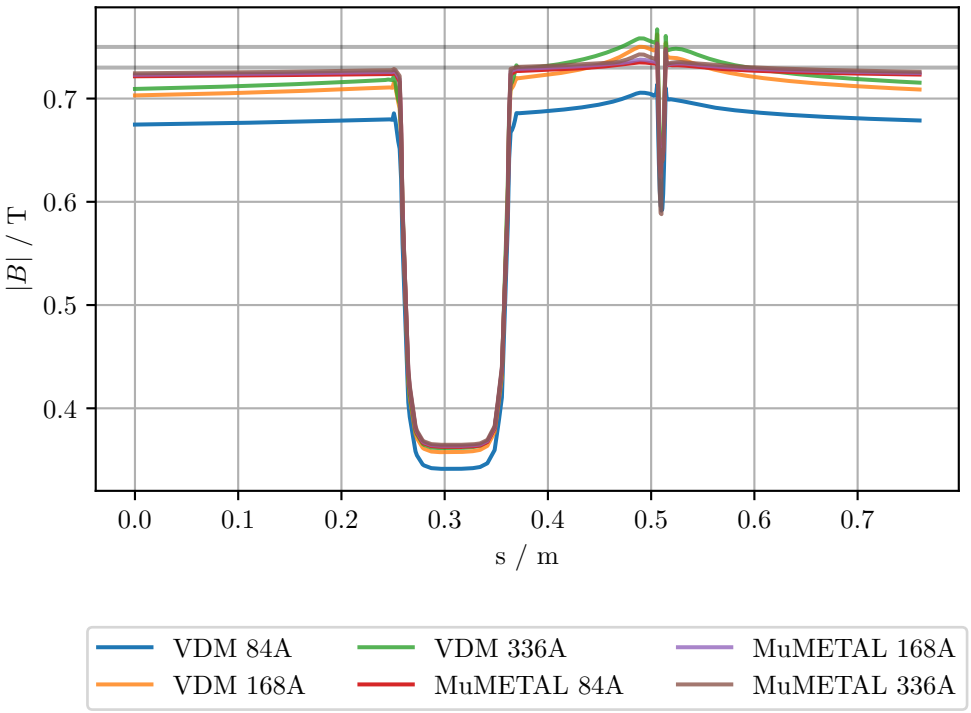

Figure 5.4: Plot showing the flux density in a geometry with overlaps for three currents and two materials VDM® MAG 7904 and MuMETAL®.

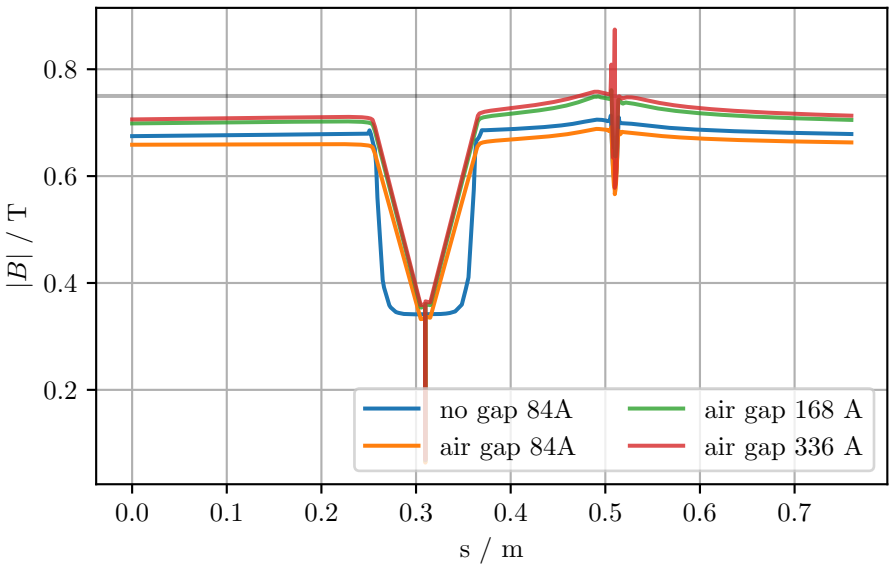

Figure 5.5: The plot shows the magnetic flux density along the line shown in figure 5.3. Blue: no air gap in the overlap with a current of 84 A, in the overlap the flux density drops by a factor 2. Orange: an air gap of 0.5 mm in the overlap changes the flux density distribution, and drops to only 10% of the saturation value in the air gap. The current is also 84 A but the flux density far from the overlap is also reduced. This is an effect that can only be compensated by applying much higher currents.

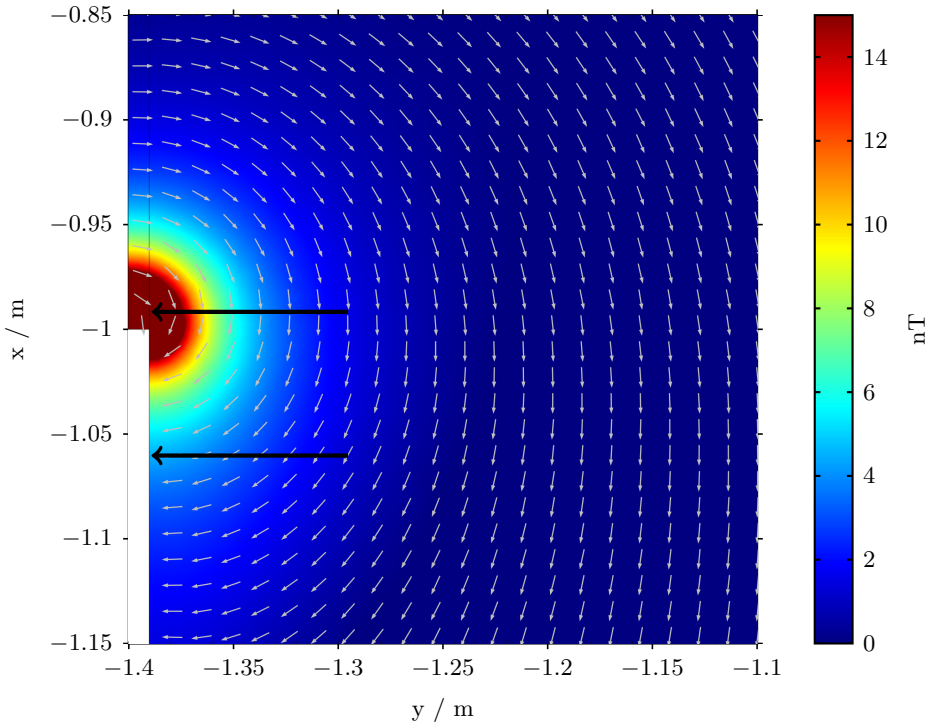

Figure 5.6: Simulated field at an overlap with an air gap of 0.5 mm inside the MSR. The arrows indicate the position of the overlap. The field distribution and magnitude is of similar shape as has been measured for the TUM MSR as shown in figure 4.4(a).

inside the material. But many MSRs have been built and successfully equilibrated to low residual fields, where strips cover the gaps between mumetal sheets (eg. [65]).

When a material has been magnetized by an external field and the field is switched off, the material retains a magnetization. If the external field was strong enough to saturate the magnetization of the material, the remaining magnetization is called remanence, and this is the biggest magnetization that remains after the field is switched off. For smaller external fields, the remaining magnetization is also smaller. To remove the remanence, the coercivity field H_c has to be applied in opposite direction to the magnetizing field and this H_c is also the maximum field that is needed to remove the magnetization. As long as the equilibration field strength is bigger than H_c of the material, equilibration is also possible even when saturation is not achieved. The magnetization will then cycle through minor hysteresis loops (schematically shown in figure 5.7), as it does for equilibration after the amplitude of the field is below saturation.

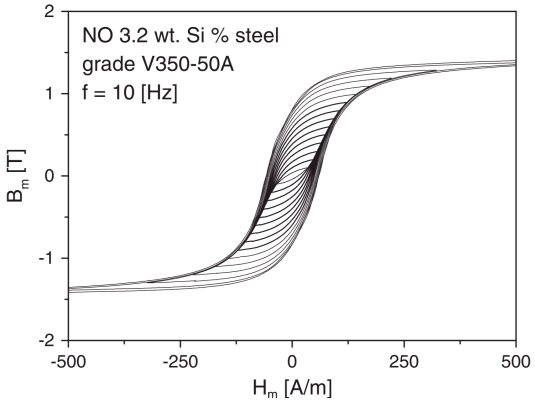

Figure 5.7: Minor hysteresis loops for a sample of steel. Note: for mumetal the hysteresis loops are much more narrow, with a value for the coercivity of $H_c = 1\,\mathrm{A/m}$. Picture taken from [87].

5.2 Placement of equilibration coils

The placement of the equilibration coils has a major influence on the residual field, as has already been shown in chapter 4. Usually, equilibration coils were placed along all of the 12 egdes of a cuboid to sequentially equilibrate in all three spatial directions. When the spatial directions are equilibrated sequentially, there is always the problem that the equilibration coils for this direction have to penetrate the adjacent faces of the cube, which are not part of the closed loop of flux for the respective direction. Stray magnetic fields can create local spots of magnetization there, which will not be properly removed by the equilibration process. The simulations presented here allow to study alternative placement of the equilibration coils. The flux density distributions in the material have been investigated for different coil configuration with the goal to reduce the resulting residual fields.

The L-shaped coil arrangement that was implemented as described in chapter 4 has also been simulated. For this, the geometry of the inner layer of the MSR is set up in Comsol, together with loops for the equilibration coils, shown in figure 5.8.

Instead of having only four coils along the edges, the equilibration coils can be spread out over the whole face of the cube. Then there are 20 coils, in our case, homogeneously distributed around the circumference. Accordingly, the current in each one can be smaller by a factor five. This has two advantages. On the one hand, smaller currents mean that the local spots where the wires penetrate the walls are exposed to smaller flux densities. On the other hand, the magnetic flux is distributed more uniformly over the faces of the cube.

A comparison of the four cases, single vs L-shaped for distributed and not-distributed coils, is shown in figure 5.9. Distributing coils leads to more homogeneous flux densities in the material, and the L-shaped arrangement can be used to reduce the influence of overlaps. With the L-shaped coils, two faces of the cube are permeated by the magnetic flux along their face diagonal (cf. figure 5.9(c)). If one of these faces contains the door, the diagonal flux can reduce the influence of the door overlaps.

A prototype shield for the Harbin Institute of Technology with dimensions of $1.865\,\mathrm{m(X)} \times 1.875\,\mathrm{m(Y)} \times 1.875\,\mathrm{m(Z)}$ has been built with the option to test different

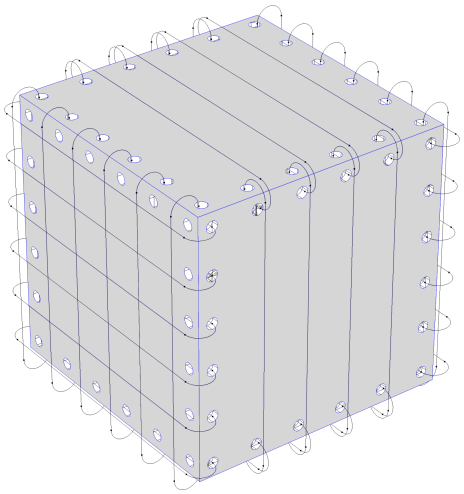

Figure 5.8: Implemented geometry for the simulation to study the placement of equilibration coils. The black loops are the equilibration coils, of which any combination can be used.

equilibration coil configurations. The results for these measurements are in preparation for publication [88]. For the tests, this shield has been mounted inside the TUM MSR, and residual field maps for the different coil configuration have been measured using a SQUID sensor with a procedure similar to that described in chapter 4. Here, accuracies of $\approx 32\,\mathrm{pT}$ have been achieved, with the residual field being mapped inside a $0.5\,\mathrm{m}\times0.5\,\mathrm{m}\times0.5\,\mathrm{m}$ cube around the center of the room. The equilibration was run with an current amplitude of 200 Ampere $\times$ turns.

Already, for the I-shaped coils, the resulting residual field is below 150 pT. With the L shaped coils, the residual field can be improved further, as predicted by the simulation, and the flux density is below 121 pT. Furthermore, the gradients, which are estimated by calculating the difference to the central point, are strongly reduced in the case of L coils. For the I coils, the maximum gradients are 227 pT, 144 pT, and 87 pT in X, Y and Z direction, respectively. With the L coils, they are reduced to 41 pT, 79 pT, and 100 pT in X, Y and Z direction. This effect is caused by the more homogeneous flux density distributions in the walls.

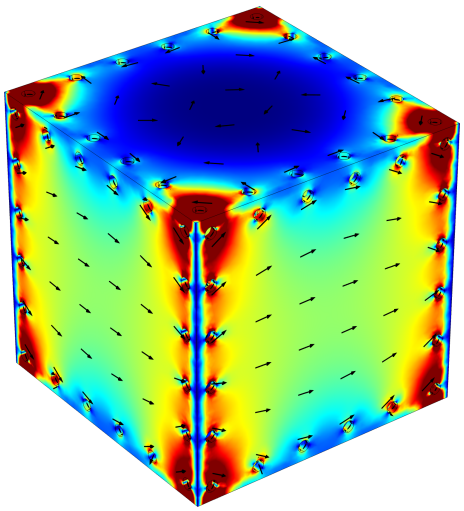

(a) Four single coils at the edges of the cube.

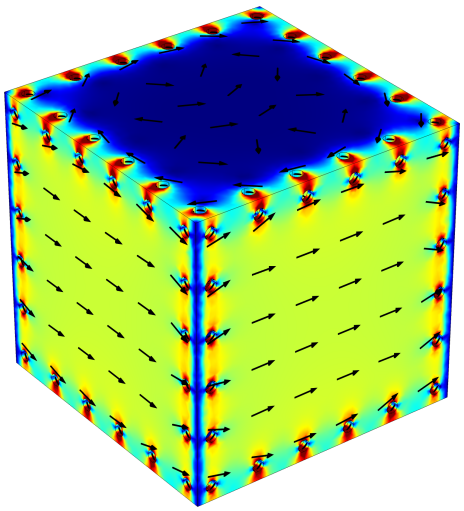

(b) 20 single coils distributed evenly around the circumference.

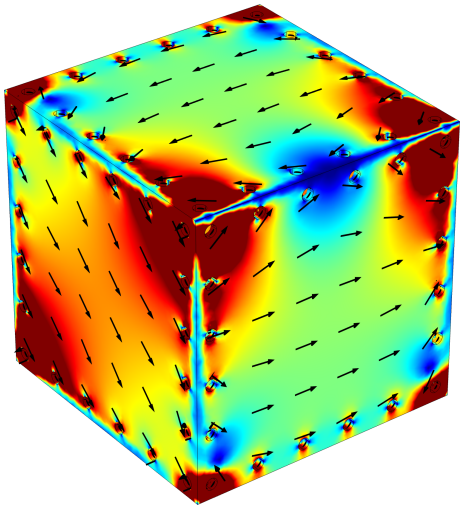

(c) Four L-coils at the edges of the cube.

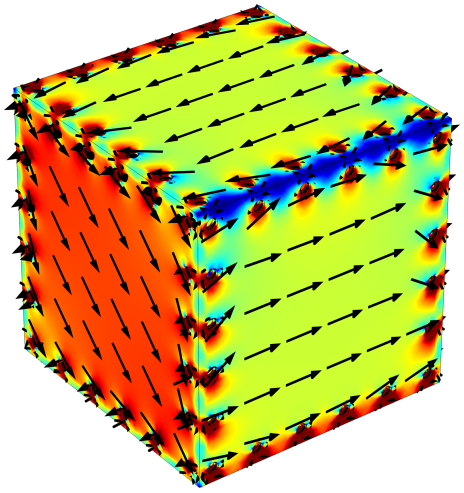

(d) Distributed L-shaped arrangement

Figure 5.9: Simulation plots showing the flux density distribution over the faces of the cubes for four different coil configurations. The color indicates the magnetic flux density, given in arbitrary units, but with the same scale for all plots. The black arrows show the direction of the magnetic flux. All simulations were run with the same current×turns value. (a) four single coils are placed at the edges, with strongly magnetized spots at the edges. (b) distributed coils create a more homogeneous magnetization with smaller spots. (c) very strongly magnetized spots can be seen at the corner were both arms of the L-shaped coils meet. (d) again more homogeneous magnetization across the walls with smaller spots.

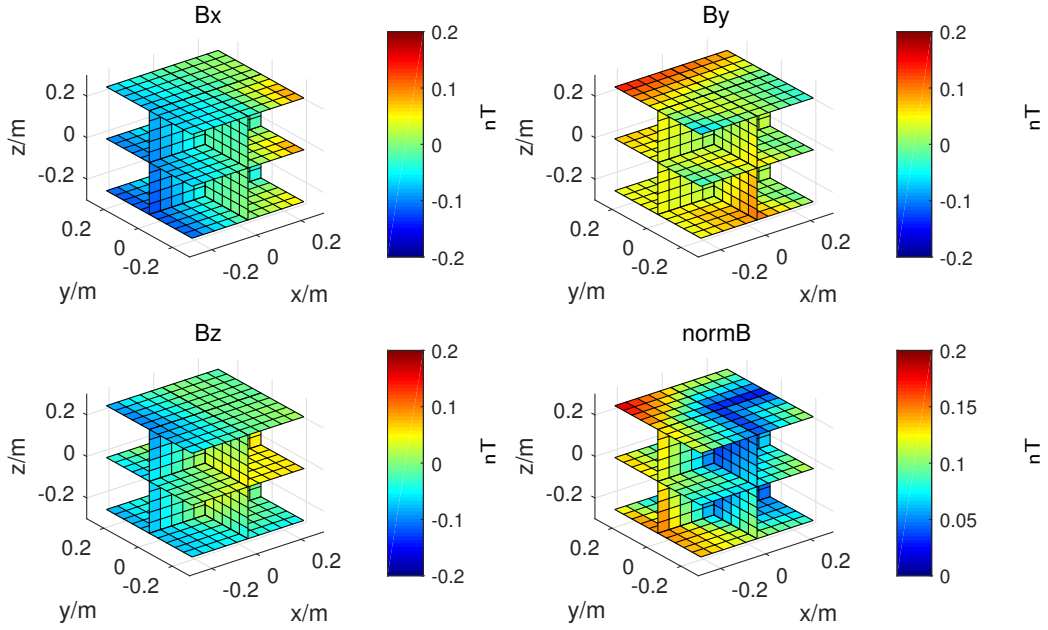

Figure 5.10: Plots of the measured residual fields for distributed I coils.

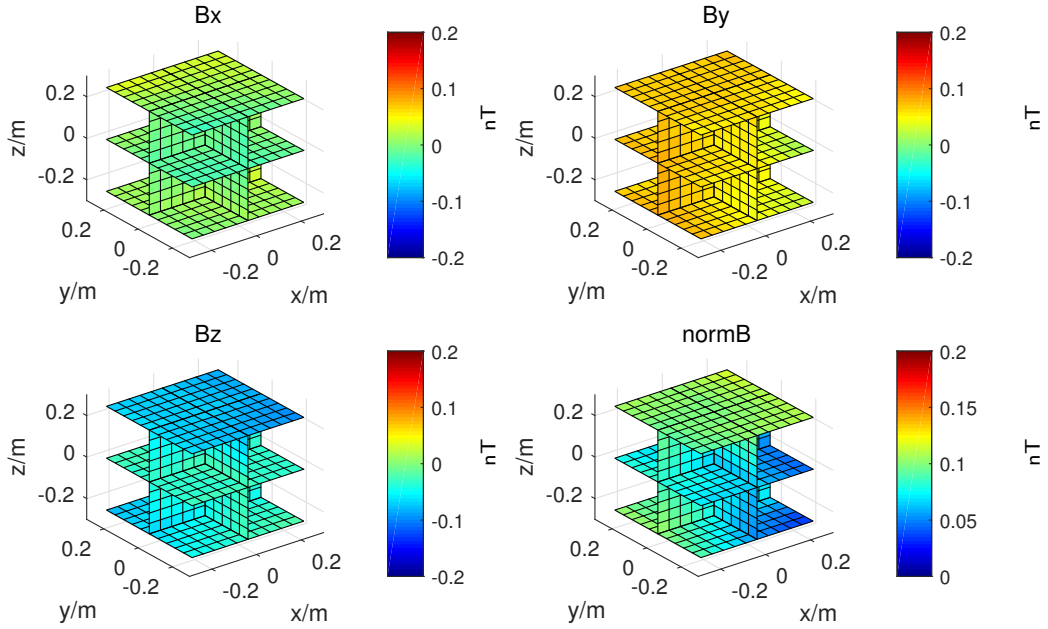

Figure 5.11: Plots of the measured residual fields for distributed L coils.

5.3 A shield for an atomic fountain experiment

For other types of fundamental experiments, magnetic shielding is also essential. Tests of the weak equivalence principle with light-pulse atom interferometry observe the free fall of two test masses. Even though magnetic field insensitive $|m_F = 0\rangle$ states are used, they are sensitive to magnetic field inhomogeneities due to second order Zeeman shifts.

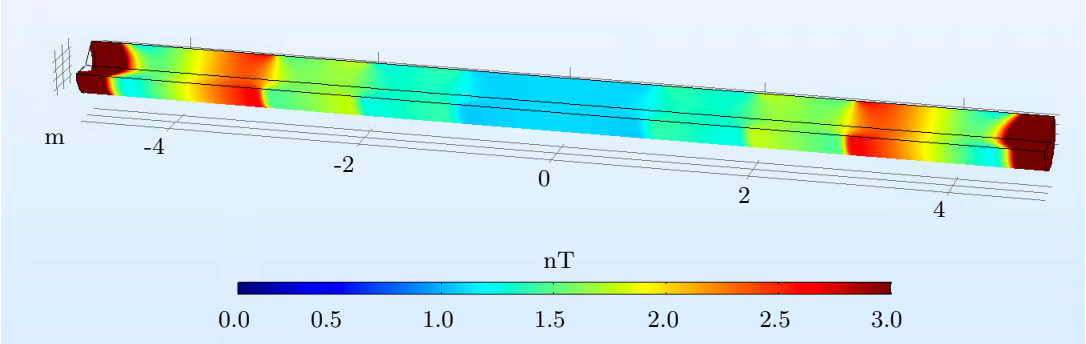

Figure 5.12: Cut away view of of the simulation, showing the residual flux density in the 10 m long tube. In the central meter it is on the order of 1 nT. Towards the end caps it increases to 3 nT.

For the Very Long Baseline Atom Interferometer (VLBAI) at the Leibniz University Hannover a 10 meter long magnetic shield has been built [89]. It consists of two cylindrical layers with an inner diameter of 60 cm and lids at the end. The residual field inside this shield can be estimated by the static simulations described previously in this chapter. The geometry has been modeled in a 2D rotation symmetric Comsol model shown in figure 5.12, containing both layers of shielding material and end caps with the 130 mm hole for the vacuum tube. The shielding layers have the original dimensions in the simulation but are not segmented; in reality they are, due to the size of the annealing ovens for the mumetal heat treatment.

The material parameters were taken from the implemented Nickel Steel Mumetal. An external field of 20 µT, which corresponds to the approximate earth magnetic field in the direction of the cylinder, was added to the simulation in order to create the magnetization state of the shielding material, and the red dashed line in figure 5.13 shows the resulting field inside the shield along the central axis.

The measured data in figure 5.13 are taken with a fluxgate sensor mounted on wooden slider, which was pulled through the 10 m long tube with strings. Since the slider rotated around the longitudinal axis during the movement, the individual vector components of the magnetic flux density are not given, instead only the absolute value is presented. The measured residual fields match the structure of those predicted by the simulation. Especially the four steps of field increase towards the end caps, which originate from the distribution of mumetal in the inner layer, are clearly reproduced. Accurate sensor calibration proved to be difficult in the 10 m long shield, which is a probable cause for the offset between measured data and simulation.

The measured residual field marks an improvement of over a factor of 30 compared to previous, similar shields, where approximately 100 nT have been reported [29]. With magnetic equilibration, this field distribution can be further improved for smaller gradients.

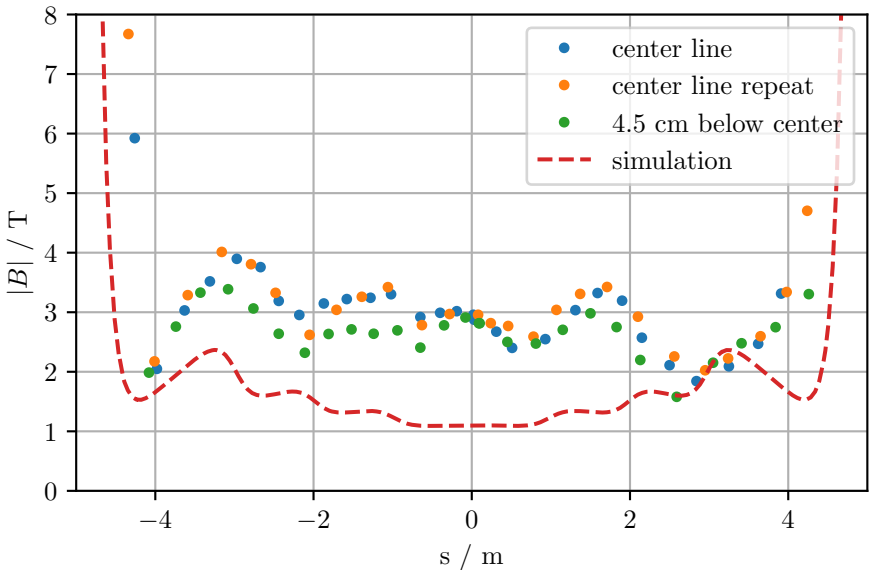

Figure 5.13: Plot of the magnetic flux density inside the 10 m long shield for the VLBAI, plotted along the central line. The measured results (blue) are compared to the simulated field (red dashed line). In green the flux density along a line at $r = 4.5$ cm below the center is shown, which allows a rough estimate of the radial gradients. The points in orange are a reproducibility test for the data shown in blue, measured on a second passage through the tube.

5.4 Proton EDM

A possible experiment to improve the limit of the proton electric dipole moment (pEDM) by almost five orders of magnitude compared to the current limit of $|d_p| < 7.9 \times 10^{-25}$ ecm is designed to consist of an all-electric storage ring of about 500 m circumference. Without an EDM contribution, protons with a so-called "magic" momentum will propagate around the ring with their spin frozen in the momentum direction (i.e. spin and momentum will precess at the same rate). If there is an EDM, an applied radial electric field will rotate the precession out of the storage plane. The magnetic field requirements for this are very strict, because also radial magnetic fields will cause the spins to rotate out of the plane and thus mimic an EDM signal. An average radial magnetic field of only 10 aT will already produce a signal the size of the targeted EDM limit [90]. However, this magnetic field will also split the proton beam and the counter-propagating beam. SQUIDs are capable of detecting the magnetic field caused by this splitting and can be used to monitor the beams. Hence, with continuous beam measurement, in principle no magnetic shield would be necessary. However, geometric phase effects cannot be corrected by the described monitoring. Thus, magnetic shielding is necessary. In the course of this thesis, studies for such a geometry have been performed.

The requirement will be that magnetic field is below 10 - 100 nT everywhere in the ring. Shields of that size, have to be manufactured from many segments, and between each of these segments, there will be an air gap. The corresponding disturbance of the residual field inside the shield can be compensated by a simple, smaller cylinder placed

inside the outer one, which catches flux leaking from the overlap and prevents the fields from entering the inner volume (see figure 5.14). This was demonstrated with a 2D axially symmetric simulation of two cylinders with the same radii, arranged co-axially next to each other with a small gap in between them. At the air gap, an additional cylinder is placed with a smaller radius and a short length. The cylinders have the material properties of mumetal assigned to them, the rest is air. The magnetization of the material is simulated by setting a magnetic scalar potential that results in the cylinder being magnetized in axial direction.

The first simulation without the correction ring shows how the flux density in the air increases close to the air gap and how that field reaches into the shielded volume. In the second simulation, the correction ring catches the leaking flux and keeps it from increasing the flux density in the central volume.

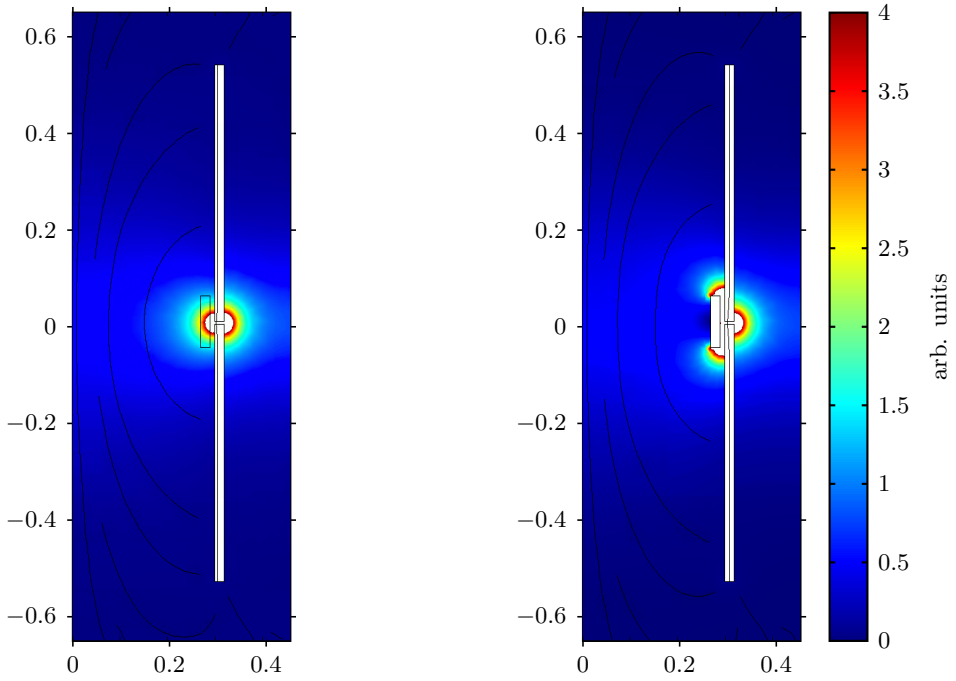

Figure 5.14: For very long shields that have to be segmented, the air gaps influence the residual field distribution inside the shield. A small ring that sits inside the long shield can act as a trap for the leaking flux through the air gap and reduce the residual field in the center.

5.5 Conclusion

Even though static simulations do not allow the study of the hysteretic behavior of high permeability materials used to construct MSRs, they provide useful information for the design of shielding enclosures. They have been used to study the paths magnetic flux will take around the volume to be shielded and how boundary conditions from construction influence these guiding or shielding properties. For this, only simple calculations for the geometries are necessary. With the correct parameters of the actually used materials, the currents needed for saturation can be investigated.

6. From degaussing to magnetic equilibration

The residual field inside an MSR is determined by the magnetization of the wall material. The purpose of magnetic equilibration is to remove the residual magnetization in order to have fields as small as possible in a volume of interest. But the procedure to optimize magnetic equilibration processes is quite complex and it is not obvious beforehand how to achieve the lowest possible field. Still, fields as low as 100 pT (as seen in chapter 4) have been achieved. The way to reach these low fields is based on experience and empirical evidence.

Many factors influence the achievable residual field, for example the waveform parameters for magnetic equilibration (c.f chapter 3), MSR and coil geometry, and also environmental conditions, like temperature or ambient magnetic fields.

Therefore, a way to study the interplay between these factors would be quite useful, in order to have guidance for the optimization of the equilibration processes. For this, the non-linear behavior of ferromagnetic materials has to be modeled in time-dependent calculations. In this work, two models were used for this. One is the well-established model of ferromagnetic hysteresis introduced by Jiles and Atherton in 1984 [91]. Its main advantage is that it is based on the microscopic behavior of ferromagnets and the model parameters correspond to physical properties of the material.

The other model is a purely phenomenological model used to describe the effect of equilibration on the hysteretic material instead of the hysteretic behavior of the material itself. This chapter is based on [92].

6.1 Time-dependent simulations of residual fields

6.1.1 Jiles Atherton

According to the JA model, the fundamental origin of ferromagnetic hysteresis in solids lies in the fact that domain walls cannot move freely throughout the material. Instead, their movement experiences some "friction type" force in the form of so-called pinning sites. The nature of these pinning sites is not considered or defined more closely, it is only assumed that they are uniformly distributed in the material and that an average energy is needed for the domain wall to overcome a pinning site. Possible reasons for the existence of pinning sites are non-magnetic inclusions or voids in the material structure or regions of inhomogeneous stress. Starting from a mean field consideration, the so-called anhysteretic magnetization curve can be explained. The equations for hysteresis can then be derived from an energy balance equation.

It is first considered how a magnetic domain within the material couples to the bulk magnetization of the rest of the material:

$$E = -\mu_0 m \cdot (H + \alpha M) \tag{6.1}$$

where $(H + \alpha M) = H_e$ is an effective mean field from the bulk and α represents the interdomain coupling. This models the response of an isotropic material to an externally applied magnetic field and only considers an averaged interaction of a domain with the

rest of the solid, included as αM. The general response is of the form

$$M = M_s f(H) \tag{6.2}$$

where f is an arbitrary function with $f(0) = 0$ and $\lim_{H_e \to \infty} f(H_e) = 1$, and M_s is the saturation magnetization. So far only the response of the material to a magnetic field and the averaged interaction has been taken into account, pinning has not yet been considered. In a real solid this is only true in the case when the material is on the ideal or anhysteretic curve, i.e. where the domain walls are in true equilibrium for the given field H:

$$M_{an} = M_s f(H). \tag{6.3}$$

Typically, the modified Langevin function is chosen for f [68]:

$$M_{an}(H_e) = M_s \left(\coth\left(\frac{H_e}{a}\right) - \left(\frac{a}{H_e}\right) \right). \tag{6.4}$$

However, the magnetization of a real ferromagnet does not behave exactly like this because, in a ferromagnet, the domain walls cannot move freely. The change of magnetization is impeded by pinning sites. Therefore, the initial magnetization curve always lies below the anhysteretic curve.

Due to the presence of pinning sites, the domain wall needs additional energy to move past this pinning site. So, when calculating

$$\Delta E = \int M \, dB_e \tag{6.5}$$

an energy loss due to overcoming the pinning sites has to be included

$$\int M \, dB_e = \int M_{an} \, dB_e - k \int \left(\frac{dM}{dB_e} \right) dB_e \, . \tag{6.6}$$

The parameter k is related to the mean pinning energy and the magnetic moment per unit volume of the domain [68].

Differentiating with respect to B_e leads to the differential equation for hysteresis

$$\frac{dM_{irr}}{dH} = \frac{1}{\frac{\delta k}{\mu_0} - \alpha(M_{an} - M_{irr})} (M_{an} - M_{irr}). \tag{6.7}$$

The energy required to overcome the pinning site always opposes the change in magnetization; this is reflected in the parameter δ, which takes the value 1 when H increases ($dH \,/\, dt > 0$) and -1 when H decreases ($dH \,/\, dt < 0$). When the external field is removed, the magnetization does not return to its initial state, because the same amount of energy would be needed to overcome the pinning sites.

Equation 6.7 shows that, when $M_{an} - M = 0$, there is no change in magnetization. The anhysteretic magnetization represents the global minimum energy state, where the domain walls are in equilibrium with the external field.

Domain walls are not rigid, they can bulge when their movement is impeded by two pinning sites. This leads to an additional contribution M_{rev} to the magnetization, which is reversible when the external field H is removed. Therefore, the domain

walls bend in a way to reduce the difference between existing magnetization and the anhysteretic one:

$$M_{rev} = c(M_{an} - M). \tag{6.8}$$

The parameter c can be accessed experimentally by measuring the ratio of initial differential susceptibilities for the normal and anhysteretic magnetization curves. On the anhysteretic curve $M_{rev} = 0$ and the domain walls are therefore planar. Summing reversible and irreversible contributions yields

$$\frac{dM}{dH} = \frac{dM_{irr}}{dH} + \frac{dM_{rev}}{dH} \tag{6.9}$$

$$= \frac{1}{1+c}\frac{1}{\frac{\delta k}{\mu_0} - \alpha(M_{an} - M)}(M_{an} - M) + \frac{c}{1+c}\frac{dM_{an}}{dH} \tag{6.10}$$

This gives the basic principle of the JA model. These equations are scalar and only apply to isotropic materials. A generalization to three dimensions that can also be used for anisotropic materials can, e.g., be found in [93]. Furthermore the JA model has been extended to include frequency dependence [94].

For the simulation of equilibration processes, these generalizations as well as a time dependence of the differential equation have been included. So the set of equations implemented in Comsol is (from [92]):

$$\frac{d\boldsymbol{M}}{dt} = (1-c)\frac{d\boldsymbol{M_{irr}}}{dt} + c\frac{d\boldsymbol{M_{an}}}{dt}, \tag{6.11}$$

$$\boldsymbol{M_{an}} = M_s\left(\coth\left(\frac{|\boldsymbol{H}_e|}{a}\right) - \left(\frac{a}{|\boldsymbol{H}_e|}\right)\right)\frac{\boldsymbol{H}_e}{|\boldsymbol{H}_e|}, \tag{6.12}$$

$$\boldsymbol{H}_e = \boldsymbol{H} + \alpha\boldsymbol{M} \tag{6.13}$$

$$\boldsymbol{M}_{rev} = c(\boldsymbol{M}_{an} - \boldsymbol{M}_{irr}), \tag{6.14}$$

$$\frac{d\boldsymbol{M}_{irr,dc}}{dt} = g\left(\frac{\boldsymbol{M}_{rev}}{ck}\frac{\boldsymbol{H}_e}{dt}\right)\frac{\boldsymbol{M}_{rev}}{|\boldsymbol{M}_{rev}|}, \tag{6.15}$$

$$\frac{d\boldsymbol{M}_{irr,ac}}{dt} = g\left\{\frac{\boldsymbol{M}_{rev}}{ck}\frac{d\boldsymbol{H}_e}{dt} - \frac{1}{\delta k(1-c)}\left[\frac{\mu_0 d^2}{2\rho\beta}\left(\frac{d\boldsymbol{M}}{dt}\right)^2\right.\right. \tag{6.16}$$

$$\left.\left. + \left(\frac{\mu_0 G d w H_0}{\rho}\right)^{\frac{1}{2}}\left(\frac{d\boldsymbol{M}}{dt}\right)^{\frac{3}{2}}\right]\right\}\frac{\boldsymbol{M}_{rev}}{|\boldsymbol{M}_{rev}|}. \tag{6.17}$$

Where, M_S is the saturation magnetization, a is the domain wall density, α is a mean field parameter, k is the average energy required to overcome a pinning site, c is the coefficient of M_{rev}, ρ is the resistivity, β is a geometrical factor, d and w are the cross-sectional dimensions of the material, G is a dimensionless constant, and H_0 represents the fluctuating internal potential. $g(x) = x$ if $x \geq 0$ and $g(x) = 0$ if $x < 0$.

When performing the calculations in the FEM software Comsol, the magnetization is set as the constitutive relations for the geometric domain that is set to be permalloy. The partial differential equation interface is used to solve for the magnetization M from the above equations.

To test the implementation of the JA model in Comsol and to see the effect of the added frequency dependence, two cases have been simulated. In the first case, three cycles of an alternating current with a linearly decreasing amplitude (cf. figure 6.1) is supplied to the excitation coil wound around a small cylindrical sample of permalloy. The equilibration curve is calculated based on equations without a frequency dependence. In the second case, equations are used to calculate the equilibration curve for the same geometry with a 10 Hz current, where eddy current losses and anomalous loss during hysteresis loops are considered. In conductive materials, eddy currents are induced by changing magnetic fields that dampen the field inside the material. Therefore, the equilibration curves are wider (figure 6.2).

Furthermore the interesting case with an applied background field can be studied. This is the usual situation when a MSR is equilibrated in an ambient field. The background field is included in the simulation as an offset for the equilibration current. The field increases linearly to 2 A/m, then the equilibration waveform with the sinusoidal current is applied. Without the offset field the magnetization ends with B close to zero after H has reached zero. In the other case, the end point is at a higher B value, on the anhysteretic curve M_{an} of the material with $H = 2\,\mathrm{A/m}$.

6.1.2 Phase Model

As a second way to describe hysteretic behavior during equilibration, a phenomenological model was developed in the course of this thesis. It is a mathematical model which does not specifically relate to physical parameters of the material. It is, however, much simpler to solve than the differential equations from the JA model, resulting in faster calculation times.

During equilibration the magnetic flux density B in the material and the magnetic field H typically have a phase shift φ due to the hysteresis and a time-dependent ratio between the amplitudes due to saturation, as shown in figure 6.4. The model described in this section is based on these two facts. A material is subject to a magnetic field

$$H(t) = H_0\, f(t) \sin(\omega t), \tag{6.18}$$

where $f(t)$ is the envelope function for the amplitude. The materials response is modeled by

$$B(t) = B_0 f\left(t - \frac{\varphi}{\omega}\right) \sin(\omega t - \varphi), \tag{6.19}$$

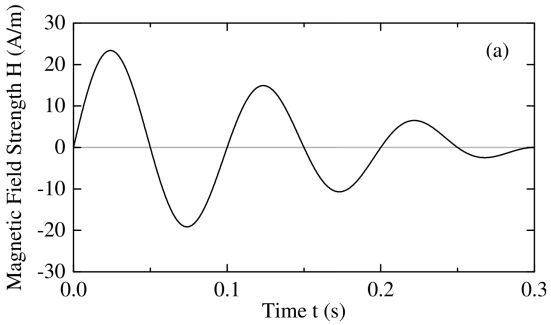

Figure 6.1: Applied magnetic field for the simulation of equilibration processes. Only a small number of cycles is used to keep calculation time within reasonable limits.

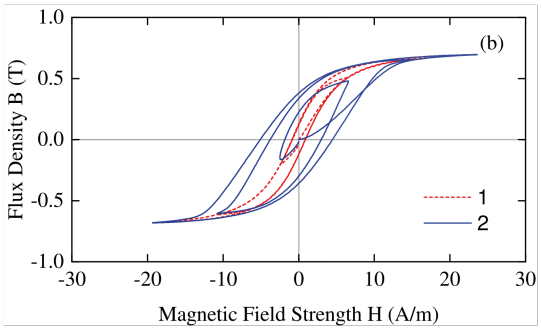

Figure 6.2: Hysteresis loops calculated with the following parameters for the JA model: $M_S = 6 \times 10^5\,\mathrm{A/m}$, $a = 1.8\,\mathrm{A/m}$, $\alpha = 1 \times 10^{-6}$, $k = 2\,\mathrm{A/m}$, $c = 0.5$, $\rho = 1 \times 10^{-5}\,\Omega\mathrm{m}$, $\beta = 16$, $d = 1\,\mathrm{mm}$, $G = 0.1356$, $w = 3\,\mathrm{cm}$, $H_0 = 0.0075\,\mathrm{A/m}$. The plot shows equilibration curves both without frequency dependence (curve 1) and with frequency dependence (curve 2).

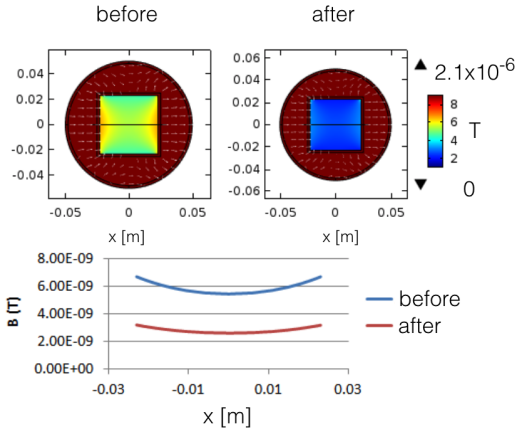

Figure 6.3: A simulation showing the effect of equilibration in a background field. The simulation started with ramping a background field to a value of $H = 2\,\mathrm{A/m}$, the field distribution in this background field is shown on the left hand side labeled "before". Then an equilibration process is simulated and the resulting field is shown on the right hand side labeled "after". The lower plot shows the field magnitude along the central black line across the shielded volume and the change in field magnitude due to the equilibration process.

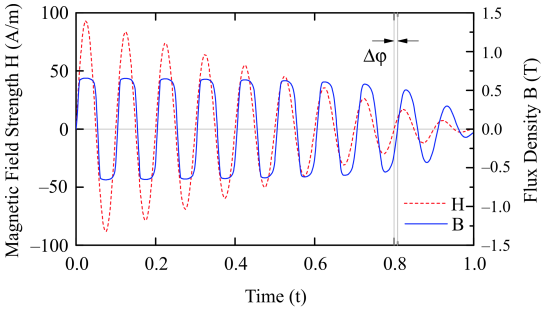

Figure 6.4: Calculated $H(t)$ and $B(t)$ during equilibration. The applied field $H(t)$ is shown in red and the response of the material $B(t)$ in blue, including a phase shift $\Delta\phi$ between the two.

a sinusoidal function with a phase shift and a variable amplitude. In Comsol the dependent variable is the vector potential $\boldsymbol{A}$ and the model has to be set up using the relation

$$\nabla \times \boldsymbol{A} = \boldsymbol{B} = \mu_0(\boldsymbol{H} + \boldsymbol{M}). \tag{6.20}$$

Expressing M as a function of B instead of H yields:

$$\begin{aligned}
M &= \frac{B_0}{\mu_0} f\Big(t - \frac{\varphi}{\omega}\Big) \sin(\omega t - \varphi) - H_0\, f(t) \sin(\omega t) \\
&= \frac{B_0}{\mu_0} f\Big(t - \frac{\varphi}{\omega}\Big) \sin(\omega t - \varphi) \\
&\quad - H_0\, f(t)[\sin(\omega t - \varphi)\cos(\varphi) + \cos(\omega t - \varphi)\sin(\varphi)] \\
&= \left[\frac{B_0}{\mu_0} f\Big(t - \frac{\varphi}{\omega}\Big) - H_0\, f(t)\cos(\varphi)\right] \sin(\omega t - \varphi) \\
&\quad - \frac{H_0\, f(t)\sin(\varphi)}{B_0 \omega f\big(t - \frac{\varphi}{\omega}\big)} \left[\frac{dB(t)}{dt} - B_0 \frac{df\big(1 - \frac{\varphi}{\omega}\big)}{dt} \sin(\omega t - \varphi)\right] \\
&= B_0\, f\Big(t - \frac{\varphi}{\omega}\Big) \sin(\omega t - \varphi) \left[\frac{1}{\mu_0} - \frac{H_0\, f(t)\cos(\varphi)}{B_0\, f\big(t - \frac{\varphi}{\omega}\big)}\right. \\
&\quad \left. + \frac{H_0\, f(t)\sin(\varphi)}{B_0 \omega f^2\big(t - \frac{\varphi}{\omega}\big)} \frac{df\big(1 - \frac{\varphi}{\omega}\big)}{dt}\right] - \frac{H_0\, f(t)\sin(\varphi)}{B_0 \omega f\big(t - \frac{\varphi}{\omega}\big)} \frac{dB(t)}{dt}
\end{aligned} \tag{6.21}$$

where $F(t) = \frac{f(t)}{\omega f\left(t - \frac{\varphi}{\omega}\right)}$. The ratio of B to H is given by the permeability function

$$\mu(B) = \mu_0 \mu_r(B) = \frac{B_0}{H_0}. \tag{6.22}$$

The magnetization then becomes

$$M = \left[1 - \frac{\omega F(t)\cos(\varphi)}{\mu_r} + \frac{F(t)\sin(\varphi)}{\mu_r\, f\big(t - \frac{\varphi}{\omega}\big)} \frac{df\big(t - \frac{\varphi}{\omega}\big)}{dt}\right] \frac{B(t)}{\mu_0} - \frac{F(t)\sin(\varphi)}{\mu_0 \mu_r} \frac{dB}{dt}(t) \tag{6.23}$$

By implementing M this way, the resulting B has a phase shift with respect to H and a field-dependent amplitude related to μ_r. With μ_r the shape of the modeled hysteresis loops can be changed. For example figure 6.5 shows equilibration curves obtained with a constant μ_r and a nonlinear $\mu_r(B)$, which allows saturation to occur. These equations are generalized to three dimensions for the simulations, by treating the spatial dimensions independently, which is valid for isotropic materials.

To describe the behavior of permalloy, $\mu_r(B)$ is fitted to equilibration measurement curves on the material. To enforce a symmetric behavior of μ_r with respect to B, an even polynomial function is used as a continuous and differentiable function. The first and second parameter v_1 and v_2 were chosen to be

$$v_1 = 2\frac{1 - \mu_{max}}{(\mu_0 M_s)^2} + \sum_{i=3}^{N} (i-2) v_i (\mu_0 M_s)^{2(i-1)} \quad \text{and} \tag{6.24}$$

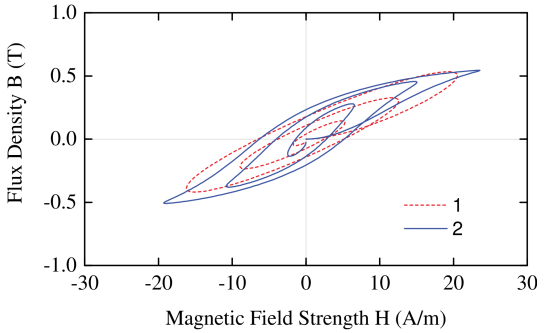

Figure 6.5: Two equilibration curves showing the effect of a nonlinear $\mu_r(B)$ in the phase shift model. Curve 1 is calculated with a constant $\mu_r = 20000$, curve 2 used the parameters: $\mu_{max} = 40000$, $\mu_0 M_S = 0.73\,\mathrm{T}$, $v_3 = -13\mu_{max}\mathrm{T}^{-6}$, $v_4 = -30\mu_{max}\mathrm{T}^{-8}$, $v_5 = 42\mu_{max}\mathrm{T}^{-10}$, $v_6 = 15\mu_{max}\mathrm{T}^{-12}$.

$$v_2 = 2\frac{\mu_{max} - 1}{(\mu_0 M_s)^4} - \sum_{i=3}^{N}(i-1)v_i(\mu_0 M_s)^{2(i-2)}. \tag{6.25}$$

so that $\mu_r(B)$ smoothly decreases at saturation. An order of $N = 6$ proofed to be sufficiently large for our purpose.

To also include additional background fields as with the JA model, M was recalculated as follows:

$$\begin{aligned} M = &\left(1 - \frac{\omega F(t)}{\mu_r(B)}\cos(\varphi) + \frac{\tilde{F}(t)}{\mu_r(B)}\sin(\varphi)\right)\frac{B - B_a}{\mu_0} \\ &- \frac{F(t)}{\mu_0\mu_r(B)}\sin(\varphi)\frac{d(B - B_a)}{dt} + M_a(H_a) \end{aligned} \tag{6.26}$$

where $M_a = \frac{B_a(t)}{\mu_0} - H_a(t)$, $H_a(t)$ and $B_a(t)$ are time-dependent but quasi-static ambient fields. An equilibration curve calculated with this model is shown in figure 6.6.

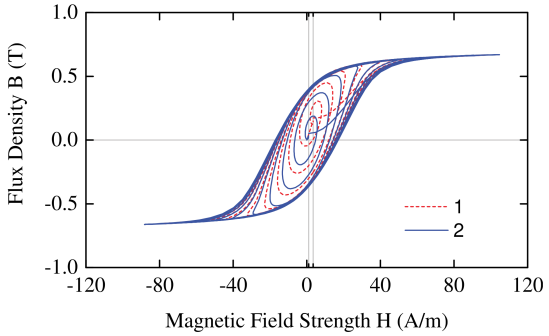

Figure 6.6: Equilibration curves calculated with the phase model with an offset of 1 A/m (curve 1) and an offset of 1 A/m (curve 2). The same parameters as in figure 6.5 were used.

6.2 Experimental cross check

To check the simulation results against real samples, equilibration curves were calculated and measured for simple geometries. As a first example, a cylindrical sample made of permalloy with 1 mm thickness, 30 mm width and 100 mm diameter was used. The equilibration current was fed to a 10-turn primary coil wound toroidally around the cylinder. A 50-turn secondary coil wound the same way, was used as a pick-up coil to measure the magnetization. In this coil, a voltage

$$U_s \propto N\frac{d\phi}{dt} \propto N\frac{dB}{dt}A_C \tag{6.27}$$

is induced. The magnetic flux is then obtained by integrating the induced voltage, either with an RC circuit or digitally after recording. Plotting this flux against the equilibration current, hysteresis can be measured. Five cycles with the same amplitude were supplied to the primary coil before each equilibration cycle to achieve reproducible and stable initial conditions. In figure 6.9 (b) it can be seen that the measured flux matches the simulated one during equilibration, and that the residual flux at the end after $t = 1\,\mathrm{s}$ is correctly predicted. The measurements were done inside the MSR at TUM in a residual field less than 1 nT.

For a more qualitative comparison between simulation and experiments, a normalized root mean square deviation (NRMSD) and the coefficient of determination R^2 are calculated for both the measured and simulated curves. They show that both simulation methods are in good agreement with the experimental data, and also that the results from the JA model provide better accuracy than those from the phase shift model.

The second sample tested had a more complex geometry. A “snake” panel was cut

(a) Sample cylindrical ring

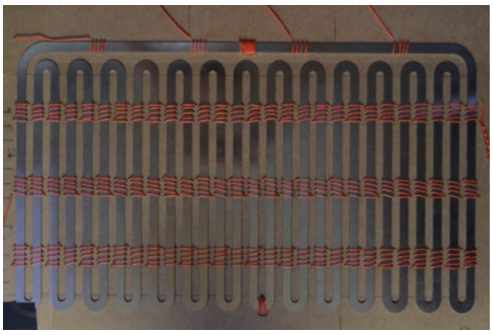

(b) Sample: snake panel

Figure 6.7: Pictures of the used samples.

Table 6.1: Comparison of the performance of the different models according to NRMSD and R^2 values. The JA model shows slightly better agreement with the experimental data than the phase model.

Simulation	NRMSD(%)	R^2
JA model	4.77	0.9762
Phase shift model with constant φ	9.74	0.9336
Phase shift model with time-dependent φ	6.44	0.9710

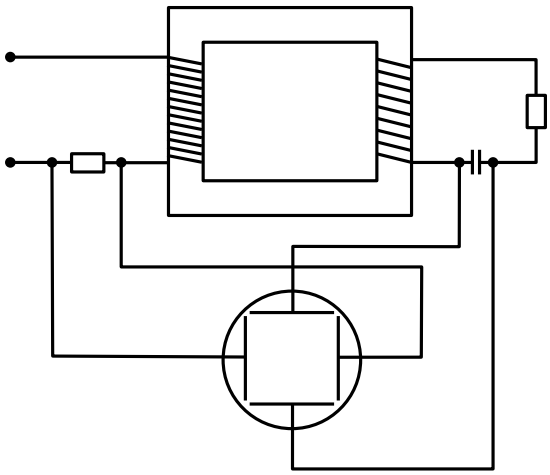

Figure 6.8: Circuit diagram for the measurement of hysteresis loops. Two coils are wound around a material core. The primary coil is supplied with a sinusoidal current in order to magnetize the material, and the corresponding voltage is recorded as the x channel on an oscilloscope. The secondary coil serves as pickup coil and the induced voltage is integrated with a capacitor and recorded on the y channel of the oscilloscope.

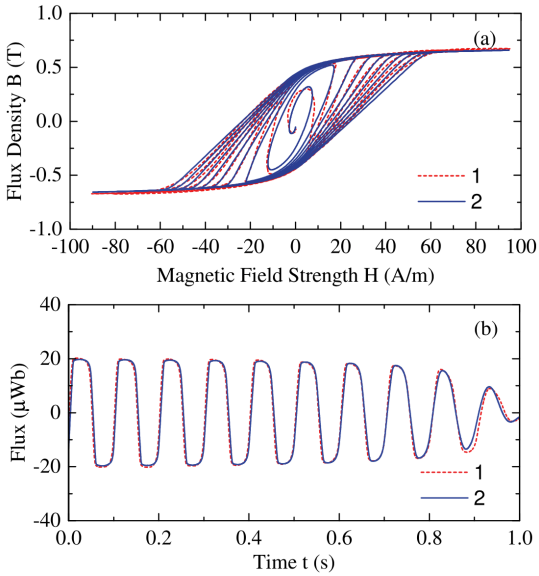

Figure 6.9: Measured (curve 1) and calculated (curve 2) equilibration curves using the JA model (a) and (b) measured and calculated flux. Fitted parameters are: $M_S = 5.5 \times 10^{-5}\,\mathrm{A/m}$, $a = 5\,\mathrm{A/m}$, $\alpha = 1.5 \times 10^{-5}$, $k = 2.4\,\mathrm{A/m}$, $c = 0.9$, $\sigma = 6 \times 10^{-5}\,\mathrm{S/m}$, $\beta = 16$, $d = 1\,\mathrm{mm}$, $G = 0.1356$, $w = 3\,\mathrm{cm}$ and $H_0 = 0.0075\,\mathrm{A/m}$.

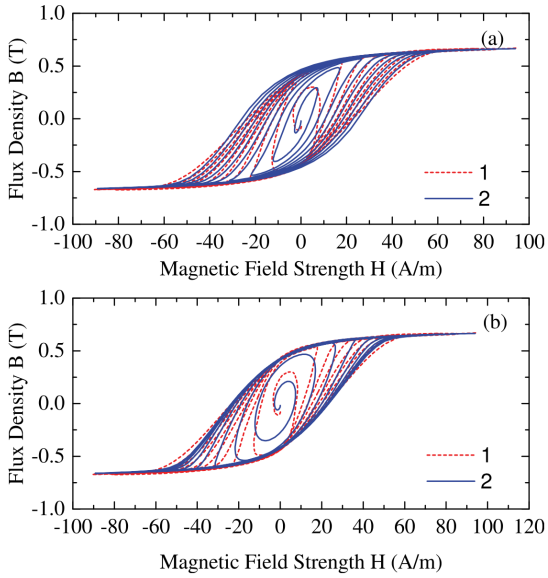

Figure 6.10: Measured (curve 1) and calculated equilibration curves using the phase shift model (curve 2) with constant φ (a) and with time dependent φ (b). Fitted parameters are: $\mu_{max} = 40000$, $\mu_0 M_S = 0.73\,\mathrm{T}$, $\varphi = 21°$, $v_3 = -13\mu_{max}\mathrm{T}^{-6}$, $v_4 = -30\mu_{max}\mathrm{T}^{-8}$, $v_5 = 42\mu_{max}\mathrm{T}^{-10}$, $v_6 = 15\mu_{max}\mathrm{T}^{-12}$, $c_1 = 0.9\,\mathrm{s}^{-1}$, $c_2 = 1.3\,\mathrm{s}^{-2}$.

from a sheet of permalloy. Its had a constant cross section and formed a closed loop. After equilibration, the flux density was measured 85 mm above the sample, again inside the MSR. The maximum magnitude of the measured flux was $(5.2 \pm 0.1)\,\mathrm{nT}$. The observed magnetic flux distributions match the simulations (c.f figure 6.11). Both simulation models produce the same patterns of field distributions for each of the three spatial components with B_x showing high field values in the central region of the panel, B_y exhibiting a quadrupolar shape and B_z resembling a dipolar distribution. With these simulations qualitative predicts of residual field distributions can be made.

The calculations were run on a computer with 16 3.2 GHz CPUs and 40 GB of RAM. Computations times were 16 h and 18 h for the phase shift model and for the JA model, respectively.

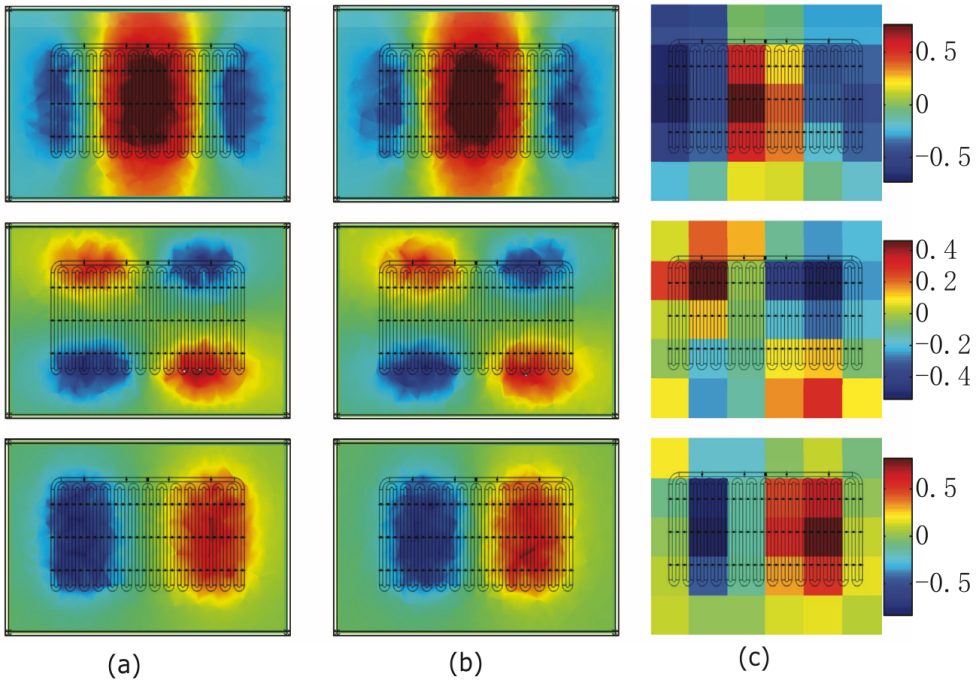

Figure 6.11: Measured and simulated field distributions above a panel of mumetal, showing the good qualitative agreement for each of the flux density components. Each columns shows the relative magnitude $\frac{\boldsymbol{B}}{|B|_{max}}$ for each of B_x,B_y and B_z for (a) simulations according to the JA model, (b) simulations of the phase shift model and (c) measured fields.

6.3 Results

Two models were used to calculate equilibration curves for 3D geometries in FEM software. Both are able to calculate equilibration in an ambient or background field, situations that can occur for any real experiment where magnetic shielding is employed. The large-scale simulations for real MSRs will need considerable computing power because of the tracing of the space- and time-dependent magnetic field during the whole equilibration process. The phase shift model was specifically tailored for faster computation, but it resulted in only minor performance gains. The models for small objects already help us to understand the theoretical principles and fundamental problems of equilibration. The empirical optimization of the main equilibration parameters used up to now can be replaced or at least assisted by an optimization based on the proposed calculation methods. This work provides a basis for improved modeling of residual fields and their temporal stability inside complex geometries of magnetizable materials, in particular for MSRs.

Only recently the modeling of hysteretic behavior has been included in the FEM software Comsol[1].

1 Comsol v.5.3

7. Development of the NMR coil system

The coil system for the nEDM experiment has been developed, designed and studied with the help of finite element method (FEM) simulations. The commercial FEM suite Comsol[1] has been used for this.

For a Ramsey-type experiment, two magnetic fields are necessary: the first one, usually called B_0 is the holding field around which the polarization precesses during the observation time. The second one is the flipping field, called B_1, perpendicular to B_0. The coil system produces both of these fields. The B_0 system produces the homogeneous holding field. The B_1 system is a copy of the whole B_0 system, rotated by 90° and slightly adapted to geometry boundary conditions.

Naming convention for the coils

In total, the coil system consists of 44 individual coils. They are named according to their function and their position. All coils that have a symmetry to each other have the same number. There is the B_0 main coil. Additionally, there are so called correction coils, which have one loop and are similar to the B_0 coil. They are labeled with a "c", two letters designating their respective position and a number. The letters for the positions indicate in which quadrant the coil is located, there are:

- TL for top left at -X and +Y
- TR for top right at +X and +Y
- BR for bottom left at +X and -Y
- BL for bottom left at -X and -Y

The numbers for the correction coils go from zero to five. Two c0 coils lie in the XY plane at Z = 0, consequently their names contain only one letter, cL0 and cR0. Correction coils are shown in blue in figure 7.1(a).

The coils at the end caps of the cylinder are called end coils and labeled with an "e", two letters and a number. The letters again correspond to their position:

- TF for top front at -Y and +Z
- BF for bottom front at -Y and -Z
- TB for top back at +Y and +Z
- BB for bottom back at +Y and -Z

The numbers for the end coils go from one to four, where one corresponds to the largest diameter and four to the smallest. End coils are shown in green in figure 7.1(a).

1 Comsol Multiphysics, with AC/DC module, in different versions from 3.5 to 5.3, `https://www.comsol.com/comsol-multiphysics`

7.1 FEM simulations for the coil system

7.1.1 Main coil

A sketch of a first, simplified model can be seen in figure 7.1(a). Due to the symmetry of the insert, the model can be reduced to an eighth of the whole setup for simulation purposes. Basic principles of the coil system, i.e. the number of B_0 wires, the number of correction coils and the basic shape of the end coils have been developed and studied with this.

It is well-known that the solution of the classical text book example of an infinitely long cos θ coil produces a perfectly homogeneous magnetic field in transverse direction inside the enclosed cylindrical volume [95]. Because it is also easy to realize, a discretized cos θ current distribution is widely used to create uniform magnetic fields in experiments [34, 96, 97, 98] with a cos θ coil which is adapted and optimized for the specific situations. The dimensions of the coils depend on the required field quality and the space available due to experimental constraints. Furthermore, shielding factor considerations ($SF \propto \frac{1}{D}$) and field homogeneity requirements influence design decisions.

For the nEDM experiment, the following points were considered. The size of the neutron chamber will be 480 mm in diameter with a height of 2 times 100 mm. Above and below the neutron chambers similar sized cells for Hg magnetometry will be placed. The high voltage electrodes will be shielded with corona rings to prevent discharges.

Furthermore, additional online magnetometry, like Cs magnetometers and SQUID systems, is going to be used to track and monitor magnetic field changes. These have to be placed as close to the experimental volume as possible to track the actual field in which the nEDM measurement takes place; however, they also have to be distanced far

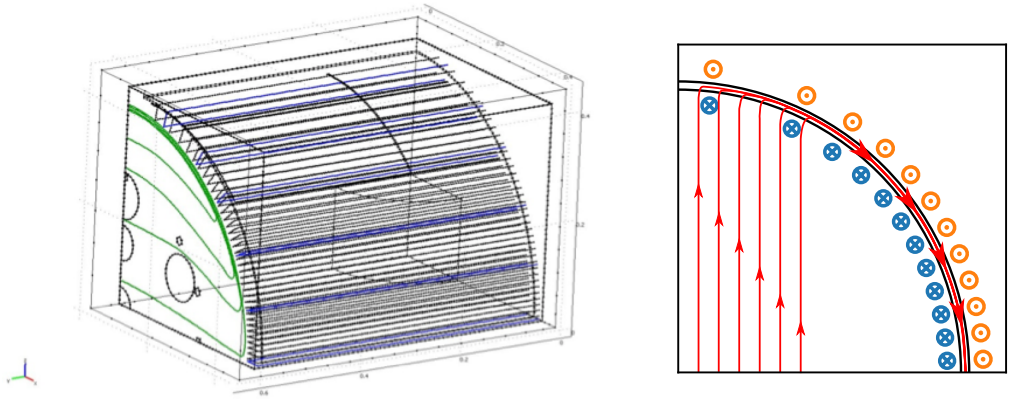

(a) Schematic of an eighth of coil system. **(b)** Principle of the cos θ coil.

Figure 7.1: In a) a schematic drawing of a quarter of coil system is shown. The black lines represent the B_0 main coils wires. In blue the correction coil wires are shown and the end coils in green. The holes in the end cap can be seen, as well as the cylindrically shaped fiducial volume in which the field will be optimized. In b) the operating principle of the cos θ coil is shown. For illustration only a third of the wires are included. The crosses indicate a current into the paper plane, the dots out of the paper plane. The currents outside the mumetal contribute a reduced amount to the field inside the cylinder because they are shielded. The mumetal works as a return yoke for the flux. The red lines symbolize field lines.

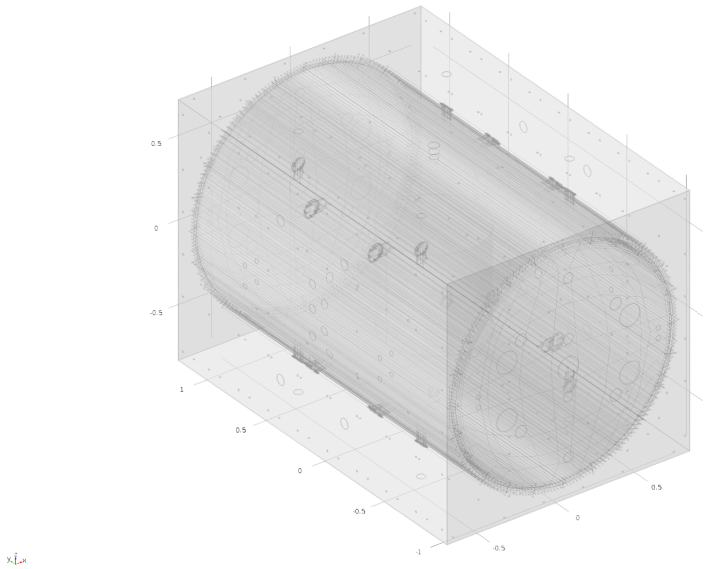

Figure 7.2: Full geometry of the Comsol model for the cylinder, coil system and the innermost layer of the insert. The FEM mesh consists of 3.55 million mesh elements. Solution of the model takes approximately five hours an 4 x 4.5 GHz CPU with 64 GB RAM.

from the coil system so that their signal is not dominated by individual coils. These magnetometers are not supposed to monitor localized field effects. They are inserted into the shielded volume via online access channels shown in figure 1.4 each with a diameter of 70 mm.

Vacuum and neutron guides are required to have a diameter of at least 130 mm, to ensure sufficient pumping power to keep the vacuum at the required level of 1×10^{-5} mbar. For the neutron guides, the size is determined by the necessity to transport the polarized neutrons without destroying the polarization. The vacuum chamber itself has an inner diameter of 1060 mm and a height of 640 mm.

These boundary conditions lead to a diameter of the innermost shielding layer of 1400 mm and a length of 2160 mm. This cylindrical layer plays an essential role not only as additional shielding (SF_t about 3) but also as a part of the B_0 coil system for the homogeneous field creation. The mumetal, VDM® MAG 7904, with a thickness of 1.6 mm is mounted in a support structure made of glass-fiber reinforced plastic (GFRP). Six bars support the cylinder and house the copper tubes for the coil system. These tubes are placed in precision holes that were machined with a placement accuracy of 0.1 mm, and a diameter of 2.1 mm.

The B_0 coil itself consists of 144 loops of copper tubes, which were chosen as conductors because they have sufficient stability to not bend measurably in the 400 mm between the GFRP supports.

To connect the individual copper tubes into loops, golden pins soldered to printed circuit boards were used. Each loop is closed on the back side of the cylinder, whereas the connection to the next loop is made on the front side of the insert. This connection to the next loop makes the correction discussed in section 7.1.2 necessary. The distance in Z direction between the wires of the coil is 18.9 mm. The inner B_0 coil wires are

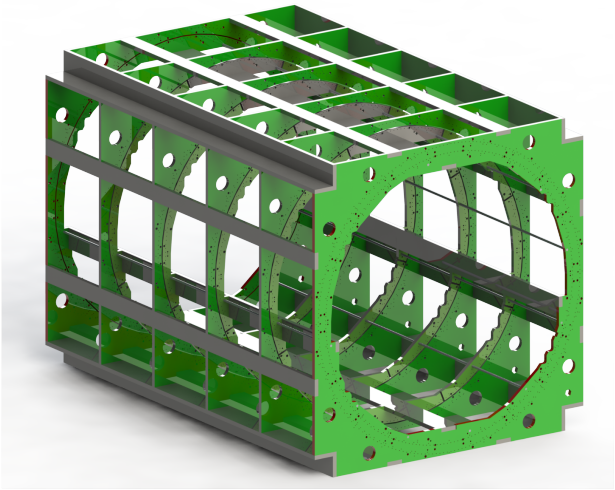

Figure 7.3: Rendering of the insert's GFRP structure, that gives support to the mumetal cylinder and houses the B_0 and B_1 coil systems.

placed on a circle with a radius of 679.6 mm (cf. blue crosses in figure 7.1(b)) and for the current return on the outside of the mumetal the radius of the circle is 720.7 mm (cf. orange dots in figure 7.1(b)).

The magnetic field inside the cylinder is produced by an interplay between the mumetal and the field produced by the wires, as illustrated in figure 7.1(b). The highly permeable material, on the one hand, shields the inside from the magnetic field produced by the current return wires. On the other hand, it serves as a yoke for the magnetic flux. In figure 7.4, the results for three simulations are shown. The B_z component is plotted along a line at Y = 0 and Z = 0. In these simulations, a current was supplied only to the wires inside the mumetal cylinder (blue), only to the wires outside the mumetal (orange), and both wires inside and outside (green), respectively. The outer wires produce a field in the opposite direction than that produced by the inner wires, but since the outside is shielded, and therefore much smaller, the total sum of both is not close to zero. In figure 7.4(b), the resulting distribution of fields is shown.

In an infinitely long cylinder with a cos θ coil, the field would be perfectly uniform. For a finite length, the influence of the end caps have to be taken into account. Specially designed coils on the end caps are used to compensate this influence. These coils will be discussed in section 7.1.4.

Maps of the simulated field produced by the full main B_0 coil are shown in figure 7.5. The model for this simulation includes the connecting wires to the next loop, as well as the irregular wiring necessary to bypass holes in the magnetic shield, which cannot be blocked. A current of 20 mA was simulated in the coil. There are some points to be noted. The saddle shape in the B_z component originates from the facts that on the one hand, the field increases when getting closer to the wires (in X direction). On the other hand, the field decreases towards the cylinder end caps (in Y direction). The B_x component is symmetric with respect to the YZ plane at $x = 0$ but asymmetric with respect to the XZ plane at $Y = 0$. Lastly, the B_y component has no symmetry

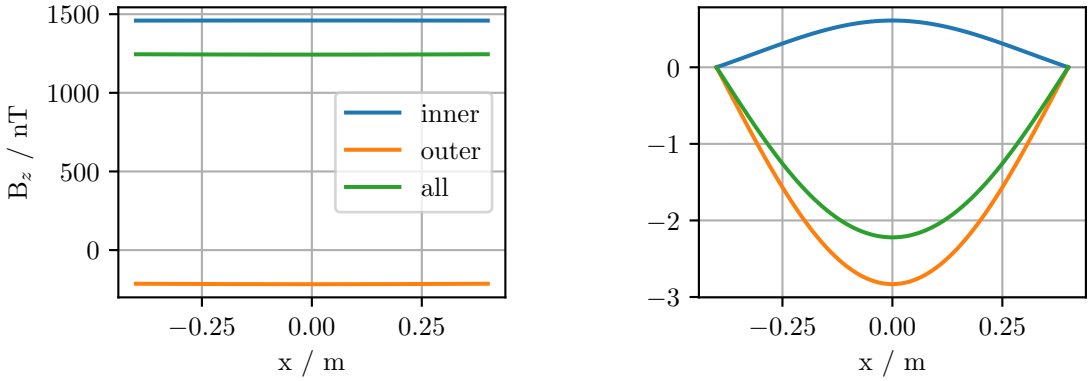

(a) Field produced by the individual segments.

(b) Fields offset to zero at $X = -0.4\,\mathrm{m}$.

Figure 7.4: Field produced by different segments of the B_0 main coil, plotted along a line at $Y = 0$ and $Z = 0$. Only the inner wires carried a current (blue), only the outer wires carried a current (orange) and the whole coil (green). Even though they are shielded, the outer wires have a strong influence of the distribution of the field inside.

and has higher values in the front of the insert (at negative Y values). In the lower XY plane at $Z = -0.2\,\mathrm{m}$, the transverse components are increased with regard to the central plane at $Z = 0$.

The asymmetry in Y direction for both B_x and B_y will be addressed in the next section.

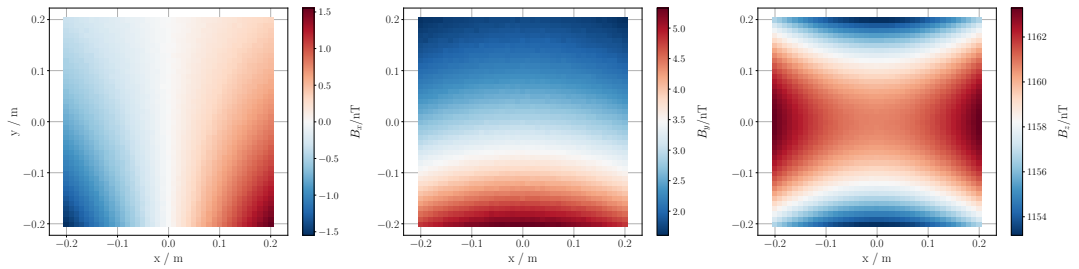

(a) In central plane $Z = 0$.

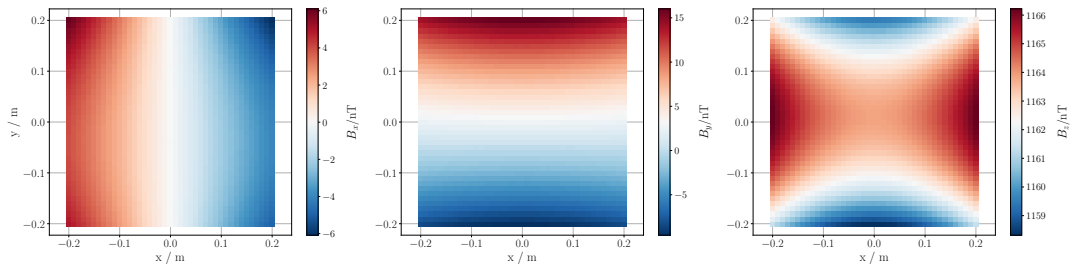

(b) At $Z = -0.2\,\mathrm{m}$.

Figure 7.5: Simulation of the field produced by the B_0 coil with a current of 20 mA in two different planes. The three plots show the B_X, B_Y and B_Z component, respectively.

7.1.2 Single loop correction for tangential current in the B0 coil

At the front side of the insert the individual loops of the B_0 main coil are connected to each other via printed circuit boards. The currents in these circuits have a radial component, from the inner part of one loop to the outer one, as well as a tangential component, from one loop to the next. This results in a net current flowing around a single loop producing a magnetic field mainly in y direction. These fields produce the asymmetry in the transverse components mentioned before. B_x and B_y components on the order of 1.5 nT and 5 nT respectively are produced in the central plane.

By placing an additional wire onto the connecting circuit boards (as indicated by the yellow circle in figure 7.6(a)) and supplying it with a current of the same magnitude, but with opposite direction as the B_0 main coil this disturbance can be compensated for. In simulations, this works extremely well on the central plane at $Z = 0$, see figure 7.7, but at the lower plane $Z = -0.2$ m the correction is only on the order of 30%. For this, additional coils have to be employed.

7.1.3 Correction coils

There are 22 additional coils, consisting of single loops similar to the B_0 main coil loops. These coils are placed at angles of 90, 75, 60, 45, 30 and 15 degrees with respect to the vertical direction (see also the blue coils in figure 7.1(a)). They are labeled c0 to c5. These coils mainly produce B_x and B_z components with different magnitudes according to their positions. Not all of their field maps will be presented here; as an example only the field produced by cTL4 will be shown (figure 7.8), results for the other coils are similar and can be found in the appendix. cTL4 produces B_x and B_z components, but only very small B_y components. Comparing the field distributions of the correction coils with the one from the B_0 main coil in the lower plane, shows that they can be used to compensate for the B_x components of the B_0 coil.

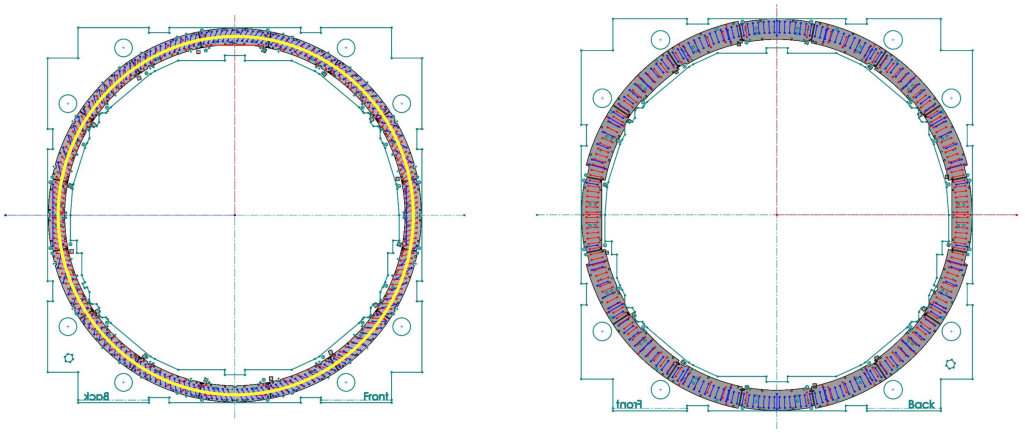

(a) Front **(b)** Back

Figure 7.6: Drawing of the connections for the B_0 (red) and B_1 (blue) on the front side (a) and on the back side (b) of the insert. On the back the connectors are oriented radially, whereas on the front side the connection to the next loop has to be made, resulting in a net current loop.

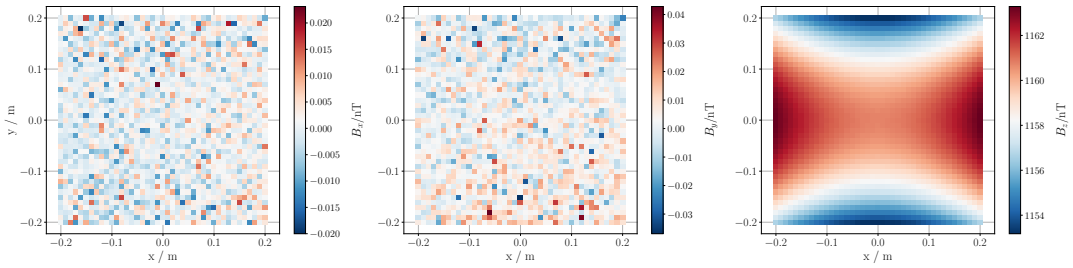

(a) In central plane Z = 0

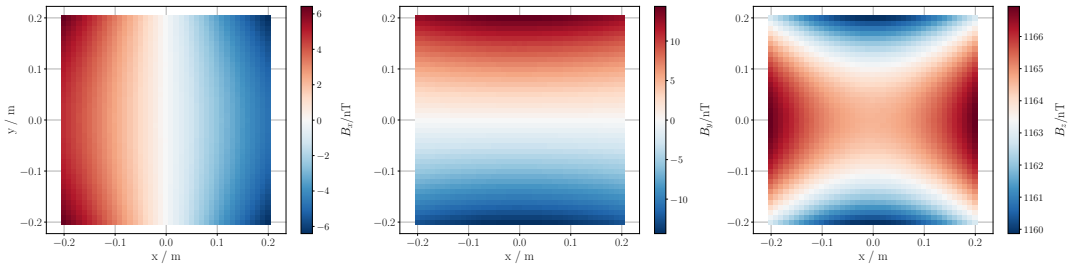

(b) At Z = -0.2 m.

Figure 7.7: Simulation of the field produced by the B_0 coil with a current of 20 mA and the additional single loop eF in two different planes.

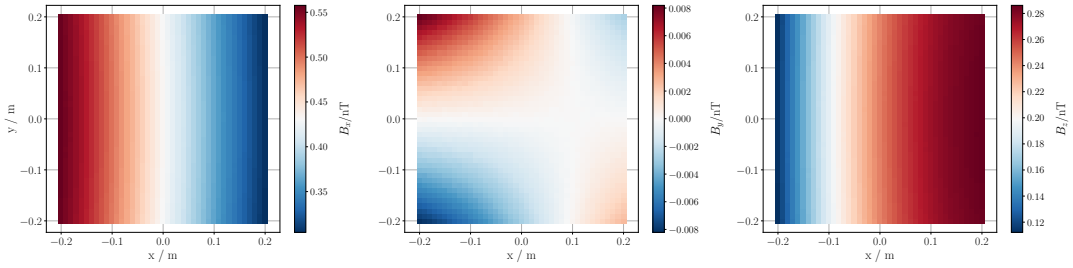

(a) In central plane Z = 0

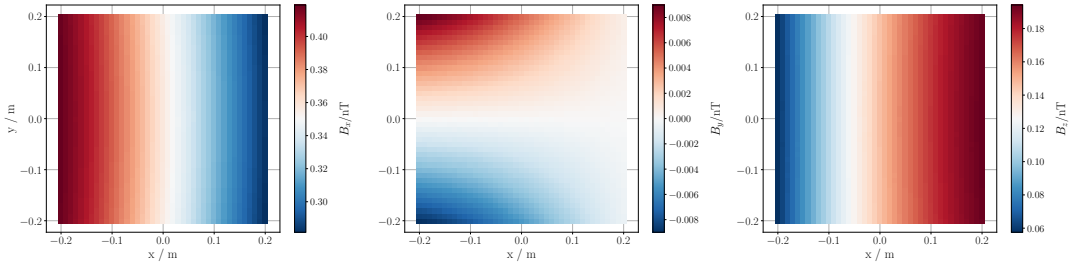

(b) At Z = -0.2 m.

Figure 7.8: Simulation of the field produced by the cTL4 coil with a current of 1 mA in two different planes.

7.1.4 End coils

The end coils are placed, as their name already implies, on the end caps of the insert. Their purpose is to compensate the drop-off of the magnetic field from the B_0 main coil along the Y direction (cf. figure 7.5).

These coils have not been designed following an analytical approach via the magnetic scalar potential as for example in [99]. Instead, their shape and position have been developed and optimized with the help of Comsol simulations.

The coils are wound from a flat copper wire with adhesive on one side and an isolating foil on the other side. The adhesive also allows the coils to keep their convex shape. The frames holding the coils and giving them stability are made from aluminum. Each coil consists of 20 loops, plus one additional loop, that can be added if small additional changes are necessary for a single coil.

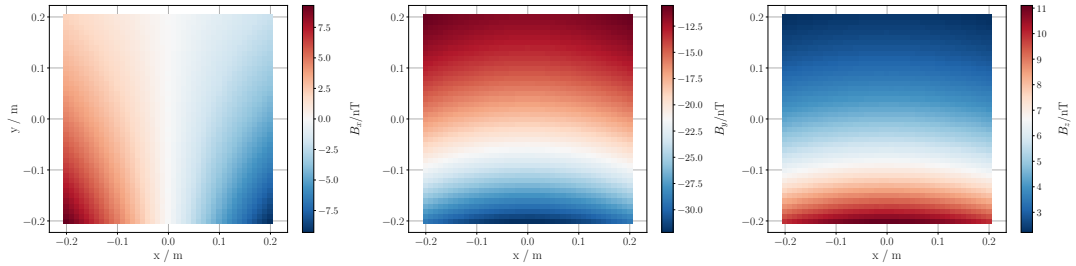

(a) In central plane Z = 0

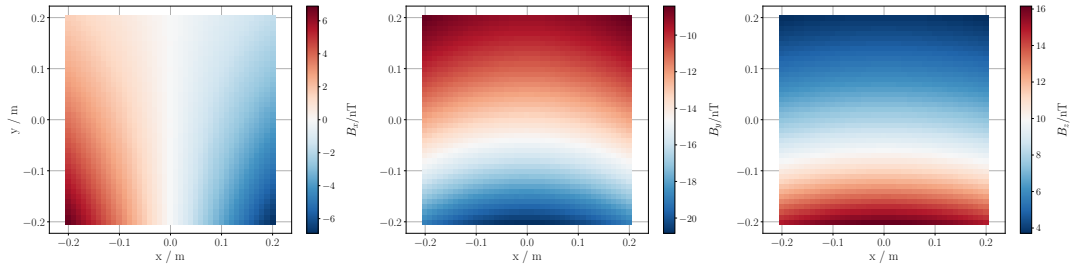

(b) At Z = -0.2 m.

Figure 7.9: Simulation of the field produced by the eTF1 coil with a current of 330 mA in two different planes.

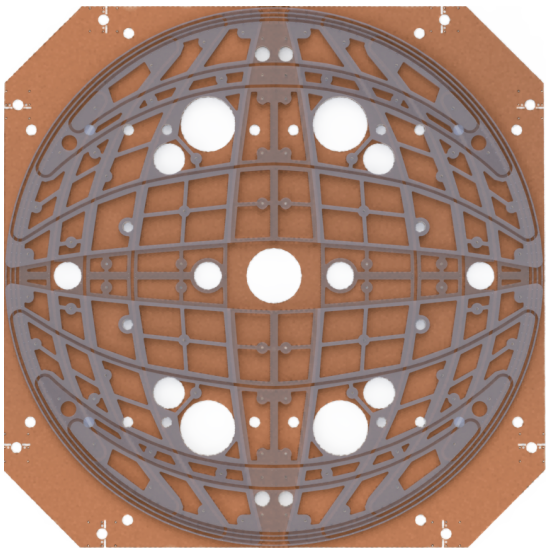

Figure 7.10: Rendering of the support structure for the end coils. B_0 and B_1 end coils are mounted on top of each other. On each end cap of the insert, one of the shown plates is mounted.

7.2 Current determination

The field at a position within a volume of interest is the sum of the individual contributions of each coil at this position. This can be expressed as a system of linear equations:

$$S\boldsymbol{I} = \boldsymbol{B}. \tag{7.1}$$

$\boldsymbol{B} = (B_{1,x}, B_{1,y}, B_{1,z}, \ldots, B_{m,z})$ is the resulting field at m positions. The vector

$$\boldsymbol{I} = (I_1, I_2, I_3, \ldots, I_n) \tag{7.2}$$

contains the current values for each of the n coils. The sensitivity matrix $S_{m,n}$ contains the proportionality factors between current and resulting field at the m positions for all n coils

$$S_{m,n} = \left(\frac{\partial B_m}{\partial I_n}\right)_{m,n}. \tag{7.3}$$

The sensitivity matrix for each of the coils can either be obtained from simulations or by measuring it. When S is known the resulting field for a set of currents can be calculated. On the other hand, the currents to achieve a field $\boldsymbol{B}$ can be determined by solving the system of linear equations for I. For $m = n$ this is a simple matrix inversion. But since this linear system is over-determined ($m > n$), it is solved with a least-squares method that minimized the sum of squared residuals

$$R = \sum_{i=1}^{n} \left(B_i - \sum_{j=1}^{m} S_{i,j} C_j \right)^2. \tag{7.4}$$

The optimal currents to minimize R are obtained by:

$$\boldsymbol{I}_o = (S^T S)^{-1} S^T \boldsymbol{B}. \tag{7.5}$$

S^T is the transposed matrix of S. $(S^T S)^{-1} S^T$ is called the Moore-Penrose Inverse [100], which can be calculated with singular value decomposition for the matrix S [101]. To include an additional, external field the targetfield has to be replaced by $\boldsymbol{B} - \boldsymbol{B}_{ext}$.

The calculation of currents via this method is implemented in a Python script, which reads sensitivity maps from either simulated or measured maps and assembles the sensitivity matrix. The volume of interest is selected with the coordinates of the maps; usually a cylindrical volume in the center of the insert with the dimensions of the nEDM chambers is chosen (cf. the cylindrical shape in figure 7.1(a)). Then, the inverse is calculated, yielding the currents to create the desired field inside this volume.

With simulated sensitivity maps the resulting field with optimized currents is homogeneous on the level of 5×10^{-5}, as can be seen in figure 7.11 for two different planes.

In equation 7.1, a linear dependence of the field on the current is assumed. Since the mumetal of the cylinder is an essential part of the coil system, this assumption does not hold in reality. Furthermore, the coils couple to each other over the magnetization of the mumetal. In simulations, the effect of the non-linearity is strongest for the end coils and results in differences on the order of percent compared to the purely linear case.

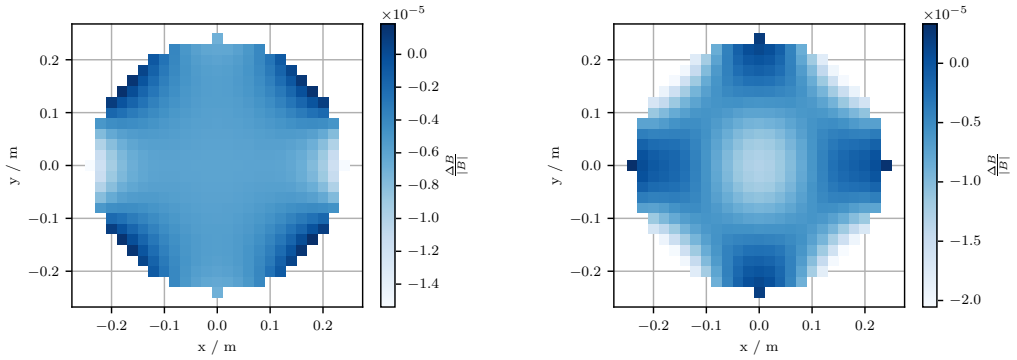

(a) Z = 0 **(b)** Z = -0.2

Figure 7.11: Relative homogeneity in the central plane for optimized currents with simulated sensitivity maps.

To address this non-linearity, an iterative approach is used for the current determination, for simulations as well as for the measurements discussed in chapter 8. A set of currents is supplied to the coils to produce a field close to the targetfield and to magnetize the mumetal. From this configuration, the sensitivity maps for each coil are determined by varying the current through that coil by a small percentage of the set current, in order to change the magnetization of the material only slightly. These maps are then used to calculate changes to the currents with the least-squares approach to make the field more homogeneous.

With the current optimization, geometric imperfections, like a translation or a rotation of the coil, can be compensated. As an example, figure 7.12 shows how a tilt of the cylinder end caps together with the end coils changes the field homogeneity in eight probe points. By adjusting the currents the decrease in homogeneity can be compensated to the level of the non–deformed geometry.

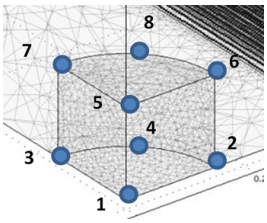

(a) Eight probe points in the volume of interest where the homogeneity is plotted.

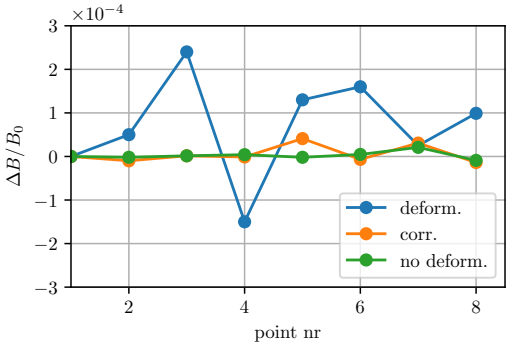

(b) Relative field homogeneity $\Delta B/B_0$ at the eight points.

Figure 7.12: The effect of a geometric deformation of the cylinder end caps. Both ends have been tilted by 1 mm, resulting in the homogeneity labeled “deform.”. With re-calculated currents (labeled “corr.”) the effect can be compensated to almost the same level as without deformation (“no deform.”).

7.3 Current sources

In this section, the current sources used for the coil system will be introduced briefly. A commercially available, modular system is used. For the B_0 main coil, a very high resolution ultra low noise DC voltage source is used[1]. To operate it as a current source, three 100 Ω resistors are connected to the sense input of the source. A second of these sources is available as a backup, and is currently used for the B_x correction with the B_1 coil.

Furthermore, six boards of six independent DC sources with lower resolution[2] are used for the correction and end coils. They can provide up to 200 mA at ±15 V. Four stronger DC current sources with 6 A at ±20 V are used for end coils which need more current[3].

The sources are mounted in a housing that provides the power supply and an interface module for remote control via an ethernet connection.

7.3.1 Field stability

According to its data sheet, the B_0 source is stable on the ppm level in 24 hours. By measuring the current with a high-accuracy multimeter[4] and calculating the Allan standard deviation, this stability could not be confirmed for 24 hours in our setup (cf. figure 7.13), only on shorter time scales of 100 s it has been achieved. For the B_0 coil, a current stability of 10^{-6} corresponds to a field stability of 10 pT.

However, this stability measurement was performed in the insert alone which was not inside the ACS. This means there was no temperature control of the insert or the measurement setup and there was no RF shielding. The field stability is dominated by the fluxgate stability, which is an order of magnitude worse than the current stability. For the measurements of field maps, which take about 30 to 60 minutes per map, the stability is sufficient to reach an accuracy of below 0.1 nT.

7.3.2 B0 value and sources noise

The value of B_0 was chosen so that in a Ramsey measurement, the precession frequencies of the involved species do not fall into a range with major noise sources. For low frequencies, these sources are mainly 50 Hz mains and mechanical vibrations of the mumetal. On the other hand, it is favorable to operate the B_0 main source in the small range up to 1.2 V, because of its higher accuracy in this range. The data presented in figure 7.14 have been recorded with a SQUID system inside the full six layer shield, when the insert was assembled in the MSR at TUM. The vertical bars indicate the Larmor precession frequencies, calculated with the gyromagnetic ratios at a field strength of 1.25 µT. The width of the vertical bars is chosen for visibility, it does not reflect the accuracy of the measured precession frequencies. The situation may be different at the ILL, and this measurement will have to be repeated and the value for the field to be adapted accordingly.

1 BE2100 http://www.bilt-system.com/Pdf/BE2100_brochure.pdf
2 BE584 http://www.bilt-system.com/Pdf/BE584.pdf
3 BE516 http://www.bilt-system.com/Pdf/BE516.pdf
4 Keithley Model 2002 Mulitmeter

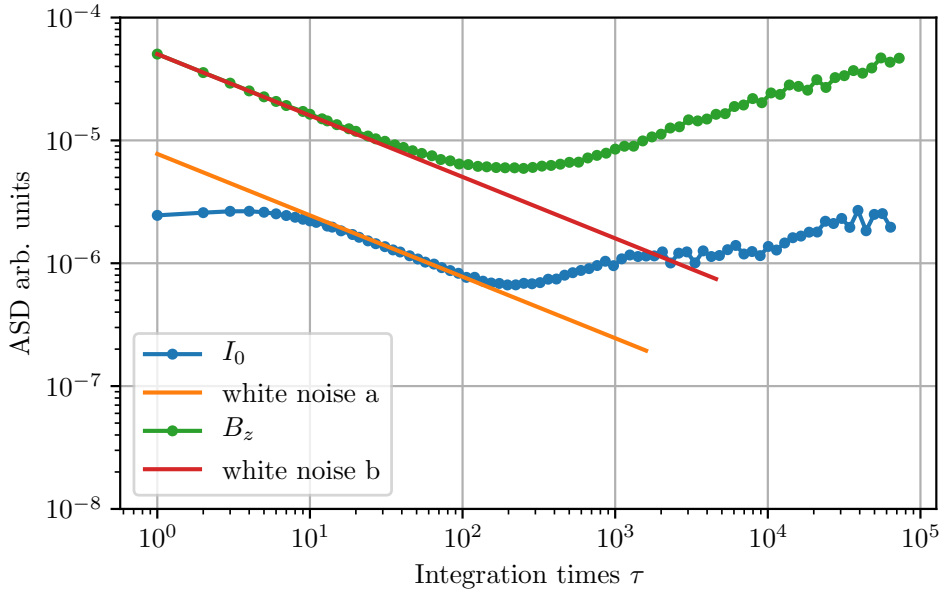

Figure 7.13: Allan standard deviation for relative current and relative field B_z, the main field component in Z direction, containing all sources of noise and drift: sensor, shield and field drifts. White noise a and b show simulated white noise data with a spectral density of $7 \times 10^{-6} 1/\sqrt{Hz}$ and $5 \times 10^{-5} 1/\sqrt{Hz}$, respectively. Note: this data has been recorded in an unstabilized environment.

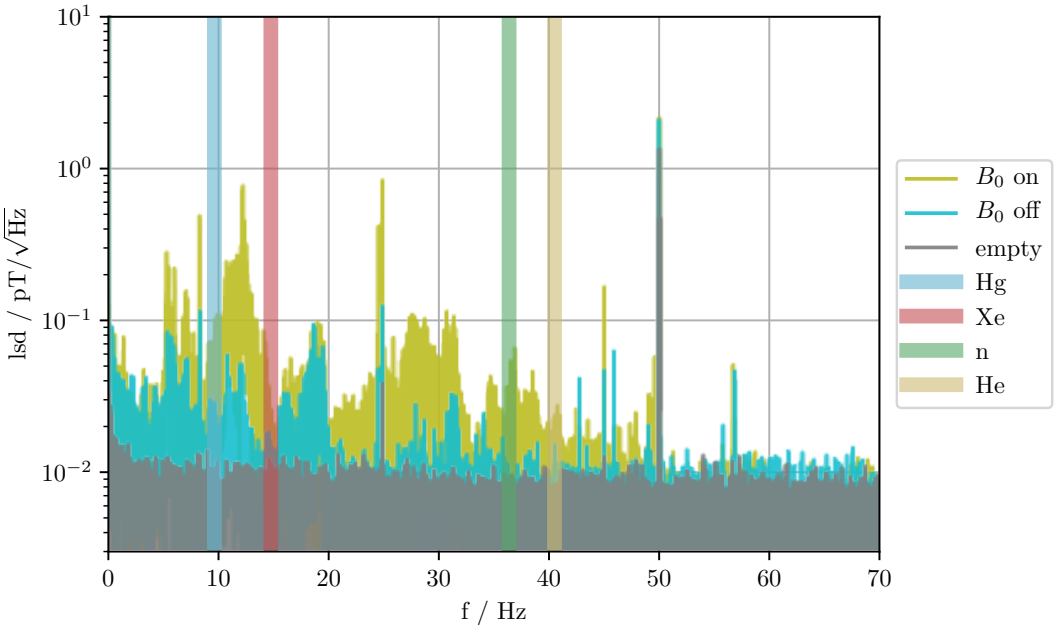

Figure 7.14: Linear spectral density for the B_0 field measured with a SQUID system. The B_0 coil was operated with the B_0 current source, that was switched on and running current, switched off but connected to the coil and an empty measurement as reference. Also shown, the precession frequencies for four different species at a field strength of 1.25 µT. Note that eigenfrequencies are best observed without stabilization of any kind.

8. Field measurements

As has been discussed in the introduction, small field gradients are essential for the next generation of nEDM experiments. Gradients on the level of 0.3 nT/m are necessary to reach an nEDM limit of 10^{-28} ecm. The coil system described in chapter 7 is designed to fulfill these requirements; in this chapter, the measurements to verify the calculated field homogeneity will be described.

Resolving transverse components of 0.1 nT in a field of 1000 nT magnitude is difficult. While resolving 0.1 nT is not a principal problem for magnetic field sensors[1], the angular resolution poses a challenge. Reproducible positioning with an accuracy of 10^{-4} requires effort.

Initially, an automated setup was planned to map the fields inside the cylinder, since repeated, manual mapping of all 44 coils is a very time-consuming task. The main problem with an automated setup is reproducible positioning without angular misalignment. The position of the sensor after the automated movement has to be checked without using any magnetic materials inside the insert in order to not disturb the field quality. The movement itself has to be transfered to the sensor also without magnetic materials. Strings or pieces made from plastic have to be used, but they are soft or can be deformed, which makes accurate positioning difficult.

As an attempt to use gravity to keep the magnetic field sensors aligned in the same direction, a pendulum device was built. A heavy piece of copper hanging in a tripod below the sensor, which was supported only on a small tip to allow swinging, always oriented the sensor along the direction of gravity, independent of the potential unevenness of the supporting floor. However, the positioning on a small tip allows an additional degree of freedom; namely rotation around the gravitational axis. The two transverse components of the field could therefore not be measured independently. Furthermore, movement of the sensor with the heavy piece of copper from outside the closed insert, with sticks and strings, again reduced positioning accuracy.

The setup eventually used to realize the measurement is a mechanically simplified device, with only a small number of components. The fluxgate sensors are aligned to one another in a cuboid holder, which itself is aligned to a base plate. The base plate is placed in a grid of defined positions on a plate, which is mounted to the insert support structure. This setup and its calibration will be described in detail in this chapter. Afterwards, the measurement procedure and current determination for homogeneous fields will be explained and the resulting fields and its consequences for the nEDM measurement will be presented.

8.1 Sensor calibration and orientation

For commercially available three axis fluxgate magnetometers, the orthogonality of the single spatial directions to each other are specified to be better than 0.5°, in some cases

1 even fluxgates reach this level

to about 0.1°. However, these sensors have magnetic parts, like D-Sub connectors in close proximity to the sensor heads. Therefore, they are not suitable for our purpose, and we chose flying lead sensors with three individual sensor heads.

To be able to resolve transverse components of 0.1 nT in a field of 1000 nT, the orthogonality error has to be below 0.1°. So, an appropriate housing and a calibration setup for the fluxgate sensors had to be built.

The sensor housing is shown in figure 8.2. It is a 3D printed structure[1] that houses each sensor in a conically shaped hole with four screws, so that the orientation of the sensor can be adjusted. M4 screws with a pitch of 0.7 mm are used. The angular positioning accuracy of 15° for the screw head means that the 30 mm long sensor heads can be rotated by $< 1 \cdot 10^{-3}$. A rendered image to illustrate how a sensor head is mounted can be seen in figure 8.3.

The calibration setup consists of three square coils to produce fields that are orthogonal to each other. The coil geometry, the influence of the mounting accuracy, and for example of bending of the copper tubes on the angle of the field with respect to the axis of the loop, was investigated by numerically solving Biot-Savart's law:

$$\mathrm{d}\boldsymbol{B}(\boldsymbol{r}) = \frac{\mu_0}{4\pi} I \mathrm{d}\boldsymbol{l} \times \frac{\boldsymbol{r} - \boldsymbol{r\prime}}{|\boldsymbol{r} - \boldsymbol{r\prime}|^3} \tag{8.1}$$

for the coil geometry. Each of the coils has only a single loop made from copper tubes,

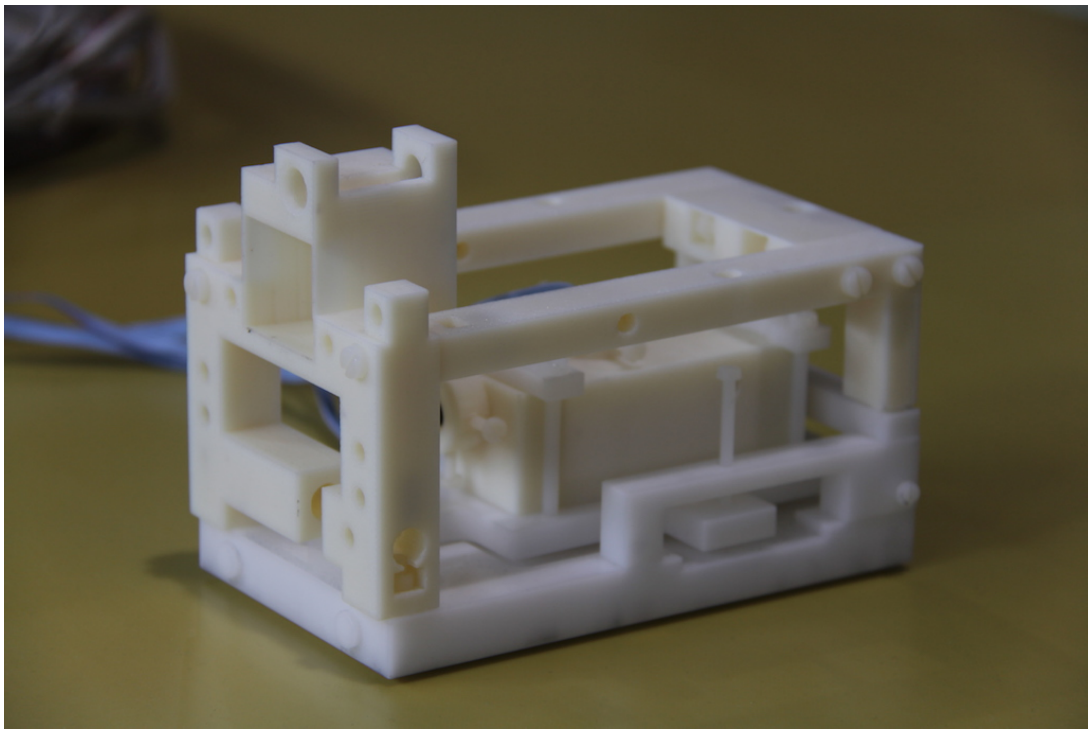

Figure 8.1: Photograph of the fluxgate holder in which the sensors are aligned and the base plate on which the whole sensor arrangement is aligned.

1 on a Stratasys Dimension Elite

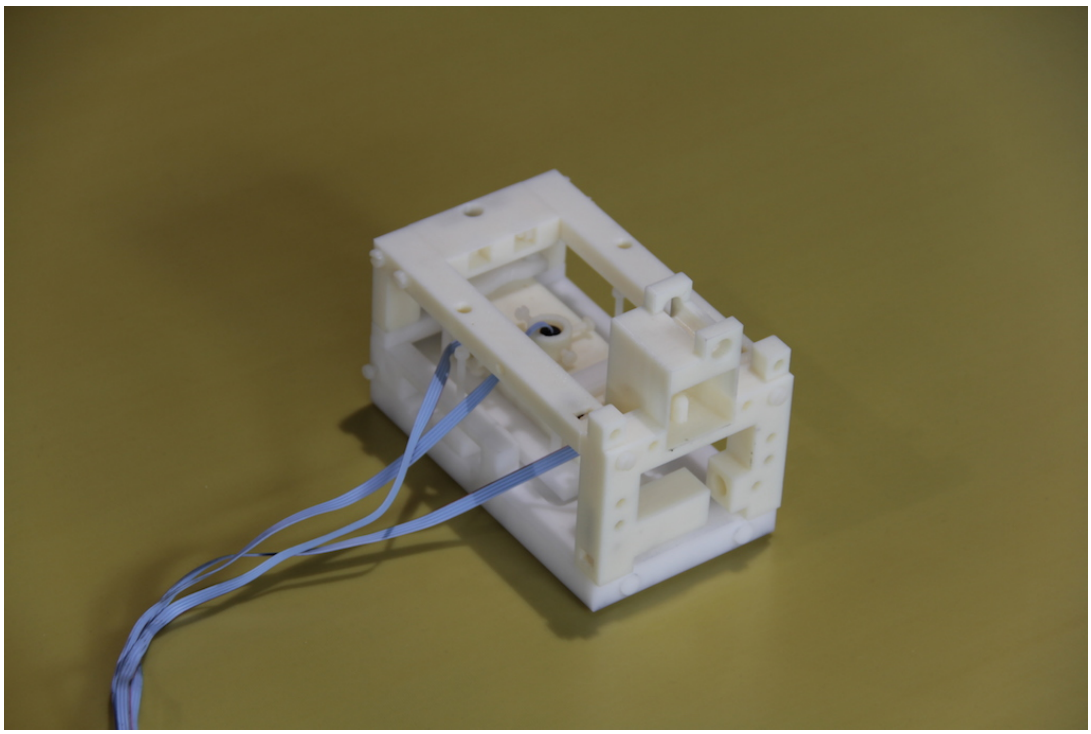

Figure 8.2: Photograph of the fluxgate holder where the screws to align the sensor head for the Z direction can be seen.

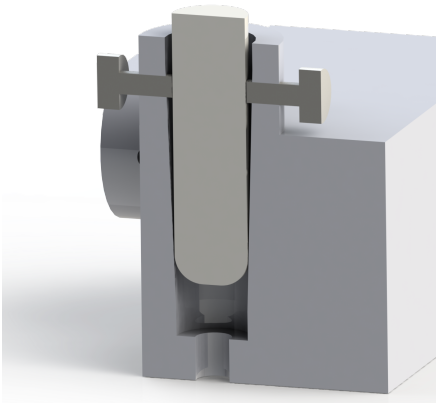

Figure 8.3: Schematic render image showing a cut-away view of one of the conical holes in which the fluxgate sensor head is positioned. Four screws are used to align the sensor the field.

so that the winding of wires does not reduce the accuracy of the coil geometry and change the field distribution. This loop is mounted on a frame made from aluminum. With a side length of $a = 2.34\,\mathrm{m}$ and a construction accuracy of 1 mm, the field produced by these coils has an angle of $< 0.1°$ with the coil axis in the central volume of $50 \times 50 \times 50\,\mathrm{mm}^3$. The calculated field direction with respect to the coil axis is shown in figure 8.4

The volume with the required accuracy had to be big enough so that the exact position of the sensor in this volume is not important. Unreproducible positioning is a source of error for this measurement. The sensor heads are placed into the center of the coil system by mounting the sensor holder onto a 2.5 m long rod, whose ends were fixed with an accuracy of 1 mm. To prevent bending of the rod, a support table was setup in the center of the coils. This way, the sensor holder could be moved along the rod direction without changing the angular orientation of the sensor heads.

To avoid external disturbances (like the earth magnetic field) and the need for accurate offset calibration, alternating magnetic fields were used for the calibration measurement. For this, the coils were driven with currents with a different frequency and the fluxgate sensor was read out with two Lock-In amplifiers synchronized to these frequencies. Low frequencies had the advantage that inductive effects are very small. Frequencies of $f_1 = 21\,\mathrm{Hz}$ and $f_2 = 37\,\mathrm{Hz}$ were used.

The procedure to orient each sensor was the following. Magnetic fields were produced by two coils in two orthogonal directions. A sensor head was aligned along the third spatial direction so that it measured neither of the two fields. By cyclic rotation of sensor heads and fields, the three sensor heads could be aligned perpendicular to each

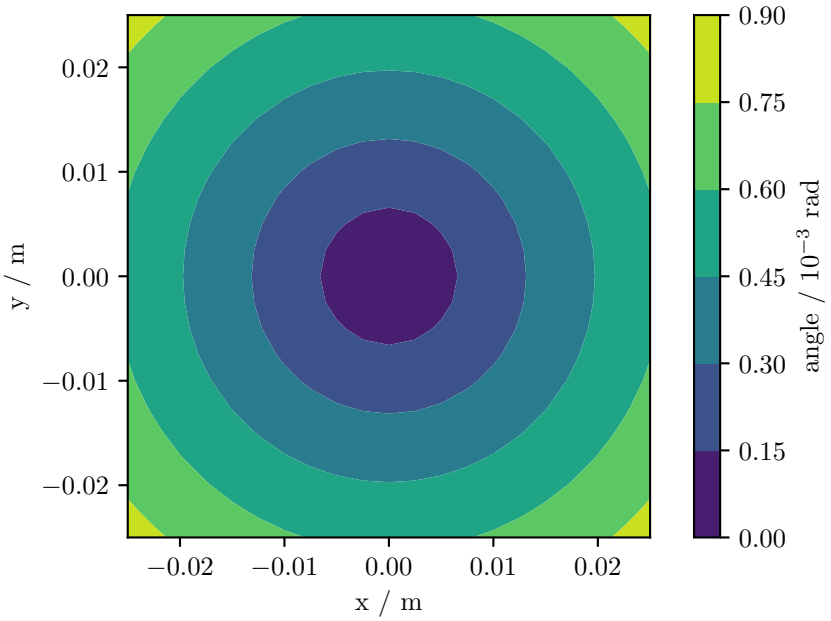

Figure 8.4: Calculated angle of the field with the coil axis at a height of 2.5 cm above the plane of the coil. The field is produced by a single square loop of wires with a side length of $a = 2.34\,\mathrm{m}$.

other. If the coils were set up perpendicular to each other. This method is preferable over directly aligning a sensor along one field direction because the angular dependence is suppressed for the cosine function for small angles. Ideally, the sensor measures a value of zero when it is perfectly aligned perpendicular to both fields. Achieving exactly zero was not possible. However, to keep the angular misalignment below $< 1 \cdot 10^{-3}$, the measured value only had to be below 1/1000 of the maximum amplitude of the field in this direction.

A minor problem with the field production were disturbances from the environment. At first, the coils were setup in the lab of our building. Even though alternating fields were used, magnetizable material in close proximity to the coils system had noticable influence on the reading from the sensors. Heating pipes in the walls or a movable 19 inch rack with computer hardware completely altered the measurement results. Therefore, the setup was moved to the outside of the building, and the measurements were done in the backyard on a lawn, where no other equipment was in close proximity to the setup. Setting up the coils inside the outer MSR was not an option, because the mumetal strongly influences the field distribution.

The calibration result is shown in table 8.1. All fluxgate sensors readings were below 1/1000 of the maximum amplitude of the corresponding field.

With this calibration procedure, the orientation of the sensor heads relative to each other has been adjusted. For the alignment of this fixed system with respect to a reference plane, the fluxgate holder was mounted to another structure, which allows rotating the entire sensor head arrangement. The holding structure has a 130 mm×80 mm plastic base plate, shown in figure 8.2. Like above, four screws can be used to adjust the orientation of the holder with respect to the base plate. This

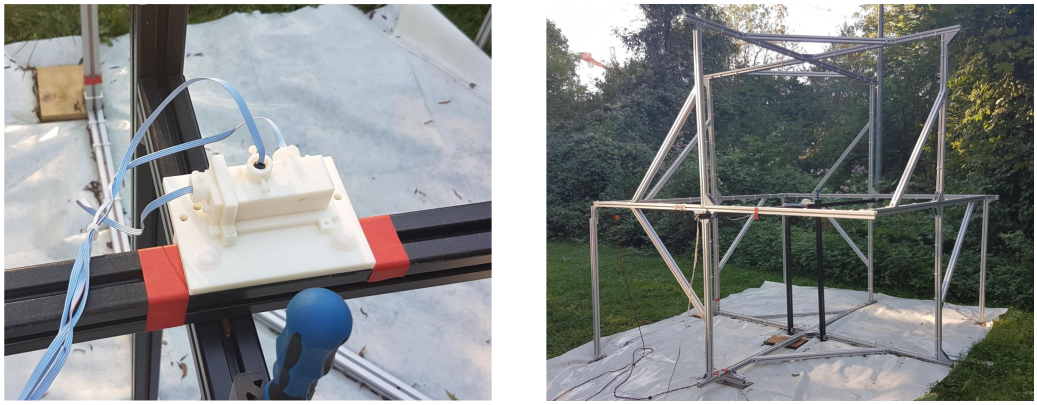

(a) Sensor holder mounted on the rod. **(b)** Three square calibration coils.

Figure 8.5: Photographs of the calibration setup in a disturbance free environment.

Table 8.1

Amplifier	Amplifier voltage/mV	Maximum FG signal / mV	Calibration threshold / mV	Calibrated signal / mV		
				x sens	y sens	z sens
TOE	600	51.81	0.051	0.027	0.050	0.020
Kepco	4500	308.41	0.308	0.090	0.030	0.090

orientation procedure was done in a similar way as for the sensor heads, with the same setup. On the bottom of the base plate, two pins allow positioning it on an aluminium plate on which the holder was moved for field mapping (cf. figure 8.7). Orientation of the aluminum plate inside the insert was achieved by adjusting the height of the plate with respect to the insert GFRP structure, at four positions where the screw heads are visible in figure 8.7.

Tests were conducted to check for and rule out cross talk between the sensor excitation field with a frequency of about 15 kHz and the conducting aluminum plate in its direct vicinity. Eddy currents in the material might change the field reading from the sensor. A simple test was performed in the MSR with an applied field of about 1.3 µT, which is in the order of the B_0 field strength. The sensor was fixed to a table and field measurements with a piece of aluminum (thickness 0.7 mm) in 2 cm distance to the sensor were compared to measurements without the piece of aluminum. With a resolution of 0.1 nT, no difference could be measured between the two cases. The distance between the sensor heads and the aluminum in the actual B_0 measurement is 4 cm because of the additional positioning structure.

An unevenness in the plate surface can cause the sensor to change its alignment with respect to the field when the sensor is moved. Aluminum was chosen as the material for the plate because it can be machined to a much higher precision than plastic; the machining precision for milled aluminum from the TUM workshop is on the order of 0.1 mm.

The evenness of the plate has been measured on a 3D coordinate-measuring machine[1]; the data is shown in figure 8.6. For this measurement, the plate was supported on the same four points it sits on in the insert. The evenness of the plate was measured in a 25 mm grid, with 896 points in total. In the central area, the maximum difference in height is 0.15 mm. A worst case estimation of the sensor tilt due to that yields a value of 1.5×10^{-3}. Since the holder plate has dimensions of 130 mm×80 mm and covers many of the grid points, variations of the height on smaller scales are averaged out and the resulting tilt is smaller than that worst case scenario.

The angular reproducibility with which the sensor holder could be positioned on the aluminum plate was determined by shining a laser pointer onto a mirror mounted to the holder, and measuring the displacement of the laser point on a paper screen. The distance between the mirror and the paper was 3.99 m, and the spread of 10 points on the paper screen after removing the sensor holder from its position on the aluminum plate and putting it back there, was 3.5 mm×2.5 mm. This corresponds to a angular reproducibility of the holder position of about 3×10^{-4}.

1 Wenzl LH1200

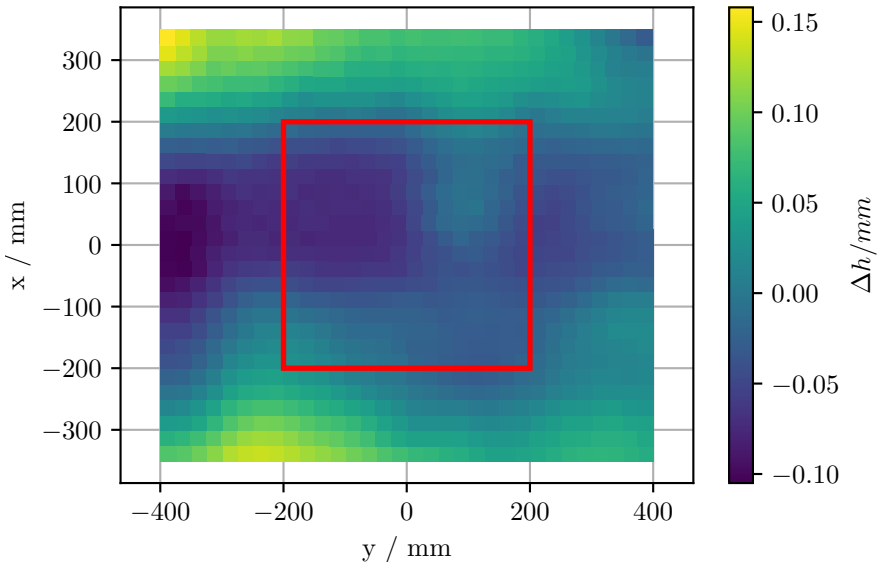

Figure 8.6: Plot of the evenness of the aluminum plate. The variation of the height with respect to a reference plane is measured. The red frame indicates the central $0.4\,\mathrm{m} \times 0.4\,\mathrm{m}$ area in which field maps are recorded.

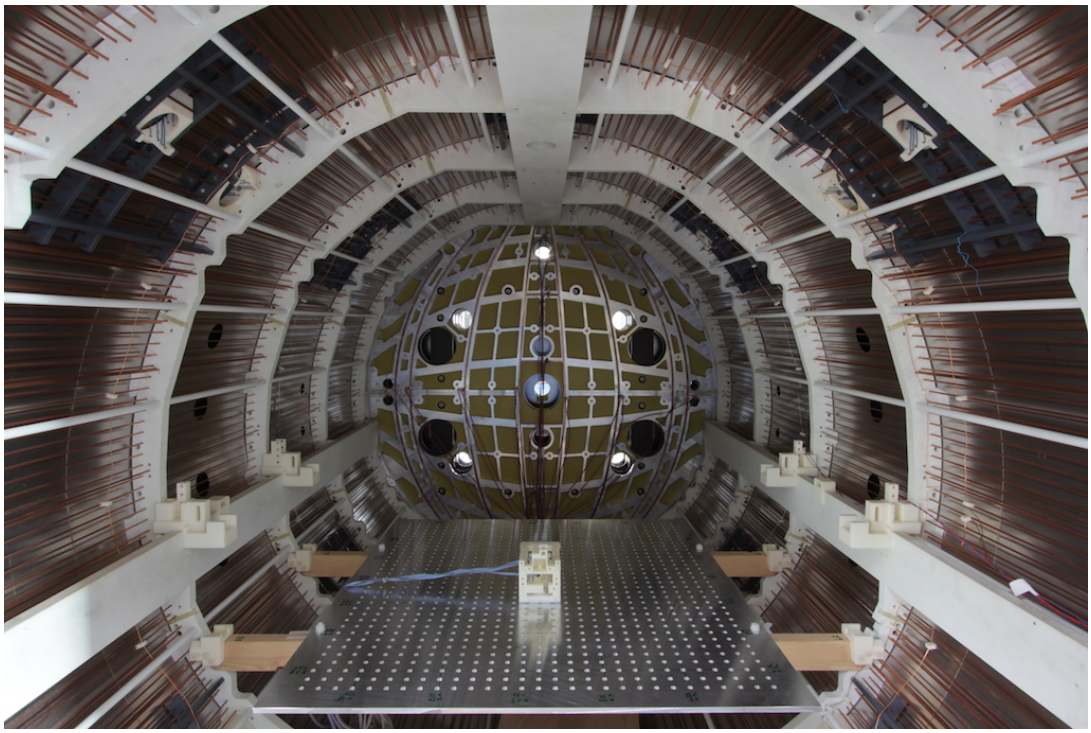

Figure 8.7: Photograph of the mapping setup inside the insert. The aluminum plate with the hole pattern allows positioning of the sensor holder over an area of $0.8\,\mathrm{m} \times 0.6\,\mathrm{m}$. In the photograph, the plate is in the lower plane at $Z = 0.24\,\mathrm{m}$. The plastic mounts for the central plane at $Z = 0$ can also be seen. The mounts for the upper plane are not included. The sensor sits in the central position at $X = 0$ and $Y = 0$.

8.2 Measurement of field maps

With the calibrated sensor in its holder, magnetic fields maps were measured inside the insert. The plate was mounted in the central plane of the insert at $Z = 0$. The insert was closed and pressure applied to the door mechanism. The shield was equilibrated without any applied currents, in order to calibrate the fluxgate offsets in the small residual field. After the currents for the desired coil configuration were set, the whole shield was magnetically equilibrated again. As a compromise between spatial resolution and duration of the measurement, field maps were usually recorded in a five by five grid around the center of the insert. The points were 100 mm apart in each direction. At each point, one data point was saved, for which the fluxgate readout was averaged over one second.

8.3 Coil system corrections

One result of the measurements was that the field of the B_0 coil behaved differently than was expected from Comsol simulations. Two major deviations can be made out in the following pictures. First, there is an excess B_x component. From simulations, B_x was expected to be symmetrical around 0 nT with a gradient of about 3 nT for 20 mA current. The measured B_x component was offset by about 11 nT with a gradient of approximately 5 nT. The B_y components were shifted also. Here, the measured gradients were on the order of 3 nT with an offset of about 5 nT. An explanation for the unexpected B_x fields was found in further FEM simulations, where the influence of the μ value on field homogeneity was investigated.

8.3.1 Influence of the permeability on the field distribution

A simple 2D simulation was setup to study how varying μ values along the cylinder circumference influence the field distribution of the B_0 coil. For that, the thickness of the mumetal was increased by a factor of 10, and the value of μ itself was decreased by a factor of 10. In this way, the number of mesh elements in the FEM simulation could be reduced, which decreased computation times. The cylinder was segmented into 12 pieces of 30°, each of which could be assigned a μ value. The geometry of the B_0 coil corresponded to the real one. In figure 8.8, the strongly exaggerated effect of varying μ values can be seen. The segments colored in blue have a permeability of $\mu_r = 2500$, in the red and green segments the μ_r value is increased and decreased by a factor of ten, respectively, to illustrate the effect. The plotted field lines bend strongly towards the segments with higher μ_r and introduce transverse field components.

In figure 8.9, more realistic μ_r variations were set for the segments, to investigate which ratio produces the measured B_x components. By setting values of $\mu_1 = 2200$ and $\mu_2 = 2600$ for the segments, the measured B_x gradient could be reproduced. A variation of approximately 10% is sufficient for the B_x gradients. These changes also seem plausible for the manufactured cylinder, since mumetal is highly optimized for very high permeabilities, and requires very sensitive handling to maintain this quality.

The main coil of the B_1 system is used to compensate the offset in the B_x component of the B_0 coil. For the gradients, the eF and correction coils are used (cf. chapter 7).

8.3.2 Correction of the B_y component

To address the additional B_y components, a Helmholtz coil pair was added to the cylinder in the insert. A compensation of the B_y field with the end coils alone was not

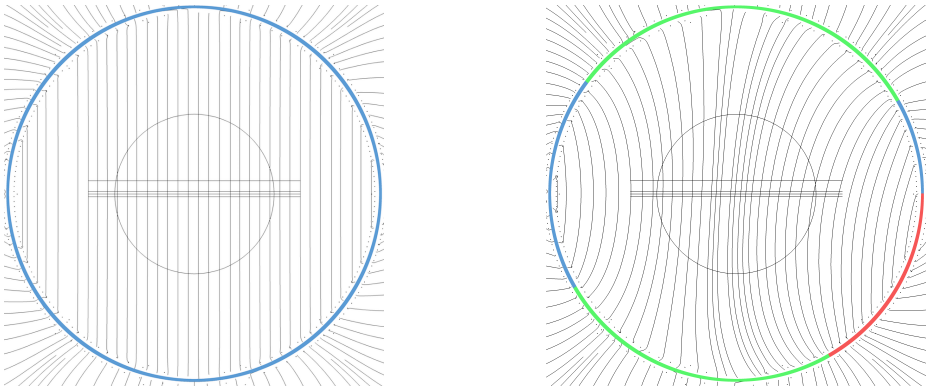

(a) Homogeneous μ.

(b) Variation of μ.

Figure 8.8: Effect of varying μ on the magnetic field produced by the B0 coil. The colors indicate the values of μ: blue: 2500, green: 250, red: 25000. For the picture the variation in μ has been greatly exaggerated to be able to show the effect in the field lines.

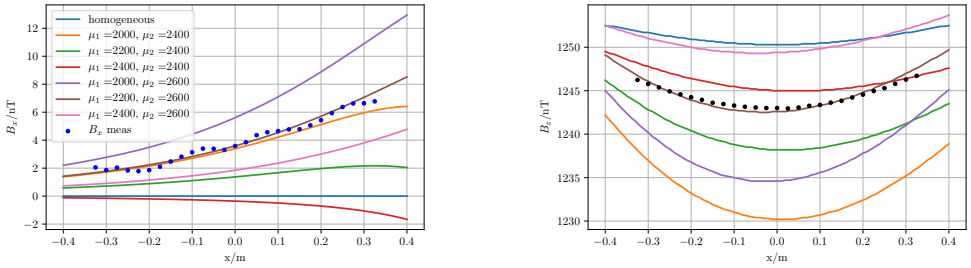

(a) B_x vs. the X coordinate along a line at $Y = 0$.

(b) B_z vs. the X coordinate along a line at $Y = 0$.

Figure 8.9: 2D simulations to investigate the influence of a μ variation on B_x and B_z components.

possible, because this would have created additional B_x components. A Helmholtz pair was simulated to determine the required accuracy and to investigate the field distortion due to the mumetal. The simulations showed that an accuracy of 1 cm was necessary, which allows for simple manufacturing. For each coil, a single wire was fixed onto one of the GFRP support structures.

With different currents in the two coils, the gradient in B_y can be compensated. In figure 8.10, the measured data along a line at $X = 0$ and $Z = 0$ is compared to the field calculated for the Helmholtz pair for different ratios of the current in the two coils. By reducing the current in one coil by 35% and increasing the other by 35% the slope of the measured data can be reproduced, starting from 2.5 mA to create approximately 5.8 nT. The current for the actual B_0 configuration will be slightly different because other coils also contribute B_y components.

8.3.3 Additional single wires in Z direction

Furthermore, the addition of two more wires became necessary to compensate local field disturbances on the -X side of the insert. The origin of these spots is not fully clear yet, but with two wires that are fed through four holes on the side of the insert, and

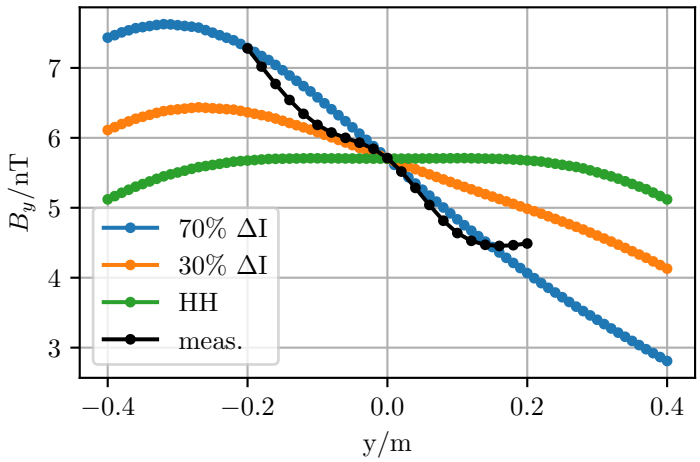

Figure 8.10: Field calculated for a pair of Helmholtz coils, with different currents in each coils and the measured B_y component along a line at $X = 0$ and $Z = 0$

run vertically on the inside, a field can be created to compensate these disturbances. They are called zWF and zWB for “front” and “back”.

8.4 Current calculation with measured sensitivity maps

The procedure to measure the sensitivity maps followed the one outlined in section 7.2. The starting point currents were set and the whole shield was magnetically equilibrated to adjust the material to the prevailing field conditions. At each position and for each coil, the current was ramped in ten steps and the field was recorded for each current step. The steps were chosen for each coil, such that they are small in comparison to the starting value. If the field changes produced by these current steps were too small to resolve the changes with the fluxgate, bigger steps were chosen. In any case, the cylindrical shield was equilibrated after each current change. The slope of the field-current dependence was used as the sensitivity for this measurement point.

To perform the least–squares calculation to optimize the currents, the sensitivity maps measured at 25 points were interpolated to a finer grid with 21×21 points. With these sensitivity maps, a set of currents could be determined that had to be added to an existing current configuration in order to achieve the targeted, homogeneous field. In figure 8.11, magnetic field maps for the different stages are shown. In a) the measured field maps for the B_0 main coil is shown. In order to get a homogeneous field, the field shown in b) has to be added to a). The least-squares method calculates a set of currents which produces the field shown in c) so that the resulting sum is homogeneous, as shown in d). The currents have been changed according to the least-squares result, and the field has been measured again, with the result shown in e).

A comparison between the predicted field and the measured field for this current set is shown in figure 8.12; it is obvious that the results are very different. One reason for that is that the resulting currents were quite large for all the coils. The homogeneous field was then obtained by strong fields that have to cancel each other to almost zero in the transverse components, which was not a viable solution. Another reason was that the fields from the individual coils could not be added linearly, because they all

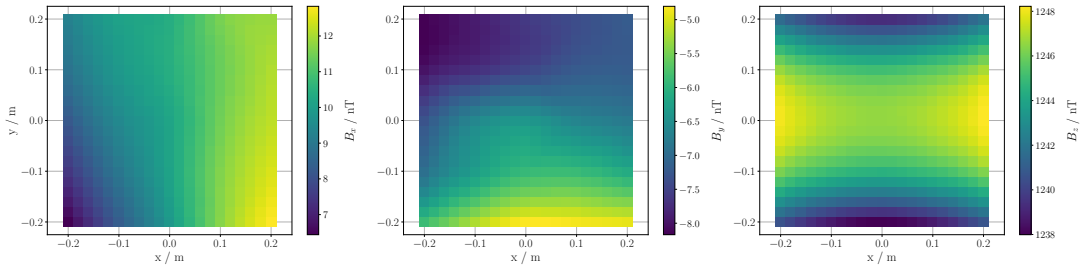

(a) Measured map of the B_0 main coil that has been used as the B_{ext} for the current calculation.

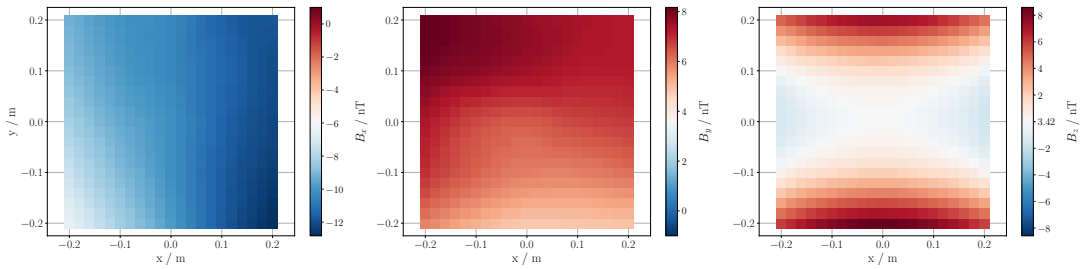

(b) Needed addition to get a homogeneous resulting field.

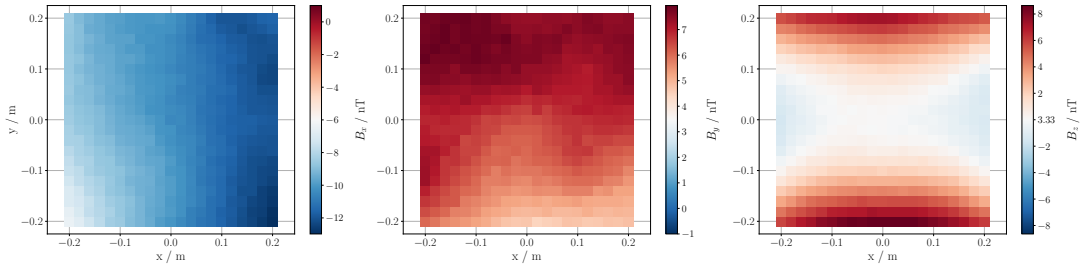

(c) Calculated addition achieved with the optimized current set.

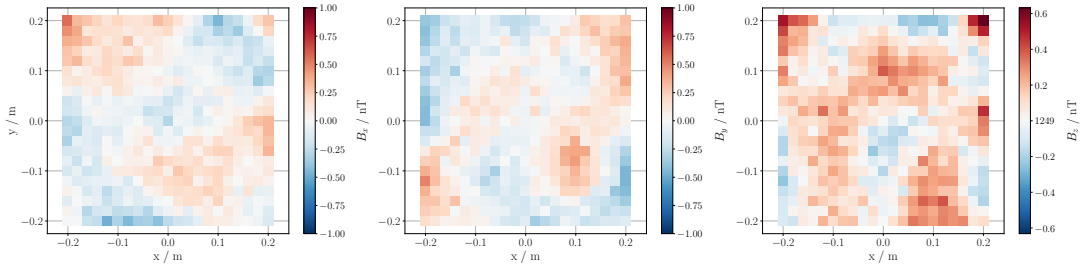

(d) Calculated resulting homogeneous field.

Figure 8.11: Current calculation to improve the field homogeneity, starting from a measured map of the B_0 main coil.

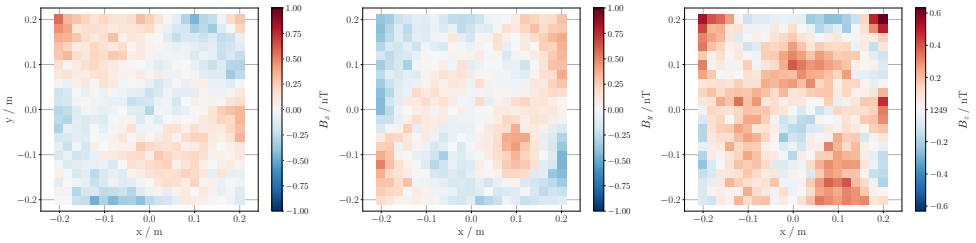

(a) Calculated resulting homogeneous field.

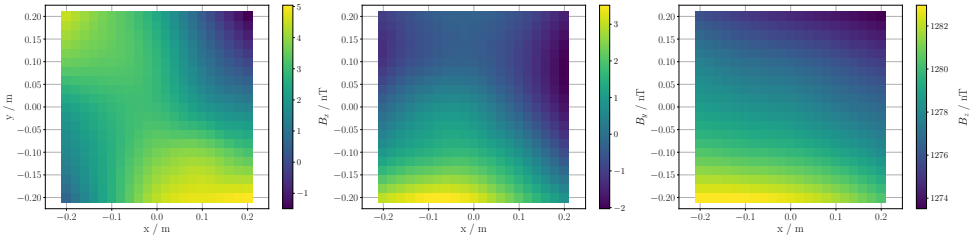

(b) Measured resulting field.

Figure 8.12: Difference between CCO result and measured map for CCO currents.

changed the magnetization state of the mumetal and in that way influenced each other more strongly. This also leads to a coupled system if one coil changes the magnetization state of the mumetal which in turn influences the sensitivity of other coils.

8.5 Iterative current determination

To achieve homogeneous field despite the above, the currents were adjusted manually. This was an iterative process, which also resulted in the previously mentioned changes of the coil system and the addition of more coils to the cylinder, because the available coils were not able to produce the necessary field components.

In order to determine which coil has the biggest influence of the field homogeneity, the measured sensitivity maps were used. The currents were estimated by adding the sensitivity maps scaled with currents in order to improve the field. The currents were set and a field map recorded. First, the four e1 coils were added to reduce the B_z gradients, cf. figure 8.13(b). Their B_x and B_y components then had to be compensated with the other coils. The eF coil produces B_x fields in the corners at -Y, and adds a B_y gradient (figure 8.13(c)). The addition of the B_1 coil reduced the strong B_x component (figure 8.13(d)). With the added Helmholtz coils the B_y components in the field could be reduced (figure 8.14(a)). The four correction coils c4 reduced the gradient in the B_x component (figure 8.14(b)). And finally, the zW wires addressed spots at the -X side. From this stage, the currents were then again adjusted slightly to produce the final field result. The resulting currents that have been used for the B_0 maps are listed in table 8.2. This procedure is still not optimal, and further improvement will be necessary. Only 15 of the available 44 coils have been used so far. With the addition of more coils, it will be possible to improve the field homogeneity further. However, for all coils a more analytical approach to determine the currents will be needed.

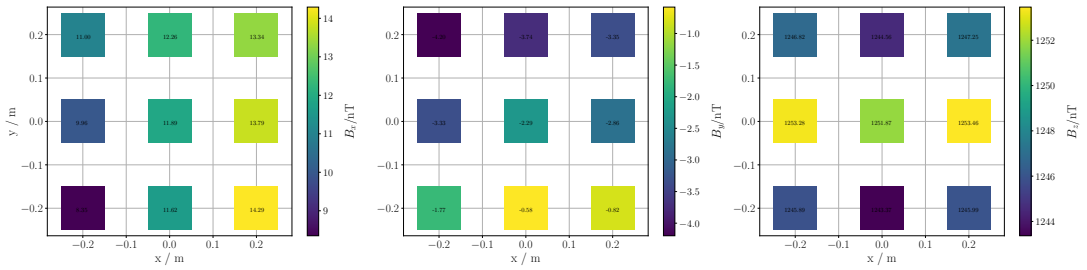

(a) B_0 main coil

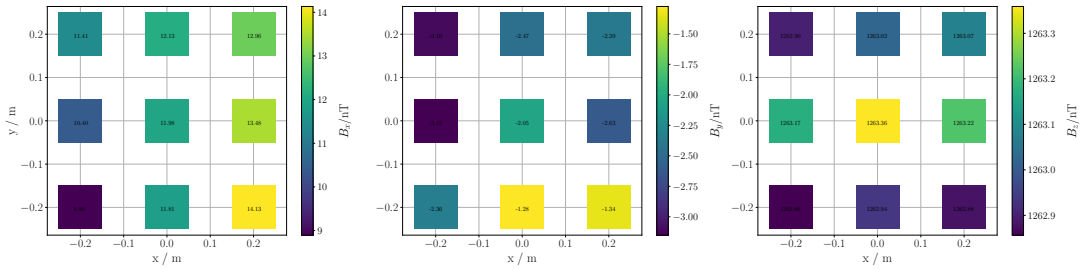

(b) B_0 main coil + e1

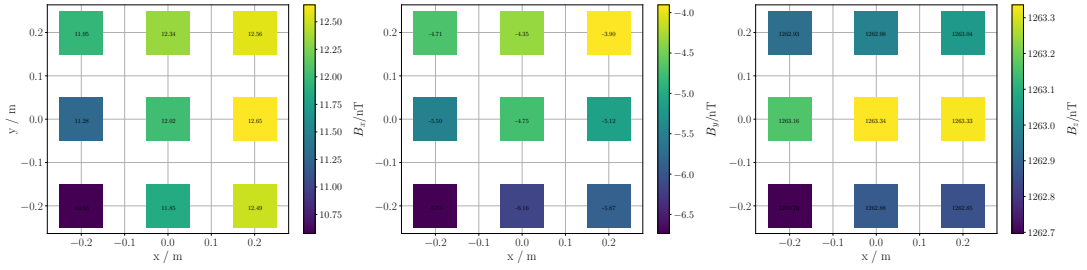

(c) B_0 main coil + e1 + eF

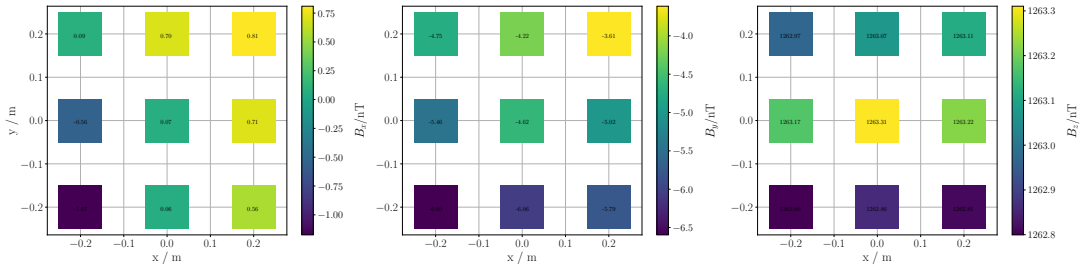

(d) B_0 main coil + e1 + eF + B_1

Figure 8.13: Stages of the iterative current setting procedure. The graphs show how the addition of the individual coils changes the field distributions.

Table 8.2: Resulting current settings for the homogeneous B_0 field. The currents for the B_0 and B_1 coil are calculated from the source settings and the value of the shunt resistor.

Coil	Current/mA	Coil	Current/mA	Coil	Current/mA
B_0	19.46	eF	-20.0	cTR4	1.7
eTF1	16.5	B1	-0.25	cBL4	-1.7
eTB1	16.5	HH1	3.7	cBR4	-1.7
eBF1	17.0	HH2	1.3	zWF	-1.5
eBB1	16.5	cTL4	1.7	zWB	-1.5

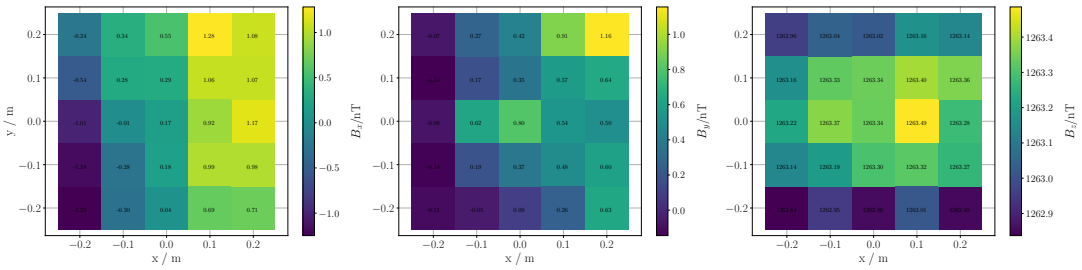

(a) B_0 main coil + e1 + eF + B_1 + HH

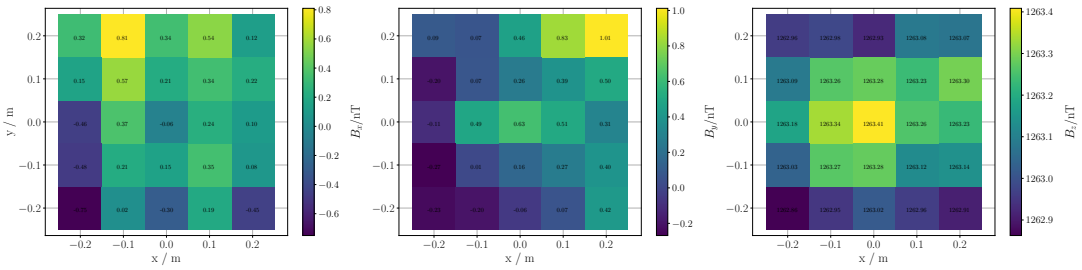

(b) B_0 main coil + e1 + eF + B_1 main coil + HH + c4

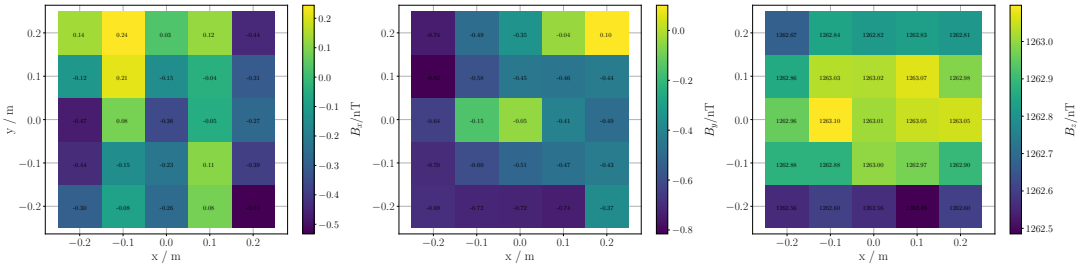

(c) B_0 main coil + e1 + eF + B_1 main coil + HH + c4 + zW

Figure 8.14: Stages of the iterative current setting procedure.

8.6 Resulting field

The resulting field in the central plane with the determined currents settings is shown in figure 8.15. B_x and B_y components are well below 1 nT and the range of the B_z components is below 0.6 nT. For the lower plane at $Z = -0.24$ m, the field result is presented in figure 8.16.

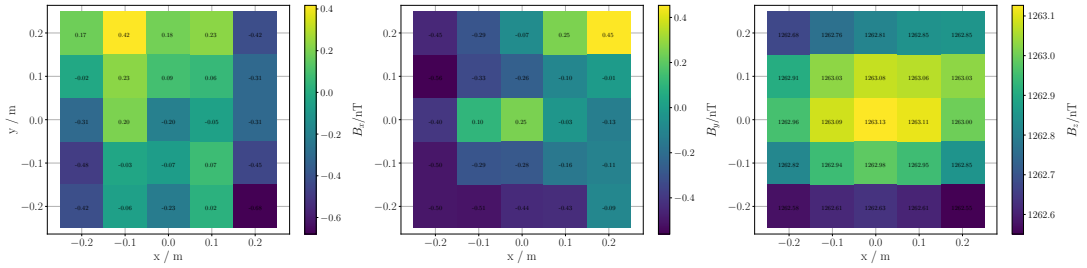

Figure 8.15: Measured map of the B_0 field components in the $Z = 0$ plane.

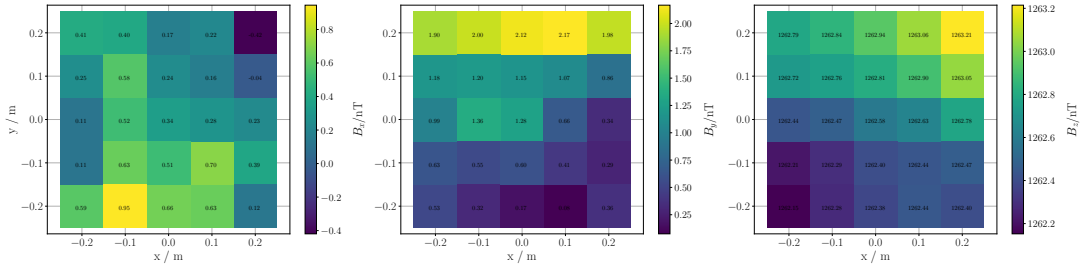

Figure 8.16: Measured map of the B_0 field components in the $Z = -0.24$ m plane.

The B_x components are increased by about 0.2 nT compared to the central plane. The B_y components show an even stronger increase, from 0.9 nT to 1.9 nT. A different structure as expected from simulations appears in the B_z component (cf. figure 7.5(b)). A more analytical approach to current optimization may be needed to address this issue with the use of additional end coils.

The achieved homogeneities for the magnetic flux density expressed as the relative difference to the central point are shown in figure 8.17, they are 4.6 $\times 10^{-4}$ for the central plane, and 7.7 $\times 10^{-4}$ over all. The neutron chambers in the nEDM experiment have a height of 10 cm. The field for the volume of the lower EDM chamber can be estimated by interpolation, yielding a homogeneity for the magnetic field for the lower nEDM cell of better than 5.0×10^{-4}.

From the measured B_z components, the worst gradient $\partial B_z/\partial z$ can be estimated. The Z dependence of the simulated field for the B_0 coil suggests a quadratic dependence. Quadratic interpolation between the measured planes results in a gradient over the 10 cm cell height of ≈ 1.25 nT/m. According to equation 1.18, this produces a false nEDM signal for the neutrons due to geometric phases of

$$d_{false}^{GP} \approx 5 \times 10^{-28} \text{ ecm}. \tag{8.2}$$

This is small enough for the first stage of the PanEDM experiment at the ILL with a goal of $d_n \approx 3 \times 10^{-27}$ ecm. For the next stage, where $d_n = 7 \times 10^{-28}$ ecm are targeted, the field homogeneity will have to be improved further by using more coils.

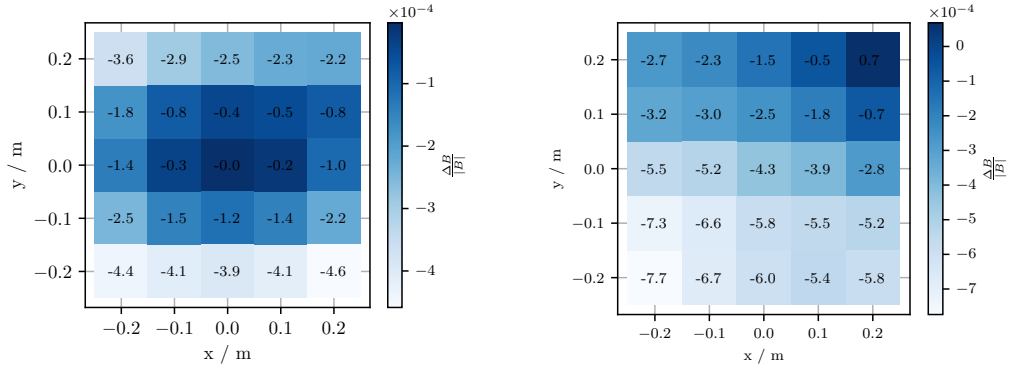

(a) Central plane at $Z = 0$ **(b)** Lower plane at $Z = -0.24\,\mathrm{m}$

Figure 8.17: Homogeneity of the magnetic flux density with respect to the center on the $Z = 0$ plane.

The alignment calibration of the sensors resulted in angles smaller than 1×10^{-3}, due to the construction of the calibration coils. So in principle, a global angle on the order of 1×10^{-3} cannot be excluded. This angle between $\boldsymbol{E}$ and $\boldsymbol{B}$ would create an additional $\boldsymbol{v} \times \boldsymbol{E}$ component parallel to B_0 (cf. figure 8.18). UCNs moving in the cell would experience this as an oscillating field in Z direction, producing a phase error but no EDM signal. A global angle of the magnetic field can be corrected for by re-aligning the $\boldsymbol{E}$ and $\boldsymbol{B}$ fields, either mechanically or by adding a homogeneous transverse component to the B_0 field. The current determination and the map measurements have shown that these components can be produced.

The observed offsets in the B_x and B_y components of the B_0 coil were on the order of 10^{-2} and not due angular misalignment. A strong misalignment like that would have been observable in the maps of the other coils as well.

Magnetic field gradient drifts over time scales of the duration of a Ramsey measurement (250 s) can be estimated from sensitivity maps in different planes. For example, the B_0 coil on its own produces a gradient $\partial B_z/\partial z \approx 1.25\,\mathrm{nT/m}$ over the height of a nEDM chamber at a current of 20 mA (cf. figure 7.5). The stability of the B_0 source is $\approx 10^{-6}$, which results in gradient change of $\approx 1.3\,\mathrm{fT/m}$. The stability of the sources for the correction and end coils has not been measured yet and is estimated from the setting resolution. For a DC source, the setting resolution also can be used to estimate the stability limit.

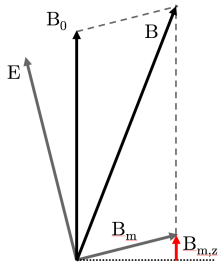

Figure 8.18: Sketch illustrating how an angle between $\boldsymbol{E}$ and $\boldsymbol{B}$ contributes to B_0. The motional magnetic field $B_m = \frac{\boldsymbol{v} \times \boldsymbol{E}}{c^2}$ has a component parallel to B_0 of $B_{m,z}$.

Another source of field drifts is the temperature dependence of the μ value for mumetal. An estimation for the relative linearized μ variation is 1%/°C[62]. Figure 8.9 shows an approximate $\Delta B = 5\,\mathrm{nT}$ for a 10 % variation of μ, yielding

$$\frac{\Delta B}{\Delta T} = 4 \times 10^{-4}\,\%/\mathrm{K} \tag{8.3}$$

With the temperature drift of 14 mK in one hour as measured in [38] follows a temperature dependent drift on the order of $6 \times 10^{-6}\ \mathrm{h}^{-1}$

Table 8.3: Gradient drift estimation for the main contributions to B_z.

Coil	gradient nT/m	source stability	gradient change fT/m
B_0	1.25	10^{-6}	1.3 fT/m
c*	0.5	10^{-5}	5 fT/m
e*	0.076	10^{-4}	8 fT/m

The magnetic field has been optimized with only 15 of the 44 available coils. By keeping the number of used coils small, the influence of disturbances and drifts from the individual current sources with respect to each other can be reduced. Measurements of the magnetic field produced by this coil system showed, that the field fulfills the requirements for the first stage of the nEDM experiment at the ILL, systematic effects due to geometric phases for neutrons are small enough to reach the goal of $d_n \approx 3 \times 10^{-27}$ ecm. For the next stage, additional coils can be added to improve the homogeneity further. In order to determine the currents in more than 15 coils, a more analytical approach may be needed.

9. Conclusion

The goal of this thesis was to provide the magnetic environment to improve the current limit for the neutron electric dipole moment (nEDM) $d_n = 3 \times 10^{-26}$ ecm. A two orders of magnitude improvement requires, besides a neutron density of $\geq 10^2$ UCN/cm^3 in the cell volume to achieve reasonable measurement times, also magnetic fields with gradients less than 0.3 nT/m and a temporal stability of the gradients of a few $10\,\mathrm{fT\,m^{-1}\,s^{-1}}$.

The magnetically shielded environment for the TUM nEDM experiment (PanEDM) consists of two passive magnetically shielded rooms (MSRs), which provide a stable low-field environment as an essential ingredient for an nEDM measurement. Magnetic equilibration ensures stable and reliable low field conditions in the operation of these MSRs. The automated equilibration setup has been built and integrated into the nEDM experimental control system.

Furthermore, tools have been developed to study and investigate magnetic equilibration numerically. With simplified simulations without time-dependence, the MSR geometry and material can be investigated, which for example led to an improved coil configuration. With this coil configuration, equilibration times can be reduced by a factor of two or larger, to directly reduce the preparation times for individual Ramsey measurements, which impacts the statistical sensitivity of the nEDM experiment. These static simulations also have been utilized to design and improve a variety of other magnetic shields. With the optimized equilibration procedure, the lowest residual field so far of $|B| = (150 \pm 25)\,\mathrm{pT}$ in the central plane over an area of $120 \times 40\,\mathrm{cm^2}$ has been achieved in the insert.

Equilibration parameters, like frequency, amplitude or duration, are usually determined from trial and error and previous experience. For a more systematic approach, time-dependent simulations including the hysteretic behavior of the shielding material are needed. If the hysteretic behavior can be modeled in simulations for the whole MSR geometry, the residual field inside the MSR can be calculated and its dependence on the equilibration parameters can be studied. For this, the well-established Jiles-Atherton model of hysteresis has been implemented in FEM software and first simulations yielded very good qualitative results in predicting the field distributions of simple geometries. For real MSR geometries however, simulations are too time consuming and not feasible yet.

Aside from ultra-low residual fields, in this thesis, also the development, implementation and characterization of the homogeneous B_0 field for the nEDM experiment is presented. Magnetic field stability and magnetic field gradients are a major source of systematic effects and have to be a small as possible. The coil system to produce these fields has been developed with the help of FEM software. A current calculation method has been implemented to determine the optimal set of currents for the most homogeneous fields. In simulations it could be shown that the coil system even exceeds the requirements.

Measurements of magnetic fields on the required accuracy prove to be quite difficult.

Detection of transverse components of 0.1 nT in a 1 µT field requires an angular alignment with 10^{-4} accuracy. To keep this alignment, automated movement of the sensor, complicated by completely non-magnetic mechanics, was discarded in favor of a simplified manual movement. Furthermore, a calibration setup was built to align the sensor heads perpendicular to each other.

The actual coil system has then been set up and characterized. Differences between the simulated and measured fields have been investigated and corresponding corrections designed. For the measured fields, the current optimization yielded unsatisfactory results, due to deviations from the assumed linear behavior. Accordingly, the currents had to be determined differently. In an iterative approach, a current set has been found that produces fields with a homogeneity of $\frac{\Delta B}{B} = 5 \times 10^{-4}$ for the volume of the lower EDM cell. From the measured field maps in two planes, the field gradients in Z direction can be estimated to be $\frac{\partial B_z}{\partial z} \approx 1.25\,\mathrm{nT/m}$ for the lower EDM cell, resulting in a maximum false nEDM signal of $d^{GP}_{false} \approx 5 \times 10^{-28}$ ecm. The shield was then moved to Grenoble, therefore no further optimization was done. However, further improvement can be envisioned by using the full set of coils, instead of only 15.

The combination of high shielding factors and low gradients in the applied fields, provides a magnetic environment which enables the improvement of the current limit on the nEDM by an order of magnitude. It also removes the need for a comagnetometer in this stage of the experiment which comprises a major experimental simplification.

Bibliography

1. Altarev, I. et al.: 'A next generation measurement of the electric dipole moment of the neutron at the FRM II'. *Il Nuovo Cimento* (2012), vol. 35(4): pp. 122–127.
2. Chupp, T., P. Fierlinger, M. Ramsey-Musolf, and J. Singh: 'Electric Dipole Moments of the Atoms, Molecules, Nuclei and Particles'. to be published. 2017.
3. Dubbers, D. and M. G. Schmidt: 'The neutron and its role in cosmology and particle physics'. *Rev. Mod. Phys.* (4 Oct. 2011), vol. 83: pp. 1111–1171.
4. Planck, Collaboration et al.: 'Planck 2013 results. XVI. Cosmological parameters'. *Astronomy and Astrophysics* (2014), vol. 571.
5. Sakharov, A.: 'Violation of CP invariance, C asymmetry, and baryon asymmetry of the universe'. *Soviet Physics Uspekhi* (1991), vol. 34(5): p. 392.
6. Wu, C. S., E. Ambler, R. W. Hayward, D. D. Hoppes, and R. P. Hudson: 'Experimental Test of Parity Conservation in Beta Decay'. *Phys. Rev.* (4 Feb. 1957), vol. 105: pp. 1413–1415.
7. Christenson, J. H., J. W. Cronin, V. L. Fitch, and R. Turlay: 'Evidence for the 2π Decay of the K_2^0 Meson'. *Phys. Rev. Lett.* (4 July 1964), vol. 13: pp. 138–140.
8. Aubert, B. et al.: 'Measurement of *CP*-Violating Asymmetries in B^0 Decays to *CP* Eigenstates'. *Phys. Rev. Lett.* (12 Mar. 2001), vol. 86: pp. 2515–2522.
9. Patrignani, C. et al.: 'Review of Particle Physics'. *Chin. Phys.* (2016), vol. C40(10): p. 100001.
10. Pospelov, M. and A. Ritz: 'Theta-Induced Electric Dipole Moment of the Neutron via QCD Sum Rules'. *Phys. Rev. Lett.* (13 Sept. 1999), vol. 83: pp. 2526–2529.
11. Pendlebury, J. M. et al.: 'Revised experimental upper limit on the electric dipole moment of the neutron'. *Physical Review D* (2015), vol. 92(9).
12. Peccei, R. D. and H. R. Quinn: 'CP Conservation in the Presence of Pseudoparticles'. *Phys. Rev. Lett.* (25 June 1977), vol. 38: pp. 1440–1443.
13. Kim, J. E. and G. Carosi: 'Axions and the strong CP problem'. *Rev. Mod. Phys.* (1 Mar. 2010), vol. 82: pp. 557–601.
14. Luty, M. A.: 'Baryogenesis via leptogenesis'. *Phys. Rev. D* (2 Jan. 1992), vol. 45: pp. 455–465.
15. Chatrchyan, S. et al.: 'Observation of a new boson at a mass of 125 GeV with the CMS experiment at the LHC'. *Physics Letters B* (2012), vol. 716(1): pp. 30–61.

16. Aad, G. et al.: 'Observation of a new particle in the search for the Standard Model Higgs boson with the ATLAS detector at the LHC'. *Physics Letters B* (2012), vol. 716(1): pp. 1–29.

17. Pospelov, Maxim and Adam Ritz: 'Electric dipole moments as probes of new physics'. *Annals of physics* (2005), vol. 318(1): pp. 119–169.

18. Ibrahim, T., A. Itani, and P. Nath: 'Electron electric dipole moment as a sensitive probe of PeV scale physics'. *Physical Review D* (2014), vol. 90(5): p. 055006.

19. Baron, J. et al.: 'Order of Magnitude Smaller Limit on the Electric Dipole Moment of the Electron'. *Science* (2014), vol. 343(6168): pp. 269–272.

20. Baron, J. et al.: 'Methods, analysis, and the treatment of systematic errors for the electron electric dipole moment search in thorium monoxide'. *New Journal of Physics* (2017), vol. 19(7): p. 073029.

21. Graner, B., Y. Chen, E. G. Lindahl, and B. R. Heckel: 'Reduced Limit on the Permanent Electric Dipole Moment of ^{199}Hg'. *Phys. Rev. Lett.* (16 Apr. 2016), vol. 116: p. 161601.

22. Rosenberry, M.A. and T.E. Chupp: 'Atomic electric dipole moment measurement using spin exchange pumped masers of 129 Xe and 3 He'. *Physical review letters* (2001), vol. 86(1): p. 22.

23. Chupp, T. and M. Ramsey-Musolf: 'Electric dipole moments: A global analysis'. *Phys. Rev. C* (3 Mar. 2015), vol. 91: p. 035502.

24. Schiff, L. I.: 'Measurability of Nuclear Electric Dipole Moments'. *Phys. Rev.* (5 Dec. 1963), vol. 132: pp. 2194–2200.

25. Khriplovich, I. B. and S. K. Lamoreaux: *CP violation without strangeness: electric dipole moments of particles, atoms, and molecules*. Springer Science & Business Media, 2012.

26. Altarev, I. et al.: 'Test of Lorentz invariance with spin precession of ultracold neutrons'. *Physical Review Letters* (2009), vol. 103(8): p. 081602.

27. Greenberg, O. W.: 'CPT Violation Implies Violation of Lorentz Invariance'. *Phys. Rev. Lett.* (23 Nov. 2002), vol. 89: p. 231602.

28. Heil, W., C. Gemmel, S. Karpuk, Y. Sobolev, K. Tullney, F. Allmendinger, U. Schmidt, M. Burghoff, W. Kilian, S. Knappe-Grüneberg, A. Schnabel, F. Seifert, and L. Trahms: 'Spin clocks: Probing fundamental symmetries in nature'. *Annalen der Physik* (2013), vol. 525(8-9): pp. 539–549.

29. Dickerson, S., J. M. Hogan, D. M. Johnson, T. Kovachy, A. Sugarbaker, S. W. Chiow, and M. A. Kasevich: 'A high-performance magnetic shield with large length-to-diameter ratio'. *Review of Scientific Instruments* (2012), vol. 83(6): p. 065108.

30. Cohen, D.: 'Magnetoencephalography: Evidence of Magnetic Fields Produced by Alpha-Rhythm Currents'. *Science* (1968), vol. 161(3843): pp. 784–786.

31. Jackson Kimball, D. F., J. Dudley, Y. Li, S. Thulasi, S. Pustelny, D. Budker, and M. Zolotorev: 'Magnetic shielding and exotic spin-dependent interactions'. *Phys. Rev. D* (8 Oct. 2016), vol. 94: p. 082005.

32. Ramsey, N. F.: 'A Molecular Beam Resonance Method with Separated Oscillating Fields'. *Physical Review* (1950), vol. 78(6): pp. 695–699.

33. Green, K., P.G. Harris, P. Iaydjiev, D.J.R. May, J.M. Pendlebury, K.F. Smith, M. van der Grinten, P. Geltenbort, and S. Ivanov: 'Performance of an atomic mercury magnetometer in the neutron EDM experiment'. *Nuclear Instruments and Methods in Physics Research Section A: Accelerators, Spectrometers, Detectors and Associated Equipment* (1998), vol. 404(2): pp. 381–393.

34. Baker, C. A., D. D. Doyle, P. Geltenbort, K. Green, M. G. van der Grinten, P. G. Harris, P. Iaydjiev, S. N. Ivanov, D. J. May, J. M. Pendlebury, J. D. Richardson, D. Shiers, and K. F. Smith: 'Improved experimental limit on the electric dipole moment of the neutron'. *Physical Review Letters* (2006), vol. 97(13): p. 131801.

35. Taubenheim, B.: 'Optical Mercury Magnetometry for Fundamental Physics Experiments'. Dissertation. Technische Universität München, 2018.

36. Stadnik, Y.V. and V.V. Flambaum: 'Nuclear spin-dependent interactions: searches for WIMP, axion and topological defect dark matter, and tests of fundamental symmetries'. *The European Physical Journal C* (2015), vol. 75(3): p. 110.

37. Brenner, T., P. Fierlinger, P. Geltenbort, E. Gutsmiedl, A. Hollering, T. Lauer, G. Petzoldt, D. Ruhstorfer, J. Schroffenegger, K. M. Seemann, O. Soltwedel, S. Stuiber, B. Taubenheim, D. Windmayer, and T. Zechlau: 'Deuterated polyethylene coatings for ultra-cold neutron applications'. *Applied Physics Letters* (2015), vol. 107(12).

38. Lins, T.: 'High Precision Physics in Low Magnetic Fields: Implementation of a Sub-Nanotesla Field with Femtotesla Temporal Stability'. Dissertation. Technische Universität München, 2016.

39. Nouri, N. and B. Plaster: 'Sensitivity requirements for accessing interior magnetic field vector components in neutron electric dipole moment experiments via exterior boundary-value measurements'. *Journal of Instrumentation* (2014), vol. 9(11): P11009.

40. Patton, B., E. Zhivun, D. C. Hovde, and D. Budker: 'All-Optical Vector Atomic Magnetometer'. *Phys. Rev. Lett.* (1 July 2014), vol. 113: p. 013001.

41. Sturm, M.: 'Measurements and Characterization of a Laser-based Cs-atomic Magnetometer'. Master Thesis. Technische Universität München, 2013.

42. Wurm, D.: 'Towards a Fiberized All Optical Cs Magnetometer'. Master Thesis. Technische Universität München, 2015.

43. Cates, G. D., S. R. Schaefer, and W. Happer: 'Relaxation of spins due to field inhomogeneities in gaseous samples at low magnetic fields and low pressures'. *Physical review A* (1988), vol. 37(8): p. 2877.

44. Ramsey, N. F.: 'Resonance Transitions Induced by Perturbations at Two or More Different Frequencies'. *Physical Review* (1955), vol. 100(4): pp. 1191–1194.

45. Bloch, F. and A. Siegert: 'Magnetic Resonance for Nonrotating Fields'. *Phys. Rev.* (6 Mar. 1940), vol. 57: pp. 522–527.

46. Byrne, J.: *Neutrons, Nuclei and Matter: An Exploration of the Physics of Slow Neutrons*. Dover Books on Physics Series. Dover Publications, 2011.

47. Berry, M. V.: 'Quantal phase factors accompanying adiabatic changes'. *Proceedings of the Royal Society of London A: Mathematical, Physical and Engineering Sciences*. Vol. 392. The Royal Society, 1984: pp. 45–57.

48. Zimmer, O., F. M. Piegsa, and S. N. Ivanov: 'Superthermal Source of Ultracold Neutrons for Fundamental Physics Experiments'. *Phys. Rev. Lett.* (13 Sept. 2011), vol. 107: p. 134801.

49. Piegsa, F. M., M. Fertl, S. N. Ivanov, M. Kreuz, K. K. H. Leung, P. Schmidt-Wellenburg, T. Soldner, and O. Zimmer: 'New source for ultracold neutrons at the Institut Laue-Langevin'. *Physical Review C* (2014), vol. 90(1): p. 015501.

50. Zimmer, O. and R. Golub: 'Ultracold neutron accumulation in a superfluid-helium converter with magnetic multipole reflector'. *Phys. Rev.* (2015), vol. C92(1): p. 015501.

51. Fierlinger, P. private communication. 2018.

52. Zechlau, T.: 'Ultra-Cold Neutron Transport and Spin Manipulation System for the Measurement of the Neutron Electric Dipole Moment'. Dissertation. Technischen Universität München, 2016.

53. Afach, S. et al.: 'Measurement of a false electric dipole moment signal from 199Hg atoms exposed to an inhomogeneous magnetic field'. *The European Physical Journal D* (2015), vol. 69(10).

54. Bales, M. J., P. Fierlinger, and R. Golub: 'Non-extensive statistics in spin precession'. *EPL (Europhysics Letters)* (2016), vol. 116(4).

55. Voigt, J.: 'Entwicklung eines Messsystems zur Charakterisierung magnetisch geschirmter Umgebungen'. Dissertation. Technische Universität Ilmenau, 2015.

56. Kaden, H.: *Die elektromagnetische Schirmung in der Fernmelde- und Hochfrequenztechnik*. Springer, Berlin, Heidelberg, 1950.

57. Freake, S. M. and T. L. Thorp: 'Shielding of Low Magnetic Fields with Multiple Cylindrical Shells'. *Review of Scientific Instruments* (1971), vol. 42(10): pp. 1411–1413.

58. Kelha, V., J. Pukki, R. Peltonen, A. Penttinen, R. Ilmoniemi, and J. Heino: 'Design, construction, and performance of a large-volume magnetic shield'. *IEEE Transactions on Magnetics* (1982), vol. 18(1): pp. 260–270.

59. Sumner, T. J., J. M. Pendlebury, and K. F. Smith: 'Convectional magnetic shielding'. *Journal of Physics D: Applied Physics* (1987), vol. 20(9): p. 1095.

60. Paperno, E., S. Peliwal, M. V. Romalis, and A. Plotkin: 'Optimum shell separation for closed axial cylindrical magnetic shields'. *Journal of Applied Physics* (2005), vol. 97(10): 10Q104.

61. Budker, D. and D. F. J. Kimball: *Optical magnetometry*. Cambridge University Press, 2013.

62. Couderchon, G. and J. F. Tiers: 'Some aspects of magnetic properties of Ni-Fe and Co-Fe alloys'. *Journal of Magnetism and Magnetic Materials* (1982), vol. 26(1): pp. 196–214.

63. Hoburg, J. F.: 'Principles of quasistatic magnetic shielding with cylindrical and spherical shields'. *IEEE Transactions on Electromagnetic Compatibility* (1995), vol. 37(4): pp. 574–579.

64. Allan, D. W.: 'Statistics of atomic frequency standards'. *Proceedings of the IEEE* (1966), vol. 54(2): pp. 221–230.

65. Altarev, I. et al.: 'A magnetically shielded room with ultra low residual field and gradient'. *Review of Scientific Instruments* (2014), vol. 85(7): p. 075106.

66. Altarev, I. et al.: 'A large-scale magnetic shield with 106 damping at millihertz frequencies'. *Journal of Applied Physics* (2015), vol. 117(18): p. 183903.

67. Bork, J., H. D. Hahlbohm, R. Klein, and A. Schnabel: 'The 8-layered magnetically shielded room of the PTB: Design and construction'. *Biomag2000, Proc. 12th Int. Conf. on Biomagnetism*. Espoo, Finland, 2001: pp. 970–73.

68. Jiles, D. C. and D. L. Atherton: 'Theory of ferromagnetic hysteresis'. *Journal of Magnetism and Magnetic Materials* (1986), vol. 61(1-2): pp. 48–60.

69. Kohlrausch, F.: *Praktische Physik, Vol. 2*. Teubner, Stuttgart, 1996.

70. Thiel, F., A. Schnabel, S. Knappe-Gruneberg, D. Stollfuss, and M. Burghoff: 'Demagnetization of magnetically shielded rooms'. *Review of Scientific Instruments* (2007), vol. 78(3): p. 035106.

71. Voigt, J., S. Knappe-Grüneberg, A. Schnabel, R. Körber, and M. Burghoff: 'Measures to reduce the residual field and field gradient inside a magnetically shielded room by a factor of more than 10'. *Metrology and Measurement Systems* (2013), vol. 20(2).

72. Thiel, F., A. Schnabel, S. Knappe-Gruneberg, D. Stollfuss, and M. Burghoff: 'Proposal of a Demagnetization Function'. *IEEE Transactions on Magnetics* (2007), vol. 43(6): pp. 2959–2961.

73. Altarev, I., P. Fierlinger, T. Lins, M.G. Marino, B. Niessen, G. Petzoldt, M. Reisner, S. Stuiber, M. Sturm, and J. Taggart Singh: 'Minimizing magnetic fields for precision experiments'. *Journal of Applied Physics* (2015), vol. 117(23): p. 233903.

74. Baum, E. and J. Bork: 'Systematic design of magnetic shields'. *Journal of Magnetism and Magnetic Materials* (1991), vol. 101(1): pp. 69–74.

75. Trahms, L. and M. Burghoff: 'NMR at very low fields'. *Magnetic Resonance Imaging* (2010), vol. 28(8): pp. 1244–1250.

76. Ledbetter, M. P., T. Theis, J. W. Blanchard, H. Ring, P. Ganssle, S. Appelt, B. Blümich, A. Pines, and D. Budker: 'Near-Zero-Field Nuclear Magnetic Resonance'. *Phys. Rev. Lett.* (10 Sept. 2011), vol. 107: p. 107601.

77. Espy, M. et al.: 'Ultra-low-field MRI for the detection of liquid explosives'. *Superconductor Science and Technology* (2010), vol. 23(3): p. 034023.

78. Serebrov, A. P. et al.: 'New measurements of the neutron electric dipole moment'. *JETP Letters* (2014), vol. 99(1): pp. 4–8.

79. Budker, D. and M. Romalis: 'Optical magnetometry'. *Nature Physics* (2007), vol. 3(4): pp. 227–234.

80. Fagaly, R. L.: 'Superconducting quantum interference device instruments and applications'. *Review of Scientific Instruments* (2006), vol. 77(10): p. 101101.

81. Primdahl, F.: 'The fluxgate magnetometer'. *Journal of Physics E: Scientific Instruments* (1979), vol. 12(4): p. 241.

82. Ripka, Pavel: 'Review of fluxgate sensors'. *Sensors and Actuators A: Physical* (1992), vol. 33(3): pp. 129–141.

83. Schnabel, A. private communication. 2015.

84. VDM Metals: *Material Data Sheet No. 9004*. [Online; accessed 25-November-2017]. 2000.

85. Magnetic Shield Corporation: *Material Data Sheet*. [Online; accessed 25-November-2017]. 2015.

86. Sun, Z., A. Schnabel, M. Burghoff, and L. Li: 'Calculation of an optimized design of magnetic shields with integrated demagnetization coils'. *AIP Advances* (2016), vol. 6(7): p. 075220.

87. Chwastek, K.: 'Modelling offset minor hysteresis loops with the modified Jiles–Atherton description'. *Journal of Physics D: Applied Physics* (2009), vol. 42(16): p. 165002.

88. Sun, Z., A. Schnabel, J. Voigt, P. Fierlinger, S. Stuiber, T. Tui, L. Li, and D. Pan: 'Realization of the lowest magnetic filed in the world by systematic optimization of the equilibration process'. *to be published* (2018), vol. (7): p. 075220.

89. Hartwig, J., S. Abend, C. Schubert, D. Schlippert, H. Ahlers, K. Posso-Trujillo, N. Gaaloul, W. Ertmer, and E. M. Rasel: 'Testing the universality of free fall with rubidium and ytterbium in a very large baseline atom interferometer'. *New Journal of Physics* (2015), vol. 17(3): p. 035011.

90. Anastassopoulos, V. et al.: 'A storage ring experiment to detect a proton electric dipole moment'. *Review of Scientific Instruments* (2016), vol. 87(11): p. 115116.

91. Jiles, D. C. and D. L. Atherton: 'Theory of ferromagnetic hysteresis (invited)'. *Journal of Applied Physics* (1984), vol. 55(6): pp. 2115–2120.

92. Sun, Z., M. Reisner, P. Fierlinger, A. Schnabel, S. Stuiber, and L. Li: 'Dynamic modeling of the behavior of permalloy for magnetic shielding'. *Journal of Applied Physics* (2016), vol. 119(19): p. 193902.

93. Bergqvist, A. J.: 'A simple vector generalization of the Jiles-Atherton model of hysteresis'. *IEEE Transactions on Magnetics* (1996), vol. 32(5): pp. 4213–4215.

94. Jiles, D. C.: 'Frequency dependence of hysteresis curves in conducting magnetic materials'. *Journal of Applied Physics* (1994), vol. 76(10): pp. 5849–5855.

95. Jackson, J. D.: *Classical Electrodynamics*. 3rd ed. Wiley, 1999.

96. Nouri, N. and B. Plaster: 'Comparison of magnetic field uniformities for discretized and finite-sized standard $cos\theta$, solenoidal, and spherical coils'. *Nuclear Instruments and Methods in Physics Research Section A: Accelerators, Spectrometers, Detectors and Associated Equipment* (2013), vol. 723(Supplement C): pp. 30–35.

97. Griffith, W. C., M. D. Swallows, T. H. Loftus, M. V. Romalis, B. R. Heckel, and E. N. Fortson: 'Improved Limit on the Permanent Electric Dipole Moment of ^{199}Hg'. *Phys. Rev. Lett.* (10 Mar. 2009), vol. 102: p. 101601.

98. Pérez Galván, A., B. Plaster, J. Boissevain, R. Carr, B. W. Filippone, M. P. Mendenhall, R. Schmid, R. Alarcon, and S. Balascuta: 'High uniformity magnetic coil for search of neutron electric dipole moment'. *Nuclear Instruments and Methods in Physics Research Section A: Accelerators, Spectrometers, Detectors and Associated Equipment* (2011), vol. 660(1): pp. 147–153.

99. Maldonado-Velázquez, M., L. Barrón-Palos, C. Crawford, and W.M. Snow: 'Magnetic field devices for neutron spin transport and manipulation in precise neutron spin rotation measurements'. *Nuclear Instruments and Methods in Physics Research Section A: Accelerators, Spectrometers, Detectors and Associated Equipment* (2017), vol. 854: pp. 127–133.

100. Penrose, R.: 'A generalized inverse for matrices'. *Mathematical Proceedings of the Cambridge Philosophical Society* (1955), vol. 51(3): pp. 406–413.

101. Barata, João C. A. and M. S. Hussein: 'The Moore–Penrose Pseudoinverse: A Tutorial Review of the Theory'. *Brazilian Journal of Physics* (Apr. 2012), vol. 42(1): pp. 146–165.

A. Parameters

A.1 Voltage and current settings for the maps

The Bilt current source was operated with the following settings for the measurement of the B0 maps.

```
HH1

            Voltage: -0.00976906,
            Voltrange: 15,
            Current: 0.00374644,
            CurrentRange: 0.2
HH2

            Voltage: -0.0125897,
            Voltrange: 15,
            Current: 0.00132783,
            CurrentRange: 0.2
zWF

            Voltage: -0.0163516,
            Voltrange: 15,
            Current: -0.0015004,
            CurrentRange: 0.2
zWB

            Voltage: -0.0162231,
            Voltrange: 15,
            Current: -0.00152038,
            CurrentRange: 0.2
B1

            Voltage: -0.0080997357,
            Voltrange: 1.2,
            Current: ---,
            CurrentRange: 0.2
B0

            Voltage: 0.649001,
            Voltrange: 12,
            Current: ---,
            CurrentRange: 0.2
eF
```

```
38
39              Voltage: -0.0274641,
40              Voltrange: 15,
41              Current: -0.0199875,
42              CurrentRange: 0.2
43  eTB1
44
45              Voltage: 0.032139,
46              Voltrange: 5,
47              Current: 0.0165655,
48              CurrentRange: 0.15
49  eBB1
50
51              Voltage: 0.0302577,
52              Voltrange: 5,
53              Current: 0.0165624,
54              CurrentRange: 0.15
55  eTF1
56
57              Voltage: 0.0221977,
58              Voltrange: 5,
59              Current: 0.0165419,
60              CurrentRange: 0.15
61  eBF1
62
63              Voltage: 0.0218158,
64              Voltrange: 5,
65              Current: 0.0170318,
66              CurrentRange: 0.15
67  cTL4
68
69              Voltage: -0.0132983,
70              Voltrange: 15,
71              Current: 0.00168585,
72              CurrentRange: 0.2
73  cBL4
74
75              Voltage: -0.0161737,
76              Voltrange: 15,
77              Current: -0.0017087,
78              CurrentRange: 0.2
79  cTR4
80
81              Voltage: -0.0136692,
82              Voltrange: 15,
83              Current: 0.00173711,
84              CurrentRange: 0.2
```

```
cBR4

            Voltage: -0.0161264,
            Voltrange: 15,
            Current: -0.0017859,
            CurrentRange: 0.2
```

A.2 Bilt configuration

The configuration file for the Bilt source from the database contains the assignment of coils to current sources and the possible ranges of operation for each source.

```
{
    "1": {
        "Name" : "i1; c1;",
        "CoilName": "HH1",
        "VoltRanges" : [15],
        "CurrRanges" : [0.02, 0.2]
    },
    "2": {
        "Name" : "i1; c2;",
        "CoilName": "HH2",
        "VoltRanges" : [15],
        "CurrRanges" : [0.02, 0.2]
    },
    "3": {
        "Name" : "i1; c3;",
        "CoilName": "zWF",
        "VoltRanges" : [15],
        "CurrRanges" : [0.02, 0.2]
    },
    "4": {
        "Name" : "i1; c4;",
        "CoilName": "zWB",
        "VoltRanges" : [15],
        "CurrRanges" : [0.02, 0.2]
    },
    "5": {
        "Name" : "i1; c5;",
        "CoilName": "eTB3",
        "VoltRanges" : [15],
        "CurrRanges" : [0.02, 0.2]
    },
    "6": {
        "Name" : "i1; c6;",
        "CoilName": "eBB3",
        "VoltRanges" : [15],
```

```
        "CurrRanges" : [0.02, 0.2]
    },
    "7": {
        "Name" : "i2; c1;",
        "CoilName": "eTF3",
        "VoltRanges" : [15],
        "CurrRanges" : [0.02, 0.2]
    },
    "8": {
        "Name" : "i2; c2;",
        "CoilName": "eBF3",
        "VoltRanges" : [15],
        "CurrRanges" : [0.02, 0.2]
    },
    "9": {
        "Name" : "i2; c3;",
        "CoilName": "eTB4",
        "VoltRanges" : [15],
        "CurrRanges" : [0.02, 0.2]
    },
    "10": {
        "Name" : "i2; c4;",
        "CoilName": "eBB4",
        "VoltRanges" : [15],
        "CurrRanges" : [0.02, 0.2]
    },
    "11": {
        "Name" : "i2; c5;",
        "CoilName": "eTF4",
        "VoltRanges" : [15],
        "CurrRanges" : [0.02, 0.2]
    },
    "12": {
        "Name" : "i2; c6;",
        "CoilName": "eBF4",
        "VoltRanges" : [15],
        "CurrRanges" : [0.02, 0.2]
    },
    "13": {
        "Name" : "i3; c1;",
        "CoilName": "cBR2",
        "VoltRanges" : [15],
        "CurrRanges" : [0.02, 0.2]
    },
    "14": {
        "Name" : "i3; c2;",
        "CoilName": "cBR3",
```

```
83          "VoltRanges" : [15],
84          "CurrRanges" : [0.02, 0.2]
85      },
86      "15": {
87          "Name" : "i3; c3;",
88          "CoilName": "cBR4",
89          "VoltRanges" : [15],
90          "CurrRanges" : [0.02, 0.2]
91      },
92      "16": {
93          "Name" : "i3; c4;",
94          "CoilName": "cBR5",
95          "VoltRanges" : [15],
96          "CurrRanges" : [0.02, 0.2]
97      },
98      "17": {
99          "Name" : "i3; c5;",
100         "CoilName": "cBL2",
101         "VoltRanges" : [15],
102         "CurrRanges" : [0.02, 0.2]
103     },
104     "18": {
105         "Name" : "i3; c6;",
106         "CoilName": "cBL3",
107         "VoltRanges" : [15],
108         "CurrRanges" : [0.02, 0.2]
109     },
110     "19": {
111         "Name" : "i4; c1;",
112         "CoilName": "cBL4",
113         "VoltRanges" : [15],
114         "CurrRanges" : [0.02, 0.2]
115     },
116     "20": {
117         "Name" : "i4; c2;",
118         "CoilName": "cBL5",
119         "VoltRanges" : [15],
120         "CurrRanges" : [0.02, 0.2]
121     },
122     "21": {
123         "Name" : "i4; c3;",
124         "CoilName": "cTL3",
125         "VoltRanges" : [15],
126         "CurrRanges" : [0.02, 0.2]
127     },
128     "22": {
129         "Name" : "i4; c4;",
```

```
        "CoilName": "cTL4",
        "VoltRanges" : [15],
        "CurrRanges" : [0.02, 0.2]
    },
    "23": {
        "Name" : "i4; c5;",
        "CoilName": "cTL5",
        "VoltRanges" : [15],
        "CurrRanges" : [0.02, 0.2]
    },
    "24": {
        "Name" : "i4; c6;",
        "CoilName": "cBL1",
        "VoltRanges" : [15],
        "CurrRanges" : [0.02, 0.2]
    },
    "25": {
        "Name" : "i5; c1;",
        "CoilName": "cTR3",
        "VoltRanges" : [15],
        "CurrRanges" : [0.02, 0.2]
    },
    "26": {
        "Name" : "i5; c2;",
        "CoilName": "cTR4",
        "VoltRanges" : [15],
        "CurrRanges" : [0.02, 0.2]
    },
    "27": {
        "Name" : "i5; c3;",
        "CoilName": "cTR5",
        "VoltRanges" : [15],
        "CurrRanges" : [0.02, 0.2]
    },
    "28": {
        "Name" : "i5; c4;",
        "CoilName": "cBR1",
        "VoltRanges" : [15],
        "CurrRanges" : [0.02, 0.2]
    },
    "29": {
        "Name" : "i5; c5;",
        "CoilName": "cR0",
        "VoltRanges" : [15],
        "CurrRanges" : [0.02, 0.2]
    },
    "30": {
```

```
177         "Name" : "i5; c6;",
178         "CoilName": "cTR1",
179         "VoltRanges" : [15],
180         "CurrRanges" : [0.02, 0.2]
181     },
182     "31": {
183         "Name" : "i6; c1;",
184         "CoilName": "cTR2",
185         "VoltRanges" : [15],
186         "CurrRanges" : [0.02, 0.2]
187     },
188     "32": {
189         "Name" : "i6; c2;",
190         "CoilName": "cL0",
191         "VoltRanges" : [15],
192         "CurrRanges" : [0.02, 0.2]
193     },
194     "33": {
195         "Name" : "i6; c3;",
196         "CoilName": "cTL1",
197         "VoltRanges" : [15],
198         "CurrRanges" : [0.02, 0.2]
199     },
200     "34": {
201         "Name" : "i6; c4;",
202         "CoilName": "cTL2",
203         "VoltRanges" : [15],
204         "CurrRanges" : [0.02, 0.2]
205     },
206     "35": {
207         "Name" : "i6; c5;",
208         "CoilName": "eF",
209         "VoltRanges" : [15],
210         "CurrRanges" : [0.02, 0.2]
211     },
212     "36": {
213         "Name" : "i6; c6;",
214         "CoilName": "x",
215         "VoltRanges" : [15],
216         "CurrRanges" : [0.02, 0.2]
217     },
218     "37": {
219         "Name" : "i7;",
220         "CoilName": "B0",
221         "VoltRanges" : [1.2, 12],
222         "CurrRanges" : [0.2]
223     },
```

```
    "38": {
        "Name" : "i8;",
        "CoilName": "B1",
        "VoltRanges" : [1.2, 12],
        "CurrRanges" : [0.2]
    },
    "39": {
        "Name" : "i9;",
        "CoilName": "eTB1",
        "VoltRanges" : [5, 20],
        "CurrRanges" : [0.000005, 0.000030, 0.000150, 0.001, 0.005, 0.030, 0.15, 1, 6]
    },
    "40": {
        "Name" : "i10;",
        "CoilName": "eBB1",
        "VoltRanges" : [5, 20],
        "CurrRanges" : [0.000005, 0.000030, 0.000150, 0.001, 0.005, 0.030, 0.15, 1, 6]
    },
    "41": {
        "Name" : "i11;",
        "CoilName": "eTF1",
        "VoltRanges" : [5, 20],
        "CurrRanges" : [0.000005, 0.000030, 0.000150, 0.001, 0.005, 0.030, 0.15, 1, 6]
    },
    "42": {
        "Name" : "i12;",
        "CoilName": "eBF1",
        "VoltRanges" : [5, 20],
        "CurrRanges" : [0.000005, 0.000030, 0.000150, 0.001, 0.005, 0.030, 0.15, 1, 6]
    }
}
```

A.3 Equilibration parameters

```
{
    "L-coil": {
        "Amp": 9,
        "Freq": 10,
        "Dur": 50,
        "Keep": 10,
        "RelayPort": 0,
        "VoltageDivider": 5
```

```
    },
    "I-X": {
        "Amp": 3.45,
        "Freq": 10,
        "Dur": 100,
        "Keep": 10,
        "RelayPort": 4,
        "VoltageDivider": 5
    },
   "A-X": {
        "Amp": 9,
        "Freq": 10,
        "Dur": 100,
        "Keep": 10,
        "RelayPort": 1,
        "VoltageDivider": 5
    },
    "A-Z": {
        "Amp": 9,
        "Freq": 10,
        "Dur": 100,
        "Keep": 10,
        "RelayPort": 3,
        "VoltageDivider": 5
    },
    "A-Y": {
        "Amp": 8.7,
        "Freq": 10,
        "Dur": 100,
        "Keep": 10,
        "RelayPort": 2,
        "VoltageDivider": 5
    },
    "Offset": 0,
    "Device": "Dev1"
}
```

A.4 L-coil configuration

In this section, the wiring connections for the MSR with the L coil configuration are described.

The black cable connects to the L coil, which combines the previous Y and Z directions. The sequence of the coils is, using the labels on the coils: input → B2 → A1 → B3 → A2 → B4 → A3 → B1 → A4 → current return

The red cable connects to the X direction in the following sequence: input → C1 → C2 → C3 → C4 → current return.

For every coil, the loops are connected as follows: the input from the last coil goes

to the brown wire, then through all the loops of the coil in numeric sequence, the blue cable then connects to the next coil.

The blue cable is disconnected.

B. Degaussing manual

Contents

1 Setting up

- The whole rack has to be supplied with a 400V/16A power line.
- The red power switch connects and disconnects the main power line for the whole rack.
- The power switch to boot the touchsceen pc is inside the top rack mount, all the other devices are switched with the main power.
- With an icon on the desktop, the degaussing software can be launched.

2 Description of the system

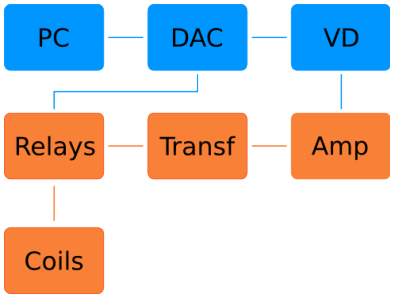

Illustration 1: Scheme of the degaussing chain

Components:

- Touchscreen PC: Joy IT Industrie PC T10
- Digital Analog Converter (DAC): NI-USB 6259 BNC for analog voltage output, digitial inputs and outputs
- Voltage Dividers (VD)
- Power Amplifier Rohrer PA614A
- Transformer
- Relaybox

The PC is used to control the system, it's a standard Windows 7 PC, with drivers for the hardware and the degaussing software.

NI-USB 6259 BNC outputs an analog voltage in the range +/- 10 V at a resolution of 16 bit to controll the current the power amplifier produces. Furthermore there are 23 digital outputs that are used to switch the relays and the voltage dividers, and 19 digital inputs that read the state of relays.

To be able to use the full digital resolution also for smaller currents, voltage dividers are used. Each one consists of a 1kOhm resistor in series to a 20kOhm potentiometer. The voltage dropping at the potentiometer is then supplied to the amplifier.
The potentiometers have to be set manually. There are three voltage dividers that can be set individually. Which one is used during degaussing has to be specified in the configuration file for each coil. It will then be activated automatically.

The power amplifier Rohrer PA614A can provide upto 30 A at 30 V. The voltage from the voltage divider is given to the AC input. The amplifier produces a current proportional to the input voltage, 10V correspond to 30A. It is possible to set a high and a low pass filter at the input side.
The amplifier has two stages that have to be switched on by pressing the corresponding button on the front panel, Power stage and Amplifier stage. Displays show the currently produced voltage and current, these values can also be displayed by connecting an oscilloscope to the monitor outputs.
See also the separate manual for this device.

The output current is filtered through a isolationg transformer to eliminate DC offsets. The transformer is designed to work with up to 30A and can transmit frequencies down to 7 Hz. The power amplifier is connected to the primary side and the secondary side is connected to the relaybox. There is also the possibility to use only half of the turns on each side to transform to half or double the voltage.

Next the relaybox distributes the current to the coils. Up to 19 coils can be connected to the terminals on the backside of the rack mount. The terminals are numbered from 0-18 from left to right, starting in the lower row, this number corresponds to the digital output port thats switches the relay. The relays are can withstand 30A. They switch cyclic and change state every time 12V is supplied to their switching connector. To read the state of each relay a microswitch is connected to it. The switch supplies 5V to a digital input of the NI device when it's pressed.
Only one coil is active at a time. This is controlled on the software side by checking the states of the microswitches.

The rack mount also holds a smaller box with three electronics boards. These are used to control the 12V needed to switch the relays with 5V povided by the NI device. Each board has 8 inputs and 8 outputs and is connected to a 5V and a 12V power supply. If a digital output of the NI device is switched to high and provides 5V to one of the boards inputs, the board supplies 12V to its corresponding output. The 12V drive a current through the relay and the relay changes its state. The PC side and the 12 V side are electrically isolated from each other.

3 Coil configuration

The degaussing software reads the coil configuration from one of several coil files. There are 4 options that can be choosen in the GUI:

- Inner Coils
- Outer Coils

- All Coils
- Custom coil file

By selecting one the first three options, the corresponding files are read, i.e. “innercoils.dict”, “outercoils.dict”, “allcoils.dict” respectivly. Of course the content of these files can be edited. The fourth option provides a text field where a custom file name can be entered.
All of these files are in the same directory as the degaussing software.

The files are simple text files containing a json dictionary with one entry for each coil.
Example.dict:

```
{
	“Coilname” : {
		“Amp”: value,
		“Freq”: value,
		“Dur”: value,
		“Keep”: value,
		“RelayPort”: value,
		“VoltageDivider”: value
	},
	“Coilname2” : {
		“Amp”: value,
		“Freq”: value,
		“Dur”: value,
		“Keep”: value,
		“RelayPort”: value,
		“VoltageDivider”: value
	}
}
```

The parameters give the values to create the degaussing waveform and also tell which Voltage divider to use and which digital port switches the relay the coil is connected to.
The degaussing process goes through all of the coils in the file in the given order. Changing the order in the .dict file is the only way to determine the degaussing sequence. For each coil a waveform will be created with the specified amplitude, frequency and duration. The parameter “Keep” specifies how long the maximal amplitude will be used before the amplitude starts to decay linearly.
Important:
The amplitude is in Volts and corresponds to the output voltage of the NI device, not the current!

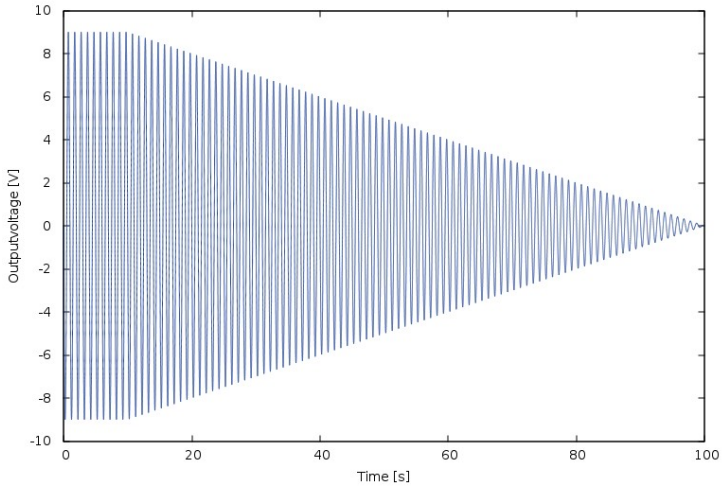

Illustration 2: Waveform example with parameters Amp = 9 V, Freq = 1 Hz, Dur = 100 s, Keep = 10 s. Frequency was set to 1 Hz for illustrative purposes only

To set the degaussing current for one of the coils, the following procedure is suggested. Set a voltage in the file at a high value, for example 9V. Choose the voltage divider to use for this coil and enter the value in the file. Next set the voltage divider so that almost no voltage is output (turn the knob clockwise). This makes sure that you don't supply a very high current to the coil when starting the degaussing. Start degaussing and during the keep time, adjust the voltage divider knob so that the desired current is produced. This can either be checked on the display of the amplifier, where you will read a rms value or by connecting an oscilloscope to the current monitor output of the amplifier. Then the current can be fine-tuned by adjusting the value for the output voltage in the config file.

4 Degaussing Software

The software for degaussing is written in Python2.7 and uses National Instruments VISA drivers to communicate with the NI device. For the graphical user interface (GUI) wxpython3.0 is used.
After starting the software by double clicking the desktop icon the follow main window is presented.

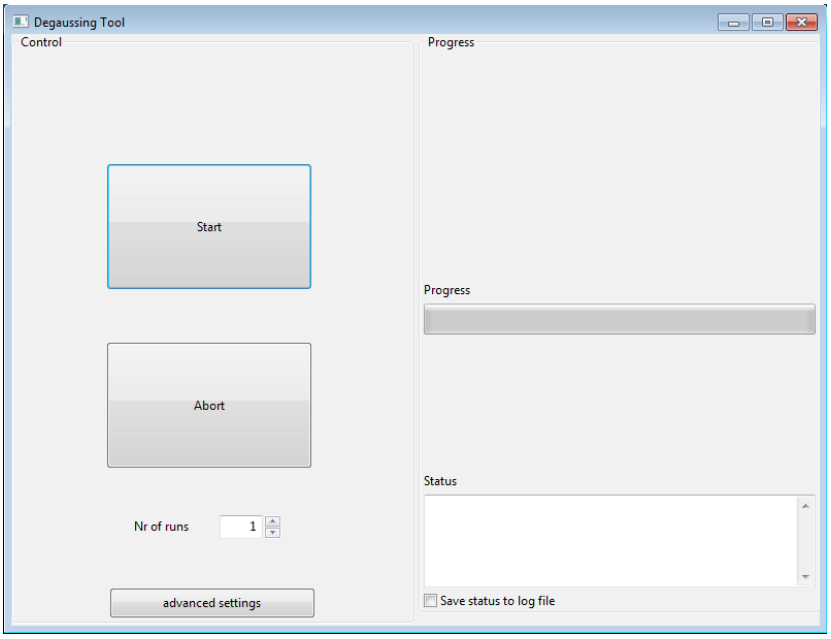

Illustration 3: Main window

The view is divided into to parts, on the left hand side are the controls and on the right hand side degaussing progress and a status field are shown.
If “Start” is pressed at this stage, right after launching the program, the coil configuration “Inner Coils” will be run, with the settings from the configuration file.
By pressing the “Abort” button you can either end the degaussing software, or cancel a currently running degaussing cycle.
The “Nr of runs” selector specifies how often the coil configuration from the file is run.

By clicking the “Advanced Settings” button a new dialog is opened where the degaussing configuration can be altered for the current session.

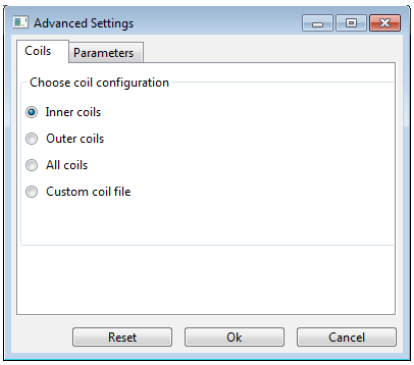

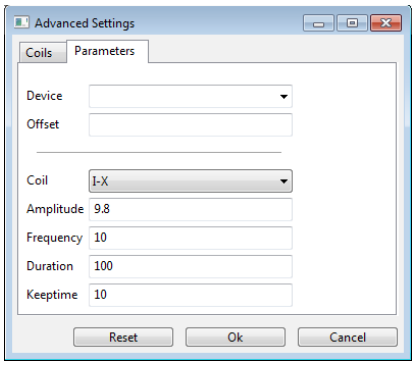

The window is split into two panel, called “Coils” and “Parameters”. In the Coils panel a coil configuration can be chosen, by changing to the Parameters panel the file will be read and the parameters will be displayed in the text fields. By clicking “Ok” on the first panel, the chosen configuration will be set directly.
In the Parameters panel, the drop down menu “Coil” shows all the coils in the order they will be used for degaussing. By selecting one of them, the parameters will be shown below. When the values in the text fields are changed they will be saved in a temporary degaussing configuration, but only when “Ok” is pressed this configuration will be used for degaussing. To revert to the previous configuration “Reset” has to be pressed. “Cancel” closes the window without changing a setting. The voltage divider and relay setting for each coil are not included in the GUI, this has to be done by changing the values in the configuration file.
There is no option to save the currently used configuration to a file. For a permanent setting the values have to be entered in the corresponding .dict file.

On the “Progress” panel a bar is indicating the approximate progress of the degaussing runs. This is a simple timer, that only takes into accout estimated switching and calculation times. It is therefore possible that the degaussing procedure will be finished some seconds before or after the bar has reached the end.
When the message “DONE” in the status field is displayed degaussing is completed.

In the status field, messages from several subprocesses of the degaussing sequence will be displayed.

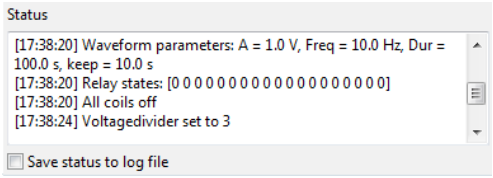

If the box “Save status to log file” is checked, everything that is displayed in the status field will also be append to a file “log.txt” in the same directory.

5 Degaussing sequence

In the beginning all coils are checked and switched off in case one was still active. Then all voltage dividers are reset.

After that the degaussing sequence is as follows for each of the coils:

- the waveform data is created with given parameters
- all coils are switched off
- the voltage divider is set
- the coil is activated
- waveform is sent to NI device and is output is started
- when waveform is finished all coils are switched off
- the voltage dividers will be reset

6 Hardware

NI USB 6259 BNC

Port assignments:

- A0: analog output voltage to the amplifier
- Digital Outputs
  - port0/line0-18 relay ports
  - port0/line19-22 voltage dividers
    - port 19: resets all
    - 20-22: set voltage divider 1,2 or 3
- Digital Inputs
  - port0/line23-31 microswitches for relays 0-7
  - port2/line0-7 microswitches for relays 8-15
  - port1/line0-2 microswitches for relay 16-18

D-Sub connectors on the relaybox:

Pin		Wirecolor
1-19	Microswitches 0-18	
20	+ 5V	Red
21	GND 5V	Grey
22	GND 12V	Black
23/24	+ 12 V	Blue
25	GND microswitches	

C. Degaussing code

```
import pynedm
import controller
import logging
logging.basicConfig(level=logging.ERROR)
print pynedm.__file__

_db = "nedm%2Fdegaussing"
po = pynedm.ProcessObject("http://server:5984",
        "username",
        "passwd",
  _db)

_dg = controller.DegaussingController()


def run_deg(t):
    print(" listener  run_deg called")

    def f():
        print(_dg.isrunning())
        print("run_deg called with t = {}".format(t))
        print(po.write_document_to_db(
            { "type": "data", "value": {"degaussing_state": 1} }))
        _dg.run_deg(t)
        print(po.write_document_to_db(
            { "type": "data", "value": {"degaussing_state": 0} }))
        print("run_deg done")

    if _dg.isrunning():
        print("in progress")
        raise Exception("Degaussing in progress")


    pynedm.start_process(f)
    return True

def isrunning():
    print("isrunning called")
    print(_dg.isrunning())
    return _dg.isrunning()

def interrupt_deg():
    print("interrupt called")
    if not _dg.isrunning():
        print("not in progress")
        raise Exception("Degaussing not in progress")
    _dg.interrupt_deg()

adict = {
    "run_deg": run_deg,
```

```
    "isrunning": isrunning,
    "interrupt_deg": interrupt_deg
    }

pylisten = pynedm.listen(adict, "nedm%2Fdegaussing",
                  username="username",
                  password="passwd",
                  uri="http://server:5984", verbose=True)

pylisten.wait()
print "Finished"
```

```
import cloudant
import json
import pynedm
import numpy as np
import digiports as dg
import waveformthread as wft
import matplotlib.pyplot as plt
import nidaqmx
from wx.lib.pubsub import pub

class DegaussingController():
    def __init__(self):
        _db = "nedm%2Fdegaussing"
        self.po = pynedm.ProcessObject("http://server:5984",
            "username",
            "passwd",
      _db)

        self.configs = self._getconfigs()
        self.settings = self._getsettings()
        self.voltagedivider = dg.VoltageDivider("Dev1")
        self.coilswitcher = dg.SwitchCoil("Dev1")
      self._running = False
        pub.subscribe(self.poststatus, "relay.update")

    def poststatus(self, status):
        print(status)
        status = [int(i) for i in status[1:-1].split(" ")]
        adoc = {
                    "type" : "data",
                    "value" :
                    {
                        "state_0": status[0],
                        "state_1": status[1],
                        "state_2": status[2],
                        "state_3": status[3]
                    }
                }

        print(adoc)
        print(self.po.write_document_to_db(adoc))

    def _getconfigs(self):
        acct = cloudant.Account(uri="http://server")
        res = acct.login("username", "passwd")
        assert res.status_code == 200
```

```
47
48          db = acct["nedm%2Fdegaussing"]
49          des = db.design("document_type")
50          the_view = des.view("document_type")
51          results = the_view.get(params=dict(descending=True,
52                                  reduce=False,
53                                  include_docs=True,
54                                  endkey = ['deg_config'] ,
55                                  startkey = ['deg_config', {}]
56                                  )).json()
57
58          confs = {row["doc"]["_id"]: row["doc"]["value"] for row in results["rows"]}
59          return confs
60
61      def _getsettings(self):
62          acct = cloudant.Account(uri="http://server")
63          res = acct.login("username", "passwd")
64          assert res.status_code == 200
65
66          db = acct["nedm%2Fdegaussing"]
67          des = db.design("document_type")
68          the_view = des.view("document_type")
69          results = the_view.get(params=dict(descending=True,
70                                  reduce=False,
71                                  include_docs=True,
72                                  endkey = ['deg_setting'] ,
73                                  startkey = ['deg_setting', {}]
74                                  )).json()
75          settings = {row["doc"]["_id"]: {"Config": row["doc"]["value"]["Config"],
76                                          "Sequence" : row["doc"]["value"]["Sequence"]}
77                      for row in results["rows"]}
78
79          return settings
80
81      def createWaveform(self, amp, freq, offset , duration, keeptime, sampleRate=1000):
82          ''' create waveform from given parameters'''
83          t = np.linspace(0, duration, duration*sampleRate + 1)
84          x = offset + ( (-1) * np.sin( 2*np.math.pi * freq * t ) * np.piecewise(t, [t<keeptime, t
>=keeptime], [amp, lambda t: -((t-keeptime) * amp/(duration-keeptime))+amp]))
85          periodLength = len( x )
86          data = np.zeros( (periodLength, ), dtype = np.float64)
87          data = x
88          return np.asarray( list (zip(t,data)), dtype=np.float64)
89
90      def playWaveform(self, device, amp, freq, duration, keeptime, offset , sampleRate=10000.0):
91          t = np.linspace(0, duration, duration*sampleRate + 1)
92          x = np.asarray(offset + ( (-1) * np.sin( 2*np.math.pi * freq * t ) * np.piecewise(t, [t<
keeptime, t>=keeptime], [amp, lambda t: -((t-keeptime) * amp/(duration-keeptime))+amp])),
dtype=np.float64)
93          self.task = nidaqmx.AnalogOutputTask()
94          self.task.create_voltage_channel("Dev1/ao0", min_val=-10.0, max_val=10.0)
95          self.task.configure_timing_sample_clock(rate=sampleRate, sample_mode = 'finite' ,
samples_per_channel = len(x))
96          self.task.write(x, auto_start=False, layout='group_by_channel')
97          self.task.start()
98          self.task.wait_until_done(duration + 5)
99          self.task.stop()
```

```
100         del self.task
101
102     def interrupt_deg(self):
103         print("controller interrupt")
104         self._running = False
105         self.task.clear()
106         print("task deleted")
107
108     def run_deg(self, sett):
109         self.configs = self._getconfigs()
110         self.settings = self._getsettings()
111         self._running = True
112         dev = self.configs[self.settings[sett]["Config"]]["Device"]
113         print("controller run_deg called: {}".format(self.settings[sett]))
114         for coil in self.settings[sett]["Sequence"]:
115             if self._running:
116                 cs = self.configs[self.settings[sett]["Config"]][coil]
117                 print (coil, cs)
118                 # all coils off
119                 print("all coils off")
120                 self.coilswitcher.alloff()
121                 # set vd
122                 print("setting voltagedivider {}".format(cs["VoltageDivider"]))
123                 self.voltagedivider.setnr(cs["VoltageDivider"])
124                 # activate coil
125                 print("setting relay {}".format(cs["RelayPort"]))
126                 self.coilswitcher.activate(cs["RelayPort"])
127
128                 # play waveform
129                 print("start waveform")
130                 self.playWaveform(dev, cs['Amp'], cs['Freq'] ,cs['Dur'], cs['Keep'], 0)
131                 # deactivate coil
132                 print("deactivate coil")
133                 self.coilswitcher.deactivate(cs["RelayPort"])
134                 # vd.resetall()
135                 print("voltagedivider reset all")
136                 self.voltagedivider.resetall()
137             else:
138         self._running = False
139                 self.coilswitcher.alloff()
140                 self.voltagedivider.resetall()
141         pub.sendMessage("relay.update", status="%s" % str(self.coilswitcher.di.read()))
142         self._running = False
143
144
145     def isrunning(self):
146         return self._running
```

```
1  import threading
2  import time
3  import ctypes
4  nidaq = ctypes.windll.nicaiu
5
6  int32 = ctypes.c_long
7  uInt32 = ctypes.c_ulong
8  uInt64 = ctypes.c_ulonglong
9  float64 = ctypes.c_double
10 bool32 = uInt32
```

```
TaskHandle = uInt32

DAQmx_Val_Cfg_Default = int32(-1)
DAQmx_Val_Volts = 10348
DAQmx_Val_Rising = 10280
DAQmx_Val_FiniteSamps = 10178
DAQmx_Val_ContSamps = 10123
DAQmx_Val_GroupByChannel = 0

class WaveformThread(threading.Thread):
    def __init__(self, device, waveform, samplerate):
        self.running = True
        self.device = device
        #self.chnnr = chnnr
        self.data = waveform[:,1]
        self.sampleRate = samplerate
        self.periodLength = len( self.data )
        self.time = waveform[:,0]
        self.taskHandle = TaskHandle( 0 )
        dev = str(self.device)
        dev = "Dev1/ao0"
        self.CHK(nidaq.DAQmxCreateTask("", ctypes.byref( self.taskHandle )))
        self.CHK(nidaq.DAQmxCreateAOVoltageChan( self.taskHandle, dev, "", float64(-10.0), float64(10.0), DAQmx_Val_Volts, None))
        self.CHK(nidaq.DAQmxCfgSampClkTiming( self.taskHandle, "", float64(self.sampleRate), DAQmx_Val_Rising, DAQmx_Val_FiniteSamps, uInt64(self.periodLength)))
        self.CHK(nidaq.DAQmxWriteAnalogF64( self.taskHandle, int32(self.periodLength), 0, float64(-1), DAQmx_Val_GroupByChannel, self.data.ctypes.data, None, None))
        threading.Thread.__init__(self)

    def CHK(self, err):
        ''' a simple error checking routine '''
        if err < 0:
            buf_size = 100
            buf = ctypes.create_string_buffer('\000' * buf_size)
            nidaq.DAQmxGetErrorString(err, ctypes.byref(buf), buf_size)
            raise RuntimeError('nidaq failed with error %d: %s'%(err, repr(buf.value)))
        if err > 0:
            buf_size = 100
            buf = ctypes.create_string_buffer('\000' * buf_size)
            nidaq.DAQmxGetErrorString(err, ctypes.byref(buf), buf_size)
            raise RuntimeError('nidaq generated waring %d: %s'%(err, repr(buf.value)))

    def run(self):
        self.CHK(nidaq.DAQmxStartTask( self.taskHandle ))
        ret_bool = bool32()
        self.CHK(nidaq.DAQmxIsTaskDone( self.taskHandle, ctypes.byref(ret_bool)))
        while( ret_bool.value == 0 ):
            time.sleep(2)
            nidaq.DAQmxIsTaskDone( self.taskHandle, ctypes.byref(ret_bool))
            #print ret_bool.value
        time.sleep(2)

    def stop(self):
        self.running = False
        nidaq.DAQmxStopTask( self.taskHandle )

```

```
65      def ___del___(self):
66          nidaq.DAQmxClearTask( self.taskHandle )
```

D. Battery box

The following two picture show schematic circuit drawings of the battery box.

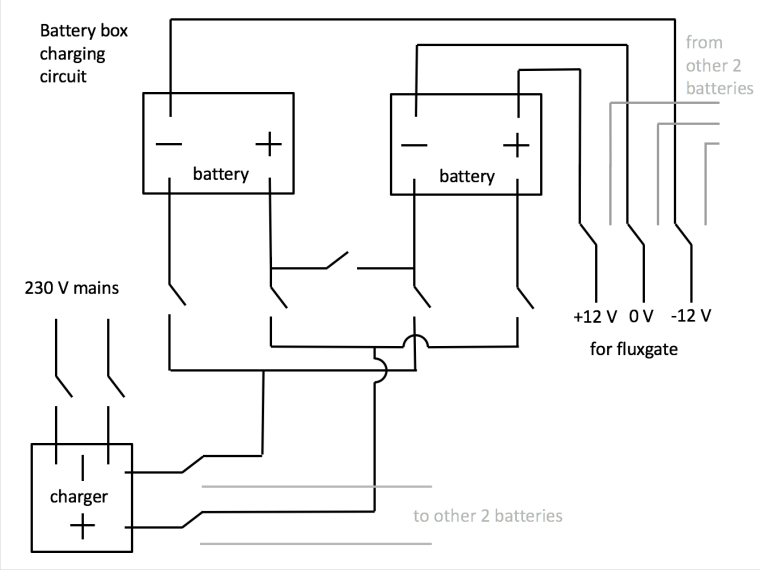

Figure D.1: Charging circuit for one set of batteries.

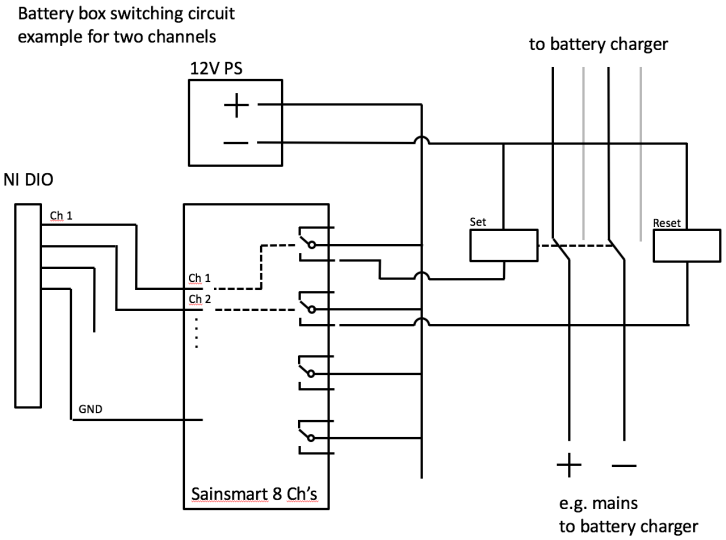

Figure D.2: Switching circuit for the relays.

E. Sensitivity maps for all coils

In this appendix, measured and simulated sensitivity maps for all coils are listed.

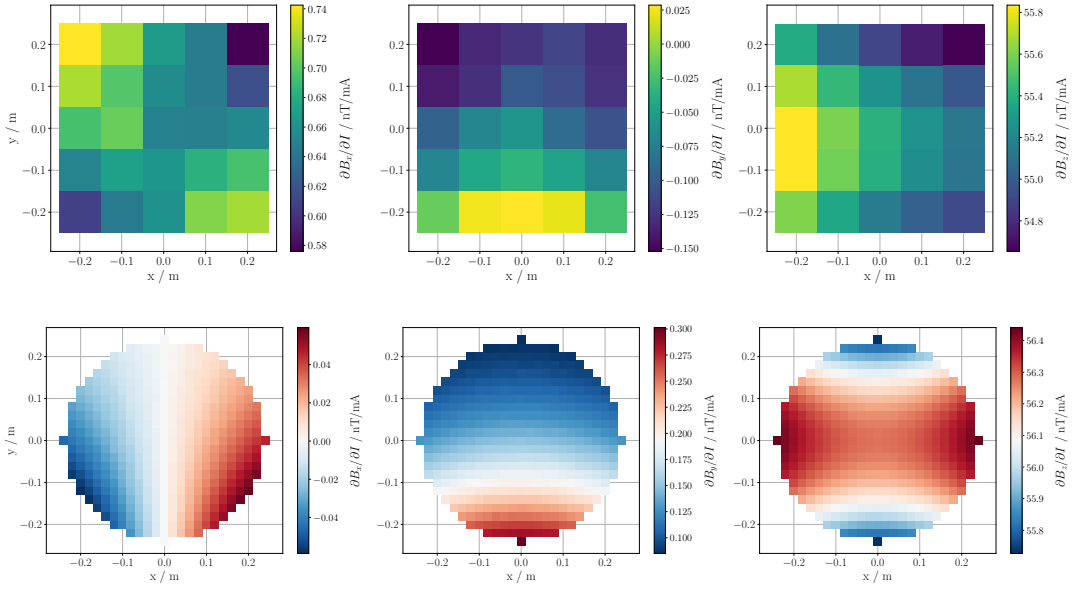

Figure E.1: B0

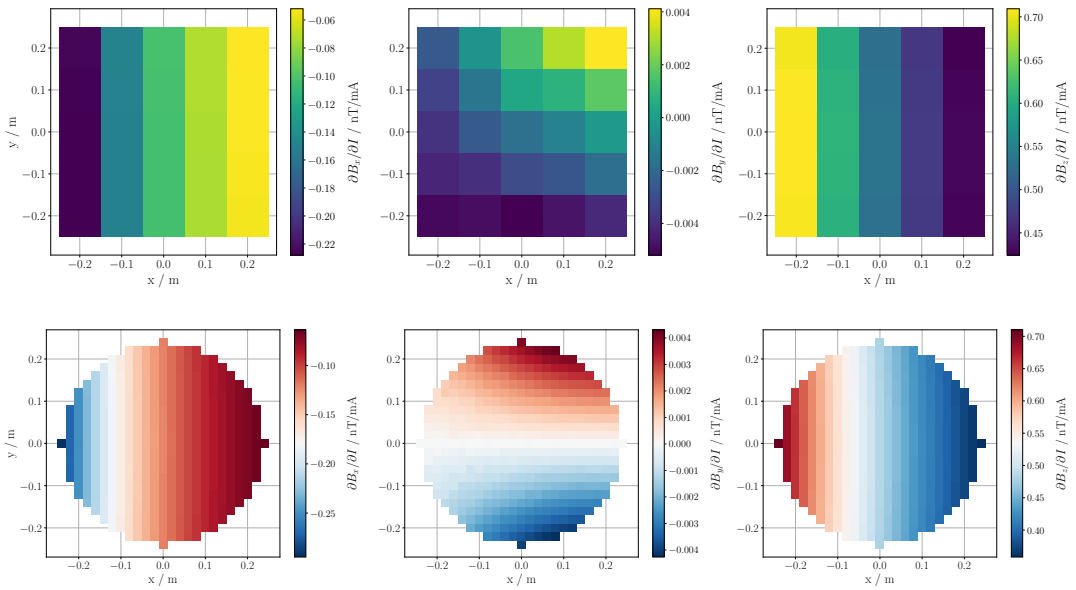

Figure E.2: cBL1

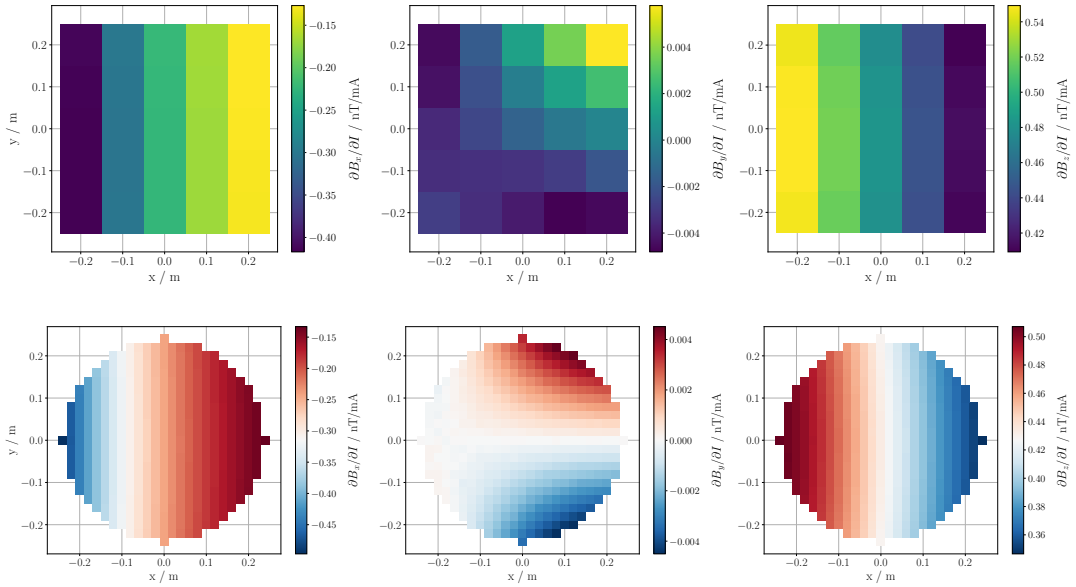

Figure E.3: cBL2

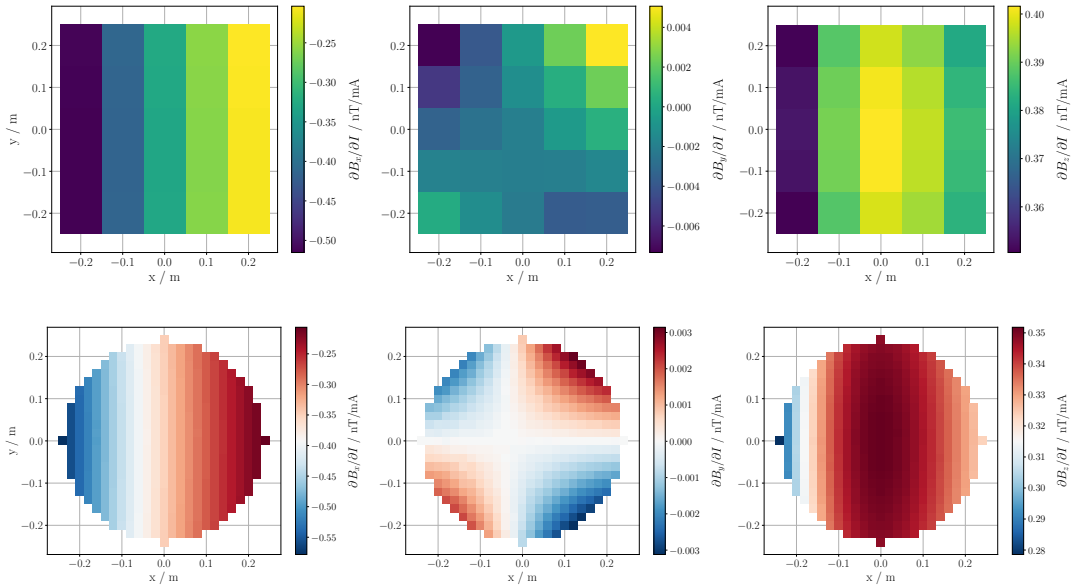

Figure E.4: cBL3

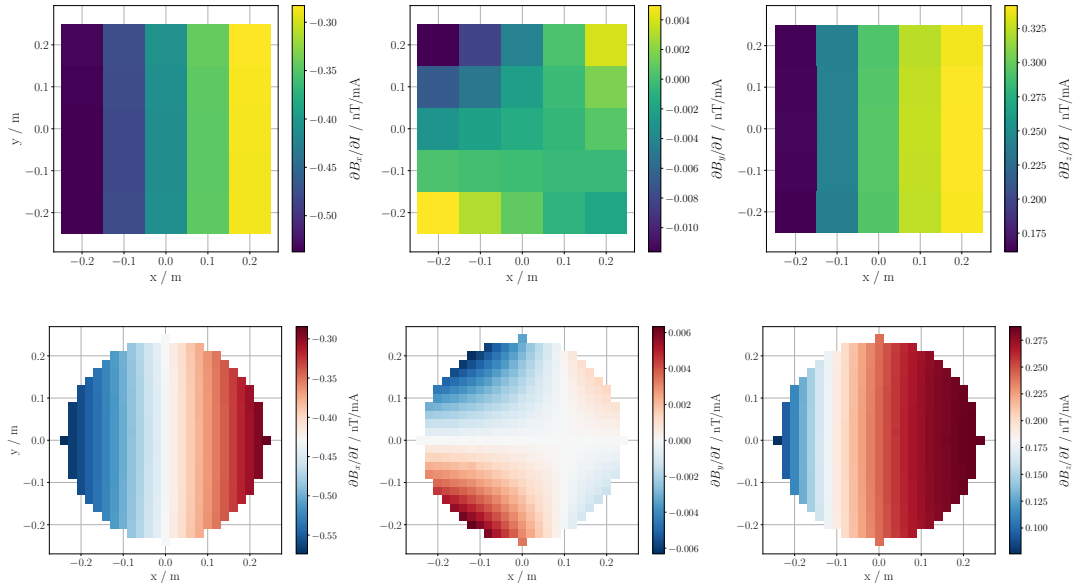

Figure E.5: cBL4

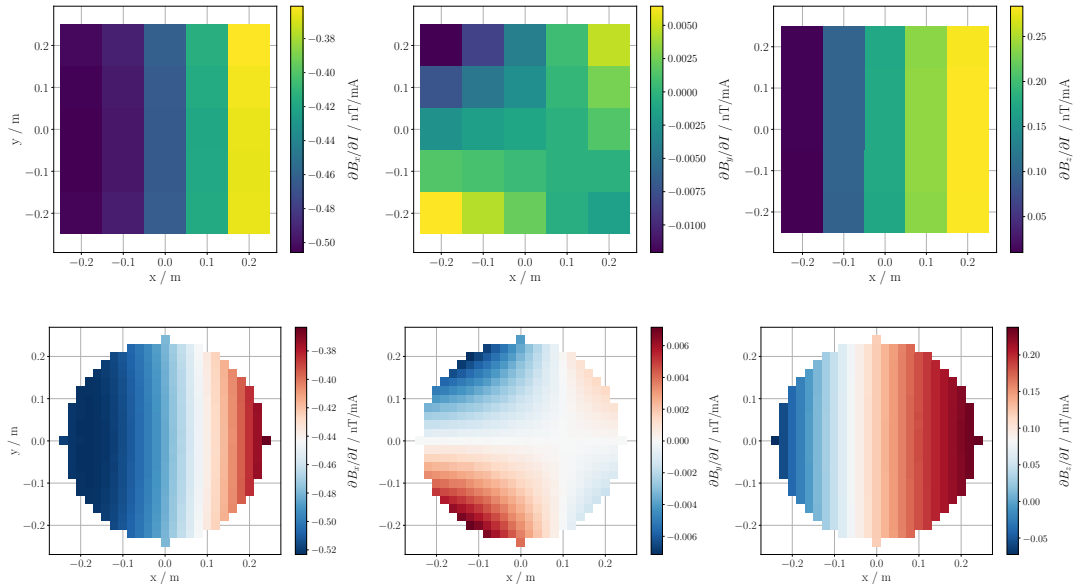

Figure E.6: cBL5

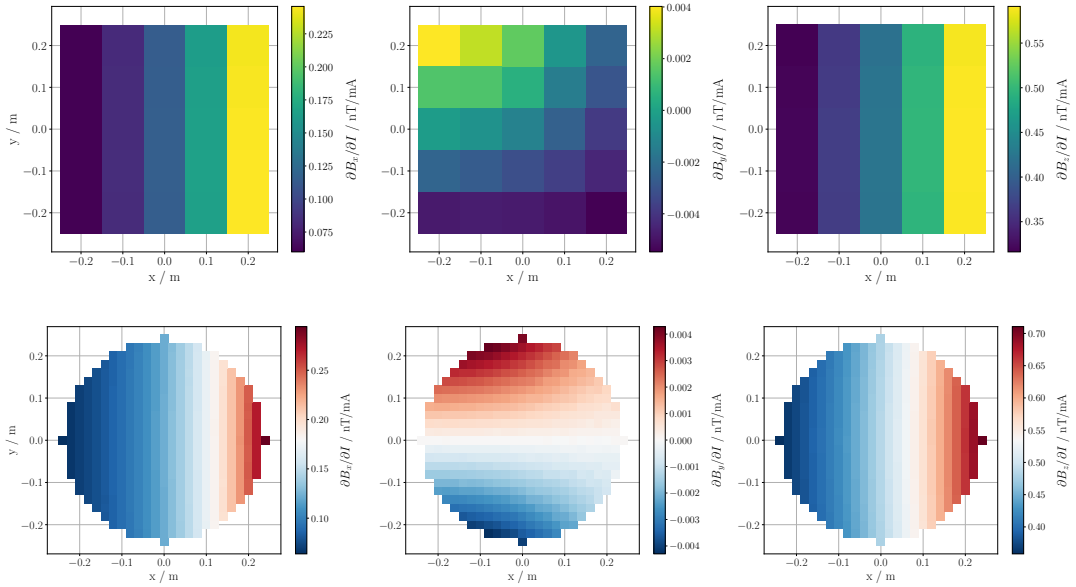

Figure E.7: cBR1

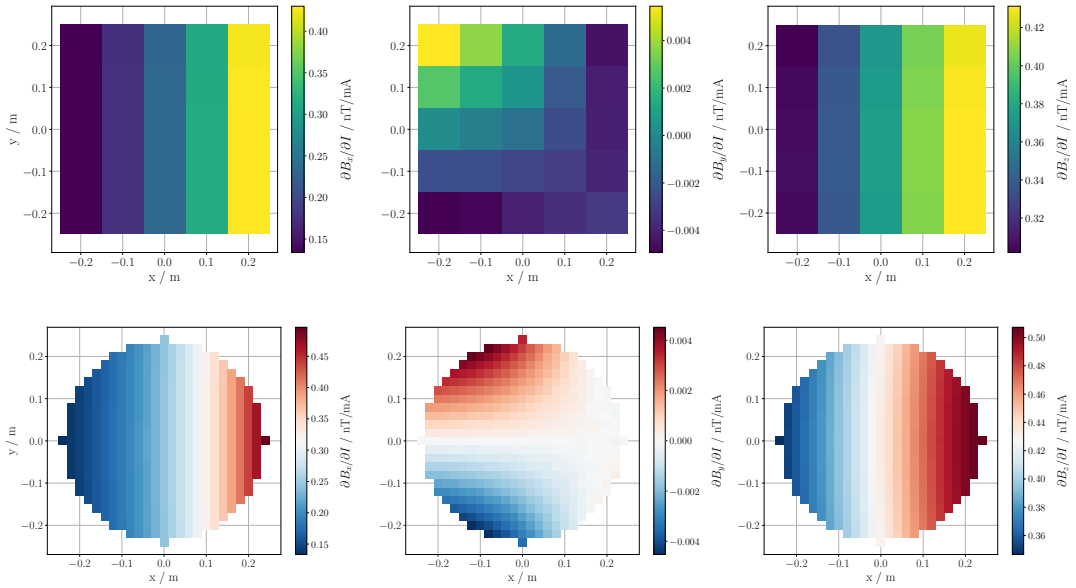

Figure E.8: cBR2

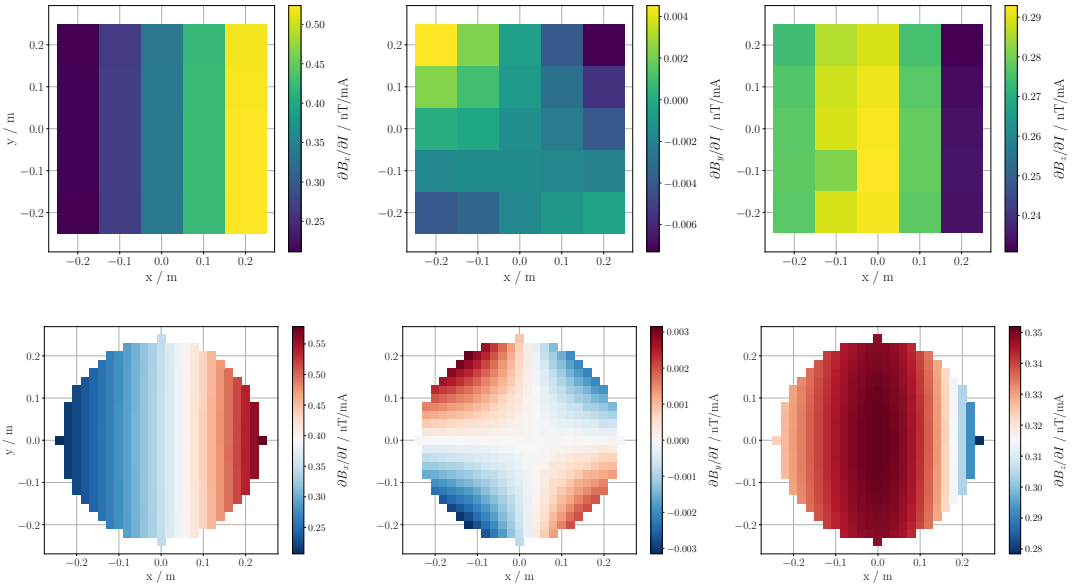

Figure E.9: cBR3

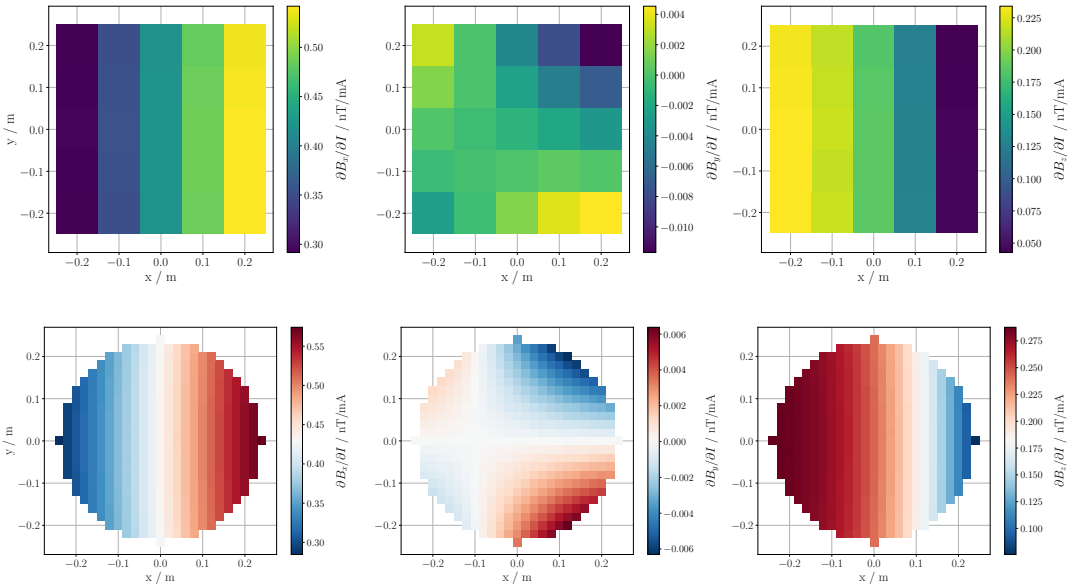

Figure E.10: cBR4

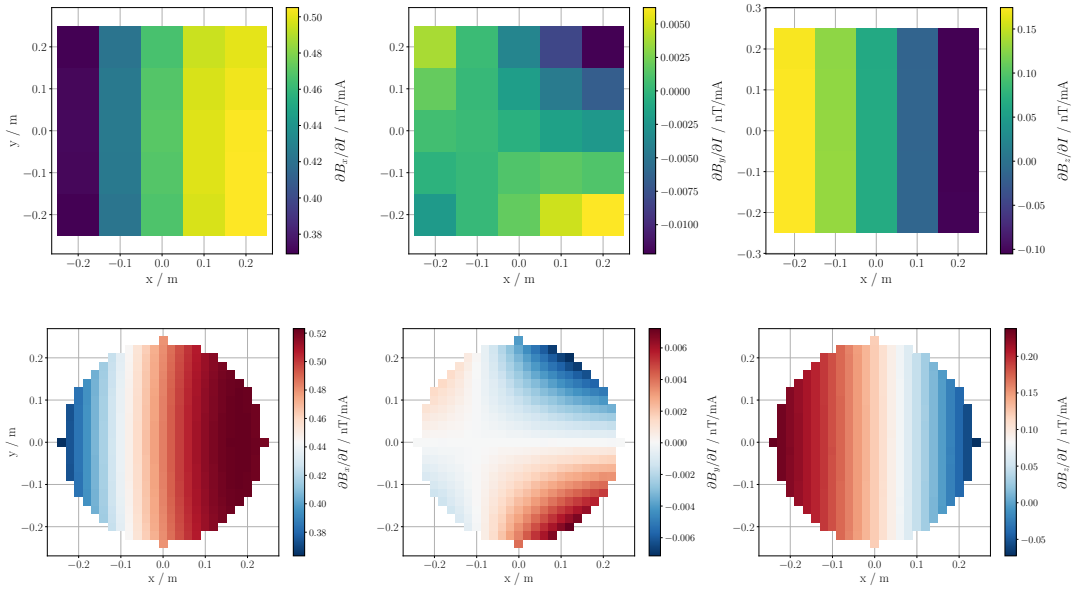

Figure E.11: cBR5

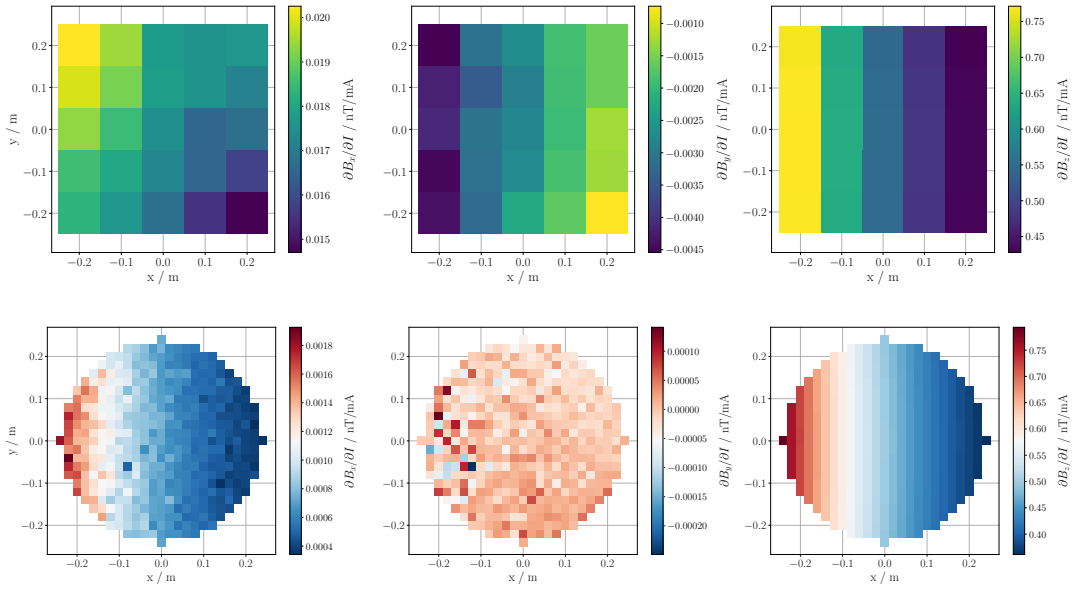

Figure E.12: cL0

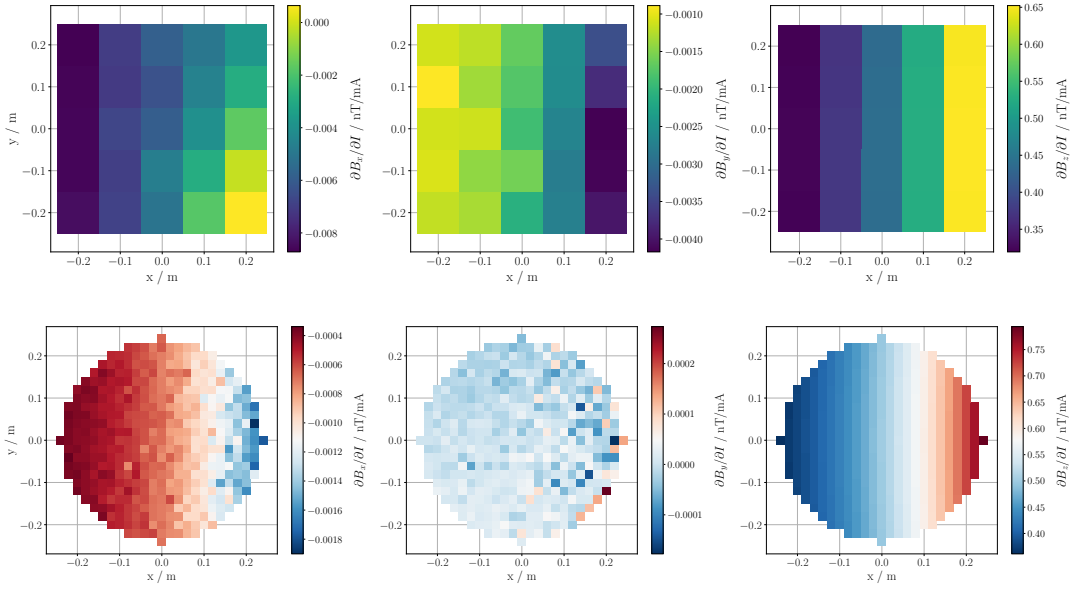

Figure E.13: cR0

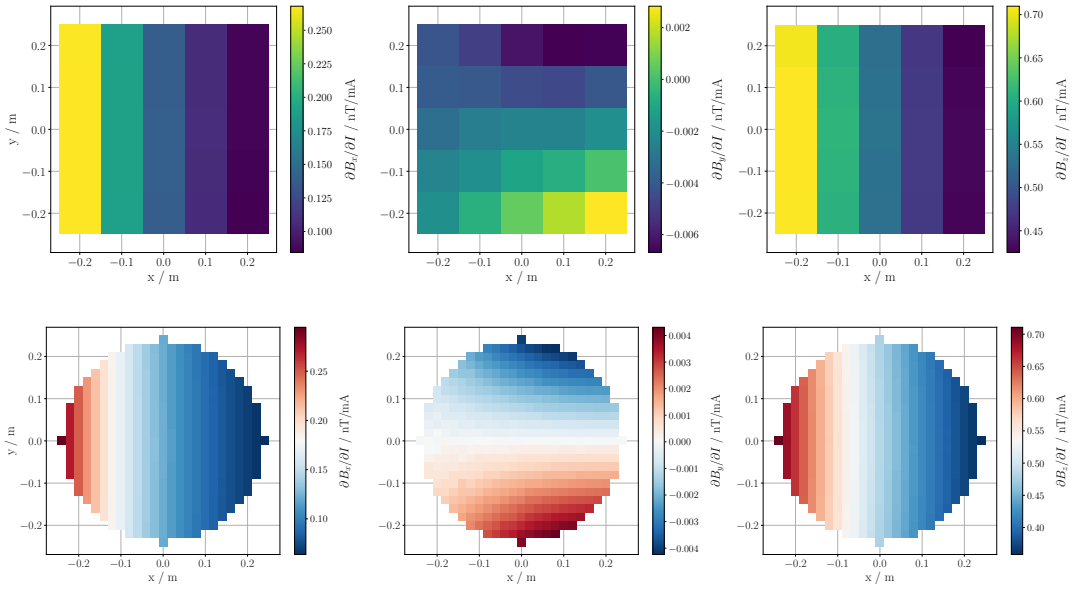

Figure E.14: cTL1

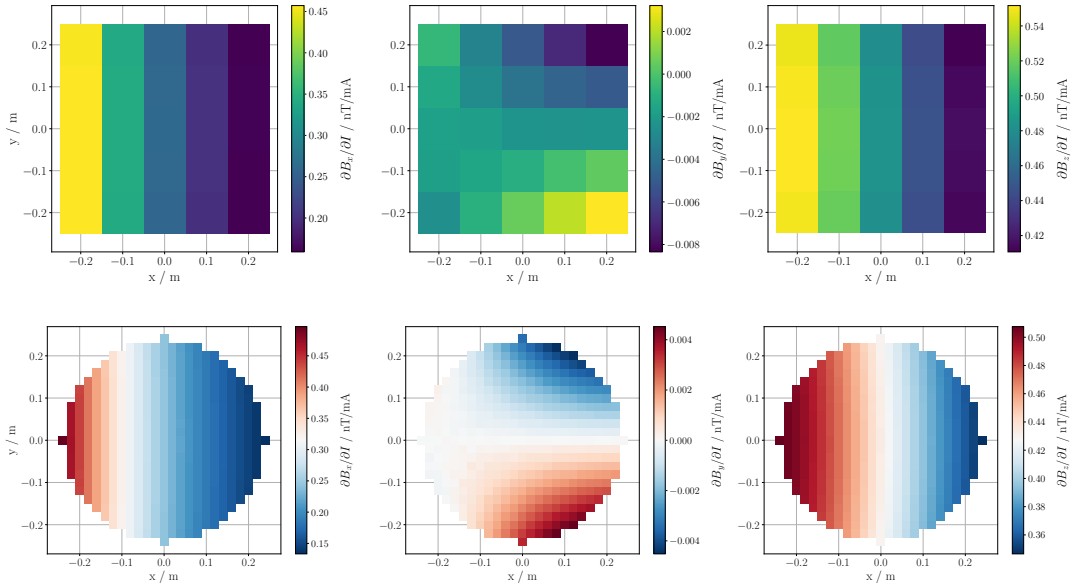

Figure E.15: cTL2

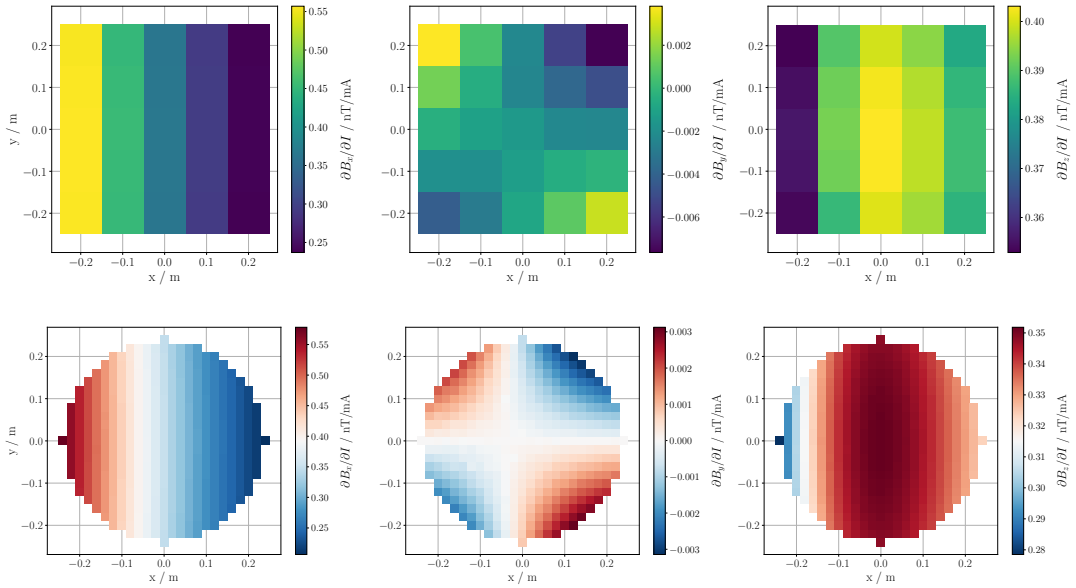

Figure E.16: cTL3

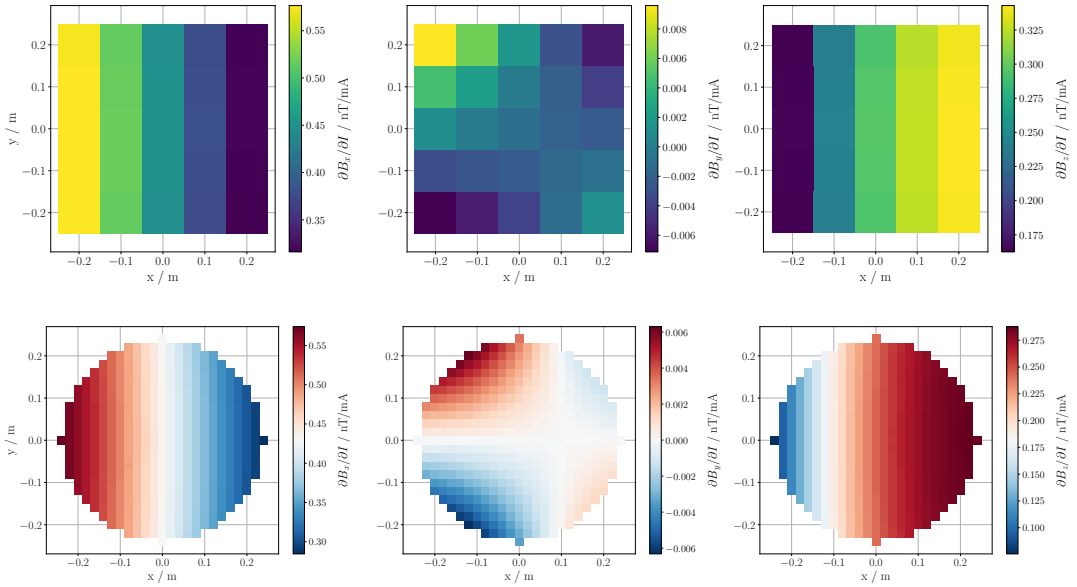

Figure E.17: cTL4

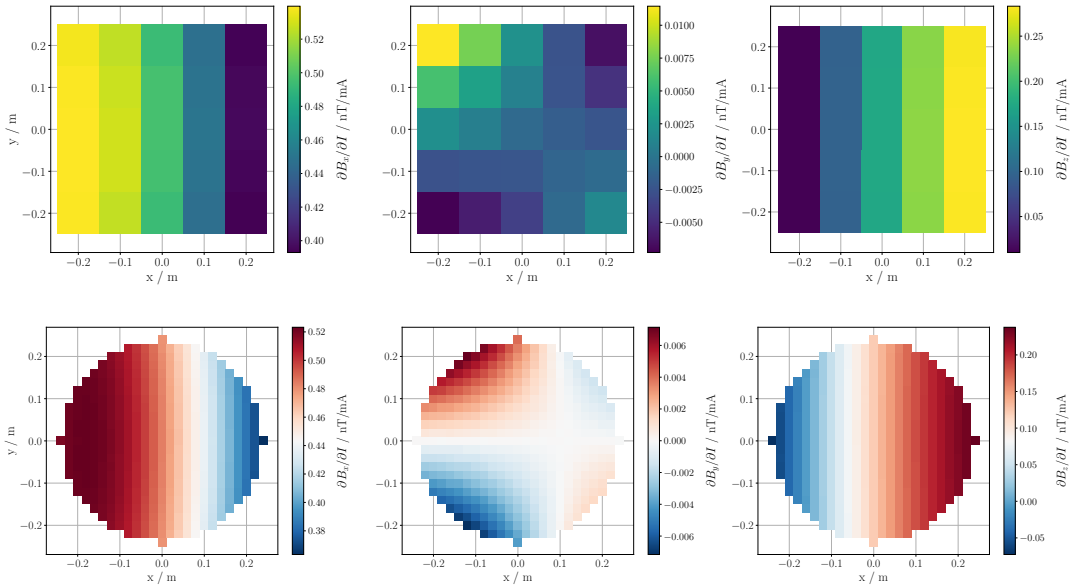

Figure E.18: cTL5

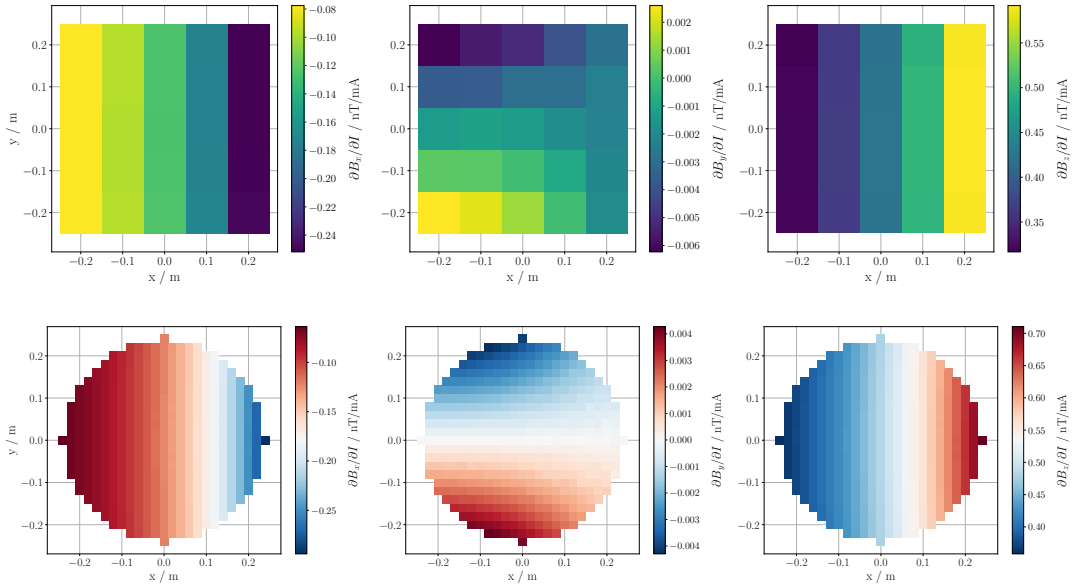

Figure E.19: cTR1

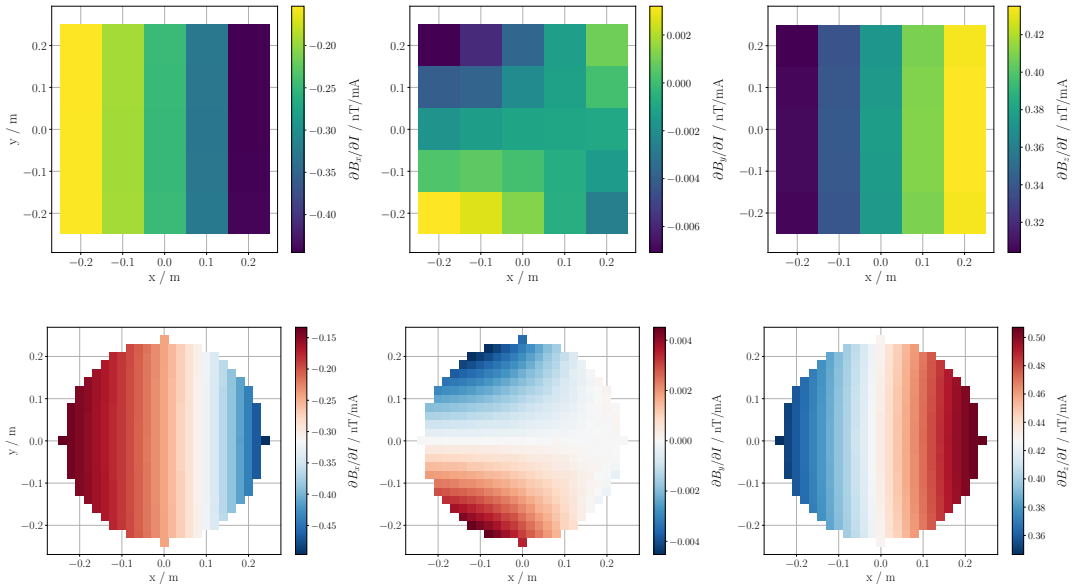

Figure E.20: cTR2

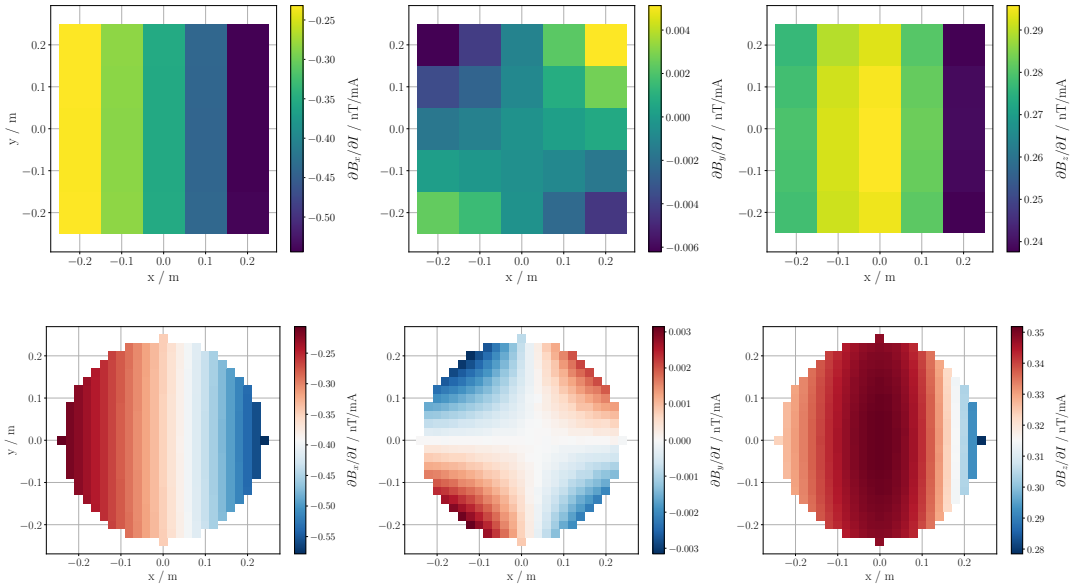

Figure E.21: cTR3

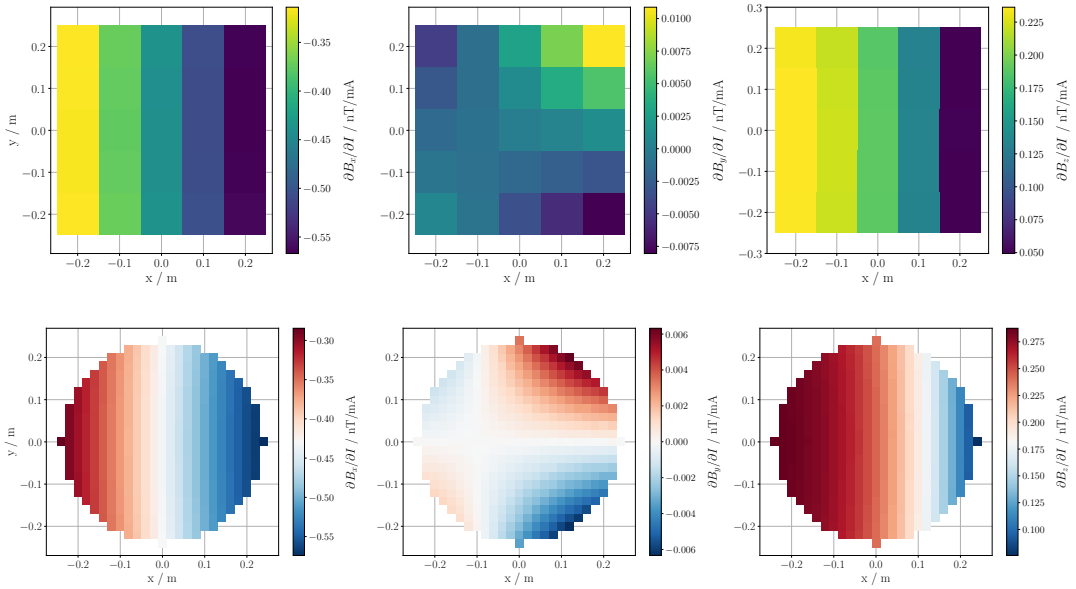

Figure E.22: cTR4

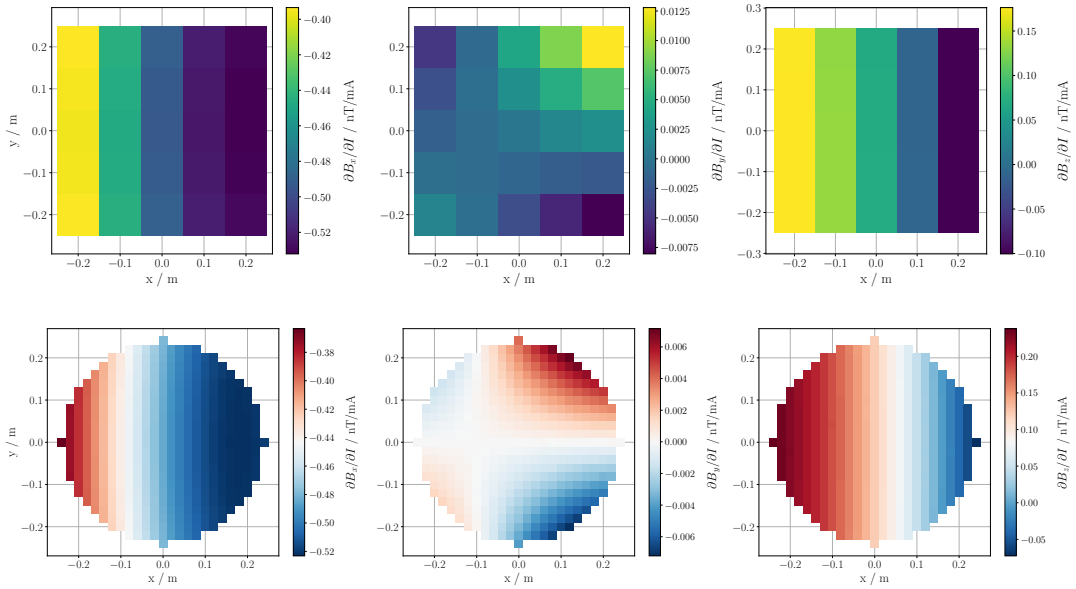

Figure E.23: cTR5

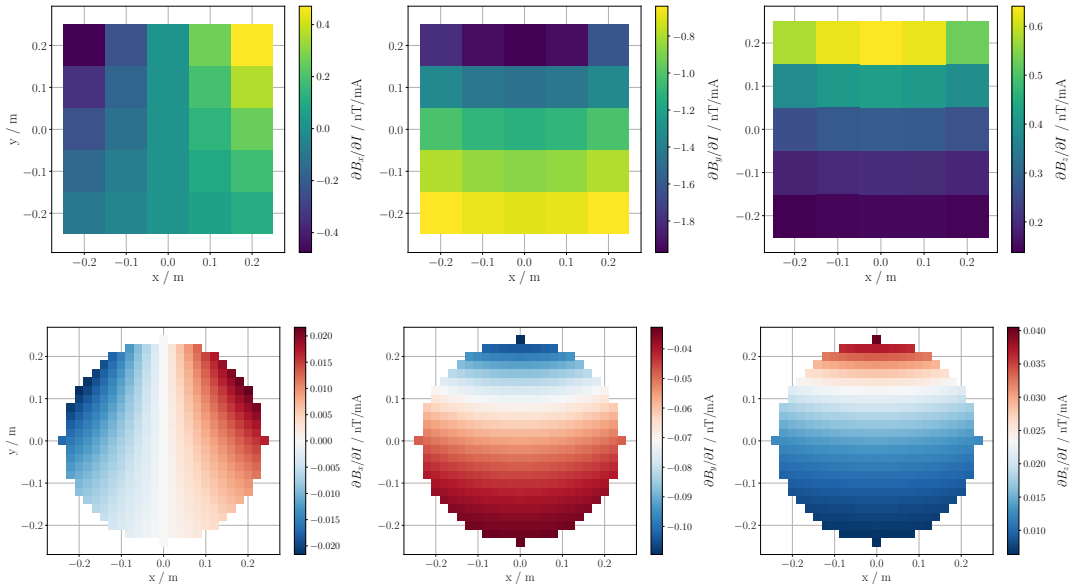

Figure E.24: eBB1

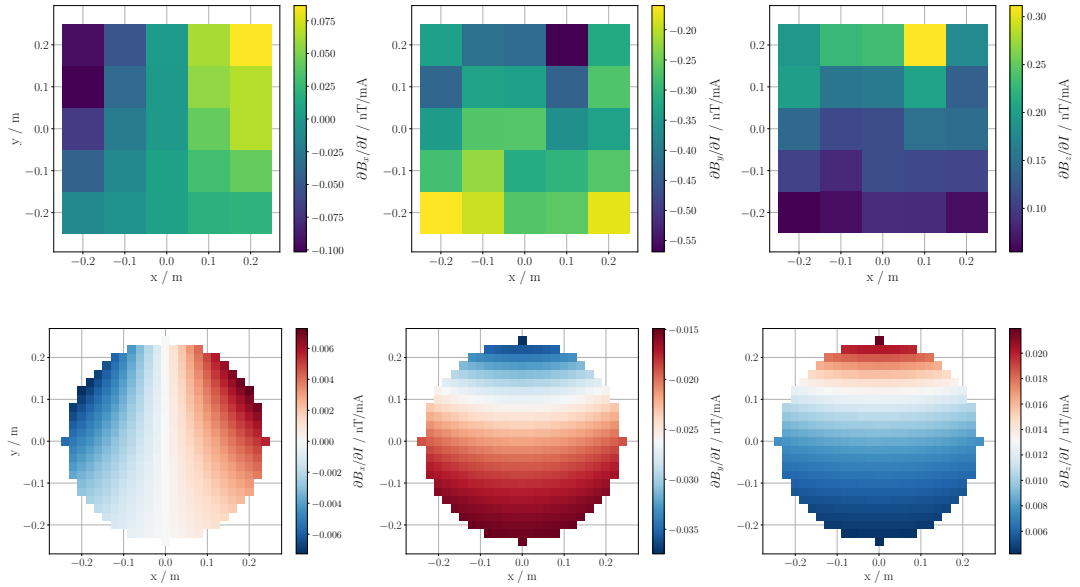

Figure E.25: eBB2

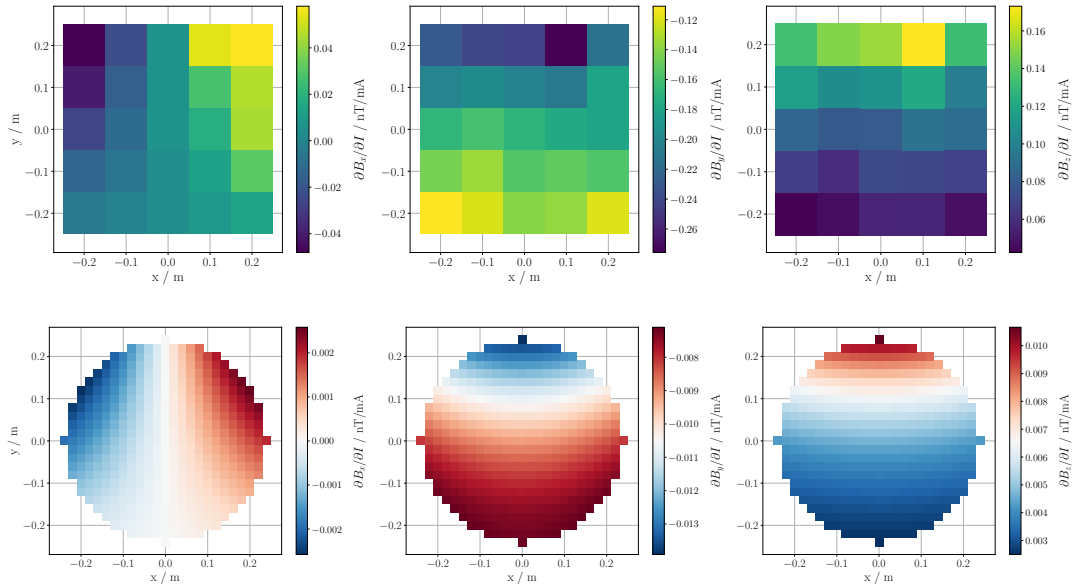

Figure E.26: eBB3

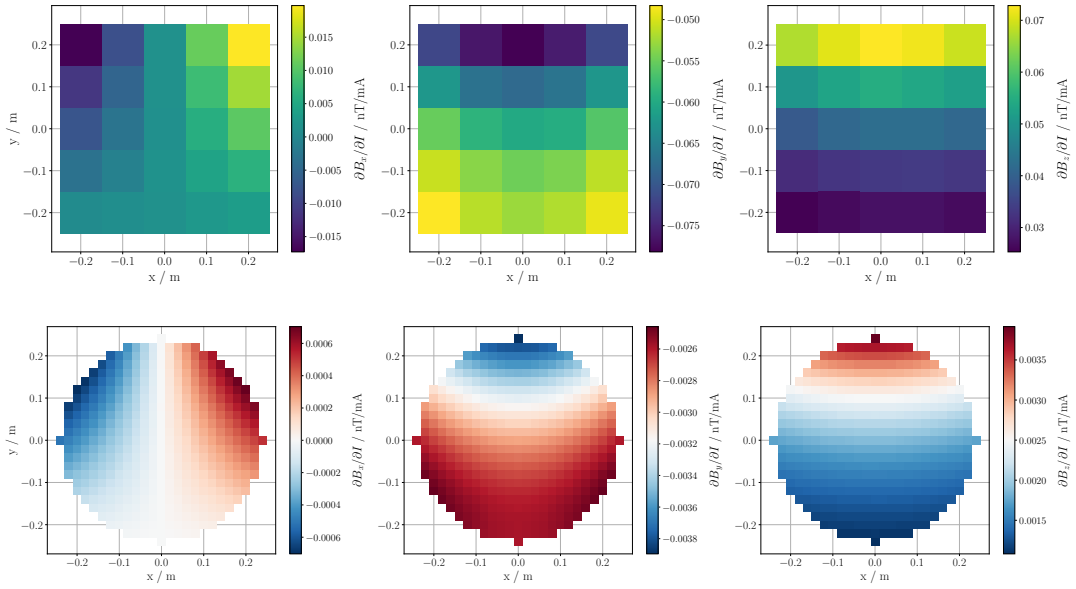

Figure E.27: eBB4

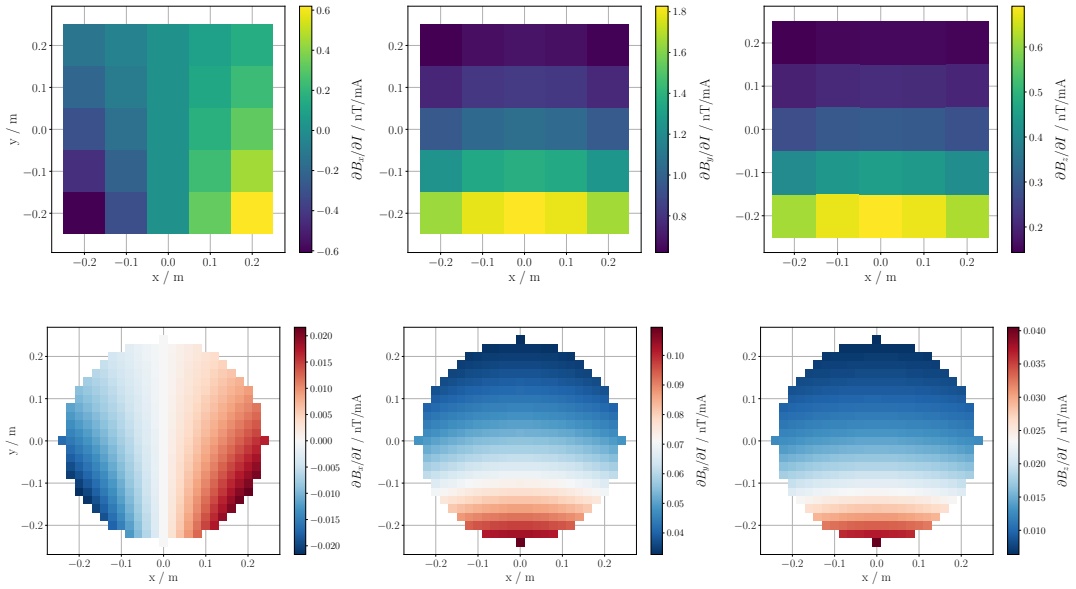

Figure E.28: eBF1

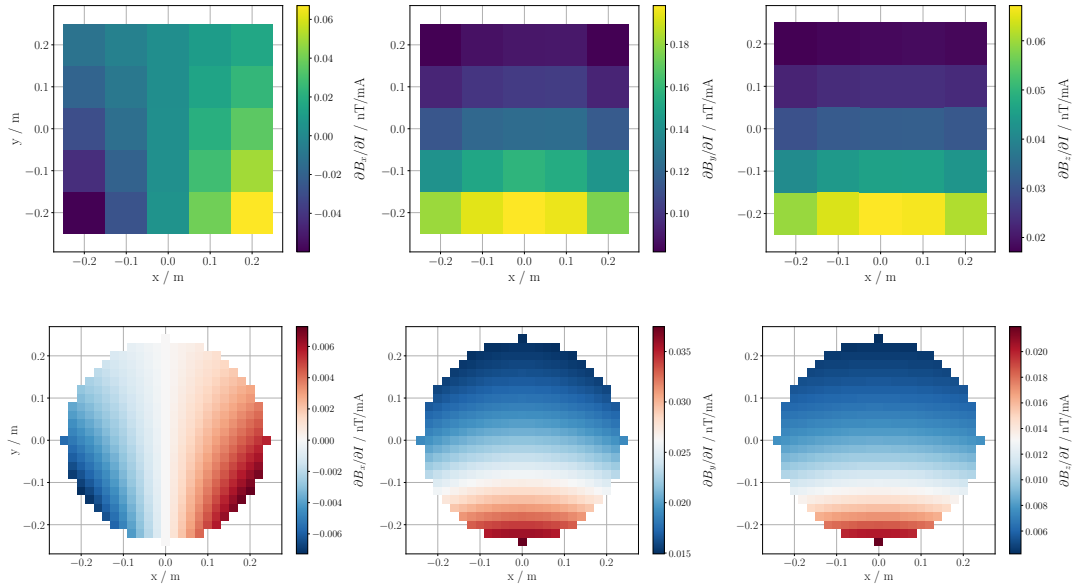

Figure E.29: eBF2

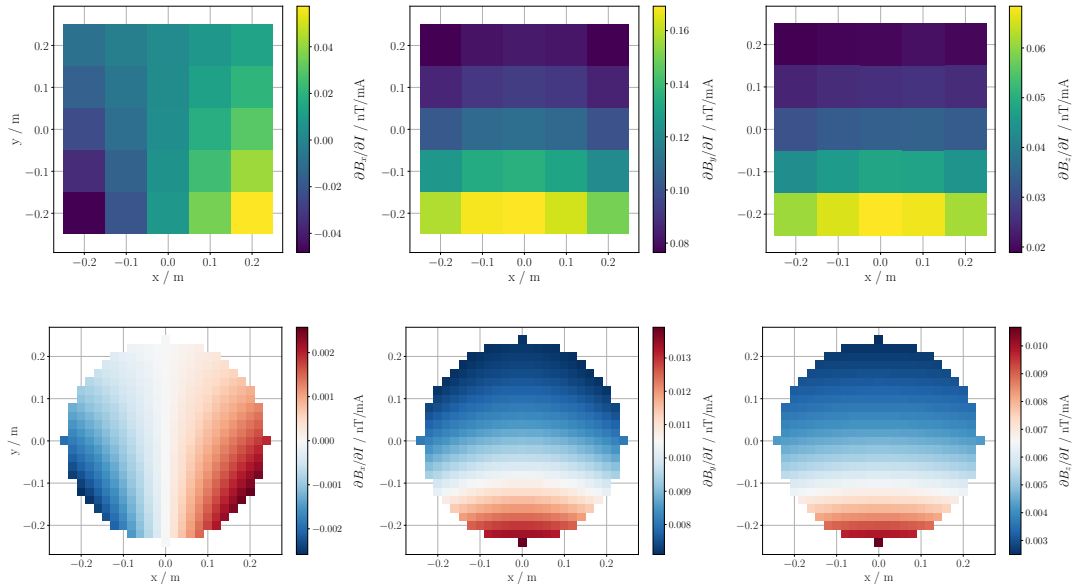

Figure E.30: eBF3

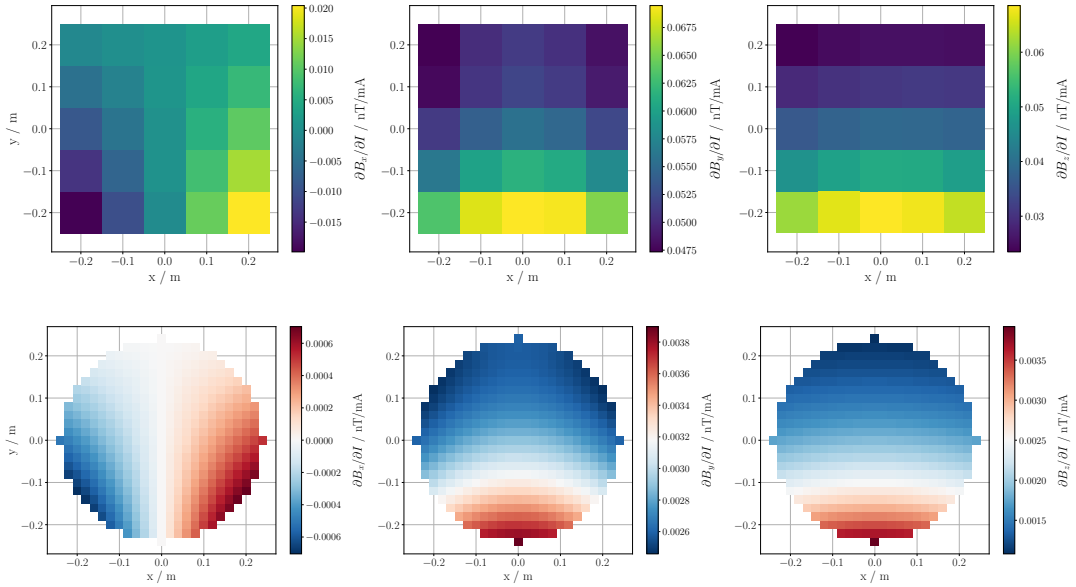

Figure E.31: eBF4

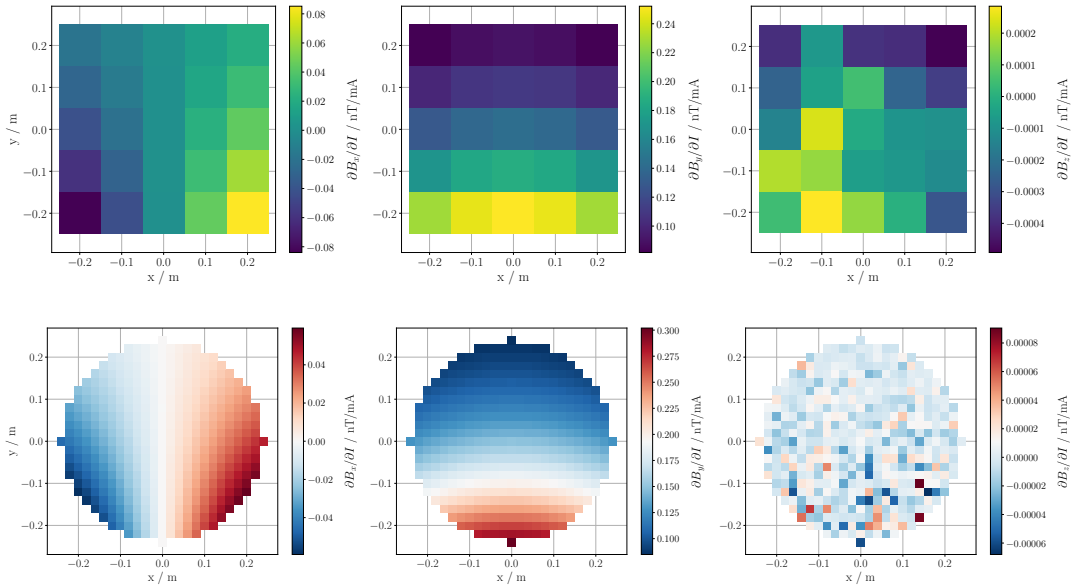

Figure E.32: eF

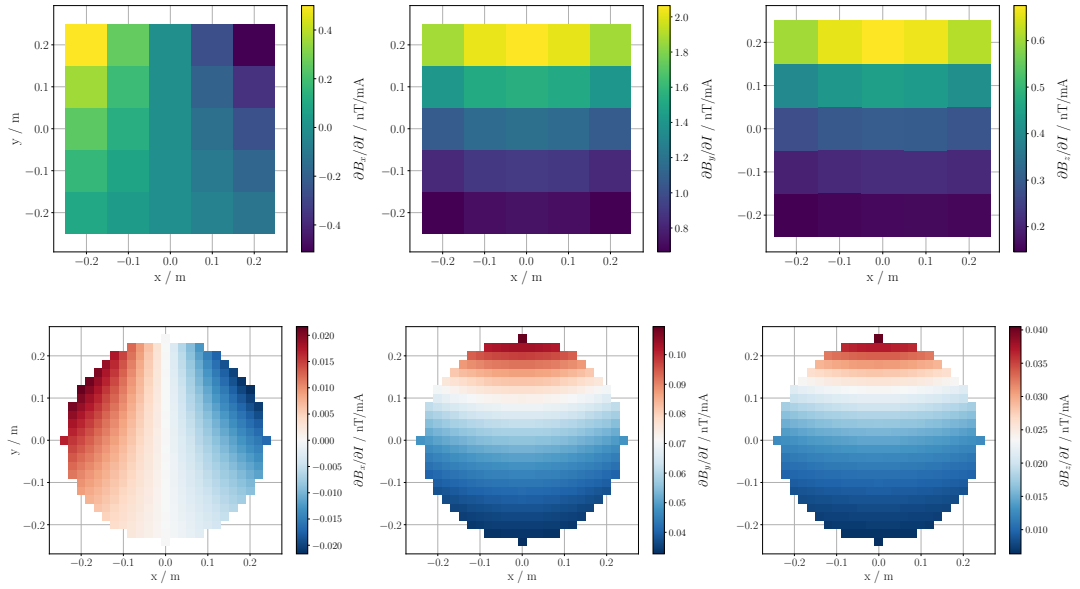

Figure E.33: eTB1

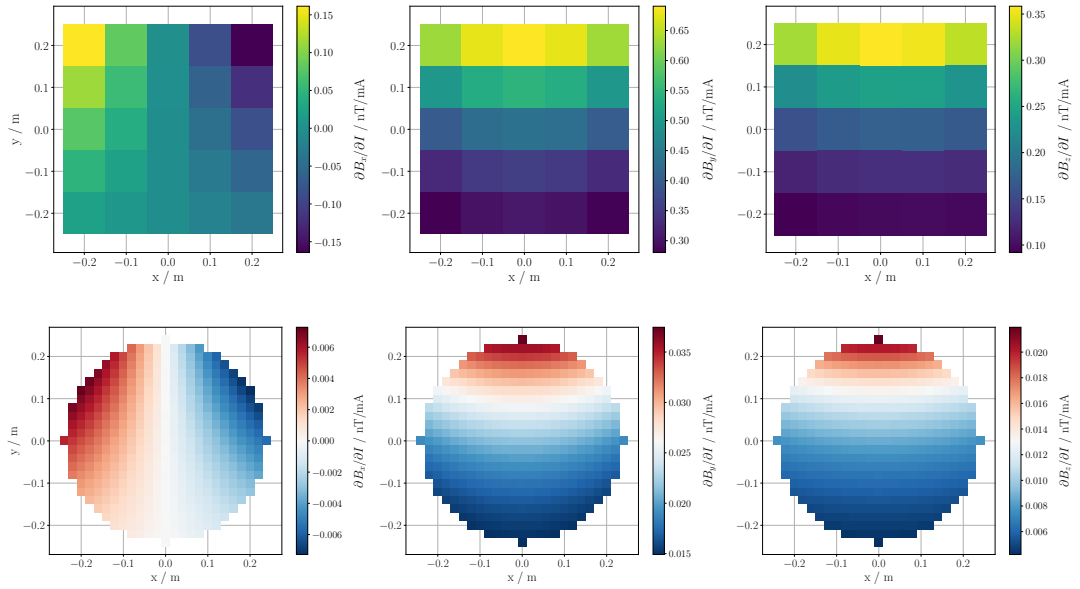

Figure E.34: eTB2

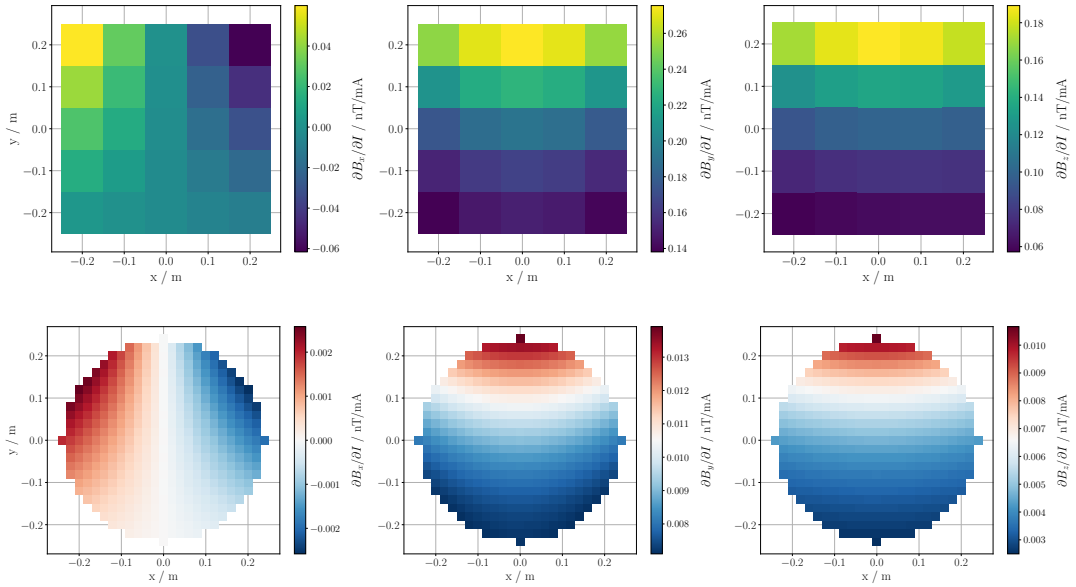

Figure E.35: eTB3

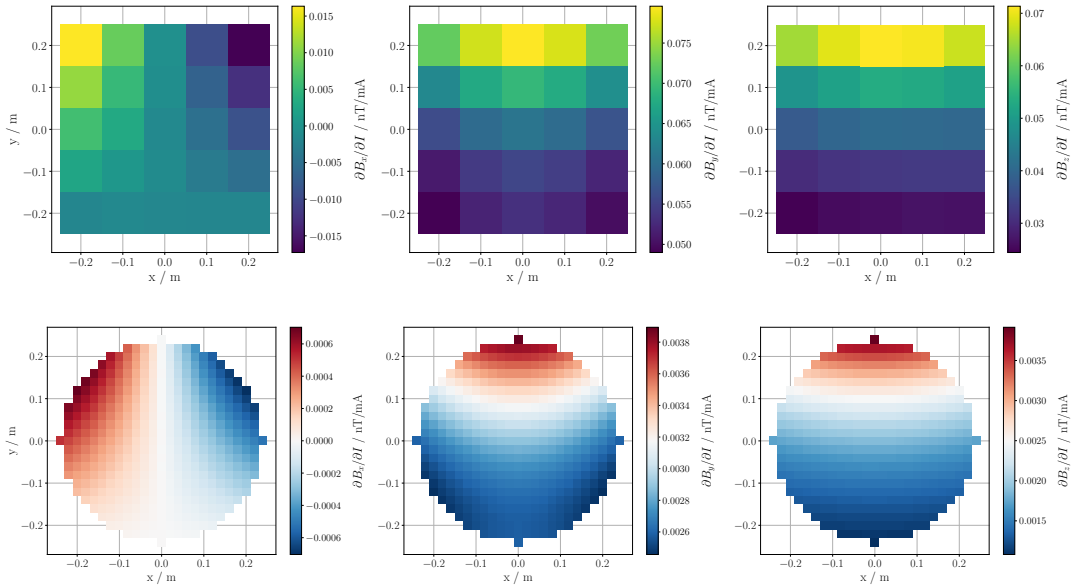

Figure E.36: eTB4

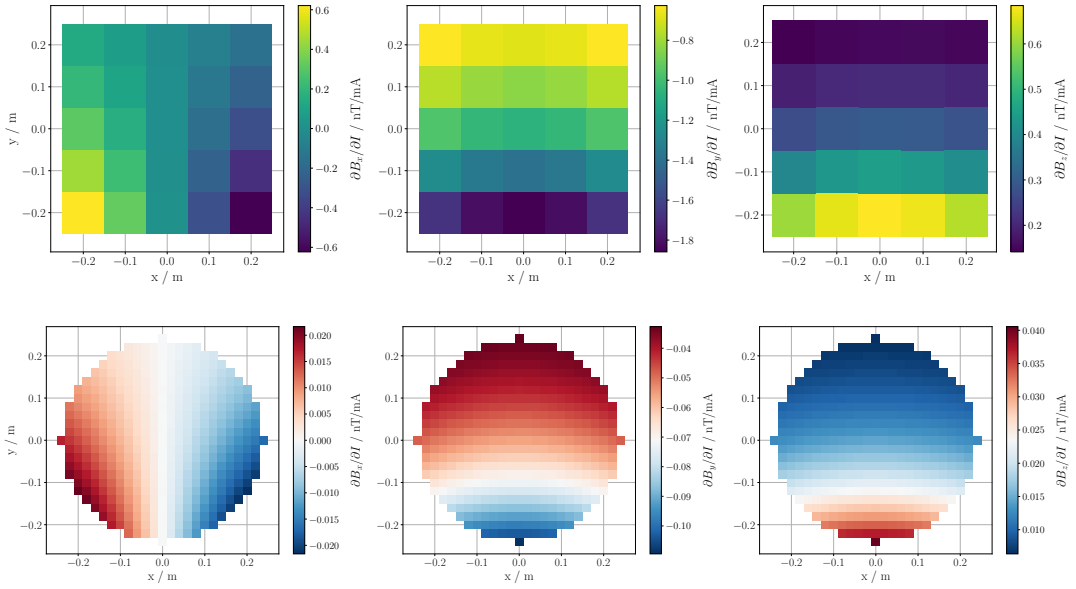

Figure E.37: eTF1

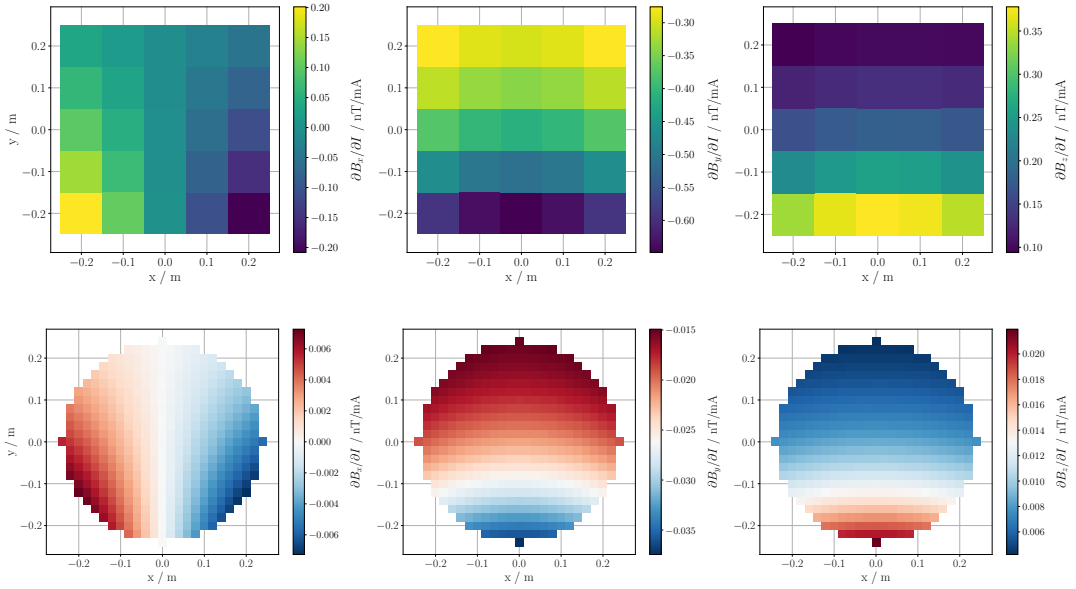

Figure E.38: eTF2

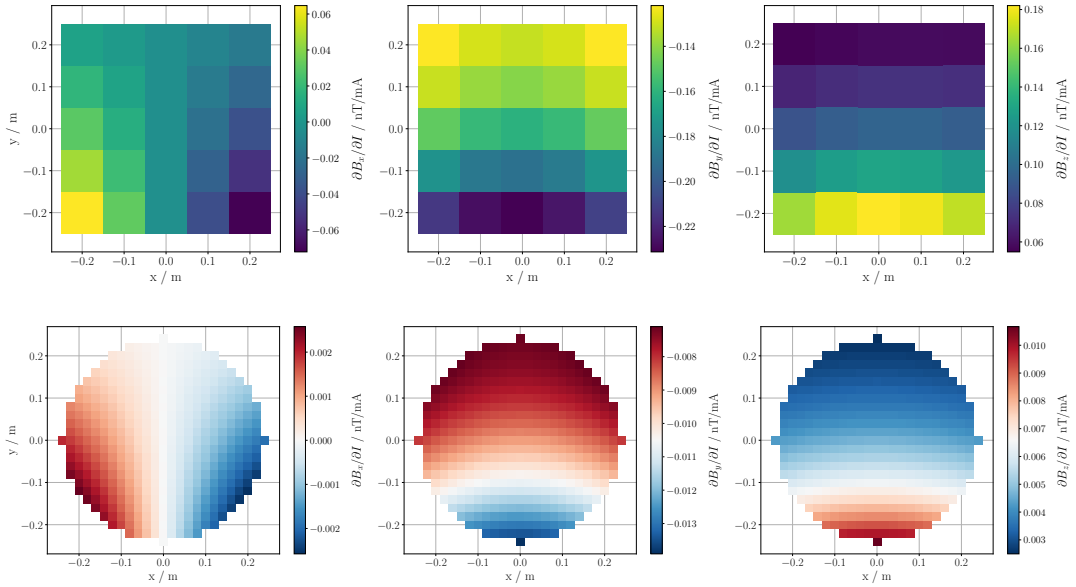

Figure E.39: eTF3

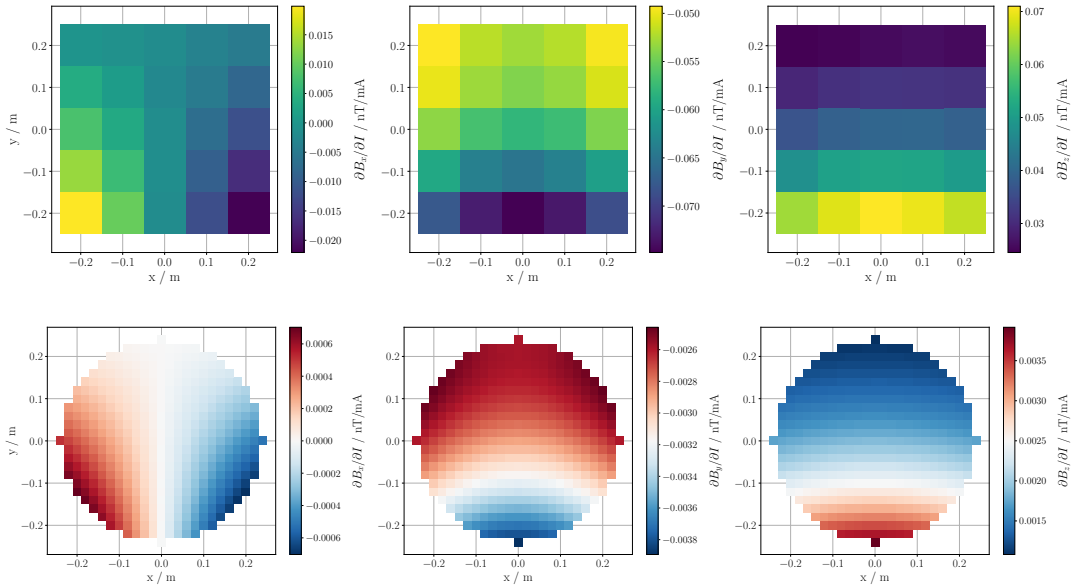

Figure E.40: eTF4